Towards many-body physics with Rydberg-dressed cavity polaritons

by

Hyeran Kong

A thesis
presented to the University of Waterloo
in fulfillment of the
thesis requirement for the degree of
Master of Science
in
Physics (Quantum Information)

Waterloo, Ontario, Canada, 2018

Abstract

An exciting frontier in quantum information science is the creation and manipulation of bottom-up quantum systems that are built and controlled one by one. For the past 30 years, we have witnessed significant progresses in harnessing strong atom-field interactions for critical applications in quantum computation, communication, simulation, and metrology. By extension, we can envisage a quantum network consisting of material nodes coupled together with infinite-dimensional bosonic quantum channels. In this context, there has been active research worldwide to achieve quantum optical circuits, for which single atoms are wired by freely-propagating single photons through the circuit elements. For all these systems, the system-size expansion with atoms and photons results in a fundamental pathologic scaling that linearizes the very atom-field interaction, and significantly limits the degree of non-classicality and entanglement in analog atom-field quantum systems for atom number $N \gg 1$.

The long-term motivation of this MSc thesis is (i) to discover new physical mechanisms that extend the inherent scaling behavior of atom-field interactions and (ii) to develop quantum optics toolkits that design dynamical gauge structures for the realization of lattice-gauge-theoretic quantum network and the synthesis of novel quantum optically gauged materials. The basic premise is to achieve the strong coupling regime for a quantum many-body material system interacting with the quantized fields of an optical cavity. Our laboratory effort can be described as the march towards "many-body QED," where optical fields acquire some properties of the material interactions that constrain their dynamical processes, as with quantum field theories. While such an effort currently do not exist elsewhere, we are convicted that our work will become an essential endeavor to enable cavity quantum electrodynamics (QED) in the bona-fide regime of quantum many-body physics in this entanglement frontier.

In this context, I describe an example in Chapter 2 that utilizes strong Rydberg-Rydberg interactions to design dynamical gauge structures for the quantum square ice models. Quantum fluctuations driven by cavity-mediated infinite-range interaction stabilize the quantum-gauged system into a long-range entangled quantum spin liquid that may be detected through the time-ordered photoelectric statistics for photons leaking out of the cavity. Fractionalized "spinon" and "vison" excitations can be manipulated for topological quantum computation, and the emergent photons of artificial QED in our lattice gauge theoretic system can be directly measured and studied.

The laboratory challenge towards strongly coupled cavity Rydberg polaritons encompasses three daunting research milestones that push the technological boundaries beyond

of the state-of-the-arts. In Chapter 3, I discuss our extreme-high-vacuum chamber (XHV) cluster system that allows the world's lowest operating vacuum environment $P \simeq 10^{-13}$ Torr for an ultracold AMO experiment with long background-limited trap lifetimes. In Chapter 4, I discuss our ultrastable laser systems stabilized to the ultra-low-expansion optical cavities. Coupled with a scalable field-programmable-gate-array (FPGA) digital-analog control system, we can manipulate arbitrarily the phase-amplitude relationship of several dozens of laser fields across 300 nm to 1550 nm at mHz precision. In Chapter 5, we discuss the quantum trajectory simulations for manipulating the external degrees of freedom of ultracold atoms with external laser fields. Electrically tunable liquid crystal lens creates a dynamically tunable optical trap to move the ultracold atomic gases over long distance within the ultra-high-vacuum (UHV) chamber system.

In Chapter 6, I discuss our collaborative development of two science cavity platforms – the "Rydberg" quantum dot and the many-body QED platforms. An important development was the research into new high-index IBS materials, where we have utilized our low-loss optical mirrors for extending the world's highest cavity finesse $F \sim 500$k! We discuss the unique challenges of implementing optical cavity QED for Rydberg atoms, which required tremendous degrees of electromagnetic shielding and field control. Single-crystal Sapphire structure, along with Angstrom-level diamond-turned Ti blade electrodes, is utilized for the field compensation and extinction by > 60 dB. Single-crystal PZTs on silica V-grooves are utilized for the stabilization of the optical cavity with length uncertainty less than 1/100 of a single nucleon, along with extreme level of vibration isolation in a XHV environment. The capability to perform in-situ RF plasma cleaning allows the regeneration of optical mirrors when coated with a few Cs atoms. Lastly but not the least, we combine single-atom resolution quantum gas microscopy technique with superpixel holographic algorithm to project arbitrary real-time reconfigurable diffraction-limited optical potential landscapes for the preparation of low-entropy atom arrays.

Acknowledgements

"If we hold on together, I know our dreams will never die."

– In the animation, "The land before time"

I would like to take this opportunity to thank the advisory committee, Prof. Kevin Resch, Prof. Raymond Laflamme and Prof. Jeff Chen. Thanks to your thoughtful consideration and advice, I was able to continue and complete my master program. I would also like to thank Prof. Na Young Kim, who came to my thesis defense as the external member and gave me critical suggestions.

My thesis is really the result of the hard work by many people. Over the past few years, we pursued the experiment with the laser-sharp focus and belief that we could make concrete steps towards the daunting goal of many-body QED. I could have only made this far, thanks to my colleagues, Prof. Kyung Soo Choi, Dr. Chang Liu, Dr, Mahmood Sabooni, Dr. Ying Dong, Yoon Seok Lee and Sainath Motlakunta.

I would like to first thank my research mentor, Prof. Kyung Soo Choi. First and foremost, he has given me a chance to prove myself, when I had absolutely nothing but heart. It has been a privilege for me to work with him as the first graduate student in the laboratory of Ultracold Quantum Matter and Light (UQML). For the better or worse, by way of his scientific integrity, he has taught me by example the true joy of doing hard science and guided me towards embarking on a scientific career. Besides tranferring scientific knowledge, Prof. Choi has taught me the importance of finding a good taste and taking a risk in research with a long-term vision. At times, when things weren't going as expected, he pursued science with brutal integrity and honesty, even if he knew that those hard decisions would end up returning back and hurt him personally. I deeply appreciate his mentorship, hardwork and all the valuable advice that I have received. I learned that details do matter. I remember the sleepless nights with him in the laboratory, turning on the first home-built external cavity diode laser. The atomic fluorescence and the first "light" in this laboratory were built upon Prof. Choi's patience (piles of electronic circuits that I had blown up to build the very power supply that powered our home-built laser controller). This experience has changed my view of doing science. For the first time, I could be passionate about learning, as if I was a child, but with a focus and conviction of an idea in life that is greater than myself. My scientific growth has been possible because of his priceless effort and creativity in the laboratory and the sincere trust on my capability, even when I had doubts on myself.

Since 2015, I have been working with Dr. Chang Liu, a talented postdoctoral fellow for more than 3 years. She was always willing to learn and acquire technical skills, and two of us transformed the initially empty room to a thriving AMO laboratory. Her quiet leadership and modest attitude for collaboration gave me a deep inspiration of doing science together. Recently, she has moved on with her new career in the QVIL, and wish her the best for her future career.

From the summer of 2016, Dr. Mahmood Sabooni joined the group and has made critical progresses to the experiment by developing quantum gas microscope and holographic image projection techniques in our laboratory. This highly technical and challenging project was only possible because of his persistency and focus, and I learned a great deal of physics from him. I sincerely appreciate him for the consistent effort on the project and sharing his valuable experience, and for the perseverance in the laboratory.

Although I only had a year to work with him, Sainath Motlakunta was a passionate colleague who taught others about electronics. He is a walking book of "Arts of Electronics." I will never forget the time we worked together in the electronics room. From the Winter 2018, I have received a great help from Youn Seok Lee to finalize our infrastructure in our lab. Even though he was leading the waveguide QED laboratory, he was available to give me a hand on the optics setup and the electronics of laser cooling systems. I would also like to thank Dr. Ying Dong, our genius theoretician, who comes up with the most brilliant ideas one could ever hope for. All of us in the laboratory side of things learned greatly from his "lectures" in the group meeting, but also from the way he discusses physics with Prof. Choi with such clarity.

I thank Karen Klassen, Claire Warner, Leo Kim, Yu Zheng, Diego Costa, and Ahreum Lee, all the undergraduate students whom I worked with. Karen programmed the first Labview program of the atom imaging system. Claire designed the necessary optoelectronic equipment such as the EOM and TA amplifier. Leo, Diego, and Yu built four laser controllers, and I'd like to especially thank Leo for being part of the arduous process of UHV viewport assembly and cleaning! They have all contributed to the laboratory building. Ahreum helped to design digital direct synthesizers, which are now ubiquitously used for laser stabilization in our laboratory. Finally, I would like to say thanks to my first lab and office-mate, Vinay Iyer. Give my regards to you.

Besides the work at Waterloo, I have been greatly supported to pursue my dream, thanks to my devoted family. First, let me just say that both my husband and I believe that my sweet little son, Eugene Choi, is a gift of God :) Eugene is the reason why we were able to pursue our dreams and to stay strong, despite the difficult journey that we all had to go through. I would like to express my gratitude and love to Kyung and Eugene. We can overcome all the hardship if we are together.

Throughout my life, I was fortunate to have been surrounded by such loving family.

I would like to thank my parents, Byung-eun Lee and Byung-goo Kong, for believing me and loving me without return. I also thank my sister (Ahran Kong) and brother (Minje Kong) for always being the closest friends. Their unconditional love has made me what I am. Lastly but not least, I appreciate my parents-in-law (Mansoo Choi and Youngsook Son) for their love and for praying for the well-being of our family.

Dedication

This thesis is dedicated our son, Eugene Choi.

Table of Contents

List of Tables

List of Figures

Chapter 1

Introduction

1.1 Towards quantum many-body network

The capability to create and manipulate entanglement and quantum states between light and matter provides crucial resources for critical applications in quantum information science [1, 2, 3, 4, 5, 6, 7]. Indeed, a major challenge in the experimental approaches with atomic, molecular, optical (AMO) systems in the past decades has been the scaling of laboratory complexities associated with the weak physical strengths of the controlled interactions between the atoms that encode some quantum information in their ground states [2]. Compared to solid-state quantum systems [7], the dynamical timescales for coherent atom-atom interactions is very weak (e.g., $\sim$ 1 kHz for state-of-art ion trap quantum gates [8] and $\sim$ 100 Hz for the tunneling term in the Bose-Hubbard model for ultracold quantum gases [9]), pushing much of the interest to equilibrium phenomena and mean-field theories [10]. Furthermore, leading quantum architectures have physical bottlenecks in their scaling in terms of the physical constraints (e.g., 2D surface code for superconducting qubits [11] and micromotion heating in ion traps with large numbers of atoms [12]) that limit the quantum connectivity of the qubits and the system size [6]. For any physical system, one could argue that there will always be a physical limitation in the system size N_s (e.g., number of atoms), in which a monolithic system is expected to practically scale, due to error correlation effects that inevitably spread across the macroscopic numbers of qubits [13].

In contrast, light-matter quantum interfaces, enabled by quantum optics toolboxes with cavity quantum electrodynamics (QED) [14, 15], provide a method to create distributed quantum systems beyond of the characteristic system-size scale N_s by way of quantum connectivities of the optical channels [6]. The strong coupling regime in cavity QED provides a method to coherently transfer quantum states of a single atom to and from optical photons [16], and single-quanta-level optical nonlinearity for quantum gate operations that generate atom-photon and photon-photon entanglement. By extension of the strong coupling physics, we could envision a quantum network [6] consisting of matter quantum nodes, which coherently interact each other through the distribution and dissemination of quantum states in the optical quantum channels. Such a quantum network could be utilized for performing distributed quantum information processing by teleporting quantum resources and quantum gates [17], for creating effective Hamiltonian dynamics of the atomic quantum nodes for quantum simulation [18], and for transporting and teleporting quantum states across the nodes for quantum communication [19, 20, 21]. In Chapter 2, I will review the technical languages that describe the theory of atom-light interactions in the new regime of many-body QED. Here, I'd like to provide the overarching physical motivations and my perspectives of the experimental program developed throughout this MSc thesis in relation to the broader scope of quantum information science.

From a more physical point of view of a quantum network, it is tempting to think about the spin dynamics for the nodes of a network as some sort of renormalization of the material system mediated by their respective interactions with the infinite-dimensional bosonic channels as with quantum field theories [22]. If then, we could provide clearer low-energy theories of the many-body network with a more natural mapping to how particles interact with each other from the viewpoint of gauge field theories. More importantly, this may imply the existence of complex quantum behaviors of atom-field quantum systems that can be designed quanta-by-quanta to mimic the emergent physics of other physical systems possibly well beyond of condensed matter and atomic molecular physics.

In the next section, I will describe the limitations of cavity QED in regards to the extensions to quantum many-body physics and to the inadequacy to gauge field theories, as speculated here. We are instead interested in introducing strong atom-atom interaction in the form of Rydberg excitation [23, 24] in the presence of non-perturbative atom-field coupling. Besides the fundamental interest in understanding the nature of the strong coupling physics for many-body quantum system interacting with the cavity field, the resulting system in the Purcell regime reveals unusual characteristics that cannot be simply attributed to the atom-atom dynamics mediated by virtual non-interacting excitations of the quantum harmonic oscillators of the quantum channels, but rather strongly coupled systems with gauge bosons that impose particular energy constraints.

The creation of quantum optics building blocks to examine this unchartered territory requires the development and integration of novel experimental AMO gadgets (optical clocks, cavity QED, and quantum gases) and addressing the key challenges in cavity QED that inhibited the progress to this direction over the past 20 years [25], namely achieving strong coupling regime in the optical domain for interacting atomic quantum systems (e.g., Rydberg atoms and trapped ions in optical cavities). The resulting laboratory infrastructure is thereby not a simple extension or combination of the standard AMO laboratory toolboxes used throughout the world. The central theme of my thesis is thus addressing these outstanding technical challenges to bring our vision to fruition, beginning with the developments of our own laser and electronic systems, but I'd like to present these questions as the high-level motivations for my experimental work described in the thesis:

1. Is it possible to create analog quantum systems whose emergent physics is related to high-energy physics and quantum gravity (holographic correspondence)?
2. Can we create, control and measure new topological orders (quantum spin liquids) in many-body atomic quantum systems by way of the quantum optics toolboxes?
3. What is the nature of atom-light interaction for strongly correlated quantum materials?

I hope that future experiments with the apparatus I helped to develop in this thesis would be able to contribute to these directions in physics.

1.2 Cavity QED in the optical domain: From Jaynes-Cummings models to Tavis-Cummings Hamiltonians

In this section, I will introduce the physics of strong coupling from the perspective of (Markov and non-Markov) open quantum systems, and associate the single-atom single-photon level cooperativity parameter C with the breakdown of statistical mechanics. That is, conventional equilibrium physics has no role to play even for describing a seemingly simple situation of a single atom strongly to a high-finesse optical cavity. I will then discuss a concrete example of the Jaynes-Cummings (JC) model [26], a reduced model of a quantum Rabi model [27], that describe the energy-conserving processes of the dipole of the atom interacting with the excitations in a single-mode cavity. By extension, I will connect the physics of JC model to that of the Tavis-Cummings (TC) model [28, 29], which describe the interaction of a single-mode field with a collection of atoms. I will then describe the inherent limitations associated with the traditional cavity QED approach in

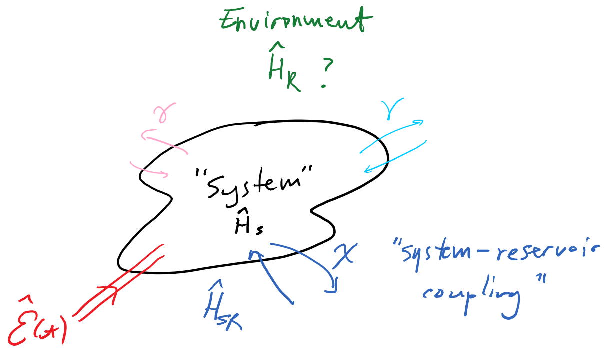

Figure 1.1: **Strong coupling parameter in open quantum dynamics.** The characteristic coupling strength χ to a particular reservoir mode (e.g., cavity mode) is compared to other dissipative rates γ_i. Sustaining quantum dynamics of the system, represented by the Hamiltonian $\hat{H}_s$, at the single quanta level in the face of decoherence requires $\chi \gg \gamma_i$ for reservoir channels $^{\forall}i$ with system-reservoir interaction $\hat{H}_{SR}$. External time-dependent driving fields are represented by $\hat{\mathcal{E}}(t)$ that populate select reservoir modes.

the strong coupling regime in terms of the scaling of the "non-classicality" or "quantum optical nonlinearity" with the characteristic system size (the atom number and the photon number).

1.2.1 Strong coupling parameter and breakdown of statistical mechanics

Quantum optics deals with dynamical processes, in which light fields are generated from the interaction with the material systems. For a realistic quantum system, we need to consider the coupling of the "system" to an infinite-dimensional environment (in our case, vacuum reservoir). For any "exotic" quantum optical state to emerge [30, 31], we are basically looking at non-equilibrium open quantum dynamics, as the equilibrium physics would be contained in the thermalized state of the reservoir at finite temperature [32, 33, 34]. The conceptual umbrella is thereby to examine the dynamics of open quantum system, for which a relatively "simple" quantum system (single atoms and photons, or many-body quantum system) is embedded in a complex environment (e.g., infinite QHO modes decomposing the free-space vacuum, or external driving fields and measurement apparatus) that constantly perturbs the system's otherwise reversible quantum evolution.

As shown in Fig. 1.1, we could consider the system Hamiltonian $\hat{H}_S$ interacting with reservoir modes $\hat{H}_R$ by a system-reservoir Hamiltonian $\hat{H}_{SR}$. The reservoir modes can take the form of the untamed free-space vacuum or inhomogeneous interactions of some fluctuating dipoles bound on the dielectric surface of a mirror, which lead to dissipation. Loss of the information and entropy of the system to the infinite continuum necessarily introduces perturbation of the system in terms of quantum noise being injected back into the system variables. This quantum fluctuation-dissipation theorem manifests the theory of Markov master equation and open quantum systems [35]. But reservoir modes can also be utilized to populate driving fields $\hat{\mathcal{E}}(t)$ that bring the system out of equilibrium, and we could design particular system-reservoir interaction into desired modes (e.g., single and multimode cavities) to mediate effective interactions between the trapped atoms. For instance, let me just concentrate on one of the reservoir modes with the largest characteristic coupling constant χ in $\hat{H}_{SR}$ (we take γ_i for all other weaker dissipative channels), in which the driving fields are utilized to populate the excitations in this mode.

In the steady-state, we could then conceive of the characteristic quanta n_s in which the system could be brought out of equilibrium as the ratio of the dissipation to all other channels γ and the coherent coupling rate χ with this driving mode. From laser theory, the characteristic quanta

$$n_s = \frac{\gamma}{\chi} \tag{1.1}$$

corresponds to the intracavity threshold photon number for population inversion and stimulated emission. That is, by populating this driving channel with excitation number $n > n_s$, the system can be brought out of equilibrium to exert dynamical unitary processes in the face of the dissipative “damping” and “drift” terms of the environment, as with the Fokker-Planck equation for brownian motion. In generic terms, we could separate the open quantum system dynamics into “strong” and “weak” coupling with respect to the characteristic quanta. This also provides the natural scaling parameter for the system evolution.

For lasers and optical parametric oscillators [36], you typically find $\sqrt{n_s} \sim 10^3 - 10^6$ in the weak coupling regime $\chi \ll \gamma$ ($n_s \gg 1$). Internal timescale χ^{-1} for the coherent dynamics are much longer than the dissipative timescales γ^{-1}, and the dynamics is well approximated by classical evolution of the c-number mean field α plus some small quantum fluctuation $\delta\hat{a}$ of some operator $\hat{a} \to \alpha + \delta\hat{a}$ (mode operator in this case). Any exotic quantum state (e.g., EPR entanglement, single photon, etc) is thereby contained within this small component $\delta\hat{a}$ of the field around which it is fluctuating. In fact, there is a beautiful connection to the equilibrium physics in statistical mechanics in terms of system-size expansion with $1/n_s$, which dictates the overall size of the fluctuation and effective temperature [32]. That is, for large n_s, the thermal equilibrium description and mean-field theory adequately describe the response of the system variables. In fact, the vast majority of quantum optics experiments is contained within this parameter space (e.g., nonclassical and entangled light beams from parametric downconversion crystal), yet providing a great utility for quantum information science.

An important frontier in quantum optics is to push the boundary of n_s, in which out-of-equilibrium phenomena could occur at the single quanta and vacuum levels. In the "strong coupling" regime of $\chi \gg \gamma$ with $n_s \ll 1$, dynamical processes could be completely stimulated even by a single quanta pumping the system [37, 38, 39, 40]. More importantly, the generic dynamical feature could be potentially highly dependent on the excitation of a single quanta even in the presence of a large number of background quanta. In this regime, reversible quantum dynamics compete non-perturbatively with the irreversible Lindblad evolution, generally resulting in non-Markov features (bound states and localized excitations). The first physical system to explore this parameter regime is in the setting of the cavity QED, where a heroic effort by Jeff Kimble's group at Caltech in the 80s led to the landmark observation of the normal mode splitting (vacuum Rabi splitting) in 1992 [37] that demonstrated the strong coupling regime of cavity QED in the optical domain, followed by the work of Serge Haroche in 1996 in the microwave domain [38]. From the perspective of the theory of a laser, this constitutes a laser operating at the single-photon level, where a gain medium of a single atom is completely saturated by a photon number much smaller than 1 [41]. From the viewpoint of nonlinear optics, this regime is where optical nonlinearity and bistability could persist down to the level of one photon [42]. From statistical mechanics, it is not possible to find an effective thermal equilibrium picture of the atom-field evolution, even when the field is populated by a quanta much less than 1.

1.2.2 Jaynes-Cummings and Dicke models

The goal of this section is to provide a basic theoretical description of cavity QED in the strong coupling regime, so that we could begin the discussion of the scaling and physical mapping to certain many-body spin models. I will begin by describing the Jaynes-Cummings Hamiltonian for atom-field interactions [26, 43], and by extension a Dicke model (also known as the Tavis-Cummings model) [28, 29]. Along the way, we will discover that cavity QED as a many-body platform has a pathology to access physics beyond of the mean-field, thereby providing the foundation of my research thesis.

Jaynes-Cummings model

We begin by discussing a closed dipole interaction between a two-level atom and a single-mode of the electromagnetic field. The atom has two internal states (ground and excited states $|g\rangle, |e\rangle$) with the energy difference $\hbar w_a$. The fields populating the designated spatio-temporal modes have the corresponding single-photon energy $E_0 = \hbar w_f$. In the dipole approximation, the Hamiltonian governing this interaction is given by

$$\hat{H}_0/\hbar = \frac{1}{2} w_a \hat{\sigma}_z + w_f \left(\hat{a}^\dagger \hat{a} + \frac{1}{2} \right) - \hat{\vec{d}} \cdot \hat{\vec{E}}, \tag{1.2}$$

where we take the dipole operator $\hat{\vec{d}} = d\hat{\sigma}_x$ with the scalar dipole matrix element d, the field's annihilation (creation) operator $\hat{a}$ ($\hat{a}^\dagger$), and the two-level system represented by the Pauli's spin operator $\hat{\vec{\sigma}}$. Similarly, we can express the electric field operator in the second quantization theory

$$\hat{E} = \sqrt{\frac{\hbar w_f}{2\epsilon_0 V_m}} \psi(\vec{r}) \left(\hat{a} + \hat{a}^\dagger \right), \tag{1.3}$$

where V_m is the physical volume of the mode, as defined by the boundary conditions imposed on the quantization procedure, $\psi(\vec{r})$ describing the variation of the zero-point fluctuation as a function of the atomic position $\vec{r}$, and ϵ_0 the vacuum's electric permittivity.

More generally, the dipole approximation may break down for nanoscopic optical fields and cavities, where the zero-point motion of the atomic position operator is comparable to that of the vacuum fluctuation. In addition, the fully vectorial treatment of the dipole operator for realistic atoms, where the electron's spin S and angular momentum L, and the nuclear spin I are all coupled, give rise to not only scalar, but also vector and tensorial decomposition of the electric dipole Hamiltonian in terms of the spherical tensor form. Furthermore, for realistic optical cavities, the electromagnetic field penetrates into the dielectric by a few wavelengths, so that it may be critical to consider the impact of the casual structure of the Krammers-Kronig-like dispersion of the dielectric medium (e.g., fields inside a photonic crystal defect cavity), as the standard Lagrangian second quantization method does not work and we need to include the Green's function formalism to appropriately include the input-output relationship [44]. For the sake of revealing the essential physics, I will not include these important effects into the formalism.

Importantly, the dipole interaction Hamiltonian

$$\hat{H}_d = \sqrt{\frac{\hbar d^2 w_f}{2\epsilon_0 V_m}} \psi(\vec{r}) \hat{\sigma}_x \left(\hat{a} + \hat{a}^\dagger \right) \tag{1.4}$$

is known as the quantum Rabi model, with recent resurgence of interests, especially in the context of superconducting circuit QED in the microwave domain. Thanks to the low energy of the microwave photons and large electric dipole moments in superconducting junctions and Rydberg atoms, it is possible to have the atom-field coupling constant

$$\begin{aligned} g(\vec{r}) &= \sqrt{\frac{d^2 w_f}{2\hbar\epsilon_0 V_m}}\psi(\vec{r}) \\ &= g_0\psi(\vec{r}) \end{aligned} \tag{1.5}$$

comparable to the qubit or the single-photon energies $g_0 \sim w_f, w_0$. This allows a pathway to have non-negligible energy-non-conserving counter-rotating processes $\sim \hat{\sigma}_+\hat{a}^\dagger + h.c.$, which generates two-mode squeezing and EPR entanglement.

However, in the optical domain, due to the large w_0 and w_f, counter-rotating terms rapidly oscillate with $\sim e^{i(w_0+w_f)t}$. Therefore, we can apply the rotating-wave approximation and integrate out the short-time correlations to arrive at

$$\hat{H}_d = \hbar g(\vec{r})\left(\hat{\sigma}_+\hat{a} + \hat{\sigma}_-\hat{a}^\dagger\right), \tag{1.6}$$

with the total Hamiltonian

$$\hat{H}_0/\hbar = \frac{1}{2}w_a\hat{\sigma}_z + w_f\left(\hat{a}^\dagger\hat{a} + \frac{1}{2}\right) + g(\vec{r})\left(\hat{\sigma}_+\hat{a} + \hat{\sigma}_-\hat{a}^\dagger\right). \tag{1.7}$$

This is also known as the Jaynes-Cummings Hamiltonian for describing the atom-field interactions in the setting of cavity QED and Wigner-Weisskopf spontaneous emission (for multimode fields) [45].

To obtain the eigensystem of $\hat{H}_0$, we take a convenient basis

$$\begin{aligned} \mathcal{B} &= \mathcal{B}_a \otimes \mathcal{B}_f \\ &= \{|g\rangle, |e\rangle\} \otimes \{|0\rangle, |1\rangle, |2\rangle, \cdots\} \\ &= \{|g,0\rangle, |e,0\rangle, |g,1\rangle, |e,1\rangle, |g,2\rangle, |e,2\rangle, \cdots\}. \end{aligned} \tag{1.8}$$

In this basis, we can express the block-diagonal Hamiltonian

$$\hat{H}_0 = \begin{pmatrix} \frac{1}{2}\hbar(w_f - w_a) & 0 & 0 & \cdots & 0 \\ 0 & \hat{H}_1 & 0 & \cdots & 0 \\ 0 & 0 & \hat{H}_2 & \cdots & 0 \\ \vdots & & & \ddots & \\ 0 & 0 & 0 & \cdots & \hat{H}_n \end{pmatrix}, \tag{1.9}$$

with the elements

$$\hat{H}_n = \begin{pmatrix} \hbar(nw_f + \frac{1}{2}(w_f - w_a)) & \hbar g(\vec{r})\sqrt{n} \\ \hbar g(\vec{r})\sqrt{n} & \hbar(nw_f - \frac{1}{2}(w_f - w_a)) \end{pmatrix} \qquad (1.10)$$

over the basis $\mathcal{B}$. We can independently diagonalize $\hat{H}_n$ over each total excitation-number subspace n, arriving at the eigenstates and eigenenergies

$$\begin{aligned} |\pm\rangle_n &= \cos(\theta_{n,\pm})|g,n\rangle + \sin(\theta_{n,\pm})|e,n-1\rangle & (1.11) \\ E_{n,\pm}/\hbar &= nw_f \pm \frac{1}{2}\sqrt{4ng(\vec{r})^2 + \Delta^2}, & (1.12) \end{aligned}$$

where we have used the atom-field detuning $\Delta = w_a - w_f$, and cavity-polariton's mixing angles

$$\begin{aligned} \cos(\theta_{n,\pm}) &= \frac{(-\Delta \pm \sqrt{4ng(\vec{r})^2 + \Delta^2})}{\sqrt{|(-\Delta \pm \sqrt{4ng(\vec{r})^2 + \Delta^2})^2 + 4ng(\vec{r})^2|}} & (1.13) \\ \sin(\theta_{n,\pm}) &= \frac{2\sqrt{n}g(\vec{r})}{\sqrt{|(-\Delta \pm \sqrt{4ng(\vec{r})^2 + \Delta^2})^2 + 4ng(\vec{r})^2|}}. & (1.14) \end{aligned}$$

These are the "dressed" states of the system, a coherently superposed "molecule" of atom-cavity excitations, caused by the interaction with the quantized field in the cavity. Importantly, in the limit of large detuning $\Delta \gg g_0$, the normal modes $|\pm\rangle_n$ become separated into atom-like $|+\rangle_n \rightarrow |e, n-1\rangle$ and photon-like $|-\rangle_n \rightarrow |g, n\rangle$ branches. Likewise, for negative detuning, the cavity-polaritons are mapped in the opposite way.

It is instructive to consider the case when the system is brought into resonance $w = w_f = w_a$ with $\Delta = 0$, and examine the scaling of the excitation spectrum. In this case, the cavity-polaritonic state reduces to $|\pm\rangle_n = \frac{1}{\sqrt{2}}(|e, n-1\rangle \pm |g, n\rangle$ with energy splitting $\Delta E_{n,\pm}/\hbar = 2\sqrt{n}g(\vec{r})$. For a weakly-driven system, in the excitation subspace $n = 1$, this implies a non-trivial temporal dynamics, in which a single atom in the excited state $|e, 0\rangle$ stimulates a photon into the cavity $|g, 1\rangle$, after which the same photon can be reabsorbed by the same atom, making a Rabi oscillation between the atom and the cavity. In terms of the excitation spectrum over n, as shown in Fig. 1.2, the direct interaction between one atom and one photon yields a "vacuum" Rabi splitting $2g(\vec{r})$ between the two energy eigenstates $|\pm\rangle$ [37]. The Jaynes-Cummings interaction maximally entangles the field and the atom via these normal modes $|\pm\rangle$. More interestingly, when probing through the excitation subspace, one finds an optical nonlinearity in the form of excitation spectra

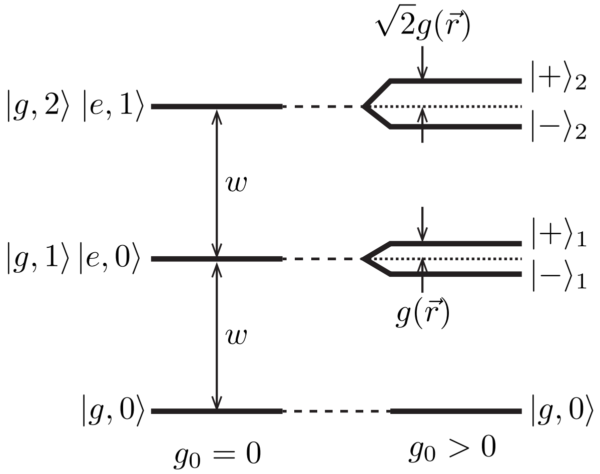

Figure 1.2: **Jaynes-Cummings spectra for a weakly-driven system.** Due the atom-cavity interaction, the cavity resonances are split by the vacuum Rabi frequency $2g(\vec{r})$ for the single-excitation manifold $n = 1$. Two normal modes arise from the atom-cavity interaction, and cavity transmission is suppressed on resonance. The Jaynes-Cummings model displays the nonlinear excitation spectra for higher n. The strong coupling parameters are $(g, \kappa, \gamma_\perp) = 2\pi \times (10, 1, 1)$ MHz, for transverse atomic decay rate $\gamma_\perp$ and cavity decay rate κ.

over n. The coupled atom-cavity system will be able to transmit an incoming photon, if the driving field is resonant with $|\pm\rangle$. Because of the anharmonicity in $E_{n,\pm} = 2\sqrt{n}g(\vec{r})$, with sufficiently small dissipation, it is possible to select a particular excitation subspace through the phenomena of photon blockade effect.

Quantum master equation for the Jaynes-Cummings model

In order to better evaluate the open nature of the coupled atom-cavity system, it is imperative to include the effect of reservoir. In fact, at some level, one could argue that the cavity mode that the atom was interacting in the previous section was only one of the reservoir modes. More generally, we need to include the dissipative evolution of both the atom, relaxing its optical polarization into free-space (transverse decay rate $\gamma_\perp$), and of the cavity photons (cavity decay rate κ), damping the field excitation through the guided mode, to which the measurement apparatus is sensitive. Understanding these dissipative mechanics gives a natural description of cavity QED and the strong coupling regime in terms of open quantum system formalism.

In our open system approach, we will thereby need to consider two distinct reservoirs – a single spatial mode in which the cavity field couples to, and the other continuum mode in which the excited atom can decay into

$$\begin{aligned} \hat{H}_r^{(a)} &= \sum_{\vec{k},l} \hbar w_{\vec{k},l} \hat{r}^\dagger_{\vec{k},l} \hat{r}_{\vec{k},l} && (1.15) \\ \hat{H}_r^{(\gamma)} &= \sum_j \hbar w_j \hat{r}^\dagger_j \hat{r}_j, && (1.16) \end{aligned}$$

where the operators $\hat{r}$ are the mode operators associated with the energy $\hbar w$. We used the subscript $\vec{k}, l$ to indicate that the atom can transversely decay into an infinite set of transversal modes of free-space. At room-temperature, the thermal excitations of the reservoir modes are extremely small around the optical frequencies of w_f, w_0, so that we simply attribute a zero-temperature bath. The corresponding system-bath couplings are given by

$$\begin{aligned} \hat{H}_{sr}^{(a)} &= \sum_{\vec{k},l} \hbar \kappa_{\vec{k},l} \hat{\sigma}_+ \hat{r}_{\vec{k},l} + h.c. && (1.17) \\ \hat{H}_{sr}^{(\gamma)} &= \sum_j \hbar \kappa_j \hat{r}^\dagger_j \hat{a} + h.c. && (1.18) \end{aligned}$$

The total atom-field-reservoir Hamiltonian is now given by $\hat{H}_{\text{total}} = \hat{H}_0 + \hat{H}_r^{(a)} + \hat{H}_r^{(\gamma)} + \hat{H}_{sr}^{(a)} + \hat{H}_{sr}^{(\gamma)}$, with the original JC Hamiltonian $\hat{H}_0$. For the global system-reservoir state $\hat{\rho}_{\text{total}}$, we would like to obtain the effective system dynamics of the atom-cavity system $\hat{\rho}_s(t) = \text{Tr}_r[\hat{\rho}_{\text{total}}(t)]$. With the standard approach of input-output formalism, we can then relate the response of the system, when it is weakly driven, in terms of the transmission or reflection of the cavity.

To proceed further, we assume that these reservoirs are Markovian, in that the excitations in the reservoir decohere over a time scale (memory time) much shorter than any observable dynamics of the system. We will also assume that the response of the reservoir is narrowed near the transition frequency of interest, upon the introduction of density of states to transform the mode indices in an integral form. Indeed, excitations that migrate over to the field will have a characteristic lifetime of $1/w_0$, and the system-reservoir coupling κ's or the internal system dynamics $\sim g_0$ will clearly not have comparable dynamical timescales in the optical domain. I would like to comment that, in the microwave domain, it is not clear if this approximation is quite valid, especially in the ultrastrong coupling regime, and extra care must be taken in order to interpret the resulting "system"'s dynamics. Using these approximations and separation of timescales, we can arrive at the coarse-grained Schrodinger equation for the reduced system of motion $\hat{\rho}_s(t)$ in the interaction picture, where we integrate out the reservoirs, and obtain the quantum master equation for the atom-field system

$$\dot{\hat{\rho}}_s = -\frac{i}{\hbar}[\hat{H}_0, \hat{\rho}_s] + \mathcal{L}_\kappa \hat{\rho}_s + \mathcal{L}_{\gamma_\perp} \hat{\rho}_s, \tag{1.19}$$

with the action of the Lindblad superoperator

$$\mathcal{L}_\Gamma \hat{\mathcal{O}} = 2\hat{c}_\Gamma \hat{\mathcal{O}} \hat{c}_\Gamma^\dagger - \{\hat{c}_\Gamma^\dagger \hat{c}_\Gamma, \hat{\mathcal{O}}\}. \tag{1.20}$$

In writing the equations above, we have defined the photonic and atomic quantum jump operators $\hat{c}_\kappa = \sqrt{\kappa}\hat{a}$, $\hat{c}_a = \sqrt{\gamma_\perp}\hat{\sigma}_-$ with transverse spontaneous emission rate $\gamma_\perp = \frac{d^2 w^3}{6\pi\hbar\epsilon_0 c^3}$. In order to see the excitation spectrum and dynamics, we also need to consider a drive to bring the system out of equilibrium. For instance, we could assume that one mode of the reservoir modes in Eq. 1.16 is populated by a driving field with strength ϵ, and include back into the system, so that the system Hamiltonian is

$$\hat{H}_0/\hbar = \Delta_a \hat{\sigma}_z + \Delta_f \hat{a}^\dagger \hat{a} + g(\vec{r}) \left(\hat{\sigma}_+ \hat{a} + \hat{\sigma}_- \hat{a}^\dagger\right) + \left(\epsilon^* \hat{a} + \epsilon \hat{a}^\dagger\right), \tag{1.21}$$

where we now introduced the atomic and cavity detunings $\Delta_a = w_a - w_p, \Delta_f = w_f - w_p$.

Before we move onto the mapping into the spin models, it is instructive to look at the dynamics in the single excitation subspace $\hat{\rho}_1(t) = |\psi_1(t)\rangle\langle\psi_1(t)|$ with $|\psi_1(t)\rangle = \alpha(t)|g,1\rangle + \beta(t)|e,0\rangle$. From the master equation with $\langle \hat{a}^\dagger \hat{a}\rangle = \mathrm{Tr}[\hat{a}^\dagger \hat{a} \hat{\rho}_s] = |\alpha|^2$ and $\langle \hat{\sigma}_z \rangle = \mathrm{Tr}[\langle \hat{\sigma}_z \hat{\rho}_s] = |\beta|^2$, we arrive at the following coupled differential equation

$$\begin{aligned} \dot{\alpha}(t) &= -(\kappa + i\Delta_f)\alpha(t) - ig(\vec{r})\beta(t) - i\epsilon && (1.22) \\ \dot{\beta}(t) &= -(\gamma_\perp + i\Delta_a)\beta(t) - ig(\vec{r})\alpha(t). && (1.23) \end{aligned}$$

In the absence of the drive $\epsilon = 0$, Eqs. 1.22-1.23 yield coherent Rabi oscillations between $|g,1\rangle$ and $|e,0\rangle$, as predicted in the closed formalism before. Specifically, one finds that the intracavity photon number coherently oscillates with

$$n(t) = |\alpha(t)|^2 = \frac{|g|^2 e^{-(\kappa+\gamma_\perp)^2}}{|g|^2 - (\kappa - \gamma_\perp)^2/4} \sin^2[\sqrt{|g|^2 - (\kappa - \gamma_\perp)^2/4t}] \tag{1.24}$$

for $g(\vec{r}) \gg |\kappa - \gamma|/2$. In the frequency domain, we can obtain the analytic solution to the

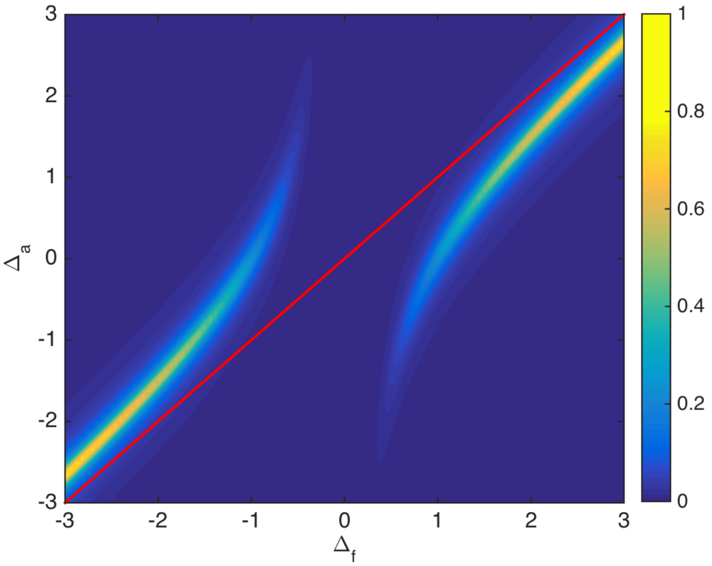

Figure 1.3: **Photon-like amplitude for a weakly-driven dissipative JC model.** The photon-like amplitudes of the dressed states are shown for various detunings Δ_f, Δ_a for vacuum Rabi frequency $g_0 = 1$, cavity and atomic decay rates $\kappa = \gamma = 0.1$. The strong coupling regime is manifested by the well-resolved vacuum Rabi splitting at $\Delta_a = 0$. By comparison, the red line shows the characteristic energy spectrum for an empty cavity with $g = 0$.

steady-state spectra of Eqs. 1.22-1.23, such that

$$n_s(\Delta) = |\alpha_s|^2 = \frac{|\epsilon|^2(\gamma_\perp^2 + \Delta^2)}{(g^2(\vec{r}) + \gamma_\perp\kappa - \Delta^2)^2 + \Delta^2(\gamma_\perp + \kappa)^2}, \tag{1.25}$$

where we assumed $\Delta_f = \Delta_a = \Delta$ for simplicity. As shown in Fig. 1.3, the atom-cavity system reveals the same eigenvalue spectrum in Fig. 1.2. In contrast, in the absence of atom-field coupling $g = 0$,

$$n_s(\Delta) = \frac{|\epsilon|^2}{\kappa^2}\frac{\Delta^2}{\Delta^2 + \kappa^2}, \tag{1.26}$$

which is the classical Lorentzian response of the intracavity photon number for an empty Fabry-Perot cavity driven by a coherent field ϵ. The inclusion of dissipation is that the two resonances are broadened by the damping forces of the interaction with the external reservoirs. The implication of the strong coupling regime, where one expects unitary

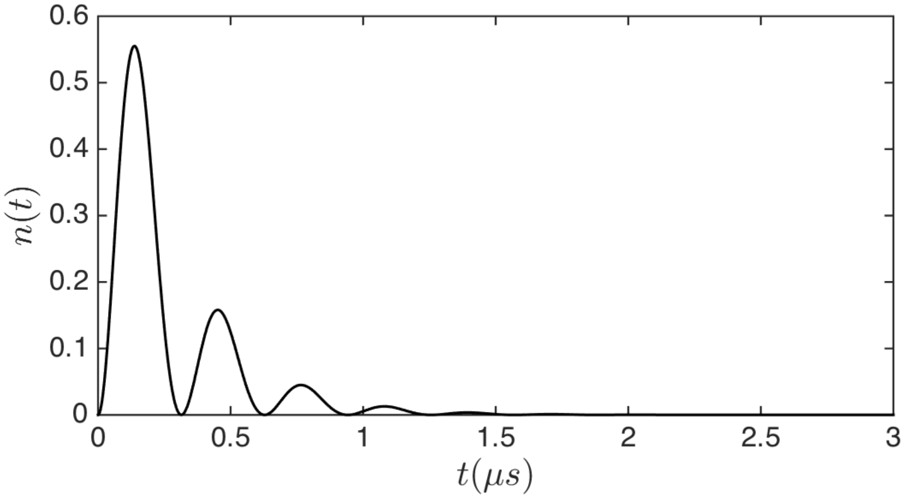

Figure 1.4: **Vacuum Rabi oscillation in cavity QED.** The cavity population is shown for the coherent exchange of excitation between the cavity mode and the single atom. The strong coupling parameters are $(g, \kappa, \gamma_\perp) = 2\pi \times (10, 1, 1)$ MHz, where g is the atom-cavity coupling rate, κ is the cavity decay rate, $\gamma_\perp$ is the transverse atomic decay rate.

evolution for the atom-field interaction, is that the transmission of the cavity on resonance is reduced by placing just one atom into the cavity with the creation of two dressed states of the system. Likewise, by putting just one photon in the system, we should expect non-trivial quantum dynamics to persist with a real photon being absorbed and revived in a coherent manner over the dissipative timescales $1/\kappa, 1/\gamma_\perp$, where the atomic quantum emitter is completely saturated by the intensity of one photon.

There are several key rates that determine the driven-dissipative dynamics of the system:

1. Vacuum Rabi splitting $g(\vec{r}) = \sqrt{\frac{d^2 w_f}{2\hbar\epsilon_0 V_m}}\psi(\vec{r})$.
2. Transit (interaction) time T of atoms in the cavity
3. Cavity damping rate $\kappa = \frac{\pi c}{L_c \mathcal{F}}$ (for lossless mirrors)
4. Transverse spontaneous emission rate $\gamma_\perp = \frac{d^2 w^3}{6\pi\hbar\epsilon_0 c^3}$ (for D2-line transition $|6S_{1/2}\rangle \leftrightarrow |6P_{3/2}\rangle$[a], $\gamma_{D_2} = 2\pi \times 2.6$ MHz)

---

[a] We use the spectroscopic notation $|nL_J\rangle$, where n is the principal quantum number, L is the angular

The strong coupling regime of cavity QED is given by the parameter space

$$g \gg \max(\kappa, \gamma_\perp, 1/T). \tag{1.27}$$

In terms of considering the atom-like excitations, one may consider the "critical" atom number N_0 to completely switch off the optical response of the cavity

$$N_0 = \frac{2\beta\kappa}{g^2}. \tag{1.28}$$

This is the minimal number of atoms required to observe a bistable output. Qualitatively, placing N_0 atoms in the cavity produces an output cavity field resonant with one of the dressed states. Cavity response on resonance is terminated, because of the strong atom-light interaction. Likewise, one could consider the "critical" photon number n_0 to populate the cavity to observe nonlinear excitation dynamics

$$n_0 = \frac{\beta^2}{2g^2}, \tag{1.29}$$

where $\beta = \max(\gamma_\perp, 1/T)$. This intracavity photon number n_0 gives precisely the saturation intensity $I_0 \simeq 1$ mW/cm^2 (for Cs D2-line), where the atom scatters photons at the maximal rate $\Gamma/2$ and the dipole response is saturated. This is the domain of quantum nonlinear optics at the n_0 photon and N_0 atom level, with modern optical cavities achieving $n_0, N_0 \ll 10^{-5}$!

We can introduce the cooperativety parameter C to quantify the overall ratio of coherence to dissipation in the driven-dissipative dynamics

$$C = \frac{4g^2}{\kappa\gamma_\perp}. \tag{1.30}$$

Using the cavity mode volume $V_m = A_c L_c$ and the expression for the resonant cross-section $\sigma_0 = 6\pi/k_0^2$, we obtain the scaling of the cooperativity parameter

$$C = \frac{4\mathcal{F}}{A_c k_0^2} \simeq \frac{2\mathcal{F}}{3\pi}\frac{\sigma_0}{A_c}, \tag{1.31}$$

where A_c is the effective mode area, L_c is the cavity length, $k_0 = 2\pi/\lambda$ is the wave-vector, and $\mathcal{F}$ is the optical finesse of the cavity.

---

momentum, and J is the total spin-orbital momentum.

There is a very natural interpretation of the cooperativity parameter in terms of the laser theory. In the presence of the atom, we expect the loss of the photon given by the ratio of the resonant absorption cross-section σ_0 to the mode area A_c. When the atom is in the cavity, the optical depth of the atom-cavity system is enhanced by the number of round trips $\sim \mathcal{F}$ that the photons take, before being lost into the environment. The cooperativity parameter C, hence, plays the role of the "optical depth" of a single atom. Furthermore, with this classical mapping, there is one important lesson to be learned in direct relevance to our experiment. That is, for an ideal Fabry-Perot cavity with no optical loss, where the effective mode area is $A_c \simeq \pi w_0^2$, we find that a short length cavity is not a pre-requisite for $C \gg 1$. For realistic cavities with losses, it is still desirable to have small mode volumes V_m. Nonetheless, it may be possible to achieve the strong coupling in $C > 1$ with long distance optical cavity $L_c \simeq 1$ mm with beam waist $w_0 \simeq 30\mu$m by improving the optical finesse $\mathcal{F} \sim 500,000$ by a factor of two relative to the state-of-the art.

Dicke model

Here, I will first describe the open system dynamics of the Dicke model, where an array of atoms with spacing a_0 interacts with the quantized fields of free space. There is a very elegant mapping to a quantum spin model and quantum-correlated jumps for sub-wavelength lattices $\xi = k_{eg}a_0 \ll 1$. I will then describe an extension of this model in terms of the Tavis-Cummings physics, where virtual excitations in an optical cavity induce infinite-range interaction between the trapped atoms.

Dicke model in free space When a quantized field interacts with a collection of atoms in free-space, the atoms radiate new source fields, which then interact collectively with the other atoms. A semiclassical model was developed in 1970 by Lehmberg [46, 47]. Here, I'd like to write a fully quantum model, incorporating the quantum fluctuations of the reservoir fields. Using the powerful tool of quantum stochastic calculus, we will rigorously derive the many-body master equation. To the best of my knowledge, we are not aware of other methods that extend the quantum stochastic calculus to the multi-atom case for deriving the quantum master equation.

In particular, we will find that the explicit inclusion of the reservoirs creates renormalizations to the transition frequency w_{eg} in the form of photonic "Lamb" shift with the vacuum modified by the surrounding dielectric environment (the presence of other atoms). The Casimir-Polder shift, which arises from this formalism, is tightly coupled to the emission probability of correlated photons into the reservoir, in terms of the casual-structure of the Kramers-Kronig relationship. A more modern framework, utilizing Green's function quantization method [44], is well beyond the scope of my thesis, and is more relevant to my colleagues work in the waveguide QED lab in the UQML.

To set up the problem, we consider the set of atoms at positions $\vec{x}_i$ with transition frequency w_{eg} collectively interacting with the vacuum fields. In the interaction picture, the system-reservoir interaction can be modeled as

$$\begin{aligned} \hat{H}_{SR}(t)/\hbar &= \sum_{i,k} \sum_{|w_k - w_{eg} < \delta w|} i(\kappa_k^* \hat{b}_k^\dagger e^{i(w_k - w_{eg})t - k\vec{k}\cdot\vec{x}_i} \hat{\sigma}_{ge}^{(i)} + h.c) && (1.32) \\ &= i \sum_i \hat{f}_i(t) \hat{\sigma}_{ge}^{(i)} + h.c, && (1.33) \end{aligned}$$

where we take the quantum noise operator $\hat{f}_i(t) = \sum_{k,|w_k - w_{eg} < \delta w|} \kappa_k \hat{b}_k e^{-i(w_k - w_{eg})t + i\vec{k}\cdot\vec{x}_i}$ and δw is the system's response bandwidth that we will later integrate over in the Born-Markov approximation. The noise operators have particular commutator relationship that reflects the physical characteristics of the reservoir fields (in our case, vacuum state),

$$\begin{aligned} [\hat{f}_i(t), \hat{f}_j^\dagger(t')] &= \gamma_{i,j}(t - t'), && (1.34) \\ \gamma_{i,j}(\tau) &= \sum_{k,|w_k - w_{eg} < \delta w|} |\kappa_k|^2 e^{-i(w_k - w_{eg})\tau + \vec{k}\cdot(\vec{x}_i - \vec{x}_j)}. && (1.35) \end{aligned}$$

In particular, we assume an initial vacuum state for the reservoir system $|\chi, 0\rangle = |\psi\rangle_S \otimes \prod_k |0_k\rangle_R$.

In order to first formulate the quantum stochastic Schrödinger equation (QSSE), we would like to solve

$$\frac{d}{dt}|\chi, t\rangle = -\frac{i}{\hbar}\hat{H}_{SR}(t)|\chi, t\rangle \tag{1.36}$$

for the overall system-reservoir state $|\chi, t\rangle$. By formally integrating twice, we obtain

$$\begin{aligned} |\chi, t\rangle &= \sum_i \left(1 + \int_0^t dt_1 \left(\hat{f}_i^\dagger(t)\hat{\sigma}_{eg}^{(i)} - \hat{f}_i(t)\hat{\sigma}_{ge}^{(i)}\right)\right)|\chi, 0\rangle && (1.37) \\ &+ \sum_{i,j} \int_0^t dt_1 \left(\hat{f}_i^\dagger(t_1)\hat{\sigma}_{eg}^{(i)} - \hat{f}_i(t_1)\hat{\sigma}_{ge}^{(i)}\right) \int_0^{t_1} dt_2 \left(\hat{f}_j^\dagger(t_2)\hat{\sigma}_{eg}^{(j)} - \hat{f}_j(t_2)\hat{\sigma}_{ge}^{(j)}\right)|\chi, t_2\rangle. \end{aligned}$$

In the Born approximation, the system-reservoir interaction is weak, and we could define a time step $t = \Delta t$, where $|\chi, t_2\rangle \to |\chi, 0\rangle = |\psi\rangle_S \otimes \prod_k |0_k\rangle_R$ for $0 < t_2 < \Delta t$. Within this assumption and utilizing Eq. 1.34, the time-evolution of Eq. 1.37 reduces to

$$
\begin{aligned}
|\chi, \Delta t\rangle &= \sum_i \left(1 - \sum_{i,j} \hat{\sigma}_{eg}^{(i)} \hat{\sigma}_{ge}^{(j)} \int_0^{\Delta t} dt_1 \int_0^{t_1} dt_2 \gamma_{i,j}(t_1 - t_2)\right) |\chi, 0\rangle \\
&+ \sum_i \hat{\sigma}_{ge}^{(i)} \int_0^{\Delta t} dt_1 \hat{f}_i^\dagger(t_1) |\chi, 0\rangle,
\end{aligned} \tag{1.38}
$$

to the order $\mathcal{O}(\Delta t^2)$.

Let's first inspect the integral

$$
\int_0^{\Delta t} dt_1 \int_0^{t_1} dt_2 \gamma_{i,j}(t_1 - t_2) \equiv \left(\frac{1}{2}\Gamma_{ij} + i\Delta_{ij}\right) \Delta t. \tag{1.39}
$$

To proceed with the evaluation of the collective decay Γ_{ij} and Lamb shift Δ_{ij}, we are reminded that the coupling constant κ_k is defined with respect to the electric dipole Hamiltonian, where we perform the summation over the polarization states λ of the radiation field

$$
\begin{aligned}
\sum_{\vec{k},\lambda} |\kappa_k|^2 e^{-i(w_k - w_{eg})\tau + \vec{k}\cdot(\vec{x}_i - \vec{x}_j)} &= \sum_{\vec{k}} \frac{w_{\vec{k}}}{2\hbar\epsilon_0 V} \sum_\lambda |\vec{d}_{eg} \cdot \vec{e}_\lambda|^2 e^{-i(w_k - w_{eg})\tau + \vec{k}\cdot(\vec{x}_i - \vec{x}_j)} \\
&= \sum_{\vec{k}} \frac{w_{\vec{k}}}{3\hbar\epsilon_0 V} |\vec{d}_{eg}|^2 (P_0(\hat{k}\cdot\vec{d}_{eg}) - P_2(\hat{k}\cdot\vec{d}_{eg})) e^{-i(w_k - w_{eg})\tau + \vec{k}\cdot(\vec{x}_i - \vec{x}_j)},
\end{aligned}
$$

where $P_l(x)$ are the Legendre polynomials. In order to compute the sum over all $\vec{k}$, we convert $\frac{1}{V}\sum_{\vec{k}} \to \frac{1}{(2\pi c)^3} \int w^2 dw \int d\Omega_{\vec{k}}$ for solid-angle $\Omega_{\vec{k}}$. With these, we find

$$
\gamma_{i,j}(\tau) = \frac{|\vec{d}_{eg}|^2}{6\pi^2 c^3} \int_{w_{eg} - \delta w}^{w_{eg} + \delta w} \frac{w^3}{\hbar\epsilon_0} dw \left(j_0(z) + P_2(\hat{r}\cdot\hat{d}_{eg}) j_2(z)\right) e^{-(w - w_{eg})\tau}, \tag{1.40}
$$

where j_l are the spherical Bessel functions. Using the relationship

$$
\int_0^{\Delta t} dt_1 \int_0^{t_1} dt_2 e^{-i(w - w_{eg}(t_1 - t_2))} = \left(\pi\delta(w - w_{eg}) - \frac{i\mathcal{P}}{w - w_{eg}}\right) \Delta t \tag{1.41}
$$

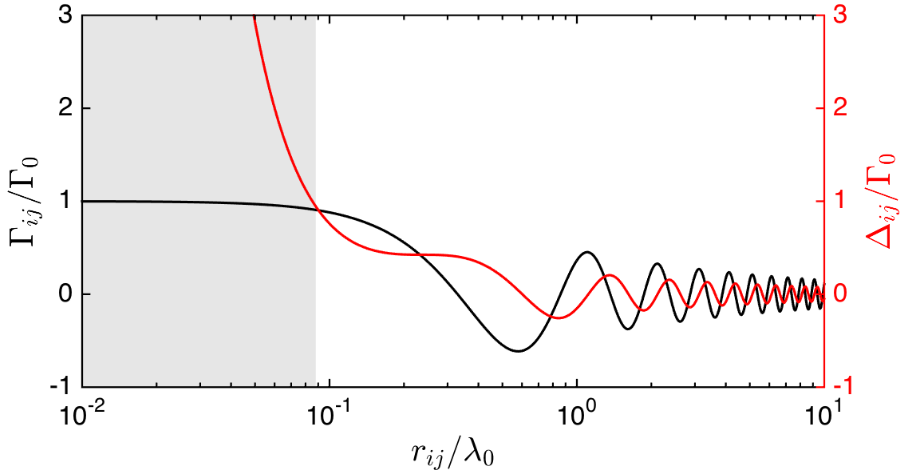

Figure 1.5: **Coherence to dissipation ratio for free-space Dicke model.** We compute the dissipative rate Γ_{ij} for correlated photon emission and the coherent spin-exchange coefficient Δ_{ij} as a function of interatomic distance r_{ij}/λ_0 in the units of transition wavelength λ_0. At distance scales $r_{ij}/\lambda_0 < 1/10$, the spin chain coherently evolves with the XX Hamiltonian with the exchange coefficient Δ_{ij}, while being damped by the collective radiation at the rate Γ_{ij}.

for the Cauchy's principal $\mathcal{P}$, we integrate over Eq. 1.39, and find the decay and level shift

$$\Gamma_{ij} = \Gamma\left(j_0(k_{eg}r) + P_2(\hat{r}\cdot\hat{d}_{eg}) * j_2(k_{eg}r)\right) \tag{1.42}$$

$$\Delta_{ij} = \frac{1}{2}\Gamma\left(n_0(k_{eg}r) + P_2(\hat{r}\cdot\hat{d}_{eg})n_2(k_{eg}r)\right) \tag{1.43}$$

with $k_{eg} \equiv w_{eg}/c$, $\Gamma = \frac{|\vec{d}_{eg}|^2 k_{eg}^3}{3\hbar\pi\epsilon_0}$, and spherical Bessel function of the second kind n_l.

Within these definitions, we could write the difference equation for Eq. 1.38 for the time-evolution with step Δt

$$\Delta|\chi, t\rangle = \left(-\frac{i}{\hbar}\hat{H}_{\text{eff}}\Delta t + \sum_i \hat{\sigma}_{ge}^{(i)}\Delta\hat{F}_i^{\dagger}(t)\right)|\chi, t\rangle, \tag{1.44}$$

where we have introduced the correlated quantum Ito increments (QII) for stochastic differential equations $\Delta F_i(t) = \int_t^{\Delta t} f_i(t')dt'$. The QII follow the Ito commutation algebra:

$$[\Delta F_i(t), \Delta F_j^\dagger(t)] = \frac{1}{2}(\Gamma_{i,j} + \Gamma_{j,i})\Delta t. \tag{1.45}$$

The multi-atom quantum stochastic differential equation can thereby be derived with infinitesimal time step $\Delta t \to 0$, so that

$$d|\chi, t\rangle = \left(-\frac{i}{\hbar}\hat{H}_{\text{eff}}dt + \sum_i \hat{\sigma}_{ge}^{(i)} d\hat{F}_i^\dagger(t)\right)|\chi, t\rangle. \tag{1.46}$$

The non-Hermitian effective Hamiltonian is expressed as

$$\hat{H}_{\text{eff}} = \hat{H}_S + \hbar \sum_{i,j}\left(\Delta_{i,j} - \frac{i}{2}\Gamma_{i,j}\right)\hat{\sigma}_{ge}^{(i)}\hat{\sigma}_{eg}^{(j)}. \tag{1.47}$$

Finally, in order to obtain the quantum master equation, we perform a partial trace of the total system-reservoir state $|\chi, t\rangle$ over the reservoir variables to obtain the evolution of the system density matrix $\hat{\rho}_S(t) = \text{Tr}_R[|\chi, t\rangle\langle\chi, t|]$. Using the commutation of the quantum Ito increments in Eq. 1.45, we obtain the multi-atom master equation driven by a classical coherent field Ω_0

$$\begin{aligned} \frac{d}{dt}\hat{\rho}_S(t) &= -i\left[\frac{\hat{H}_S}{\hbar} + \sum_{i,j}\Delta_{ij}\left(\hat{\sigma}_x^{(i)}\hat{\sigma}_x^{(j)} + \hat{\sigma}_y^{(i)}\hat{\sigma}_y^{(j)}\right), \hat{\rho}_S\right] && (1.48)\\ &+ \sum_{i,j}\frac{\Gamma_{i,j}}{2}\left(2\hat{\sigma}_-^{(i)}\hat{\rho}_S\hat{\sigma}_+^{(j)} - \{\hat{\sigma}_+^{(j)}\hat{\sigma}_-^{(i)}, \hat{\rho}_S\}\right), \\ \hat{H}_S/\hbar &= \sum_i \frac{w_{eg}}{2}\hat{\sigma}_z^{(i)} - \Omega_0\hat{\sigma}_x^{(i)}. && (1.49) \end{aligned}$$

In order to extract the essential "many-body" physics of the renormalization effect, we redefine the system Hamiltonian into XX spin model

$$\hat{H}_S/\hbar = \sum_i\left(h_z\hat{\sigma}_z^{(i)} + h_x\hat{\sigma}_x^{(i)}\right) + \sum_{i,j}\Delta_{ij}\left(\hat{\sigma}_x^{(i)}\hat{\sigma}_x^{(j)} + \hat{\sigma}_y^{(i)}\hat{\sigma}_y^{(j)}\right), \tag{1.50}$$

by absorbing the hopping terms of Eq. 1.48 into the system Hamiltonian $\hat{H}_S$, with $h_x = -\Omega_0$ and $h_z = \frac{w_{eg}}{2}$. The physical manifestation of atoms closely packed each other with

$a_0 \ll \lambda_0$ is that the radiative decay and level shift caused by the vacuum fluctuation can no longer be treated by investigating atoms coupled to independent resesrvoirs. Indeed, the atoms within a sphere of $\xi \ll 1$ are "collectively" coupled to the reservoir, as it is impossible for the reservoir modes to distinguish the radiation from the individual atoms. In fact, we are forced to treat these processes coherently, as shown in the second line of Eq. 1.48, which describe the collective processes of superradiance and subradiance well known in the quantum optics community [48, 49]. Furthermore, accompanied by correlated photon decay, we find that the atomic system is renormalized into a (short-ranged) XX spin model. Atom i in excited state $|e_i\rangle$ may virtually create a photon within a volume smaller than $\mathcal{V} \sim \lambda_0^3$, and another atom j within this volume can coherently absorb this photon to cause the coherent spin-exchange interaction between atoms i and j in the form of correlated Lamb shift for the quantum vacuum modified by "mirror" atoms [50].

On the other hand, it is important to realize that this type of XX spin model is hardly coherent for a wide range of experimental parameters in AMO physics, and is thereby more or less a conceptual playground for engineered system [51], as described in the next section. For favorable ratio between coherent and dissipative dynamics, we require

$$C_s \simeq \frac{\Delta_{ij}}{\Gamma_{ij} + \Gamma_0} \gg 1. \tag{1.51}$$

Hence, for large $\Delta_{ij} \gg \Gamma_0$, we would must consider internuclear spacing of $r_{ij} \ll 0.1\lambda_0 \simeq 100$ nm, as shown in Fig. 1.5.

Furthermore, when the atoms are so densily packed, the radiative decay is collectively enhanced by $\Gamma^{(i)}_{N_\mathcal{V}} = \sum_{j\in\mathcal{V}} \Gamma_{ij} = N_\mathcal{V}\Gamma_0$, where $N_\mathcal{V}$ is the number of atoms within the coherence volume $\mathcal{V}$, leading to unfavorable scaling $C_s \propto \frac{1}{N}$. In addition, for all known atomic species compatible with laser cooling and trapping, at distance ranges r_{ij} less than 300 nm, it is reasonable to be concerned about photoassociation processes and excited molecular formations. All these fundamental challenges, apart from the paramount technological difficulty of developing low-noise XUV light sources below $\lambda \simeq 100$ nm, provide a formidable barrier for doing many-body physics experiments with photon-mediated interactions in free-space. Even with $a_0 = 300$ nm (to avoid photomolecular formation [52]), we expect $C_s \simeq 10^{-3} \ll 1$.

Dicke model in a cavity By transitioning from the free-space into the cavity model, we expect significant modification of the density of states into a particular single mode constrained by the boundary condition of the cavity mirrors. The qualitative implication is that this cavity mode can act as an effective reservoir for the trapped atoms, and that the interatomic spacing within this condition is no longer constrained by the sub-wavelength condition $\xi \ll 1$, as described before. I will first extend the Jaynes-Cummings model of Eq. 1.7 to the multi-atom case known as the Tavis-Cummings Hamiltonian, where a collection of atoms is interacting with the single-mode quantized cavity field. Instead of utilizing the multiatom master equation derived before, we are allowed to use the original master equation in Eq. 1.19 as the foundation for arriving at the effective low-energy driven-dissipative theory of the reduced atomic system, as our dominant reservoir is much simpler in its Hilbert space (just a single-mode quantum harmonic oscillator) than the free-space reservoirs.

We begin by writing the master equation for the N atom-cavity system

$$\dot{\hat{\rho}}_s = -\frac{i}{\hbar}[\hat{H}_0^{(N)}, \hat{\rho}_s] + \mathcal{L}_\kappa \hat{\rho}_s + \sum_i \mathcal{L}_{\gamma_\perp}^{(i)} \hat{\rho}_s, \tag{1.52}$$

where I have included the cavity mode as part of the system Hamiltonian. As before, we have the photonic and atomic quantum jump operators $\hat{c}_\kappa = \sqrt{\kappa}\hat{a}$ and $\hat{c}_a^{(i)} = \sqrt{\gamma_\perp}\hat{\sigma}_-^{(i)}$ for the Lindblad dissipative superoperators,

$$\begin{aligned} \mathcal{L}_\kappa \hat{\mathcal{O}} &= 2\hat{c}_\kappa \hat{\mathcal{O}} \hat{c}_\kappa^\dagger - \{\hat{c}_\kappa^\dagger \hat{c}_\kappa, \hat{\mathcal{O}}\}. && (1.53) \\ \mathcal{L}_{\gamma_\perp}^{(i)} \hat{\mathcal{O}} &= 2\hat{c}_a^{(i)} \hat{\mathcal{O}} \hat{c}_a^{(i)\dagger} - \{\hat{c}_a^{(i)\dagger} \hat{c}_a^{(i)}, \hat{\mathcal{O}}\}. && (1.54) \end{aligned}$$

The Hamiltonian $\hat{H}_0^{(N)}$ for the N atom-cavity system is

$$\hat{H}_0^{(N)}/\hbar = \sum_i^N \Delta_a \hat{\sigma}_z^{(i)} + \Delta_f \hat{a}^\dagger \hat{a} + \sum_i^N g(\vec{r}_i)\left(\hat{\sigma}_+^{(i)}\hat{a} + \hat{\sigma}_-^{(i)}\hat{a}^\dagger\right) + \left(\epsilon_\kappa^* \hat{a} + \epsilon_\kappa \hat{a}^\dagger\right) + \sum_i^N \left(\epsilon_a^* \hat{\sigma}_+^{(i)} + \epsilon_a \hat{\sigma}_-^{(i)}\right). \tag{1.55}$$

If we assume that the positions of the atoms are aligned with respect to the antinodes of the cavity field, we can introduce the mean field in terms of the collective spin variables

$$\begin{aligned} \hat{S}_{x,y,z} &= \sum_i \hat{\sigma}_{x,y,z}^{(i)} && (1.56) \\ \hat{S}_\pm &= \frac{1}{\sqrt{N}} \sum_i \hat{\sigma}_\pm^{(i)} && (1.57) \end{aligned}$$

and rewrite the system Hamiltonian in terms of these collective variables

$$\hat{H}_0^{(N)}/\hbar = \Delta_a \hat{S}_z + \Delta_f \hat{a}^\dagger \hat{a} + \sqrt{N} g_0 \left(\hat{S}_+ \hat{a} + \hat{S}_- \hat{a}^\dagger\right) + \epsilon_\kappa(\hat{a} + \hat{a}^\dagger) + \epsilon_a \hat{S}_x. \tag{1.58}$$

This is known as the Tavis-Cummings Hamiltonian, and provides the basis for a wide range of quantum optical and quantum memory phenomena for collective light-matter interaction with $g_0 \rightarrow \sqrt{N} g_0$ with very favorable $C = \frac{N g_0^2}{\kappa\gamma} \gg 1$ for moderate single-atom coupling g_0.

In order to arrive at the reduced spin model [53], we need to be able to treat the cavity field as an effective reservoir bath that collectively dissipates the trapped atoms. For this, we consider the large detuning limit $\Delta_f \gg \kappa, \Gamma_\perp$ with $\epsilon_\kappa = 0$ and adiabatically eliminate the weakly-populated cavity degrees of freedom. Let us begin by writing the Heisenberg-Langevin equation of motion for the cavity field

$$\dot{\hat{a}} = i\left(\epsilon_\kappa \hat{a} + \sum_i^N \sqrt{N} g_0 \hat{S}_- + \Delta_f \hat{a}\right) - \frac{\kappa}{2}\hat{a} + \hat{F}_a, \tag{1.59}$$

where $\hat{F}_a$ is the delta-correlated quantum-Langevin noise force. In the steady-state, the cavity field is effectively mapped to the spin operator with

$$\hat{a}_{ss} = \frac{2\sqrt{N} g_0}{2\Delta_f - i\kappa}\hat{S}_- \tag{1.60}$$

leading to an effective quantum master equation for the spin-degrees of freedom

$$\begin{aligned} \frac{d}{dt}\hat{\rho}_S(t) &= -\frac{i}{\hbar}\left[\hat{H}_{\text{eff}}^{(N)}, \hat{\rho}_S\right] + \sum_{i,j} \frac{\Gamma_{\text{eff}}}{2}\left(2\hat{\sigma}_-^{(i)} \hat{\rho}_S \hat{\sigma}_+^{(j)} - \{\hat{\sigma}_+^{(j)}\hat{\sigma}_-^{(i)}, \hat{\rho}_S\}\right), && (1.61) \\ \hat{H}_{\text{eff}}^{(N)}/\hbar &= h_z \hat{S}_z + \frac{J_{\text{eff}}}{N}\sum_{i,j}\left(\hat{\sigma}_x^{(i)}\hat{\sigma}_x^{(j)} + \hat{\sigma}_y^{(i)}\hat{\sigma}_y^{(j)}\right) + h_x \hat{S}_x && (1.62) \\ &= h_z \hat{S}_z + J_{\text{eff}}\left(\vec{\hat{S}}^2 - \hat{S}_z^2\right) + h_x \hat{S}_x, \end{aligned}$$

with the transverse and longitudinal magnetic fields $h_x(h_z) = \epsilon_a(\Delta_a)$, the collective spin-exchange rate $J_{\text{eff}} = \frac{4N g_0^2 \Delta_f}{4\Delta_f^2 + \kappa^2}$ and the correlated dissipative rate $\Gamma_{\text{eff}} = \frac{2N g_0^2 \kappa}{4\Delta_f^2 + \kappa^2}$. In writing the above equations, I have neglected the on-site decay terms Γ_0. Importantly, we find that the decay of cavity field causes a collective fluctuation onto the atomic variables by way of the effective damping term Γ_{eff}. The key benchmark for any coherent spin dynamics is to attain $C_s = \frac{J_{\text{eff}}}{\Gamma_{\text{eff}}} = \frac{\Delta_f}{\kappa} \gg 1$. For $\Delta_f \gg \kappa$, we can in principle obtain unitary spin dynamics governed by Eq. 1.62, only limited by the independent damping term Γ_0.

Motivation for my thesis: Limitations of atom-field quantum systems for non-interacting matter

In terms of my quest to extend quantum optical toolboxes to quantum many-body systems, a major drawback with collective atom-field systems is that, while the coupling rate $\sqrt{N}g_0$ has been collectively enhanced, it has necessarily transformed the original "nonlinear" matter-light interaction of the spin-boson model to that of a boson-boson model (i.e., coupled quantum harmonic oscillator). Indeed, in the atom-field coupling term of $\hat{H}_0^{(N)}$, the atomic term can be written in terms of the quasi-bosonic mean field $\vec{S}$, where, for small number of collective excitation $\langle \hat{S}^\dagger \hat{S} \rangle \ll N$, the atomic system is described by a bosonic field

$$[\hat{S}_+, \hat{S}_-] = 1 + \mathcal{O}(1/N^2) \tag{1.63}$$

for large N [54, 55]. Hence, from the dynamical point of view, we should not expect any deviation from the classical model of coherent energy exchange between two oscillators [55]. Indeed, when carrying out similar calculations for the avoided crossings for cavity QED, we find that the collective excitation $\hat{S}$ is linearly coupled to the cavity field in the excitation spectrum. Indeed, by way of Sudarshan's optical equivalence theorem [30], it is straightforward to prove that any classical state under the evolution of linear coupling (e.g., $\hat{H}_0^{(N)}$) remains classical at all times.

Phenomenologically, we could consider the original Jaynes-Cummings spectrum in Fig. 1.2 and then try to scale the system size in terms of photon number n and atom number N (transforming into Tavis-Cummings model). For the scaling of n, if we simply take a $|n\rangle$ photon Fock state generated from the higher-order excitation subspace n by photon blockade, the degree of non-classicality measured by the auto-correlation function is given by $g^{(2)}(0) \simeq 1 - 1/n$, so that $g^{(2)}(0) \to 1$ for $n \gg 1$. Likewise, when scaling N, the excitation spectrum becomes increasingly harmonic, so that when driven by a coherent field, we expect $g^{(2)}(0) \to 1$ for $n \gg 1$. More quantitatively, as examined in Ref. [56], we could define a quantum anharmonicity parameter

$$q_a \equiv \frac{g_0\sqrt{4N-2}}{2g_0\sqrt{N}} \tag{1.64}$$

for cavity QED with harmonicity $q = 1$. In fact, we find that the maximal single-quanta level optical nonlinearity is achieved for $N = 1$ atom with $q_a = 0.71$, with $q_a \to 1$ for $N \gg 1$ (Tavis-Cummings limit).

Indeed, the "spin" Hamiltonian in Eq. 1.63 has been utilized for generation of collective spin squeezed states [57] and superradiant states in a cavity [58] (and "supersolid" phase by its extension [59]), and the non-trivial partition of the individual spins is completely masked by the overall mean field dynamics $S(t)$. While it is exciting to investigate long-range interacting system, an infinite-range system is well described by very few parameters that make the overall system exactly soluble and trivial from the point of view of many-body physics. Indeed, the Hamiltonian in Eq. 1.62 demonstrates a small quantum fluctuation around the macroscopic spin vector $S(t)$. While the sub-system comprising this macroscopic spin vector may be multipartite entangled, this is not so physically exciting (or surprising) as we could understand its entirety from an effective mean field picture. The motivation of my thesis is to expand the physical mechanisms of atom-field coupling and atom-atom interactions to restore the single-quanta quantum optical nonlinearity for large numbers of photons and atoms, and enable a new frontier of non-trivial quantum many-body systems controlled by atom-gauge-field interfaces, as envisioned in the beginning of this chapter. Considerable degrees of technological and theoretical challenges surely exist in this frontier, but I think that this is an exciting long-term avenue to understand the low-energy physics of atomic and photonic quantum systems in terms of gauge-field theories.

1.3 A new regime for many-body QED with Rydberg-dressed cavity polaritons

In Chapter 2, I will provide the theroetical primer that attempts to describe the essential physics of the regime of "many-body QED," an ambitious new regime of light-matter interaction that Prof. Choi has articulated with the beginning of his group. Here, I will provide the heuristic conviction why optical physics shall advance into this regime to be of any relevance for the exploration of non-trivial many-body physics with light.

Let's begin with an extension of infinite-range Dicke model by the inclusion of multiple cavity modes l and pump fields $\epsilon_{k,l}, \epsilon_a$ to mediate the spin-spin interactions,

$$\begin{aligned} \hat{H}_0^{(N)}/\hbar &= \sum_i^N \Delta_a \hat{\sigma}_z^{(i)} + \Delta_f \hat{a}_l^\dagger \hat{a}_l + \sum_{i,l}^N g_l(\vec{r}_i)\left(\hat{\sigma}_+^{(i)}\hat{a}_l + \hat{\sigma}_-^{(i)}\hat{a}_l^\dagger\right) \\ &+ \left(\epsilon_{\kappa,l}^*\hat{a}_l + \epsilon_{\kappa,l}\hat{a}_l^\dagger\right) + \sum_i^N \left(\epsilon_a^*\hat{\sigma}_+^{(i)} + \epsilon_a\hat{\sigma}_-^{(i)}\right). \end{aligned} \tag{1.65}$$

Multiple cavity modes l can act as the quantum channels, and internal states of the atoms can behave as quantum nodes of the quantum network model, described earlier in this chapter. Let us imagine some Raman coupling schemes through the cavity that allow the coupling, not only to the ground and electronically excited states of the atoms, but also between the well-protected hyperfine clock states of a frequency-standard atom (e.g., Cesium atom) with virtually infinite coherence time. Time-dependent control lasers $\epsilon_{l,i}$ selectively couple the cavity photons in particular mode l to a single atom, and the quantum-state of the atom can be individually imaged by a high-resolution quantum-gas microscope at the shot-noise level, and the long-range coherence can be accessed by photons leaking out of the cavity. With these toolboxes, we can in principle realize universal gate sets for cavity QED-based quantum computation, as pursued by circuit QED platforms [39]. Indeed, a major milestone in quantum information science is to utilize these atom-field interactions to digitally or continuously assemble interesting quantum spin models.

However, one major problem that even a quantum computer would have difficulty is finding the ground state of some complex Hamiltonian (technically, QMA-complete Hamiltonians) [60]. Quantum algorithms for finding a ground state are quite costly. However, if one could devise a QMA-complete Hamiltonian with a synthetic quantum system, while the quantum machine is only a single-purpose, it would be able to reach ground states of time-independent gapped Hamiltonians by dissipatively coupling to a zero-temperature bath perhaps with acceptable level of errors. For example, in an ideal case of Raman sideband cooling, the atom-light interaction transfers the system's thermal energy coherently to the entropy of the laser fields, which act as reservoir fields (zero-temperature bath) of the many-body master equation.

Upon the elimination of the cavity fields, the system as outlined above, however, can only at best simulate the translationally-invariant XX spin model of the class

$$\hat{H}_{\mathrm{XX}} = \sum_{i}^{N} \left(h_x \hat{\sigma}_x^{(i)} + h_z \hat{\sigma}_z^{(i)} \right) + \sum_{i,j}^{N} J_{ij} (\hat{\sigma}_x^{(i)} \hat{\sigma}_x^{(j)} + \hat{\sigma}_y^{(i)} \hat{\sigma}_y^{(j)}), \tag{1.66}$$

with arbitrary phase-amplitude controls of the spin-exchange coefficients J_{ij}. For $h_x = 0$, this model is just a textbook problem, where it is possible to map the model in a diagonal form with non-interacting free fermions $\hat{f}_k$ through Jordan-Wigner transformation. In fact, for $h_x \neq 0$, the problem is straightforward and can be solved numerically. In fact, this problem could be solved by mean-field approaches.

More generally, to create k-local Hamiltonians with $k > 2$ (e.g., $\hat{\sigma}_x^{(1)} \hat{\sigma}_x^{(2)} \hat{\sigma}_x^{(3)}$), one requires nonlinearity in the cavity photons. For instance, one atom may be "constrained" to generate two virtual photons, where the second and third atoms may coherently absorb them to realize 3-body interaction. That is, there must be an energy benefit for creating two photons than just one photon for the first atom, in order to realize such an exotic spin-interaction term. From the point of view of lattice gauge theory, you would like to have some gauge constraints on the bosons mediating the spin-spin interaction [61]. The problem is that the cavity fields and atoms by themselves are not really interacting, and they only talk with each other through the atom-field coupling.

We can introduce a new ingredient in the form of interacting quantum matter strongly coupled to quantized electromagnetic fields, thereby many-body QED. In this setting, we have a quantum many-body system that on its own has interesting many-body effects. We would then like to hybridize the cavity fields with the matter to retain some of the material's property to cause strong interaction. In addition, when viewed from the photons, we can equivalently consider the interacting atoms are the finite-dimensioanl "gauge bosons" (as in the quantum link models of lattice gauge theories [62]) that mediate long-range interaction between the photons. This would be a really exciting playground for new physics to emerge!

In Chapter 2, I will discuss a driven-dissipative cavity QED system for strongly interacting Rydberg atoms, where we can create tunable-range spin XXZ spin model

$$\hat{H}_{\mathrm{XXZ}} = \sum_{i}^{N} \left(h_x \hat{\sigma}_x^{(i)} + h_z \hat{\sigma}_z^{(i)} \right) + \sum_{i,j}^{N} J_{ij}^{XX} (\hat{\sigma}_x^{(i)} \hat{\sigma}_x^{(j)} + \hat{\sigma}_y^{(i)} \hat{\sigma}_y^{(j)}) + \sum_{i,j}^{N} J_{ij}^{ZZ} \hat{\sigma}_z^{(i)} \hat{\sigma}_z^{(j)}. \tag{1.67}$$

In the limiting case of $J^{ZZ} \gg J^{XX}$, the low-energy physics of this model can be constrained to give rise pure many-body interactions $\sim \hat{\sigma}_x^{(i)} \hat{\sigma}_x^{(j)} \hat{\sigma}_x^{(k)} \hat{\sigma}_x^{(l)}$. In fact, this form of Hamiltonian is QMA-complete [63]. We will apply this model for a proposal of synthesizing quantum square spin ice model in our Rydberg cavity QED platform, to discover the illusive "U(1) quantum spin liquid" phase of lattice QED with long-range quantum entanglement [64, 65, 66]. Surprisingly, the output cavity field can be utilized to measure time-ordered correlators can be used to construct the dynamical spin structural factors $S(k,w) = \frac{1}{N^2} \sum_{i,j,k,l} e^{-ka_0(i-k)} e^{-ka_0(j-l)} \int_{-\infty}^{\infty} d\tau e^{iw\tau} \langle \hat{\sigma}_z^{(i)}(0) \hat{\sigma}_z^{(j)}(\tau) \hat{\sigma}_z^{(k)}(\tau) \hat{\sigma}_z^{(l)}(0) \rangle$ to unambiguously detect this topological phase. In this direction of retaining the atomic degrees of freedom, we have also devised a method that may create string-net condensed phases of the Levin-Wen as well as Kitaev honeycomb models. On the other hand, the mapping into the pure photon model shows that, unlike the Dicke model, photons acquire the interacting character of the material, so that it is possible to create flexible bosonic platform that exhibit new phases of matter (e.g., supersolid and strip phase). More generally, it is also possible to create contact interaction for photons to make them behave fermionic, enabling the possibility to extend into extended Fermi-Hubbard model.

More generally, the most exciting physics would occur in the strong coupling regime with zero-detuning, where it is not possible to separate out neither the atomic or the photonic degrees of freedom, both of which are undergoing many-body interactions with strengths comparable to the vacuum Rabi frequency g_0. Currently, we lack the theoretical framework to understand the necessary physics of this new regime, but in an open-ended fashion, I believe that it would be an essential endeavor to create complex systems interacting with light at extremal theoretical and technological parameter spaces to discover new physics, as it was for the discoveries of Lamb shift, laser, cavity QED, and Bose-Einstein condensates.

Figure 1.6: **Empty lab photo in 2015.** The vacant laboratory in QNC1302 with two Newport optical tables.

1.4 My history in the UQML and notable omitted work

1.4.1 Timeline

In 2015, I joined the UQML as the first student of Prof. Kyung Choi, initially working on the laboratory renovation and construction, installing furnitures, and putting two optical tables. These experiences were one of the most memorable experience of my life, as I am winding down my master program. In 2015, I was joined by another group member, Dr. Chang Liu, and with the two of us, we were responsible for the majority of the laboratory construction. In the middle of 2016, Dr. Mahmood Sabooni joined and he took charge of the quantum gas microscopy system, and Sainath Motlakunta joined our group, where he made some contributions to the photodiode circuit designs before his departure. More lately, Youn Seok Lee has helped our laboratory capabilities in its final building stage. Little did I know in 2015 that we would end up installing two more optical tables and fill the entire four optical tables with optical and electronic, and vacuum components to push forward with the experimental program in this thesis. It was a great run and a collaboration with these group mates. As the only student in the group, my thesis will describe some work that was a strong collaboration with Dr. Liu and Dr. Sabooni, and I will emphasize the credits in the upcoming sections, as appropriate.

In the previous sections, I have only discussed the physical motivation of the work and omitted much of the real technological challenges associated with this project. The main challenge is to integrate strong coupling cavity QED in the optical domain with Rydberg atoms. Because the strong coupling requires small mode volumes for $g > (\kappa, \gamma_{\perp})$, we require methods for electromagnetic shielding of the bound adatoms that create strong stray inhomogeneous electric fields for the Rydberg levels. In fact, this requirement is so stringent that, for a mirror located 100μm away, it is possible to unambiguously detect one Cs atom deposited on the dielectric surface, by Rydberg level shift caused by the stray electric field of the imbalanced work functions. Hence, we are enforced to use larger mirror spacings, and create a new optical thin film material to improve the cavity parameter κ beyond of what has been done in the past 30 years to maintain the strong coupling regime $g > (\kappa, \gamma_{\perp})$. The result is a new generation of optical cavities with ion-beam sputtered thin films made of proprietory stack and materials on a superpolished curved glass substrate (surface roughness $< 0.2\mathring{A}$) and an optical finesse $\mathcal{F} > 500,000$ highest in the world. Hence, our work would have an important application for the developments in optical clocks and frequency metrology as well as ion-trap cavity QED, as the key challenge in these fields is the very development of high-finesse optical reference cavities.

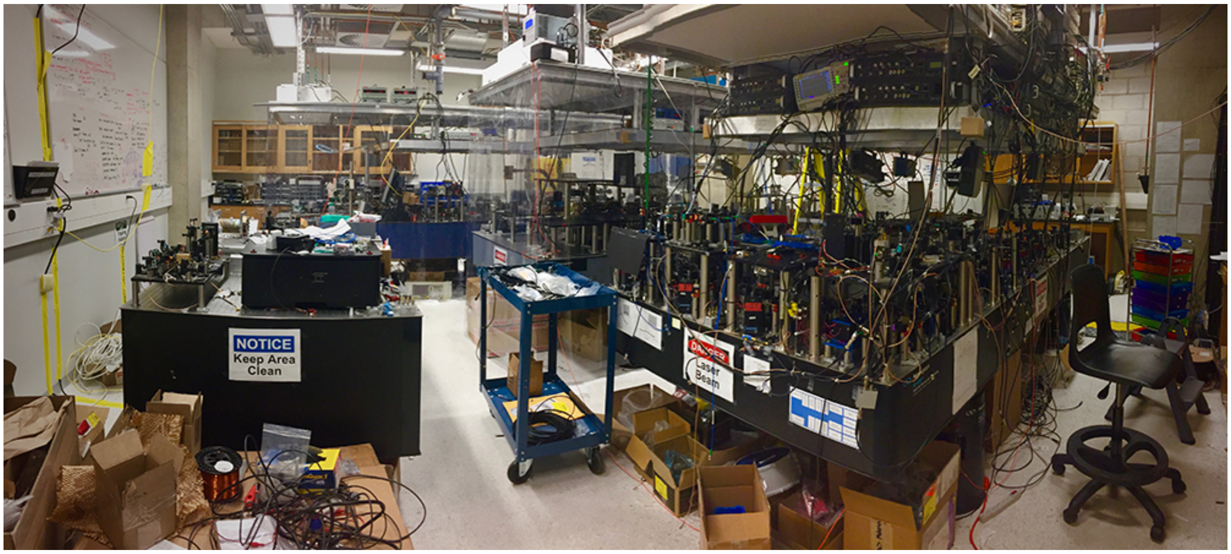

Figure 1.7: **Laboratory photo in 2017.** The four optical tables in QNC1302 filled with optical, electronical, and vacuum components.

The cavity QED platform design discussed in Chapter 6 is really a piece of art that crystalized the days and nights of Dr. Liu and myself in the laboratory. It is made of a 3-dimensional macroscopic superpolished single-crystal Sapphire, made of single-point diamond turning machines and diamond CNCs, with extreme sub-μm precision. The length stability of a single crystal material allowed us to install diamond-turned titanium blade electrodes with surface roughness $\sim 8\AA$ for Faraday shielding and bias electric field controls. The single-crystal shear-mode piezo stabilizes the mean distance of the two mirrors with length instability less than $\frac{1}{100}$ of a single nucleon. The surrounding chamber is pumped down to base pressure less than 10^{-13} Torr.

The large part of my work over the years has been the technological development of infrastructures to run a cutting-edge AMO laboratory. Dr. Liu and I have develoepd two kinds of external cavity diode lasers (ECDL) with FPGA computer-controlled phase-amplitude controls, efficient second-harmonic generation module, and our ultra-low-expansion (ULE) Fabry-Perot (FP) cavities for sub-Hz linewidth laser stabilization. The result is that we can now control several dozens of lasers in terms of the relative phase-frequency relationship down to the sub-Hz level, allowing us to rapidly progress in terms of laser cooling and trapping, as well as for performing novel cavity-sideband cooling mechanisms for the many-body system. These advances are described in Chapter 4.

One of the inital work that I have done was the development of our ultra-high-vacuum

(UHV) cluster system, where the ultracold atoms are produced and manipulated. The design of the chamber was optimized by the quantum-trajectory calculations (Chapter 5) for ultracold atom transport, both from the source chamber to the science chamber, and also for the coherent atom transport within the science chamber. The surface quality was optimized for ultra-low outgassing in order to reach extreme-high-vacuum (XHV) level at 10^{-13} Torr, a unique method that we develoepd for our UHV chambers. The surface was passivated with a thick oxide barrier that prohibits the permeation of H_2 gasses trapped inside the 316 stainless steel walls of the chamber. The AR coatings on the viewports were designed by ourselves with RF-magnetron sputtered coating stack that spans nearly 100μm in thickness to prevent the permeation of He atoms in the atmosphere through the quartz glass, which at the same time achieves remarkably low scatter and reflectance across $300-1500$ nm. Special chemical treatments were applied to reduce the surface roughnesses of the pieces that go within the UHV chamber.

Unfortunately, out of length concerns and proprietority, I have omitted some of the work, which were nonetheless integral to the developments of this thesis:

1. Quantum-gas microscopy and single-atom spectroscopy and imaging (led by Dr. Sabooni)
2. Diffraction-limited holography (led by Dr. Sabooni)
3. Design of custom DC and RF-magnetron sputter machine and chamber for thin film growth (led by me)
4. Actively-quenched ultrafast single photon detector system (led by me)
5. Development of TiZrV non-evaporative getter (NEG) pump coating (led by Sainath Motlakunta)
6. Electronic design and optimization of laser systems and other optoelectronics (led by me and Dr. Liu, other contributors: Sainath Motlakunta and Youn Seok Lee)

1.4.2 Contribution statements

For clarity, I provide a list of my contributions to the core activities described in this MSc thesis:

1. Theoretical activities (Chapter 2 and Chapter 5):

    (a) Quantum defect theories: Estimation of Rydberg atom properties (Primary contributor: Hyeran Kong): I have led all aspects of the work.
    (b) Quantum Monte-Carlo wavefunction toolboxes for numerically simulating quantum optics experiments with home-built numerical packages (Primary contributor: Hyeran Kong): I have led all aspects of the work.

2. UHV-XHV Chamber (Chapter 3, Primary contributor: Hyeran Kong): I made the initial design and led the assembly processes. During the repeated bake-out processes and assembly stages over several months, Dr. Mahmood Sabooni and Dr. Chang Liu have assisted the physical assembly of the first-generation chambers. Sainath Motlakunta assisted the second-generation chamber.

3. Optimization of atom transport process (Chapter 5) - Pushing beam and electrically-tunable optical tweezer (Primary contributor: Hyeran Kong): I have led the analytical and numerical analysis.

4. Laser systems (Chapter 3):
    (a) Littrow-based external cavity diode lasers (Primary contributor: Prof. Choi and Hyeran Kong): I have led the mechanical analysis of the external cavity geometry and the CAD design, based on the initial work by Prof. Choi at KIST. During the implementation (mass production), I have assembled 10 external cavity diode lasers, while the remaining lasers have been assembled by other group members (Dr. Chang Liu, Dr. Mahmood Sabooni, Youn Seok Lee).
    (b) Cat-eye interference filter laser (Primary contributors: Prof. Choi and Dr. Chang Liu): The initial mechanical/CAD design was done by Prof. Choi, and was further optimized by Dr. Liu. My role has been the ray-trace optimization of the optical feedback loop and development of the assembly and alignment procedure for maximizing the mode-hop-free-tuning range of the system. During the implementation (mass production), I have assembled two interference filter lasers, while the initial laser has been assembled by Prof. Choi.
    (c) Master Oscillator Power Amplifier (Primary contributor: Claire Warner, Hyeran Kong): I have supervised the undergraduate researcher, Claire Warner, and was involved in the design processes. I have assembled and implemented the first MOPA with the help of Sainath Motlakunta.
    (d) Cavity-enhanced second-harmonic generation module (Primary contributor: Prof. Choi, Hyeran Kong): Prof. Choi has optimized the cavity parameters, and I have led the CAD designs and its realization.

    (e) Ultrastable ULE reference cavities (Primary contributor: Hyeran Kong): I have designed and optimized the parameters of the ULE reference cavities.
    (f) Thermally-compensated medium finesse cavities (Primary contributor: Dr. Chang Liu): Dr. Liu has designed and assembled the medium-finesse cavities. I have implemented one cavity, and realized the sub-kHz linewidth clock laser in UQML with this cavity.

5. Many-body QED platform (Chapter 6, Primary contributor: Prof. Choi and Dr. Liu): Prof. Choi led the initial concept and design of the many-body QED platform. Dr. Liu implemented the CAD design and the Faraday shield systems. I have theoretically computed the modified cooperativity parameter, taking into account the Rydberg decoherence to optimize the design.

6. Rydberg quantum-dot platform (Chapter 6, Primary contributor: Prof. Choi and Hyeran Kong): Prof. Choi led the initial concept and design of the Rydberg quantum-dot platform. I have led the theoretical simulation to optimize the cavity parameters. I led the CAD design stages and field-compensation schemes.

1.4.3 Summary of remaining chapters: Addressing the experimental challenges towards many-body QED

The main challenge of realizing bonafide many-body QED spans three distinct research areas in AMO physics, namely quantum gas (Chapter 3 and Chapter 5), optical clock (Chapter 4), and cavity QED (Chapter 6). The main workhorse of our experiment is the ultracold quantum matter machine, where we reliably produce and transport ultracold atoms near its quantum-degeneracy in a ultra-high-vacuum environment (Chapter 3 and Chapter 5) to the interaction region of the experiment platforms (many-body QED platform and the Rydberg quantum-dot platform). Once the laser-cooled atoms are trapped in the 2D holographic optical potential landscape, we apply a set of ultrastable phase-synchronized laser fields across octave-spanning bands (Chapter 4) to excite and dress the hyperfine ground states with high-lying Rydberg levels, and to stabilize the vacuum fields of the cavity. Finally, the cavity vacuum renormalizes the Rydberg ice system by injecting quantum fluctuations to melt the spin ice into a quantum spin liquid in a many-body QED platform (Chapter 6).

In the following, I provide the summary of the individual chapters.

Chapter 2

I provide a theoretical description of many-body QED and introduce a range of realizable physical models with the quantum optics toolkits available to our experimental platform. I will first discuss my theoretical work on evaluating the Rydberg properties by way of the quantum defect theory. I will introduce a new regime of Rydberg quantum-dot, wherein Rydberg-dressed atomic ensemble represents a single SU(2)-spin with collectively enhanced atom-cavity coupling rate $\sqrt{N}g_0$. Due to the Rydberg blockade mechanism, we restore the original nonlinear Jaynes-Cummings physics of the strong coupling regime. I will then discuss the proposal developed by Dr. Dong and Prof. Choi, along with my numerical simulations, of creating quantum spin ice models with Rydberg-dressed atomic lattices in an optical cavity. We describe a new method of enforcing local conservation rules (Gauss laws) with system-reservoir engineering, and of injecting quantum fluctuations with cavity-mediated spin-spin interactions. I will then conclude with the experimental feasibility of the proposal.

Chapter 3

In our experiment, we must satisfy two competing requirements. On the one hand, we require a relatively large vapor pressure in the UHV regime to load and laser-cool highly dense Cs atoms. On the other hand, we require the base pressure at the XHV domain to avoid collisional losses, thereby trapping and cooling the Cs atoms to its quantum degeneracy. In this chapter, I describe the considerations for designing such an UHV chamber system, and introduce special vacuum techniques to reach XHV level optimized for AMO experiments. A cluster UHV-XHV chamber system is realized with a base pressure $\sim 10^{-13}$ Torr, the lowest operating pressure for an AMO experiment. I describe the rationale behind our design and the detailed methods for cleaning, passivation, assembly, and bake-out.

Chapter 4

In this chapter, I describe our laser infrastructure and technologies. First, I describe the scientific objective of the diverse lasers and a high-level overview of the optical and microwave clock distribution network. I then describe the experimental procedure and laser sequences. I describe our home-made laser systems: Grating-based Littrow external cavity diode laser and the cat-eye interference-filter laser. Our Science lasers need to be stabilized with absolute linewidth below 1 kHz with instantaneous stability of less than 1

Hz to operate with high-lying Rydberg states and phase synchronized with other octave-spanning laser fields. I discuss my work on developing an ULE Fabry-Perot cavity as the local temporary optical clock, and the SHG module to frequency convert optical fields for Rydberg excitations.

Chapter 5

In this chapter, I develop the open-system formalism that takes into account the internal and external dynamics of neutral atoms. I apply this formalism for the two atom-transport processes used in our experiments: Pushing beam and electrically-tunable optical tweezer techniques. I then account for the quantized motion of the atoms to self-consistently treat the case of Raman sideband cooling, and project the connection of the Rydberg-dressed nonlinearity in quantum motion to self-organized quantum spin models as future work.

Chapter 6

In this chapter, I describe our experimental platforms for reaching the strong coupling regime of many-body QED. In the first platform (Rydberg quantum-dot platform), we utilize the collective encoding of atomic ensembles and Rydberg-blockade effect to realize a Jaynes-Cummings model with unprecedented cooperativity $C \sim 10^4$. In the second platform (many-body QED platform), we developed a new generation of IBS thin film mirrors that allow the state-of-art optical finesse $\sim$ 500k. I also discuss the field compensation method based on the 8-point electrode model.

Chapter 7

Finally, I provide a vision for future experiments in many-body QED with the apparatus that I have developed, and conclude the MSc thesis.

Chapter 2

Rydberg-dressed cavity polaritons

In spite of the advances over the last decades with the manipulation of microscopic quantum optical systems, much of the underlying physics of atom-light interactions has not changed fundamentally in that the atomic and field degrees of freedom (DOFs) were largley non-interacting and were independent of each other. For a large scale system, the ranges of “quantum many-body” models are thereby limited by the absence of interactions that cannot be understood in terms of the mean fields, and the dynamical processes of photons dressed by the non-interacting matter are well-understood in terms of their nearly linear optical response (Chapter 1). In fact, we could understand much of the physics of macroscopic light-matter interactions simply in terms of the largely non-interacting polaritons with a negligible amount of quantum fluctuations in their density-density correlations, similar to sub-threshold optical parametric oscillators.

On the other hand, as an analog quantum simulator, we would like to map the DOFs of the simulated system to those of the simulating one. The latter can be controlled in the laboratory and its dynamics can be tailored (in particular, the corresponding Hamiltonian) to be equivalent to those of the system we are trying to observe. This allows us to extract the information about systems that can not be accessed easily, by investigating some non-trivial quantum systems where state preparation and measurements are much easier tasks. Since an analog quantum system not only emulates the real-time unitary dynamics but also directly map the target Hamiltonian into the real physical object, it would be exciting if we can create quantum models beyond the scope of the condensed matter physics, as the physical system would be of an interest by its own virtue for investigation. Using these ideas, there have been tremendous success with natural AMO systems in simulating condensed matter counterparts, such as the Bosonic and Fermionic Hubbard models, and the transverse Ising model. Typically, the ranges and the localities of

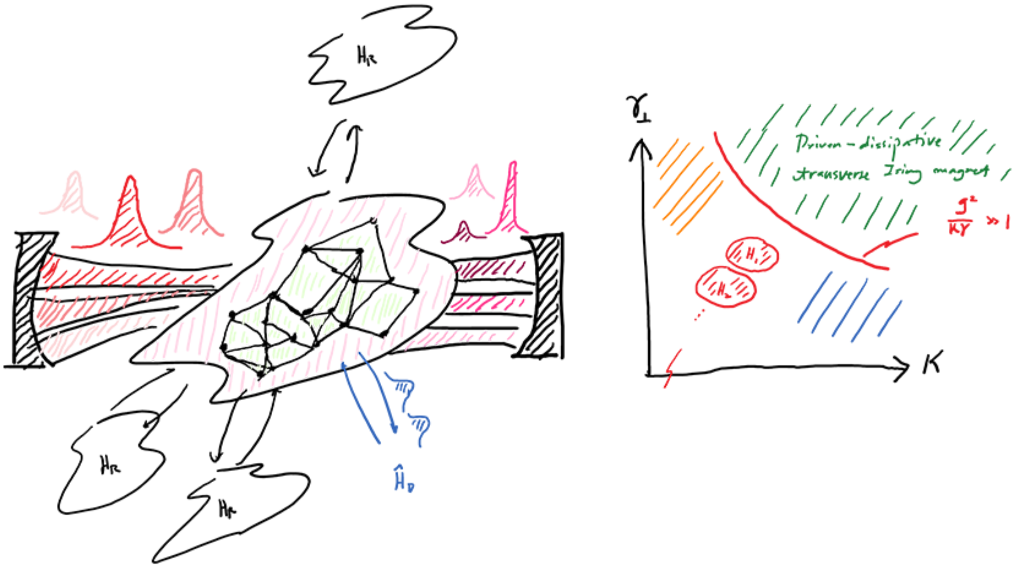

Figure 2.1: **Atom-field interactions for many-body QED.** a, Cavity QED with a quantum many-body system, represented by a spin network (with characteristic interaction strength λ). The intrinsic coupling g to the optical cavity dominates over the dissipative rates κ_i to other reservoirs $\hat{H}_R$. b, The parameter space for atom-field interactions g for non-perturbative Rydberg interactions $g \simeq \lambda$. The red line depicts the boundary for which the strong coupling regime $g \gg \kappa_i$ persists. Above the curve, the optical cavity can be utilized as a driven-dissipation channel for the transverse Ising model for Rydberg atoms for cooling and steady-state preparation. In the strong coupling regime ($g^2/\kappa\gamma_\perp \gg 1$), the atomic degrees of freedoms (DOFs) are removed with $\gamma_\perp \gg \kappa$ (photon regime) to induce many-body interactions among the cavity photons (for degenerate optical cavities), enabling the novel optical interactions (e.g., n-photon Effimov bound states and Fermionization of "contact" photons in 1D). For $\kappa \gg \gamma_\perp$ (Purcell regime), the optical cavity is adiabatically eliminated to create quantum gauged materials (e.g., quantum square ice and string-net models) for the underlying atomic DOFs. In the "spaghetti" regime, it is not possible to separate out the timescales of different DOFs, cavity polaritons are expected to behave with a completely different effective quantum model within each of the gauge sectors, which are separated and excited by a single characteristic quanta. Due to the atom-photon entanglement, the dynamical phenomena in the spaghetti regime must be understood holistically by incorporating both atomic and photonic DOFs, opening a new physical domain for light-matter interactions.

atomic interactions are limited to translationally-invariant nearest-neighbor and two-body (2-local) terms, reducing the applicability of these models.

In this Chapter, I discuss the ranges of physical models available to our new hybrid light-matter toolkits in the new regime of many-body QED and the atomic physics of Rydberg states for computing the dipole and van der Waals interactions between Rydberg atoms. I will begin with the restoration of the Jaynes-Cummings physics in the strong blockade regime, and the favorable scaling with respect to the collective strong coupling. I will then discuss the proposal, developed by Dr. Dong and Prof. Choi, for the creation of quantum square ice models with Rydberg-dressed atomic lattices in an optical cavity, as an example of U(1) lattice gauge theory, and the detection of dynamical spin structure factors, a particular nonlocal time-ordered correlator for witnessing $k > 2$-body interactions, through cavity relaxations. Such a model is expected to support a quantum spin liquid phase with long-range topological entropy, and is well within reach with our experimental capabilities.

2.1 Coupling strongly interacting quantum matter to optical cavities

The general framework of my thesis is to examine the nature of atom-light interaction for long-range interacting quantum matter, described by some atomic Hamiltonian $\hat{H}_a$. In the rotating frame, we can try to couple some properties of the material system (represented by the operator $\hat{c}_a^{(\alpha)}$) to some excitations in the quantized electromagnetic field. In the strong coupling regime $g_0 \gg (\kappa, \gamma_\perp)$, with the photon Hamiltonian $\hat{H}_p/\hbar = \sum_\beta \delta_\beta \hat{c}_p^{(\beta)\dagger}\hat{c}_p^{(\beta)}$, denoted by the jump operator $\hat{c}_p^{(\beta)}$ of transverse mode β. We can describe the atom-field interaction

$$\hat{H}_I/\hbar = \sum_{\alpha,\beta} g_{\alpha,\beta}(\hat{c}_a^{(\alpha)\dagger}\hat{c}_p^{(\beta)} + \hat{c}_a^{(\alpha)}\hat{c}_p^{(\beta)\dagger}). \tag{2.1}$$

Let us consider a general atomic Hamiltonian with arbitrary k-body density-density interactions

$$\hat{H}_a/\hbar = \sum_{\alpha} \Delta_\alpha \hat{n}_a^{(\alpha)} + \sum_{\{\alpha\}} \lambda^{(k)}_{\{\alpha\}} \prod_{\{\alpha\}} \hat{n}_a^{(\alpha)}, \tag{2.2}$$

with the number density $\hat{n}_a^{(\alpha)} = \hat{c}_a^{(\alpha)\dagger}\hat{c}_a^{(\alpha)}$ from atom α.

If we consider the fields as part of the cascade atomic quantum system, we can adiabaticaly eliminate the fields altogether and derive the effective model of the reduced atomic system

$$\hat{H}_s^{(a)}/\hbar = \sum_{\alpha} \Delta_\alpha \hat{n}_a^{(\alpha)} + \sum_{\alpha,\alpha'} J_{\alpha,\alpha'}(\hat{c}_a^{(\alpha)\dagger}\hat{c}_a^{(\alpha')} + h.c) + \sum_{\{\alpha\}} \lambda_{\{\alpha\}}^{(k)} \prod_{\{\alpha\}} \hat{n}_a^{(\alpha)}. \tag{2.3}$$

In a complementary fashion, we can also consider the underlying virtual excitations $(\hat{c}_a^{(\alpha)}, \hat{c}_a^{(\alpha)\dagger})$ of the trapped atoms as the mediator between the optical photons with a photonic many-body Hamiltonian

$$\hat{H}_s^{(p)}/\hbar = \sum_{\beta} \delta_\alpha \hat{n}_p^{(\beta)} + \sum_{\beta,\beta'} \tilde{J}_{\beta,\beta'}(\hat{c}_p^{(\beta)\dagger}\hat{c}_p^{(\beta')} + h.c) + \sum_{\{\beta\}} \tilde{\lambda}_{\{\beta\}}^{(k)} \prod_{\{\beta\}} \hat{n}_p^{(\beta)}. \tag{2.4}$$

For both cases, the tunneling terms $J_{\alpha,\alpha'}$, $\tilde{J}_{\beta,\beta'}$ and k-body terms $\lambda_{\{\alpha\}}^{(k)}, \tilde{\lambda}_{\{\beta\}}^{(k)}$ are of independent origins (derived from the atom-field coupling and the internal atomic many-body Hamiltonian), and is not a simple perturbation of the atom-field interaction. It is thereby possible to dynamically tune the system from $J > \lambda$ to $J < \lambda$. In particular, for the later case, we may design dynamical gauge constraints $\hat{G}_\boxtimes = \sum_\boxtimes \hat{O}_\boxtimes$ over some plaquette $\boxtimes$ with an energy penalty $\lambda \hat{G}_\boxtimes^2$ with $\lambda > 0$ into the density-density term, where we assume $\hat{O}_\boxtimes$ is the system operator that represents some gauge fields. Surprisingly, the lowest order dynamical process for such a constrained system would give rise to many-body interactions $\sum_i \hat{S}_i$ for the k-body string operator $\hat{S}_i$. For instance, for commutative $\hat{S}_i$, we will obtain a general stabilizer Hamiltonian for self-correcting quantum memories.

Perhaps, the most exciting situation would arise when it is not possible to eliminate the field nor the atomic DOFs (See the caption of Fig. 2.1). In this case, we are left with the full Hamiltonian

$$\hat{H}/\hbar = \sum_{\beta} \delta_\beta \hat{c}_p^{(\beta)\dagger}\hat{c}_p^{(\beta)} + \sum_{\alpha} \Delta_\alpha \hat{n}_a^{(\alpha)} + \sum_{\alpha,\beta} g_{\alpha,\beta}(\hat{c}_a^{(\alpha)\dagger}\hat{c}_p^{(\beta)} + \hat{c}_a^{(\alpha)}\hat{c}_p^{(\beta)\dagger}) + \sum_{\{\alpha\}} \lambda_{\{\alpha\}}^{(k)} \prod_{\{\alpha\}} \hat{n}_a^{(\alpha)}, \tag{2.5}$$

where an already highly complex atomic many-body system is strongly coupled to infinite-dimensional bosonic quantum fields, with little pathway for further understanding. Unlike the case of cavity QED (the first three terms), the total atom-field state of such a system cannot be understood simply from the cavity polaritons, dressed quasiparticle excitations between light and matter, or even some perturbative expansion of interacting cavity polaritons, due to the many-body term $\sum_{\{\alpha\}} \lambda_{\{\alpha\}}^{(k)} \prod_{\{\alpha\}} \hat{n}_a^{(\alpha)}$. Because of the absence of generic theoretical tool sets, we denote this regime the ’ ’spaghetti” regime.

In the simpler case with a large gauge constraint $\lambda \gg g$, the atom-field system may develop different effective quantum many-body models $\hat{H}_{\text{eff}}^{(Q)}$ of cavity polaritons within

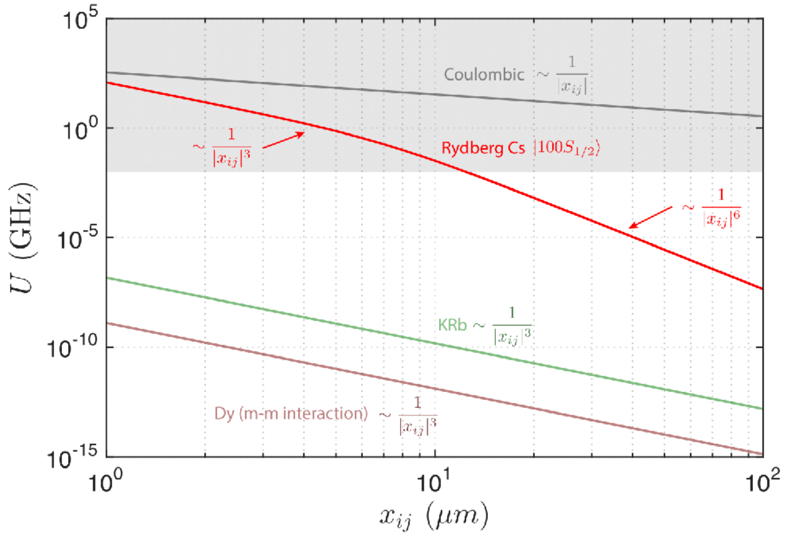

Figure 2.2: **Comparison of "strong" atom-atom interactions.** We compare the level shift of atom-atom interactions across distance scales currently available in our experimental platform for prominent architectures for "long-ranged" AMO systems – Rydberg atoms (Cs atom with $|100S_{1/2}\rangle$), polar molecules (KRb molecule with permanent electric dipole moment ~ 1 Debye), and magnetic neutral atoms (Dy with permanent magnetic dipole moment $10\mu_B$). By comparison, two Cesium atoms in the Rydberg state $|100S_{1/2}\rangle$ separated by a modest distance $10\mu m$ experiences a level shift 8-order of magnitude larger than that of KRb[b]. The Coulomb interaction between two singly-charged ions is also shown (gray line). Unlike the other dipolar interactions, the ionic interactions do not directly couple to the spin states due the decoupling between the internal and external atomic DOFs, and is not relevant for the discussion. State-of-art ion trap architecture can only mediate Ising term with characteristic strength 10 kHz [67].

each of the gauge-invariant subspaces, whose energy scales are separated by the single-quanta gauge-field excitation (e.g., analogous to a creation of a single electrical charge $Q = \langle \hat{G}^2 \rangle$, pumped by a single photon). Indeed, in such a strong coupling regime, the dynamical processes governed by the unitary atom-field evolution $\hat{H}_{\text{eff}}^{(Q)}$ would produce remarkably different physical behaviors for each of the subspaces Q. In the general case without an effective gauge symmetry, we would be left with many-body QED with atoms and photons and possibly a pathway for the discovery of new ultracold quantum "optical" systems that cannot be anticipated theoretically.

So begins our bumpy road!

2.2 Rydberg states

In my thesis, we use Rydberg-dressing techniques to mediate and design the parent atom-atom interaction in the form of a transverse Ising model. To see the advantages of Rydberg states, it is instructive to compare the characteristic energy shifts for two proximal atoms among prominent "long-ranged interacting" AMO platforms [68, 69, 70]. In Fig. 2.2, I compare the atom-atom interactions across distance scales currently available with our quantum-gas microscope of our platform. All other existing methods for inducing long-range interactions U between atomic and ionic internal states do not have sufficient strengths relative to the vacuum Rabi splitting $2g > 100$ MHz in the strong coupling regime of cavity QED. On the other hand, Rydberg excitation to $|100S_{1/2}\rangle$ in Cs offers Ising exchange coefficient 10^8 times larger than those of ultracold KRb molecules [71, 72] (with the largest permanent electric dipole moment in the periodic table)! Here, we use the spectroscopic notation $|nL_J\rangle$. The shaded region illustrates the minimal requirement $U \gg g$ for the spaghetti domain of many-body QED. The interaction coefficients for Rydberg states can be readily tuned across a wide dynamic range, and the shape function of the interatomic potential can be designed through Rydberg-dressing techniques, enabling switchable, long-range atom-atom interactions with the capability to explore complex phase diagrams. The coherence of the system can be dramatically enhanced by dressing the ground-state hyperfine clock states to Rydberg states [73, 74, 75].

The large orbital radius ($\langle r\rangle \sim n^2$) of the Rydberg electron implies a macroscopic electric dipole moment $d \sim e\langle r\rangle$ that induces the transitions between proximal Rydberg states where n is the principal quantum number. Indeed, the dipole-dipole interaction between Rydberg atoms has an extremely favorable scaling relative to its coherence time, as depicted in Table 2.1.If the dipole-dipole shift for two atoms separated by distance r_B is larger than the power-broadened linewidth, the excitation probability for multiple Rydberg atoms in ultracold atomic gas is highly suppressed by the phenomena of Rydberg blockade [76, 77, 78, 79]. Indeed, a driven Rydberg gas obeys an Ising-like Hamiltonian

$$\hat{H}_s^{(a)} = \sum_i \Delta_r \hat{\sigma}_{rr}^{(i)} + \Omega(\hat{\sigma}_{gr}^{(i)} + h.c) + \sum_{ij} \Lambda_{ij}^{(p)} \hat{\sigma}_{rr}^{(i)} \hat{\sigma}_{rr}^{(j)}, \tag{2.6}$$

where Δ_r and Ω are the detuning and Rabi frequency of the driving field for the transition $|g\rangle \to |r\rangle$, and $\Lambda_{ij}^{(3)} = \frac{C_3}{|x_{ij}|^3}(\Lambda_{ij}^{(6)} = \frac{C_6}{|x_{ij}|^6})$ depicts the dipole-dipole (van der Waals)

Binding energy W_n	n^{-2}
Energy gap Δ_n	n^{-3}
Electric dipole moment d	n^2
Atomic polarizability α	n^7
Radiative lifetime τ	n^3
C_3-coefficient	n^4
C_6-coefficient	n^{11}

Table 2.1: Scaling laws for Rydberg states [24].

interactions between the Rydberg atoms for $p = 3$ ($p = 6$). Utilizing Rydberg states for applications in quantum information science has several advantages over using other systems in that ultracold atoms offer a large degree of control with laser cooling and trapping techniques readily available to cool the systems. Moreover, the strong atom-atom interactions can be switched on and off over a dynamic range of 8 orders of magnitude. Large n principal quantum number Rydberg states have remarkably large coherence times, which could be extended over a few seconds [77].

Rydberg states were originally conceived for the understanding of spectral lines of atomic Hydrogen within the framework of Bohr's model of the atom [80]. Namely, the binding energy for the outer electron was found to be $W_n = -Ry/n^2$ for principal quantum number n, where the Rydberg constant is $Ry = \frac{Z^2 e^4 m_e}{16\pi^2 \epsilon_0^2 \hbar^2} = 109737.315685\ \text{cm}^{-1}$. Low angular momentum Rydberg states can be readily excited by optical transitions from the ground states [24, 81]. For Alkali metal atoms, a single valence electron orbits around a positively ionic core with long-range Coulombic potential $\sim -1/r$ [c]. For low angular momentum states with $l < 3$, the electronic wavefunction is highly elliptical, penetrating the inner electronic shells. In addition to the screening effect, the exposure of the inner nuclear charge as well as the induced polarization of the inner electron gas by the outer electron need to be properly accounted.

In the subsections that follow, I will describe a semi-empirical model for Rydberg atoms based on the quantum defect theory. Many properties of Rydberg states can be predicted by using experimentally determined quantum defects and model potentials to a reasonable accuracy [81], without the need for first-principle relativistic many-body field theory [83, 84]. With these computational toolboxes, we compute the Ising Rydberg-Rydberg interactions and their radiative atomic properties [24].

---

[c] There has been recent interest with the utilization of Rydberg states in Alkali-earth metal atoms [82]. Because of the presence of two valence electrons, it is possible to localize the atomic wavefunction using one of the ground-state valence electron, while inducing Rydberg-Rydberg interactions with the other electron.

2.2.1 Quantum defect theory

Quantum defect theory (QDT) [24] attempts to capture the interactions between the valence electron and the core by introducing a slowly-varying state-dependent quantum defect δ_{nlj} with a modified binding energy

$$W_{nlj} = -\frac{Ry}{(n-\delta_{nlj})^2}, \tag{2.7}$$

where I define the effective principal quantum number $n^* = n - \delta_{nlj}$, the angular momentum dependent quantum defect δ_{nlj}, and the mass-dependent Rydberg constant $Ry = R_\infty M_{\text{ion}}/(M_{\text{ion}} + M_e)$ with the mass of the ionic core (electron) M_{ion} (M_e). QDT generally accurately predicts most properties of high-lying Rydberg states $|nS_j\rangle, |nD_j\rangle$ as well as their higher order cousins. For the remainder of the discussion, I will use atomic unit with $m_e = \hbar = \frac{1}{4\pi\epsilon_0} = 1$ [85]

The quantum defect δ_{nlj} depends on the angular momentum state, with $|nS_j\rangle$ having the largest δ_{nlj} due to its deep core-penetration. The Coulombic interaction of Rydberg electron with the core shell gives rise to a modified principal quantum number n^*. Empirically, we can set δ_{nlj} from the Rydberg-Ritz formula $\delta_{nlj} = \delta_0 + \delta_2/(n-\delta_0)^2 + \delta_4/(n-\delta_0)^4 + \mathcal{O}(1/n^6)$, associated with the phase shift for low-energy Fano scattering processes between the electron and the ions [86]. For $l > 3$, the overlap between the electronic wavefunction and the core is negligible, and, thereby, the quantum defects are zero with a purely Coulombic core potential. These states are known as Hydrogenic states, and, in the absence of spin-orbit coupling, they are degenerate for a given n. Because the dependence on j is typically weak, it is relevant for high-resolution spectroscopy. By fitting the quantum defect to previous measurements (based on optical and microwave spectroscopy), we then obtain the defects δ_{0-4}.

Model potentials

In order to take into account the core penetration and polarization, I use the parametric model potential by Marinescu *et al.* [87], with the core potential given by

$$V_c = -\frac{Z_{nl}}{r} - \frac{\alpha_c}{2r^4}(1 - e^{-(r/r_c)^6}), \tag{2.8}$$

where $Z_{nl}(r)$ accounts for the core penetration with radial charge $Z_{nl}(r) = 1 + (Z - 1)e^{-a_1 r} - r(a_3 + a_4 r)e^{-a_2 r}$, and α_c accounts for the long-range core polarization induced

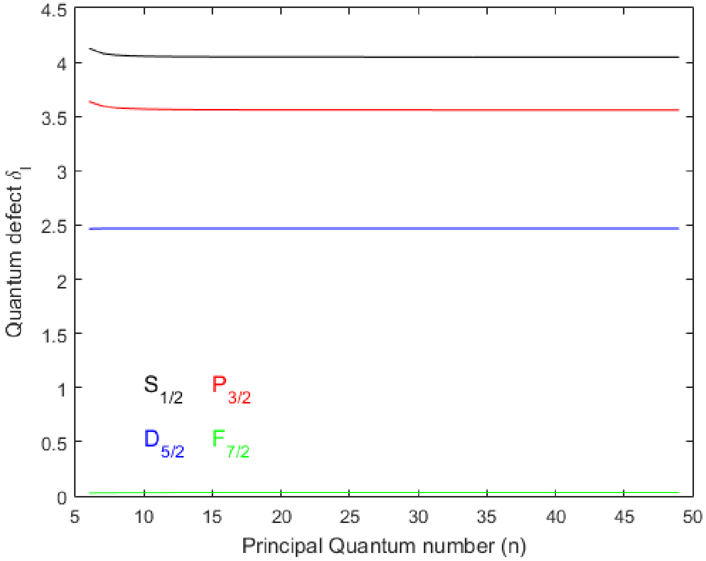

Figure 2.3: **Angular momentum dependent quantum defects of Cs atom.** We plot the fitted Rydberg-Ritz formula of the quantum defect δ_{nlj} based on previous measurements available in the NIST database. As expected, δ_{nlj} is most significant for $|nS\rangle$.

by the valence electron. The core polarizability α_c increases with the number of inner electrons. The values a_{1-4}, r_c, α_c are taken from Ref. [87], with the optimal parameters for Rb and Cs provided in Tables 2.2–2.3.

In order to include the fine structure, I include the spin-orbit interaction

$$V_{so} = \frac{\alpha^2}{r^3}\vec{L}\cdot\vec{S} \tag{2.9}$$

where $\vec{L}\cdot\vec{S} = \frac{j(j+1)-l(l+1)-s(s+1)}{2}$ and $\alpha = \frac{1}{137}$ is the fine structure constant. The total model potential is thereby $V(r) = V_c + V_{so}$. Hyperfine splitting scales with $\sim 1/n^{*3}$ [88, 89, 90], and is negligible [91], where $n^* = n - \delta_{nlj}$ is the effective principal quantum number.

	a_1	a_2	a_3	a_4	r_c
$l = 0$	3.69628474	1.64915255	−9.86069196	0.19579987	1.66242117
$l = 1$	4.44088978	1.92828831	−16.79597770	−0.81633314	1.50195124
$l = 2$	3.78717363	1.57027864	−11.65588970	0.52942835	4.86851938
$l \geq 3$	2.39848933	1.76810544	−12.07106780	0.77256589	4.79831327

Table 2.2: Summary of state-dependent parameters a_{1-4}, r_c for Marinescu model potential [87] of Rb with the core polarizability $\alpha_c = 9.0760$.

	a_1	a_2	a_3	a_4	r_c
$l = 0$	3.49546309	1.47533800	−9.72143084	0.02629242	1.92046930
$l = 1$	4.69366096	1.71398344	−24.65624280	−0.09543125	2.13383095
$l = 2$	4.32466196	1.61365288	−6.70128850	−0.74095193	0.93007296
$l \geq 3$	3.01048361	1.40000001	−3.20036138	0.00034538	1.99969677

Table 2.3: Summary of state-dependent parameters a_{1-4}, r_c for Marinescu model potential [87] of Cs with the core polarizability $\alpha_c = 15.6440$.

Rydberg wavefunctions

The valence electron wavefunction is described by the Schrödinger equation

$$\left[-\frac{1}{2\mu}\nabla^2 + V(r)\right]\psi(r,\theta,\phi) = W_{nlj}\psi(r,\theta,\phi) \tag{2.10}$$

The wavefunction $\psi(r,\theta,\phi)$ can be divided into radial $\Psi_{n,l}(r)$ and angular part $Y(\theta,\phi)$ by separation of variables. The angular part can be solved analytically, and the the selection rules can be derived. Compared to the Hydrogen atom case, the radial part $\Psi(r)$ of wavefunction is modified by the corrections of the quantum defects δ_{nlj} and the model potentials. In Fig. 2.4, I compute the radial Rydberg wavefunction by integrating over the radial part of Eq. 2.10 with the model potential (Eq. 2.8) using the 1D Numerov algorithm.

Matrix elements

With the numerically obtained wavefunction $\psi(r,\theta,\phi)$, we can also obtain the electric dipole matrix element $\langle n,l,j,m_j|r_q|n',l',j',m_j'\rangle$ with the inclusion of the fine-structure basis $j = l+s$. We work in the spherical basis $r_q = r\sqrt{\frac{4\pi}{3}}Y_1^q(\theta,\phi)$ for $q = \pm1, 0$ corresponding

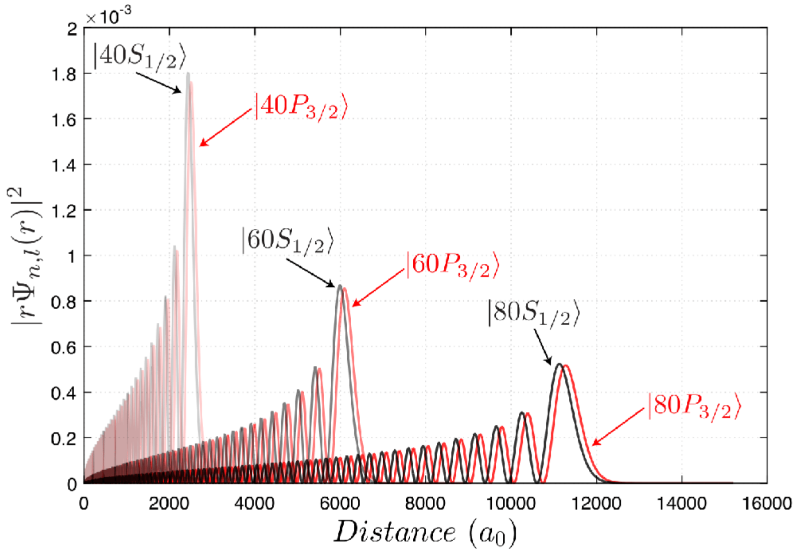

Figure 2.4: **Radial wavefunctions of Cs atom.** We perform the Numerov integration of the Schrodinger equation to obtain the radial wavefunction $\Psi_{n,l}(r)$ [92]. We use the spectroscopic notation $|nL_J\rangle$, where n is the principal quantum number, L is the orbital angular momentum and J is the electron's total angular momentum.

to $\sigma^{\pm}, \pi$ transitions, which can be decomposed to rank-2 spherical tensorial components of the atomic dynamical and static polarizabilities (See Ref. [93] for the detailed expressions). Using the Wigner-Eckart theorem, we write the matrix element

$$\begin{aligned}\langle n,l,j,m_j|r_q|n',l',j',m_j'\rangle &= (-1)^{j-m_j+s+j'+1}\sqrt{(2j+1)(2j'+1)(2l+1)(2l'+1)}\begin{Bmatrix} j & 1 & j' \\ l' & s & l \end{Bmatrix} \\ &\quad \begin{pmatrix} j & 1 & j' \\ -m_j & q & m_j' \end{pmatrix}\begin{pmatrix} l & 1 & l' \\ 0 & 0 & 0 \end{pmatrix}\langle n,l,j|r|n',l',j'\rangle, \end{aligned} \tag{2.11}$$

where I numerically evaluate the overlap integral

$$\langle n,l,j|r|n',l',j'\rangle = \int r^2 dr \Psi_{n,l,j}(r)\Psi_{n',l',j'}(r). \tag{2.12}$$

I can then determine important parameters to understand the radiative interactions with Rydberg atoms, such as the transition probabilities, radiative (partial) lifetimes, and black-body ionization rates, as well as the light-shift potentials.(Appendix A)

2.2.2 Rydberg-Rydberg interaction

Dicke's QED

For highly excited Rydberg states $|nL_J\rangle$, we can perturbatively derive the coefficients of the spin-exchange interaction $\Lambda_{ij}^{(p)}$ in the Ising Hamiltonian in Eq. 2.6. In the limiting case of large $n \gg \delta_l$, with Eq. 2.7, we can express the n-scaling of the energy defect $\Delta W_{n',L',J';n,L,J}$ between the Rydberg angular momentum states as

$$\Delta W_{n',L',J';n,L,J} \propto -\frac{\Delta\delta_{L,L'}}{n^3}, \tag{2.13}$$

where $\Delta\delta_{L,L'} = \delta_L - \delta_{L'}$ is the difference between the quantum defects for the two closest Rydberg states $|nL_J\rangle$ and $|nL'_{J'}\rangle$ (i.e., the fine structure of the Rydberg levels).

For these two Rydberg levels, we can formulate a QED for a Dicke model as with Section 1.2.2. Here, a collection of neutral atoms at sites $\vec{x}_i, \vec{x}_j$ in the Rydberg levels $|nL_J\rangle$ and $|nL'_{J'}\rangle$ with energy defect $\Delta W_{n',L',J';n,L,J}$ is coupled to a fluctuating vacuum field of the free space. The physics of this Dicke interaction essentially describes the driven-dissipative spin-exchange Hamiltonian between the two vacuum-induced Rydberg dipole moments $\hat{\mu}_i, \hat{\mu}_j$. As I formally derive in Section 1.2.2, the vacuum-mediated XX term gives rise to the characteristic scaling $\sim 1/|x_{ij}|^3$ scaling (Eq. 1.50). For highly excited Rydberg states $|nL_J\rangle$ with a large orbital radius $\sim n^2$, two neutral atoms would then experience a non-resonant dipole-dipole interaction between the energetically neighboring Rydberg states $|nL_J\rangle$ and $|n'L'_{J'}\rangle$ with

$$\hat{H}_{ij}^{(dd)}(\vec{x}_{ij}) = \frac{\hat{\mu}_i^\dagger \cdot \hat{\mu}_j}{|\vec{x}_{ij}|^3} - \frac{3(\hat{\mu}_i^\dagger \cdot \vec{x}_{ij})(\hat{\mu}_j \cdot \vec{x}_{ij})}{|\vec{x}_{ij}|^5} \tag{2.14}$$

for the electric dipole transitions $\hat{\mu}_i = \langle n'L'_{J'}|e\hat{r}_i|nL_J\rangle \hat{\sigma}^{(i)}_{n',L',J';n,L,J}$ with projection operators $\hat{\sigma}^{(i)}_{n',L',J';n,L,J} = |n'L'_{J'}\rangle_i\langle nL_J|$. For the S-orbitals, we expect an isotropic, non-resonant dipole-dipole interaction $\hat{H}_{ij}^{(dd)}(\vec{x}_{ij}) \simeq \frac{C_3}{|\vec{x}_{ij}|^3}\hat{\sigma}^{(i)}_{n,L,J;n',L',J'}\hat{\sigma}^{(j)}_{n',L',J';n,L,J} + h.c$, with the dipole-dipole coefficient $C_3 = |\langle n'L'_{J'}|e\hat{r}|nL_J\rangle|^2 \propto n^4$, where the dipole-dipole interaction causes a coherent spin flips in the form of XX Hamiltonian in the manifold of $|nL_J\rangle$ and $|n'L'_{J'}\rangle$.

For atoms with interatomic distance $|x_{ij}| \gg r_c$ beyond the crossover distance r_c[d] in the van der Waals regime, the energy defect ΔW is much larger than the spin-exchange inter-

---

[d] r_c is the crossover distance at which the atom-atom interaction transitions from the van der Waals to the dipole-dipole regimes, with the crossover at $\Delta W = \frac{C_3}{r_c^3}$.

action $\frac{C_3}{|\vec{x}_{ij}|^3}$. The atoms thereby do not directly experience spin-flip interaction between Rydberg states $|nL_J\rangle$ and $|n'L'_{J'}\rangle$ due to the non-degeneracy ΔW, but rather non-local renormalization akin to the Lamb shifts, caused by the modified QED vacuum in proximity to the dielectric materials (i.e., the two atoms themselves). We apply a non-degenerate second-order perturbation theory to obtain an effective Ising Hamiltonian

$$\hat{H}_{ij}^{(\mathrm{vdW})}(\vec{x}_{ij}) \propto \frac{C_6}{|\vec{x}_{ij}|^6} \hat{\sigma}_{rr}^{(i)} \hat{\sigma}_{rr}^{(j)}, \tag{2.15}$$

for the renormalization of the levels for the Rydberg state $|r\rangle = |nL_J\rangle$ with $\hat{\sigma}_{rr}^{(i)} = \hat{\sigma}_{n,L,J;n,L,J}^{(i)}$, and the van der Waals (vdW) coefficient $C_6 \simeq |C_3|^2/\Delta W \propto n^{11}$.

Pair-state basis

While our above description of Rydberg-Rydberg interaction bears its physical foundation of quantum electrodynamics (QED) of Chapter 1, a semi-classical model has been developed in the languages of pair-state basis for the AMO community. While this model is incomplete for short-ranged interactions (below the crossover distance r_c), this dressed state treatment is applicable for most experimental parameters, and connects our conceptual understanding of QED with the terminologies developed in the Rydberg community [24].

In this picture, I only consider the dynamics of the two-atom subspace spanned by $|r_i, r_j\rangle$ and $|r'_i, r''_j\rangle$. The non-resonant dipole-dipole interaction (Eq. 2.14) coherently admixes the initial Rydberg states $|r_i, r_j\rangle$ with $|r'_i, r''_j\rangle$ with "Rabi" frequency

$$\Omega_{ij} = \frac{C_3}{|\vec{x}_{ij}|^3} \left(1 - \frac{3(\vec{e}_i \cdot \vec{x}_{ij})(\vec{e}_j \cdot \vec{x}_{ij})}{|\vec{x}_{ij}|^2}\right), \tag{2.16}$$

where $\vec{e}_i$ is the unit vector for the orientation of the electric dipole. Because of the total energy defects $\Delta_{ij} = \Delta W_{n',L',J';n,L,J} + \Delta W_{n'',L'',J'';n,L,J}$ for the two atoms, we have the Hamiltonian subspace in the pair-state basis expressed as

$$\hat{H}_{ij}^{(\mathrm{pair})} = \begin{bmatrix} 0 & \Omega_{ij} \\ \Omega_{ij}^* & \Delta_{ij} \end{bmatrix}, \tag{2.17}$$

with eigenenergies $\Lambda_{ij}^{\pm} = \left(\Delta_{ij} \pm \sqrt{|\Delta_{ij}|^2 + 4|\Omega_{ij}|^2}\right)/2$ associated with the dressed states $|\Lambda_{ij}^{\pm}\rangle$.

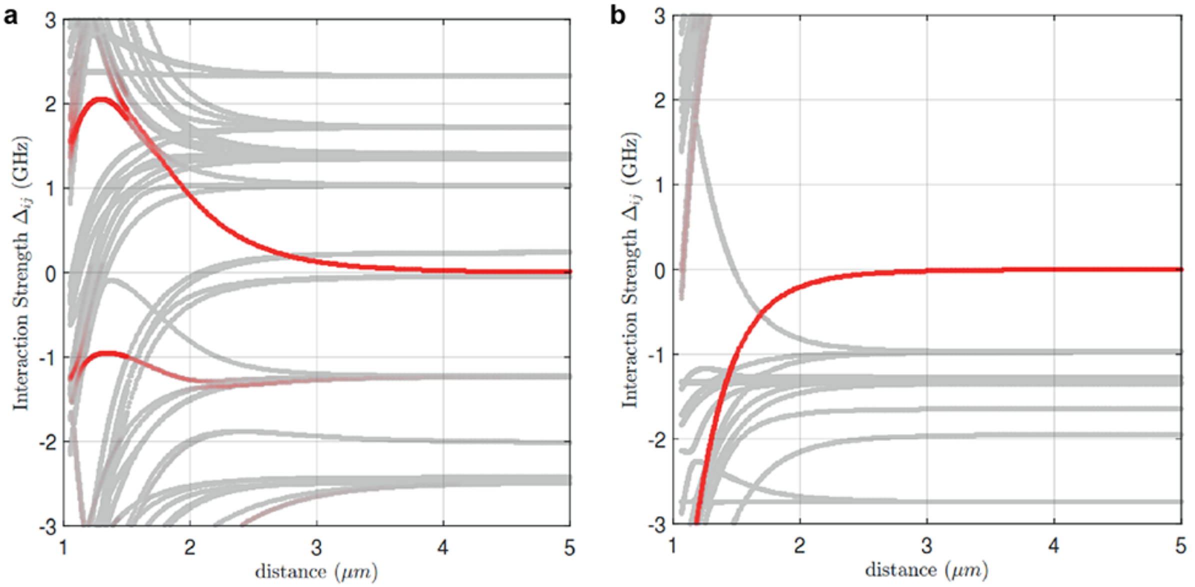

Figure 2.5: **Atom-atom interaction between two Cs atoms.** **a,** Interatomic potential between two atoms in the state $|60S_{1/2}\rangle$. **b,** Interatomic potential between two atoms in the state $|60P_{3/2}\rangle$. The red contour depicts the population of the target Rydberg state in the dressed states $|\Lambda_{ij}^{\pm}\rangle$.

In this dressed state picture, I can compute $\Lambda_{ij}^{\pm}$ as well as the population of $|r_i, r_j\rangle$ of the dressed state $|\Lambda_{ij}^{\pm}\rangle$ as a function of the interatomic distance $\vec{x}_{ij}$ with the matrix elements $\langle n'L'_{J'}|e\hat{r}_i|nL_J\rangle$ obtained from Section 2.2.1. I numerically include other dipole-allowed matrix elements (typically $\sim$ 10 other levels) across different Rydberg admixtures $|n'L'_{J'}\rangle$ to accurately predict the van der Waals (vdW) level shifts with the ARC package [92]. With our MATLAB-Python translator, I integrated the Python ARC packages with our open system treatments for driven-dissipative dynamics, written and pre-compiled in the mpicc of MATLAB that can extend to our lab's Andromeda cluster compute server (Rocks Cluster Server with Infiniband interconnected with all-to-all topologies over 128 physical cores, and 1 TB of RAM) developed by Youn Seok Lee on our group for electromagnetic FDTD and quantum Monte-Carlo wavefunction methods.

As an example, in Fig. 2.5, I numerically determine the Born-Oppenheimer potential of two Cs atoms in Rydberg states $|60S_{1/2}\rangle$ and $|60P_{3/2}\rangle$ by block-diagonalizing the Hamiltonian subspaces of other 50 Rydberg admixtures. The red contour depicts the population of $|60S_{1/2}\rangle$ and $|60P_{3/2}\rangle$ in the dressed states $|\Lambda_{ij}^{\pm}\rangle$, as the admixtures of other Rydberg levels

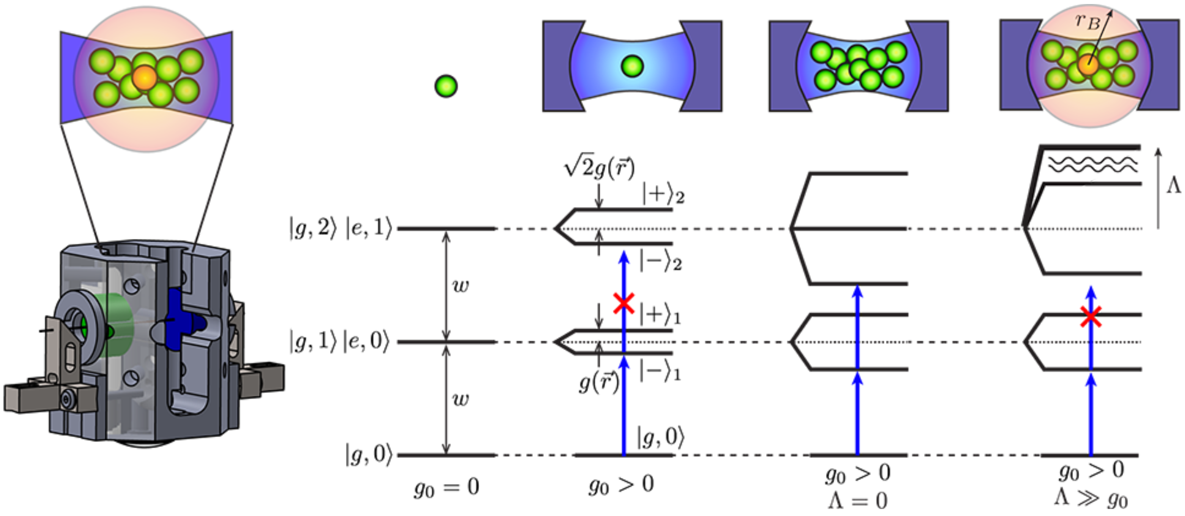

Figure 2.6: **Cavity QED with Rydberg quantum-dot.** **a,** Experimental platform for cavity QED with a Rydberg-dot. **b,** The progressive transformation of atom-field interaction from resonance fluorescence, to cavity QED with single atoms, to the Dicke model in an optical cavity, and to the revival of Jaynes-Cummings physics of collectively enhanced cavity QED with Rydberg blockade.

enter through the spin-exchange inteaction. We emphasize that the quantum defect theory does not provide an accurate result below the LeRoy radius $r_L \simeq 1\mu m$, at which the two orbital wavefunctions of the Rydberg atoms significantly overlaps with each other to form a Rydberg molecule. In Appendix A, I summarize our simulation results in the tabular form for the transition frequency (THz), radiative lifetime (s), blackbody-limited photoionization lifetime (s), reduced matrix element $\langle J'||e\hat{r}||J\rangle$ (ea_0), LeRoy radius r_L (μm), and van der Waals coefficient C_6 (GHz $\cdot\mu m^6$) for transitions $|6S_{1/2}\rangle \rightarrow |nP_{1/2}\rangle$, $|6S_{1/2}\rangle \rightarrow |nP_{3/2}\rangle$, $|6P_{3/2}\rangle \rightarrow |nS_{1/2}\rangle$, $|6P_{3/2}\rangle \rightarrow |nD_{3/2}\rangle$, and $|6P_{3/2}\rangle \rightarrow |nD_{5/2}\rangle$.

2.3 Rydberg quantum-dot media coupled to an optical cavity: Revival of the Jaynes-Cummings physics!

As a prelude to our proposal to lattice gauge-theoretic models, I would like to discuss a conceptually simple physical mechanism to realize the Jaynes-Cummings (JC) model with Rydberg-blockaded atomic ensembles coupled to a quantized field in a single-mode optical cavity [94].

2.3.1 Physical motivation

I consider an ultracold gas of neutral atoms in a moderate Finesse optical cavity in the weak coupling regime $g_0 < (\kappa, \gamma)$. As discussed in the Dicke model of Chapter 1, the vacuum Rabi freqeucny $g_N = \sqrt{N} g_0$ is collectively enhanced by $\sqrt{N}$, where N is the number of trapped atoms at the antinodes of the cavity. As illustrated in Fig. 2.6, the Tavis-Cummings (TC) model exhibits a largely linear coupling between the collective atomic spin excitation and the quantized electromagnetic field,

$$\hat{H}_{\text{TC}}^{\text{int}} = \sqrt{N} g_0 (\hat{a}^\dagger \hat{S} + \hat{a} \hat{S}^\dagger) \tag{2.18}$$

and much of its physics is encapsulated by the classical mean field

$$\hat{S} = \frac{1}{\sqrt{N}} \sum \hat{\sigma}_-^{(i)}, \tag{2.19}$$

in the form of the quasi-bosonic collective spin operator. The TC model do not possess the requisite structural nonlinearity in the excitation manifolds for the photon blockade to inhibit the propagation of higher-order photons (See Fig. 2.6 for the illustration). Hence, there is no quantum optical nonlinearity in such a collective atom-field system, besides the highly perturbative optical nonlinearities in the parametric domain[e].

With the strong Rydberg-Rydberg interactions $\Lambda \gg g_0$, it is possible to design an energy penalty in excitation spectrum of the collective atomic variables to constrain the atomic dynamics into a particular subspace. Within this subspace, we show that the resulting atom-field system is effectively reduced to the original JC Hamiltonian with collective coupling $\sqrt{N} g_0$. At a phenomological level, the collective physics behind this 2-level reduction is analogous to that of a quantum dot, where multiexcitation of electron-hole pairs (excitons) in a semiconductor host defect is suppressed by the Coulomb and exchange interactions (Coulomb and Pauli spin exchange blockades) [15].

The technological merit of our Rydberg-dot approach is quite significant, because the coupling parameter $\sqrt{N} g_0$ of the effective JC model is not limited by the optical physics that governs light propagation and diffraction limit (See Eq. 1.31), with the collectively-enhanced cooperativity factor

$$C = \frac{4 N g_0^2}{\kappa \gamma} \simeq \frac{2N}{3\pi} \frac{\sigma_0}{A_c} \mathcal{F} \tag{2.20}$$

---

[e] Counter-rotating counterparts of Eq. 2.18 depict the generation of two-mode squeezed states and EPR entanglement.

as the critical scaling parameter for coherent light-matter operations. Indeed, our conservative estimates point an unprecedented value for the cooperativity factor $C > 10^5$. As a reference, our expected C is 10^4 times larger than those reported in the state-of-art experiments with W1-defect photonic crystal cavities by the groups of Mikhail Lukin and Vladan Vuletic's group [95, 96] for quantum-state transfer and quantum logic operation (e.g., photonic controlled phase gate) with high entanglement fidelity $F = 1 - \mathcal{O}(1/C)$ [f].

2.3.2 Atom-field Hamiltonian in the regime of strong blockade

As a physically realizable model, we consider a two-step process in a typical ladder configuration investigated for Rydberg atoms. We consider the ground-state $|g\rangle = |6S_{1/2}\rangle$ coupled to the intermediate excited state $|e\rangle = |6P_{3/2}\rangle$ through the vacuum mode of the optical cavity with vacuum Rabi spliting g_0 and detuning Δ_c, which is coherently coupled by a strong laser field to the Rydberg levels $|r\rangle = |nS_{1/2}\rangle$ with Rabi frequency Ω_c. We adiabatically eliminate the intermediate state $|e\rangle$ for $\Delta_c \gg (g_0, \Omega_c)$, and obtain the effective atom-field Hamiltonian

$$\hat{H}_{\mathrm{TC}}^{\mathrm{int}} = \sqrt{N} g_{\mathrm{eff}} (\hat{a}^\dagger \hat{S} + \hat{a} \hat{S}^\dagger), \tag{2.21}$$

with the effective coupling constant $g_{\mathrm{eff}} = \frac{g_0 \Omega_c}{\Delta_c}$ for $|g\rangle \leftrightarrow |r\rangle$. If we neglect the radiative decay rate γ_r of the Rydberg states, we derive the effective Lindblad atomic superoperator with decoherence rate $\gamma_{\mathrm{eff}} \simeq \gamma_e \frac{|\Omega_c|^2}{\Delta_c^2}$, given by the displacement of the intermediate state $|e\rangle \to |e\rangle + \frac{\Omega_c}{\Delta_c} |r\rangle$. The resulting strong coupling parameter $C = \frac{4g_0^2}{\kappa\gamma} \simeq \frac{4g_{\mathrm{eff}}^2}{\kappa\gamma_{\mathrm{eff}}}$ is equivalent in this effective dressed state picture.

In the high n limit of Rydberg states, the dipole-dipole interactions can be treated as an uniform energy shift Λ within a blockade radius r_B, as long as Ising interaction Λ is the dominant energy scale of the problem across r_B. As further justified in Ref. [97], this is a reasonable statement because the particular value of the level shift is not important as long as it can effectively act as a Rydberg blockade mechanism. Furthermore, it is possible to engineer the spatial profiles of $\Lambda^{(ij)}$ (Eq. 2.17) as step functions through Rydberg mixing techniques [98]. Within these approximations, we can simplify the all-to-all Ising Hamiltonian in Eq. 2.15 to on-site interaction

$$\hat{H}_{\mathrm{Ising}} = \Lambda \hat{n}_S (\hat{n}_S - 1), \tag{2.22}$$

---

[f] By comparison, it would have been necessary to reduce cavity mode volume $V_m \sim 10^{-4}\lambda^3$ in the nanophotonic experiments [95, 96] to match our purported C, a physically impossible task due to the hybridization of the atomic wavefunctions with the surrounding dielectric.

where the magnon number operator

$$\hat{n}_S \equiv \sum_i \hat{\sigma}_{ee}^{(i)} = \frac{N}{2}(1 - [\hat{S}, \hat{S}^\dagger]). \tag{2.23}$$

Since $[\hat{S}, \hat{S}^\dagger] = \frac{1}{N}\hat{S}_z \simeq 1$ for a small number $\langle \hat{n}_S \rangle \ll N$ of magnon population, $\hat{n}_S$ indicates the degree of the "violation" of the bosonized magnon operators $\hat{S}, \hat{S}^\dagger$ defined within the blockade volume $V_{r_B} \simeq \frac{4\pi}{3} r_B^3$.

The total atom-field Hamiltonian is then given by

$$\hat{H}_{\text{dot}} = \frac{\Delta_{rr}}{2}\hat{S}_z + \Delta_c \hat{a}^\dagger \hat{a} + \sqrt{N} g_{\text{eff}}(\hat{a}^\dagger \hat{S} + \hat{a}\hat{S}^\dagger) + \Lambda \hat{n}_S(\hat{n}_S - 1). \tag{2.24}$$

From the perspective of the quasi-bosonic operators $\hat{a}, \hat{S}$ in the limit of small excitation and large N, the atom-field Hamiltonian is equivalent to a two-site Bose-Hubbard model, where the "phase" diagram is dictated by the competition between the tunneling rate $t = \sqrt{N} g_{\text{eff}}$ (related to the phase coherence of the polaritonic superfluid and the fluctuation of $(\Delta \hat{n}_S)^2$) and the on-site interaction $U_0/2 = \Lambda$ (projecting the fluid into the number state n_S of the collective spin excitation, and destroying the long-range phase coherence). The detunings Δ_{rr}, Δ_c are related to the chemical potentials of the two sites.

We recognize that the fully Rydberg blockade regime is formally equivalent to that of the hard-core boson mapping in the Mott regime with large on-site interaction $U_0 \gg t$ (i.e., $\Lambda \gg 2\sqrt{N} g_{\text{eff}}$). We can capture the low-energy physics of Eq. 2.24 by mapping the SU(N) collective operators to the SU(2) operators with $\hat{S}(\hat{S}^\dagger) \to \hat{\sigma}_-(\hat{\sigma}_+)$, and deriving the effective Hamiltonian within the spin subspaces $\langle \hat{n}_S \rangle = 0, 1$ ($\langle \hat{H}_{\text{Ising}} \rangle = 0$) while leaving the photonic Hilbert space intact,

$$\hat{H}_{\text{JC}}^{\text{eff}} = \frac{\Delta_{rr}}{2}\hat{\sigma}_z + \Delta_c \hat{a}^\dagger \hat{a} + \sqrt{N} g_{\text{eff}}(\hat{a}^\dagger \hat{\sigma}_- + \hat{a}\hat{\sigma}_+). \tag{2.25}$$

As depicted in Fig. 2.6b, this is precisely the Jaynes-Cummings model that we have departed from by adding a large number of atoms into the optical cavity! To proceed further, we introduce the cavity polariton operators

$$\hat{d}_+ = \frac{1}{\sqrt{2}}(\cos\theta \hat{a} + \sin\theta \hat{S}) \tag{2.26}$$

$$\hat{d}_- = \frac{1}{\sqrt{2}}(\sin\theta \hat{a} - \cos\theta \hat{S}) \tag{2.27}$$

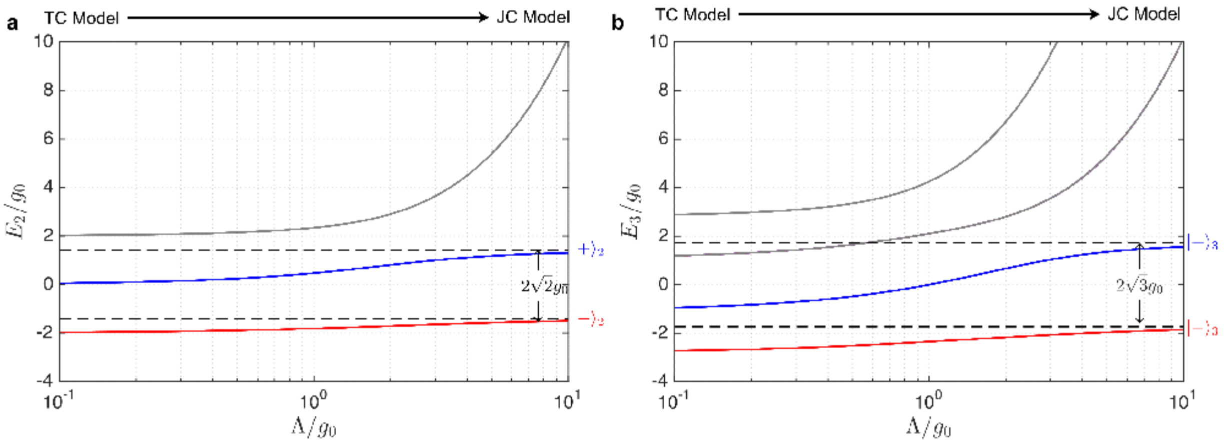

Figure 2.7: **Transformation of the atom-field Hamiltonian under strong Rydberg blockade to the Jaynes-Cummings model. a,** Excitation spectrum E_2 for the $n = 2$ subspace. **b,** Excitation spectrum E_3 for the $n = 3$ subspace. The dashed lines depict the two cavity polaritonic branches expected for the ideal Jaynes-Cummings model with vacuum Rabi splitting $2\sqrt{n}g_0$.

and diagonalize the effective JC Hamiltonian into two-component polaritonic branches

$$\hat{H}_{\mathrm{JC}}^{\mathrm{eff}} = \sqrt{N} g_{\mathrm{eff}} \left(\hat{n}_+ - \hat{n}_- \right) \tag{2.28}$$

with polariton number $\hat{n}_\pm = \hat{d}_\pm^\dagger \hat{d}_\pm$, as expected for the original JC model (Chapter 1) but with collectively-enhanced vacuum-Rabi frequency $\sqrt{N} g_{\mathrm{eff}}$!

2.3.3 Transition of the low-energy excitation spectrum from the Tavis-Cummings model to the Jaynes-Cummings model

The effective Hamiltonian in Eq. 2.28 is only accurate under the strong Rydberg blockade $\sqrt{N} g_{\mathrm{eff}} \ll \Lambda$ across the entire atomic ensemble. Instead, for $\sqrt{N} g_{\mathrm{eff}} \gg \Lambda$, the dynamical processes are well-described by the linearized Tavis-Cummings Hamiltonian. At the intermediate regime, the polaritonic picture breaks down and there is no immediate description in terms of simple normal modes. In this section, I will numerically evaluate this crossover as to how the normal modes of the original atom-cavity system emerge again as the atom-cavity system is swept from $\Lambda/g_0 = 0$ to $\Lambda/g_0 \gg 1$ with $g_0 = \sqrt{N} g_{\mathrm{eff}}$.

In the Tavis-Cummings limit, the polaritonic operators analogous to Eqs. 2.26–2.27

describe the normal modes of the two bosonic modes (atomic and cavity modes). Hence, it is possible to create arbitrary polaritonic branches $\hat{d}_{\pm}$ to populate a particular excitation subspace n without any constraint on the spin excitation number n_S. For instance, for $n = 2$ subspace, it is possible to create polaritonic branches $|\pm\rangle_2 = \hat{d}_{\pm}^{\dagger 2}|g\cdots g\rangle \otimes |0\rangle$ and $|0\rangle_2 = \hat{d}_{\pm}^{\dagger}\hat{d}_{\mp}^{\dagger}|g\cdots g\rangle \otimes |0\rangle$, associated with eigenenergies $\epsilon = \pm 2g_0, 0$, as shown in Fig. 2.7a for $\Lambda/g_0 \to 0$. Likewise, for the $n = 3$ and higher order subspaces, the polaritonic modes spread over the spectrum of $\{ng_0, (n-2)g_0, \cdots, -(n-2)g_0, -ng_0\}$.

However, in the Jaynes-Cummings limit with $\Lambda \gg g_0$, the on-site interaction term Λ drives the Bose-Hubbard model (Eq. 2.24) to the atomic limit, where the collective spin operators are no longer energetically high-dimensional and become effectively hard-core bosons. Hence, the polaritonic excitations cannot be described by the bosonic counterparts of the TC model. Remarkably, the spin nature of $\hat{d}_{\pm}$ only permits a single collective excitation in the atomic medium (due to the Rydberg blockade), effectively reducing low-energy dynamics into the atomic subspace of $|g\cdots g\rangle$ and a single symmetrized excitation $|W\rangle = \frac{1}{\sqrt{N}}\sum_i |g\cdots r_i\cdots g\rangle$. Creating two Rydberg atoms would be prohibitively expensive from the perspective of the energy penalty of $\mathcal{O}(\Lambda)$, thereby constraining the original SU(N) spin subspace (in reality, it is a hard-core boson). In Fig. 2.7, I numerically investigate this crossover transition from the TC to the JC regimes for large N of atoms, by performing exact diagonalization (ED) of the block Hamiltonians within each of subspaces. Fully open system description of this model is beyond the scope of my thesis. But I would like to mention in passing that, with the collective cavity relaxation, Prof.Choi has constructed the input-output formalism for the antibunching parameter $g^{(2)}(\tau) \propto \sum_{ijkl}\langle\hat{\sigma}_+^{(i)}(0)\hat{\sigma}_+^{(j)}(\tau)\hat{\sigma}_-^{(k)}(\tau)\hat{\sigma}_-^{(l)}(0)\rangle$ as the nonlinear witness for genuine multipartite entanglement of the symmetrized massive W states of the trapped atoms within each excitation manifold [99]. Further details will be discussed elsewhere.

2.3.4 Physical implementation and the ultrastrong coupling regime

As discussed further in Chapter 6, in our Rydberg quantum dot platform, we intentionally relax the atom-cavity parameters $(g_0, \kappa, \gamma_\perp) = (0.4\text{ MHz}, 0.5\text{ MHz}, 2.5\text{ MHz})$ in the weak coupling regime. With the adiabatic elimination of the intermediate state with detuning $\Delta_c \simeq 100$ MHz and coupling laser $\Omega_c = 1$ MHz, I obtain the effective coupling rate $g_{\text{eff}} = \frac{g_0\Omega_c}{\Delta_c} \simeq 2\pi\times 4$ kHz and the radiative decay $\gamma_{\text{eff}} = |\frac{\Omega_c}{\Delta_c}|^2\gamma_\perp + \gamma_r \simeq 2\pi\times 500$ Hz (including the blackbody limited decay rate of the Rydberg state $|100S_{1/2}\rangle$ in the Appendix). The single-atom cooperativity parameter is given by $C_1 = \frac{4g_{\text{eff}}^2}{\kappa\gamma_{\text{eff}}} \simeq 0.25 < 1$.

For Rydberg state $|100S_{1/2}\rangle$, I numerically obtain the vad der Waals coefficient $C_6 = 4.6$

THz$\cdot\mu m^6$ from the quantum defect theory (Appendix A). Given the effective coupling rate $g_{\text{eff}} \simeq 2\pi \times 4$ kHz, it is possible to achieve a blockade radius $r_B \simeq \sqrt[6]{C_6/g_{\text{eff}}} \simeq 30\mu m$. As a conservative estimation, I consider a trap volume of $20\mu m^3$, and evaluate a practical atom number $N = 10^3$ (typical atom density in a dipole trap is given by $\rho > 10^{12}/\text{cm}^3$). Remarkably, the collective cooperativity parameter is given by $C_N \to 250 \gg 1$ deep in the strong coupling regime with $\Lambda/g_0 \simeq 20 \gg 1$ (Jaynes-Cummings limit)! In Chapter 6, I further provide the technical description of our experimental platform.

The benefit of our collective encoding with Rydberg blockade is evident in that the nonlinear spectrum of cavity QED is maintained with $q_p \equiv \frac{\sqrt{2nN}g_0}{2\sqrt{nN}g_0} \to \frac{1}{\sqrt{2}}$ by adding more atoms due to the growth of the coupling rate $\sqrt{N}g_0$, without compromising the structural behavior of the anharmonicity parameter $q_a = \frac{\sqrt{4N-2}g_0}{2\sqrt{N}g_0} \to 1$ of the TC model. Because of the scaling $C_N \propto N$, with a smaller radius of curvature 5 cm of the mirrors, if we load ~ 1000 atoms in a single plane ($\sim 60 \times 60\mu m^2$) of the antinode of the cavity field across 1000 sites, we would be able to obtain an unprecedented value for the cooperativity $C_N \simeq 5 \times 10^5 \gg 1$ of cavity QED, enabling ultra-high-fidelity ($F \simeq 1 - 1/C_N$) quantum logic operations. Furthermore, in this regime, because the broadband nature of the atom-field coupling $\sqrt{N}g_0 \simeq FSR = c/2L \simeq 1$ GHz, it would be possible to access the extremely difficult ultrastrong coupling regime in the optical domain[g]. The simultaneous atom-field coupling to the longitudinal cavity modes allows the capability to design arbitrary pairwise spin-exchange interactions $J(x_i, x_j)$ for the creation of synthetic quantum matter, similar to the photonic bandgap physics of the waveguide QED [100, 101]!

2.4 Quantum spin ice models

For most materials, when a system is cooled to near absolute zero, the constituents of the many-body system typically condense into a short-range ordered phase consistent with their symmetries or acquire the long-range coherence of superfluids within the paradigm of Landau's symmetry breaking. Apart from the finite-size effect, much of the physics in these conventional systems can be well understood by local observables (specific heat, magnetization) that monitor the components of the many-body system. Instead, for a quantum spin liquid (QSL), the quantum fluctuations prevent the spins from being driven into a long-range ordered phase even at zero temperature. Similar to fractional quantum

---

[g] Unlike the microwave domain of circuit QED, the ultrastrong coupling regime in the optical domain is defined as the enhancement of the vacuum Rabi splitting relative to the free-spectral range of the optical cavity (instead of the qubit energy).

Hall states, QSLs appear as being completely disordered from any measurement that locally probes the sub-system, but rather the underlying topological order is non-locally spread across the entire quantum spin system by long-range quantum entanglement. Furthermore, the excitations in QSLs fractionalize with the microscopic DOFs separated by the strong quantum correlations. Spin ices are the natural host of the "vacuum" field, subject to local energy constraints by a background gauge structure, over which dynamical spin excitations caused by quantum fluctuations can drive the spin system into a QSL. Remarkably, the long-range entangled states of "quantum" spin ices are associated with the "deconfined" phases of an emergent lattice gauge theory! Here, "deconfined" implies that emergent fractional gauge charges can be spatially separated with a finite amount of energy. Such a QSL remains to be discovered in experimentally.

In this section, we describe an experimental proposal of creating, manipulating, and detecting topologically ordered quantum spin ice models. By significantly departing from our free fermionic cavity QED models, local dynamical gauge structures are designed by the Rydberg-Rydberg interaction and the quantum fluctuations are introduced by dressing the spins with quantized cavity fields. This idea was largely developed by Dr. Dong in our group. Similar ideas laid out in this proposal can be applied to other esoteric models (string-net condensates, Kitaev honeycomb, and AdS$_2$-CFT holographic Sachdev-Ye models) in a fully gauge-constrained and analog manner, as investigated theoretically by Dr. Dong and Prof. Choi. Some of these ideas are beyond the scope of the technical capabilities developed in my MSc thesis, but would be accessible in the near future with better controls. Instead, I focus on the currently feasible quantum square ice models, to which I have contributed by way of my modeling of Rydberg states. Remarkably, for this model, we have identified a powerful method to unambiguously validate the existences of the illusive U(1) QSL and gapless artificial photons of emergent QED within the low-energy sector via the measurement of time-ordered correlation functions of optical photons leaking out through cavity-relaxation.

Before I move on, let me briefly discuss the physics of classical Ising spin ice of frustrated quantum magnetism, as originally conceived by P. W. Anderson [102, 103]. The classical spin ice states form the (frustrated) quantum vacuum, in which XX-like quantum fluctuations drive tunneling between degenerate ice states that support a U(1)-QSL phase with emergent gapless photon-like excitations. Whereas the elementary excitations of classical spin ice are the electrostatic charges (or magnetic monopoles), in a quantum spin liquid, gauge charges interact via dynamical quantum electromagnetic fields with an underlying compact QED.

2.4.1 What is a spin ice?

Highly frustrated magnets, epitomized by the geometric frustration of an anti-ferromagnetic (AF) Ising model on a triangular lattice, are characterized by an extensive ground-state degeneracy. At temperature scale much smaller than the characteristic interaction, thermal excitations have strong local correlations without spatial ordering (e.g., Neel's ordering), behaving similar to disordered and fluctuating liquid phase. Interestingly, these thermally activated liquid phase of spin magnet has a characteristic dipolar (power-law) decay of correlation functions despite the nearest-neighbor nature of the interaction. To distinguish with the QSL driven by genuine quantum fluctuations, these magnetically disordered phases are known colloquially as (classical) spin liquids [64]. The semi-classical

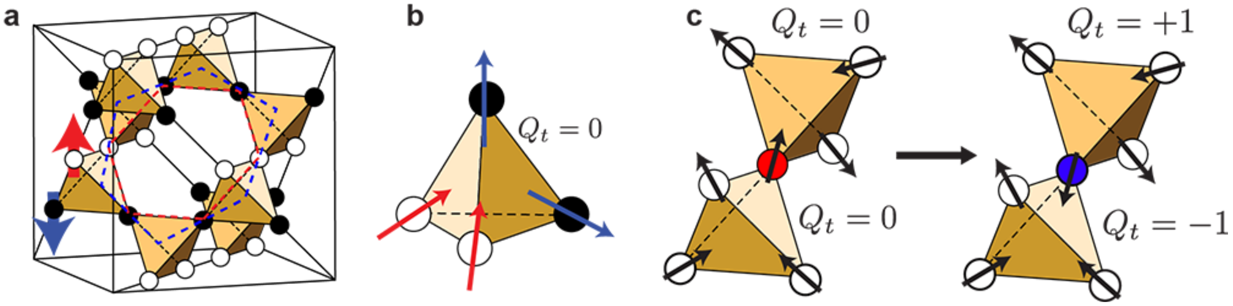

Figure 2.8: **Emergent ice rules in dipolar spin ice systems on Pyrochlore lattice.** **a,** [11] plane of a Pyrochlore lattice. Local crystal fields [111] transform local Ising spins with ferromagnetic coupling into a global AF (anti-ferromagnetic) coupling equivalent to that of the Anderson's Pyrochlore AF Ising model [102, 103]. The flippable plaquettes of quantum spin ices are shown as a red hexagon, whereas the effective spin field is introduced on the links of a diamond lattice (indicated as blue dashed line). **b,** Effective ice rules within tetrahedral crystals. Geometric frustrations within each of the tetrahedrals at vertices of the diamond sublattice locally constrains the spins to the ice rule (namely, two ins/two outs towards to the center of each the tetrahedrals). Within the ice constraints, there is an exponential ground-state degeneracy of these ice states with the system size N, akin to Pauling's analysis for water "ice." **c,** Spinon excitations and magnetic monopoles. Breaking the ice constraint by local spin flip at the red site is equivalent to the creation of magnetic monopole and anti-monopole pairs with the charge located in each of the tetrahedrals. These thermal excitations are highly suppressed by the gauge symmetry, and these effective "gauge charge" interact each other through a screened effective magnetic Coulomb potential, similar to magnetostatic interactions and the magnetic version of the Gauss law.

ground states of these geometrically frustrated magnets and thermal excitations are described by an emergent gauge invariance symmetry of local energetic constraints, and is the basis for further discussion of QSLs.

In this section, I describe a maximally frustrated quantum magnetism on a 3D lattice, a Pyrochlore lattice, consisting of sublattice of corner-sharing tetrahedrals on a diamond lattice. From an experimental point of view, Pyrochlore lattice represents magnetic lattices found in insulating rare-earth materials $\mathrm{R}_2\mathrm{M}_2\mathrm{O}_7$ and one of the first experimental platforms that have indirectly demonstrated the pinching effects in the reciprocal Bragg scattering, a signature of extensive degeneracy of classical spin ices [104]. Notably, in addition to the nearest-neighbor exchange interactions, the magnetic sites of the rare-earth ("R") atoms have a large static magnetic moment ($\mu \simeq 10\mu_B$ for $R =$Dy atoms) with long-range dipolar interactions. The elementary excitations of these constrained magnets, known as the dipolar spin ices (See Refs. [105, 106, 107] and references therein), are well described by quasiparticles that mimick the magnetic monopoles on a discretized lattice, and by an exponential ground-state degeneracy of the ice states with respect to the number N_s of spins.

Extensive degeneracy and ice rules

As shown in Fig. 2.8a, due to the cubic symmetry of the Pyrochlore lattice, a strong crystal field polarizes the magnetic sites to polarize with an Ising axis $\hat{z}_i$ orientied towards or outwards the center [111] of the tetrahedrals. Local ferromagnetic interactions on the tetrahedral $\hat{H}_{\text{ice}} = -\Lambda_F \sum_{i,j\in\boxtimes}(\vec{\hat{\sigma}}^{(i)} \cdot \hat{z}_i)(\hat{z}_j \cdot \vec{\hat{\sigma}}^{(j)})$ with $\Lambda_F > 0$ is then globally equivalent to that of the Anderson's AF all-to-all Ising Hamiltonian

$$\hat{H}_{\text{ice}} = \Lambda_{AF} \sum_{\boxtimes} \sum_{\langle i,j\rangle\in\boxtimes} \hat{\sigma}_z^{(i)}\hat{\sigma}_z^{(j)} \tag{2.29}$$

with a global AF exchange term $\Lambda_{AF} = \frac{\Lambda_F}{3}$ summed over the tetrahedrals $\boxtimes$. It is instructive to redefine Eq. 2.29 with energetic constraint $G_\boxtimes = \sum_{i\in\boxtimes} \hat{\sigma}_z^{(i)} - Q$ with $Q = 0$, such that

$$\hat{H}_{\text{ice}} = \Lambda_{AF} \sum_{\boxtimes} G_\boxtimes^2 \tag{2.30}$$

up to a constant. For AF coupling $\Lambda_{AF} > 0$, this is a highly underconstrained system that energetically follow the ice rule (two-in and two-out), as shown in Fig. 2.8b for a single tetrahedral. In fact, for N magnetic sites, the ground-state subspace is populated by exponentially large degenerate spin ice configurations. There are $\sim (3/2)^{N/2}$

possible configurations in a pyrochlore lattice, consistent with Pauling's estimate of entropy $S_0 = Nk_B/2\log(3/2)$ for water ice. Early measurements of the specific heat in $\mathrm{Ho_2Ti_2}O_7$ showed the linear scaling of the magnetic entropy S_0, revealing the spin ice's extensive ground-state degeneracy [104]. In terms of correlation functions, the exponential ground-state degeneracy in the spin ice manifold is also manifested by the bowtie-like pinch point singularities (i.e. increased density of states) in the spin structural factor $\mathcal{S}(\vec{q}) = \frac{1}{N}\sum_{ij} e^{i\vec{q}\cdot(\vec{r}_i-\vec{r}_j)}\langle\hat{\sigma}_z^{(i)}\hat{\sigma}_z^{(j)}\rangle$ [108].

Magnetostatics of classical (dipolar) spin ice and elementary excitations

I emphasize that we have artificially put a gauge charge Q by hand, which we show in the next section. More generally, for $Q \neq 0$, the ground-state subspace is populated by spin ice states that follow different ice rules (e.g., three in and one out), and can give rise to constrained subspace with an effective SU(N)-representation (See the paper by Dr. Dong and Prof. Choi in Ref. [101]). Although I do not articulate this possibility in this thesis, it is straightforward to create all-to-all quasi-random Heisenberg model for SU(N) spins for any N with our platform in connection to the physics of holographic strange metals.

For the current purpose, it suffices to mention that all spin sites i, j on a pyrochlore lattice connect two tetrahedral crystals. Hence, if you consider a single spin flip for a ground-state spin ice state as the left-hand configuration of Fig. 2.8c, the action of a local spin flip simultaneously breaks the ice rules for both tetrahedrals sharing the target spin. Remarkably, this local excitation can be understood as a fractionalization of the flipped spin into two gauge charges ± 1 (the creation of a magnetic monopole and anti-monopole pair) at the centers of the tetrahedrals, which interact each other with an effective potential.

To further understand the nature of the quasiparticle excitations Q for magnetostatically dipolar-interacting R atoms in the background of spin ice, it is instructive to consider the local spin $\vec{\sigma}^{(i)}$ as a vector field with the proper magnetic response μ. Hence, we represent the Ising spin moment as an effective field generated by the source and sink charges at the end of a "dumbbell" in the form of a magnetic dipole moment $\mu = Qa_0$ with the charge located at the centers of the tetrahedrals and the length consistent with the lattice constant a_0 [109]. The magnetic dipole-dipole interaction across all lattice sites can then be reduced into Coulombic interaction between the magnetic charges Q_α of the tetrahedrals with

$$\hat{H}_{db} = \frac{\mu_0}{4\pi}\sum_{\alpha,\beta}\frac{Q_\alpha Q_\beta}{r_{\alpha\beta}} + \frac{v_0}{2}\sum_{\alpha} Q_\alpha^2, \tag{2.31}$$

with the ice rules of Eq. 2.30 obtained in the limit of on-site interaction $v_0 \to \infty$ [110].

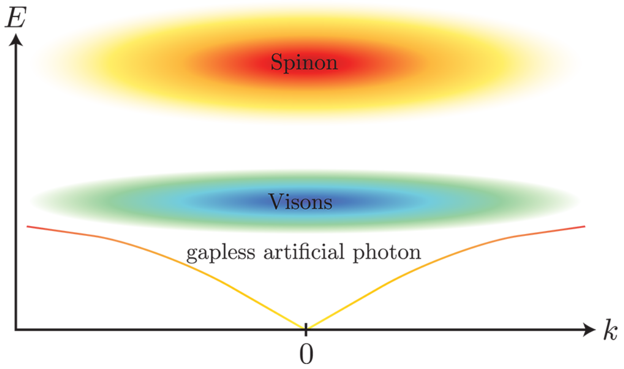

Figure 2.9: **Emergent excitations in a quantum spin ice system.** At the high energy scale $\sim \Lambda$, it is possible for an initial ice state with $Q = 0$ to create a spin excitation that creates magnetic monopole-anti-monopole pairs by breaking the ice rule in two tetrahedrals. For a quantum spin ice, quantum fluctuation inserted by an transverse XX Hamiltonian drives an effective plaquette interaction around an "empty" plaquette (the hexagonal sublattice of Fig. 2.8a for a Pyrochlore lattice). Similar to the Toric code, a gapped topological defect known as vison can be excited at energy scales $\sim J_{\text{ring}}$ of the ring exchange interaction. Vison plays the role of an electric charge in the formulation of the "compact" U(1) lattice gauge theory. At the lowest energy scales, photon-like linear dispersing modes emerge as gapless topological excitations with $S_z = 0$ in frustrated quantum electrodynamics.

To see the correspondence to the Hamiltonian lattice gauge theory, we introduce a coarse-grained vector field $\vec{B}_{r,r'} = \hat{\sigma}_z^{(i)}$ on the diamond lattice. For infinite v_0, the later term of Eq. 2.31 gives Q_α, so that the total spin field summed over the tetrahedral is zero, or equivalently the source-free zero-divergence condition of the Gauss law $\vec{\nabla} \cdot \vec{B} = G_{\boxtimes} = 0$ of electromagnetism. For finite v_0, the gauge charges are excited and create a source magnetic field $\vec{B}$, and this "spinon" excitation remarkably fractionalizes into particle-antiparticle pairs with opposite charges that interact attractively each other through an effective Coulomb potential (first term of Eq. 2.30). Because of the microscopic magnetic response of the spin flips, the particle pairs created in this manner are magnetic monopoles that interact through the Coulomb potential, as with the electron charge of the conventional electromagnetism. Thus, the low-energy physics of classical dipolar spin ice systems is equivalent to a magnetostatic version of a Coulomb gas with an underlying formulation of a local conservation rule, the Gauss law. Because the effective Coulomb potential decays with a power law $\sim 1/r$ [110], the underlying physics for the particle-antiparticle creation is consistent with a deconfined gauge theory. That is, it is possible to pull apart the monopoles with finite energies, each carrying charges that are fractions of those allowed in a finite-size system.

2.4.2 Quantum square ice model

Quantum spin ice is a long-ranged entangled topological quantum matter, where quantum fluctuations and a geometrical frustration (spin ice constraints) of magnetic interactions prevent the spins from showing any spontaneous symmetry-breaking at zero temperature. By adding quantum fluctuations to the ice states, in addition to the fractional spinon excitations, we expect emergent particles associated with deconfined Z_2 gauge fields. Within this low-energy topological sector, gapped vison excitations are formed through a magnetic vortex. Furthermore, we have an emergent U(1) lattice gauge structure that gives rise to the remarkable possibility of a gapless artificial photon, in addition to the gapped vison and spinon excitations, as well as their effective Coulomb potentials [64, 66]. From the perspective of compact QED, we have a physical model that supports stable U(1) quantum spin liquid on a frustrated spin-ice vacuum, corresponding to a deconfined Coulomb phase.

Quantum spin liquids

Because of the difficulty of realizing a Pyrochlore lattice with current AMO technologies, we consider a two-dimensional projected model of the Pyrochlore quantum spin ice, known as the quantum square ice model [111]. This reduced model shares all the necessary ingredients of the original model to support a stable (order-by-disorder) quantum spin liquid and to formulate a Hamiltonian lattice gauge theory [112]. As shown by Fig. 2.10, we are concerned with atoms arranged on a checker board lattice with all spins residing on the checked squares (equivalent to the tetrahedrals) subject to the AF Ising Hamiltonian (second term of Eq. 2.32). Like the Pyrochlore dipolar spin ices, the local conservation rules (i.e., the Gauss law for spinon charges) are energetically enforced on the checked squares. That is, the ice rules are obeyed, because breaking those rules would give rise of a large energetic penalty of the order of Ising energy Λ. Magnetic fields associated with the gauge charges can be assigned for spins on the links of a diamond lattice shown as the yellow dashed lines.

As a minimal model of a quantum spin ice system, we add quantum fluctuation to the background of the aforementioned Ising spin ice to “melt” the spin ice states into a

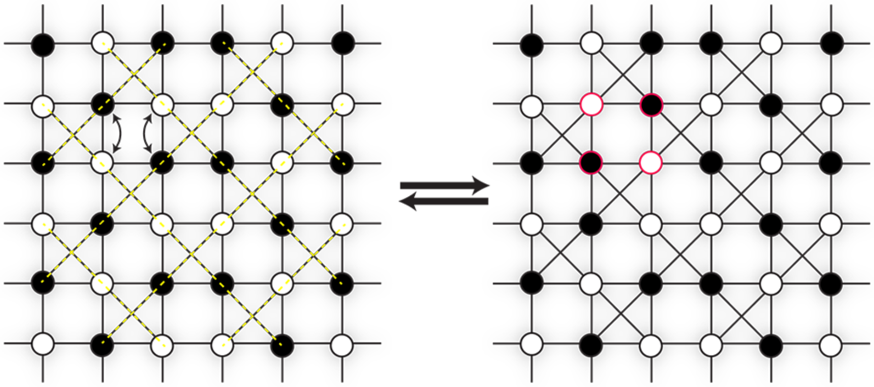

Figure 2.10: **Ring-exchange interaction mediated by gauge constraints in a quantum square ice.** Within the spin ice subspace, an effective 4-body ring-exchange interaction arises for the four spins around the empty plaquette (indicated by the black arrows). Spin exchange coupling indicated by the red arrow must virtually break the ice rules of two filled plaquettes (with a virtual magnetic charge pairs), mandating a 6-body interaction to move the spin around the plaquettes to recover the local conservation rules.

quantum liquid by a perturbative XX spin-exchange Hamiltonian

$$\hat{H}_{\mathrm{QSI}} = J_{\perp} \sum_{\langle i,j \rangle} (\hat{\sigma}_x^{(i)} \hat{\sigma}_x^{(j)} + \hat{\sigma}_y^{(i)} \hat{\sigma}_y^{(j)}) + \Lambda_{AF} \sum_{\boxtimes} \sum_{\langle i,j \rangle \in \boxtimes} \hat{\sigma}_z^{(i)} \hat{\sigma}_z^{(j)}, \tag{2.32}$$

with $J_{\perp} \ll \Lambda_{AF}$. This fluctuation lifts the extensive degeneracy of the original ground-state manifold of the spin ice. The XX term does not need to be nearest-neighbor interacting as written for Eq. 2.32, because the long-range spin exchange is highly suppressed by the Ising energy Λ_{AF}. In fact, our physical platform enables a cavity-mediated infinite-range XX interaction with the locality of the effective spin-spin interaction constrained by the ice rules.

With a large anisotropic exchange coupling $\Lambda_{AF} \gg J_{\perp}$, the spectrum of $\hat{H}_{\mathrm{QSI}}$ can be separated into nearly degenerate spin-ice manifolds with a large spinon gap $\sim \mathcal{O}(\Lambda_{AF})$. By projecting Eq. 2.32 to the the low-energy manifold, we can derive the effective Hamiltonian governing the dynamics within this spin-ice manifold using degenerate perturbation theory [111]. The lowest-order term that give rise to a non-trivial dynamics (apart from constant level shifts) is at the second order, and we arrive at the effective Hamiltonian within the gauge-invariant ice manifold

$$\hat{H}_{\text{eff}} = J_{\text{ring}} \sum_{i,j,k,l \in \square} (\hat{\sigma}_{+}^{(i)} \hat{\sigma}_{-}^{(j)} \hat{\sigma}_{+}^{(k)} \hat{\sigma}_{-}^{(l)} + h.c.) + \Lambda_{AF} \sum_{\boxtimes} \sum_{\langle i,j \rangle \in \boxtimes} \hat{\sigma}_{z}^{(i)} \hat{\sigma}_{z}^{(j)}, \tag{2.33}$$

with the 4-body ring-exchange interaction $J_{\text{ring}} = \frac{|J_{\perp}|^2}{\Lambda_{AF}}$ for spins around a flippable plaquette (Fig. 2.10).

To proceed further, we map the effective Hamiltonian into a quantum dimer model (QDM) by considering a diamond lattice $\Diamond$ (yellow dashed lines of Fig. 2.10). In this picture, the spins on the filled squares (under the ice constraints) are the link variables of QDM, with the effective 4-body ring-exchange Hamiltonian playing the role of kinetic term for the dimers

$$\hat{H}_{\text{dimer}} = -J_{\text{dimer}} \sum_{\Diamond} (\hat{\sigma}_{+}^{(r_1,r_2)} \hat{\sigma}_{-}^{(r_2,r_3)} \hat{\sigma}_{+}^{(r_3,r_4)} \hat{\sigma}_{-}^{(r_4,r_1)} + h.c.), \tag{2.34}$$

with $J_{\text{dimer}} = -J_{\text{ring}}$. In 2003, Hermele, Balents, and Fisher have argued the possibility of a stable quantum spin liquid phase for this effective dimer model [111], by analyzing the ground-state of a pseudo model with an adhoc on-site dimer interaction term U_{dimer} to put the QDM at the Rokhsar-Kivelson (RK) point $U_{\text{dimer}}/J_{\text{dimer}} = 1$ [113]. At the RK point, the ground-state is exactly soluble as a symmetric entangled state (resonating valence bond state) of all dimer configurations within the ice manifold, hence a quantum spin liquid. From a technical point of view, because RK point is a divergent quantum-critical point, it is more appropriate to call this a quantum spin liquid state not a phase. However, due to the stability of the QDM in the vicinity of the RK point [113], Hermele *et al.* argued the persistence of a quantum spin liquid phase over a finite extent $U_{\text{dimer}}/J_{\text{dimer}} < 1$, with extensive literature (numerically solving the original spin model through quantum Monte-Carlo methods) supporting the quantum spin liquid phase persisting down to $U_{\text{dimer}} = 0$ (Ref. [66] and references therein, and Ref. [112] for the direct case of 2D model concerned here).

Formulating a lattice gauge theory: Matter fields (spinons, visons) coupled to a compact (frustrated) gauge field

A quantum link model is a reduction of a lattice gauge theory [114] that attempts to capture the qualitative features of the full continuum gauge model by restraining the infinite-dimensional Hilbert space of the gauge bosons into a finite-dimensional subspace [62]. In the dumbbell model in Section 2.4.1, we have seen that gauge non-invariant spinon excitations out of the ice subspace are the magnetic monopole pairs at the centers of the filled squares (tetrahedrals for Pyrochlore lattice) that experience Coulomb interactions as if they are the gauge charges. In the spirit of the link models, by proceeding with our notation on the diamond lattice, we can now consider the spins on the vertices of the square lattices as the quantum link variables (gauge fields) of the diamond lattice, which mediate interactions between the emergent matter fields (electric or magnetic charges). Hence, it is natural to formulate a quantum link model for quantum spin ice systems.

Let us first formulate a pure gauge model to understand the behavior of quantum spin ice model in the ground-state sector. We introduce the following quantum rotor variables [111]

$$\begin{aligned}\hat{\sigma}_z^{(r,r')} &= \hat{n}_{r,r'} - \frac{1}{2} &(2.35)\\ \hat{\sigma}_+^{(r,r')} &= e^{i\hat{\phi}_{r,r'}}, &(2.36)\end{aligned}$$

which follow the canonical commutation relationship $[\hat{\phi}_{r,q}, \hat{n}_{r',q'}] = i\delta_{rr'}\delta_{qq'}$. In order to recover our original model, we can confine ourselves to the hard-core boson limit $\hat{n}_{r,r'} = 0, 1$, which we imposed with a soft constraint $\hat{Q}_I^{\Diamond} = \sum_{r,r'\in\Diamond} \hat{n}_{r,r'} = 2$. By substituting Eqs. 2.35-2.36 to the dimer model of Eq. 2.34, we obtain the quantum rotor Hamiltonian

$$\hat{H}_{\text{rotor}} = -J_{\text{dimer}} \sum_{\Diamond} \cos\left(\mathop{\sum\!\!\!\!\!\!\!\circlearrowright}_{r,r'\in\Diamond} \hat{\phi}_{r,r'} \right) + \Lambda_{AF} \sum_{r,r'} \left(\hat{n}_{r,r'} - \frac{1}{2} \right)^2 + V \sum_{\Diamond} \hat{Q}_I^{\Diamond}, \tag{2.37}$$

which is valid for $\Lambda_{AF}, V \gg J_{\text{dimer}} > 0$.

We have identified the second term of Eq. 2.37 as the Gauss law for the magnetic field $\hat{B}_{r,r'} \to \pm(\hat{n}_{r,r'} - 1/2)$[h]. Because of the canonical commutator relationship, we find that the phases $\hat{\phi}_{r,r'}$ are conjugate of $\hat{n}_{r,r'}$[i], and we can correspond $\hat{\phi}_{r,r'}$ with the vector potential $\hat{A}_{r,r'} \to \pm\hat{\phi}_{r,r'}$ of QED. Hence, the first term $\sum_{r,r'\in\Diamond} \hat{\phi}_{r,r'}$ of Eq. 2.37 corresponds to (curl) $\times \vec{A}$, the electric "flux" variable $\hat{E}^{\Diamond}$ (magnetic flux in the conventional QED). We can thereby map the rotor Hamiltonian to the pure gauge QED model

$$\hat{H}_{\text{gauge}} = -J_{\text{dimer}} \cos\left(\sum_{\Diamond} \hat{E}^{\Diamond} \right) + \Lambda_{AF} \sum_{r,r'} \hat{B}_{r,r'} \to \frac{J_{\text{dimer}}}{2} \sum_{\Diamond} (\hat{E}^{\Diamond})^2 + \Lambda_{AF} \sum_{r,r'} \hat{B}_{r,r'}, \tag{2.38}$$

---

[h] Again, our notation for electric and magnetic fields are reversed compared to conventional QED. We have a magnetic monopole that creates a Coulomb potential with a physical magnetic field response.

[i] $e^{\pm i\hat{\phi}_{r,r'}}$ raises (+) or lowers (−) the dimeroccupation numbers on links.

with the later mapping only valid for the ground-state sector with small electric field fluctuations.

At this point, it is instructive to compare the key differences between our formulation of QED with the elementary one. The ground state of the conventional QED Hamiltonian is a trivial vacuum state with no photon occupation. However, for a quantum spin ice, in the limit of $\Lambda_{AF} \gg J_{\text{dimer}}$, we actually have a frustrated quantum vacuum with $\hat{B}_{r,r'} \to \pm(\hat{n}_{r,r'} - 1/2)$ instead of $\hat{B}_{r,r'} \to \pm\hat{n}_{r,r'}$ (conventional QED). Indeed, for a spin-ice QED, the ground state is populated by a gapless artificial photon that propagates and spreads across the spin system with a linear dispersion $w(\vec{q}) \simeq c|\vec{q}|$ and speed of "light" $c/a_0 = \sqrt{\Lambda_{AF} J_{\text{dimer}}/2}$. Gapless photon-like modes near zero-temperature is thereby the signature of the illusive deconfined Coulomb phase of QED!

In comparison to conventional electromagnetism, another key difference of our link model is that the vector potential is defined over a modulo 2π. The low-energy excitations of this model are thereby manifested by the constrained electric flux. In fact, the low energy spectrum of the model shows gapped topological point defects with Z_2 gauge fluxes with energy scales on the order of the ring-exchange energy $|J_{\text{dimer}}|$ [111]. Because of this "compactness," these point defects are associated with the creation of electric monopoles, called the visons.

In order to incorporate the matter fields (spinons and visons) to the pure gauge model above, there has been recent developments using gauge mean field theory (gMFT) to assess the stability of the U(1) quantum spin liquids for finite Λ_{AF} [115]. The full formalism is beyond the scope of my thesis, and I only provide the heuristic results here. gMFT includes a soft Lagrange multiplier to allow the breaking of the ice rule with the spinon charge $\hat{Q}_r = \pm \sum_{r,r' \in \Box} \hat{\sigma}_z^{(r,r')}$ at the vertices of the diamond lattice. In an analogous fashion on how we derived the conjugate variables that create and destroy the artificial photons, we can define the phase operator $\hat{\Psi}_r = e^{-i\psi_r}$ for the spinon fields. Under this constraint, we introduce the spinons explicitly to Eq. 2.32 with the mappings

$$\begin{aligned} \hat{\sigma}_+^{(r,r')} &= \hat{\Psi}_r^\dagger \hat{s}_{r,r'}^\dagger \hat{\Psi}_{r'} \\ \hat{\sigma}_-^{(r,r')} &= \hat{\Psi}_r \hat{s}_{r,r'} \hat{\Psi}_{r'}^\dagger \\ \hat{\sigma}_z^{(r,r')} &= \hat{s}_{r,r'}^z, \end{aligned}$$

with the gauge-plus-matter model given by

$$\hat{H}_{\text{QSI}} = \sum_{r,q} \frac{J_\perp^{r,q}}{2} \hat{\Psi}_r^\dagger \hat{s}_{r,r'}^\dagger \hat{\Psi}_{r'} \hat{\Psi}_q \hat{s}_{q,q'} \hat{\Psi}_{q'}^\dagger + \Lambda_{AF} \sum_r (\hat{\Psi}_r^\dagger \hat{\Psi}_r)^2, \tag{2.39}$$

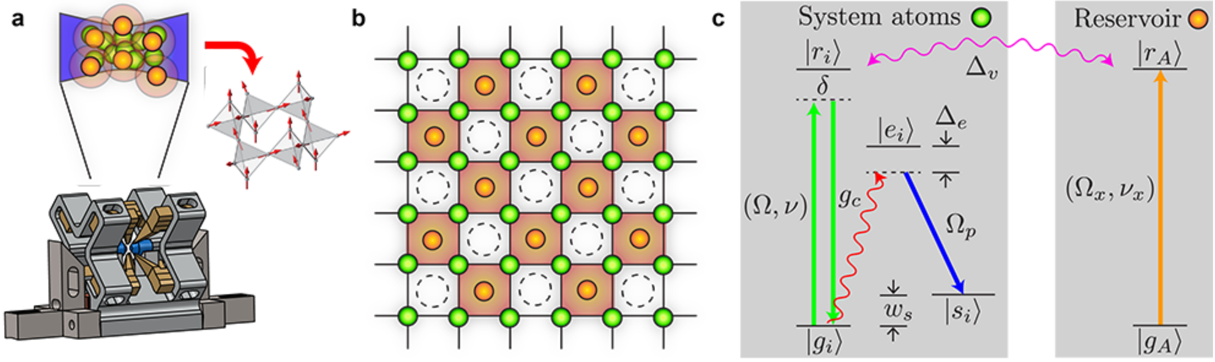

Figure 2.11: **Quantum spin ice models with Rydberg-dressed cavity polaritons. a,** Experimental platform. The full Hilbert space is constrained to degenerate spin ice manifolds by Rydberg-mediated Ising interactions on the hyperfine ground-state subspace. Quantum fluctuation is added to the spin ice vacuum through cavity mediated Dicke interaction. Artificial photons and deconfined Coulomb phase of the quantum spin ice are monitored by collective radiation through the optical cavity. **b,** Enforcing the Gauss law with system-reservoir interactions. We partition the atoms into Rydberg-dressed system atoms and Rydberg-driven-dissipative reservoir atoms. The full open system dynamics yields an effective formulation of a master equation with reservoir mediated Ising interactions and suppressed correlated spin flips for the hyperfine ground states of the system atoms. **c,** Ising interactions among system atoms are mediated by the reservoir atom. This mediated interaction allows careful adjustments to allow all-to-all connection within the filled plaquettes.

where we included the locality of the XX interaction $J_\perp^{r,q}$ on the diamond lattice.

2.5 Physical implementation with Rydberg-dressed cavity polaritons

The main challenge in simulating any quantum link model with analog quantum systems is the realization of the local dynamical gauge symmetries – The Gauss law which gave rise to the interpretation of the spinon excitations as magnetic gauge charges. This is in stark difference to other spin-boson models, where the bosonic excitations (e.g., cavity mode) have no constraint on its own. We thereby require the interacting nature of matter to be used to possibly create the requisite gauge constraints on the gauge bosons in many-body QED. Short of many-body QED, we require the following laboratory capabilities:

1. Real-time rearrangement of single atoms to low-entropic 2D atom arrays on 2D checkerboard lattice with holographic projection: Hungarian collision-path evading algorithms and GPU-accelerated superpixel DMD mapping (Chapter 6),
2. Capability to address and resolve single atoms with a quantum-gas microscope (Chapter 6),
3. Strong local Ising interaction with Rydberg atoms (Chapters 4, 6),
4. Tunable injection of quantum fluctuation to the ice manifolds with cavity-mediated all-to-all XX interaction (Chapter 6),
5. Measurement of time-resolved auto-correlation function $g^{(2)}(\tau)$ for cavity photons (Chapter 6),
6. Engineering connectivity of Ising interaction within the local plaquettes to create gauge constraints,

all of which are in principle possible favorable with our platform. In the first sight, the last requirement (i.e., energetic constraints on the Gauss law) may seem physically impossible for cold atoms in two-dimensions, because of the locality of typical atom-atom interactions (i.e., two atoms at the farthest vertices on a square lattice have weaker interaction strengths than those in nearest-neighbors). Let me first discuss our unique approach for enforcing the dynamical gauge constraints through system-reservoir engineering (Fig. 2.11b).

2.5.1 Local conservation laws with Rydberg-dressed system-reservoir engineering

Natural interactions between atoms usually display a power-law decay. While we would require locality in our Ising interactions, we also need to ensure that we have a faithful 2D mapping of the tetrahedrals of the Pyrochlore lattice. One approach is to use Rydberg-dressing methods to engineer the shape potential to an approximate box-like shape. Due to the limited degrees of freedom, it is not possible to achieve the exact mapping of the Gauss law for the ground-state spin ice configurations, as the nearest-neighbor bonds are $\sim 20\%$ stronger than those at the next-nearest-neighbors [116]. We believe that this level of disorder would be more than sufficient to break the degenerate ice subspace at energy scales even comparable to the vison. Furthermore, because the U(1) quantum spin liquid is a gapless phase with an emergent photon mode, the deconfined Coulomb phase would be very sensitive to small disorder on the order of the ring-exchange energy, thereby breaking the ice degeneracy for large system size even before quantum fluctuation is considered.

As shown in Fig. 2.11, our general approach is to separate the physical atoms into system i and bath A. For consistency, we label i for the spins in the system space, and A for the reservoir spins. From this open-system description, we use the local Ising interaction $\sim \Delta_v$ between the system and bath atoms, and attempt to integrate out the reservoir atoms from the picture (as if it is a cavity). Furthermore, we aim to adiabatically eliminate the Rydberg-degrees of freedom to arrive at an Ising constraint for the hyperfine ground-state (Cs clock state transition). Specifically, the reservoir atoms are placed at the centers of the filled plaquettes to mediate the Gauss law.

The system-reservoir interaction for the transition arranged in Fig. 2.11c is given by

$$\hat{H}_{SR} = \sum_{A} \sum_{i \in \boxtimes} [\delta \hat{\sigma}_{rr}^{(i)} + \Omega(\hat{\sigma}_{gr}^{(i)} + \hat{\sigma}_{rg}^{(i)})] \otimes \hat{\sigma}_{gg}^{(A)} + [(\delta + \Delta_v)\hat{\sigma}_{rr}^{(i)} + \Omega(\hat{\sigma}_{gr}^{(i)} + \hat{\sigma}_{rg}^{(i)}) + w_s \hat{\sigma}_{ss}^{(i)}] \otimes \hat{\sigma}_{rr}^{(A)} \quad (2.40)$$

with $\hat{\sigma}_{\alpha\beta} = |\alpha\rangle\langle\beta|$ and Rydberg-Rydberg van der Waals (vdW) shift Δ_v. In the limit of large detuning $\delta \gg \Omega, \Omega - \Delta_v$, we adiabatically eliminate the Rydberg state $|r_i\rangle$ of the system atoms, leading to an effective system-reservoir Ising coupling between the system atoms in the ground-state subspace (computational basis $|g\rangle, |s\rangle$) and the reservoir atoms still in the electronic subspace (computational basis $|g\rangle, |r\rangle$),

$$\hat{H}_{SR}^{\text{eff}} = \sum_{A} \sum_{i \in \boxtimes} \left(J_g \hat{\sigma}_{gg}^{(i)} \hat{\sigma}_{gg}^{(A)} + J_r \hat{\sigma}_{gg}^{(i)} \hat{\sigma}_{rr}^{(A)} + w_r \hat{\sigma}_{rr}^{(A)} + w_s \hat{\sigma}_{ss}^{(i)} \right) \quad (2.41)$$

with $J_g = \frac{\Omega^2}{\delta}$ and $J_r = \frac{\Omega^2}{\delta + \Delta_v}$. We now use the spin notations for the system and reservoir atoms as follows $\hat{\sigma}_0^{(i)} \equiv \hat{\sigma}_{ss}^{(i)} + \hat{\sigma}_{gg}^{(i)}$, $\hat{\sigma}_0^{(A)} \equiv \hat{\sigma}_{rr}^{(A)} + \hat{\sigma}_{gg}^{(A)}$, $\hat{\sigma}_z^{(i)} \equiv \hat{\sigma}_{ss}^{(i)} - \hat{\sigma}_{gg}^{(i)}$, $\hat{\sigma}_z^{(A)} \equiv \hat{\sigma}_{rr}^{(A)} - \hat{\sigma}_{gg}^{(A)}$, with the effective system-reservoir Ising Hamiltonian

$$\hat{H}_{SR}^{\text{eff}} = \sum_{A} \sum_{i \in \boxtimes} \frac{w_0^{(i)}}{2} \hat{\sigma}_z^{(i)} + \frac{w_0^{(A)}}{2} \hat{\sigma}_z^{(A)} + J_{iA} \hat{\sigma}_z^{(i)} \hat{\sigma}_z^{(A)}, \quad (2.42)$$

where $w_0^{(i)} = w_s - \frac{J_g + J_r}{2}$, $w_0^{(A)} = w_r + \frac{J_r - J_g}{2}$, $J_{iA} = \frac{J_g - J_r}{4}$.

In order to obtain the reduced dynamics of the system atoms, we add a perturbation

Rabi oscillation $\Omega_x(\hat{\sigma}_{rg}e^{-i\nu_x t}+h.c)$ to the reservoir atoms in the rotating frame of $\nu_x = w_0^{(A)}$

$$\hat{H}^{\text{eff}}_{SR} = \sum_A \sum_{i\in\boxtimes} \frac{w_0}{2}\hat{\sigma}_z^{(i)} + J_{iA}\hat{\sigma}_z^{(i)}\hat{\sigma}_z^{(A)} + \Omega_x\hat{\sigma}_x^{(A)}. \tag{2.43}$$

We then eliminate the reservoir atomic DOFs with $J_{iA} \ll \Omega_x$ to obtain the spin ice constraint Hamiltonian

$$\hat{H}_{\text{ice}} = \sum_i \frac{w_0}{2}\hat{\sigma}_z^{(i)} + \Lambda_{AF}\sum_{i,j\in\boxtimes}\hat{\sigma}_z^{(i)}\hat{\sigma}_z^{(j)}, \tag{2.44}$$

with an Ising energy $\Lambda_{AF} = \frac{J_{iA}^2}{\Omega_x} > 0$ that is now equal among all bonds within the filled plaquette $\boxtimes$. We emphasize that our mapping to $\hat{H}_{\text{ice}}$ with a reservoir-mediated interaction is inherently a driven-dissipative process, as spontaneous emission of the reservoir's Rydberg state (which is directly driven, unlike the system atoms) is also coupled to the system's DOFs. Hence, we derive the effective Master equation for the system atoms

$$\begin{aligned}
\dot{\hat{\rho}}_s &= -\frac{i}{\hbar}[\hat{H}_{\text{ice}},\hat{\rho}_s] + \mathcal{L}_s[\hat{\rho}_s] + \mathcal{L}_A^{\text{eff}}[\hat{\rho}_s], && (2.45)\\
\mathcal{L}_A^{\text{eff}}[\hat{\rho}_s] &= \sum_{i,j\in\boxtimes}\tilde{\gamma}_A(\hat{\sigma}_z^{(i)}\hat{\rho}_s\hat{\sigma}_z^{(j)} - \hat{\sigma}_z^{(i)}\hat{\sigma}_z^{(j)}\hat{\rho}_s - \hat{\rho}_s\hat{\sigma}_z^{(i)}\hat{\sigma}_z^{(j)}), && (2.46)\\
\mathcal{L}_s[\hat{\rho}_s] &= \sum_i \frac{\tilde{\gamma}_s}{2}(2\hat{\sigma}_-^{(i)}\hat{\rho}_s\hat{\sigma}_+^{(i)} - \hat{\sigma}_{gg}^{(i)}\hat{\rho}_s - \hat{\rho}_s\hat{\sigma}_{gg}^{(i)}), && (2.47)
\end{aligned}$$

with effective dissipation $\tilde{\gamma}_A = \frac{J_{iA}^2}{\Omega_x^2}\Gamma_r, \tilde{\gamma}_s = \frac{\Omega^2}{\delta^2}\Gamma_r$. Interestingly, the second line describes the correlated dephasing for the Ising spins around the filled plaquettes, which nonetheless do not break the ice rules!

2.5.2 Cavity-mediated interactions

Now that I have established the Ising spin ice constraints on the filled plaquettes, we now turn our attention to the quantum fluctuations of the XX Hamiltonian. For this, we utilize an infinite-range cavity-mediated interactions (See Section 1.2.2 for the Dicke model in an optical cavity)

$$\hat{H}_{\text{full}} = \Lambda_{AF}\sum_{i,j\in\boxtimes}\hat{\sigma}_z^{(i)}\hat{\sigma}_z^{(j)} + \Delta_c\hat{a}^\dagger\hat{a} + \sum_i \frac{\Omega_p g_c}{\Delta_e}(\hat{\sigma}_+^{(i)}\hat{a} + \hat{\sigma}_-^{(i)}\hat{a}^\dagger), \tag{2.48}$$

where I have eliminated the excited state $|e\rangle$ and set the cavity detuning to $\Delta_c = w_c - \nu_p - w_0 - \frac{\Omega_p^2}{\Delta_e}$.

Further eliminating the cavity field, we recover the effective quantum spin ice model as well as its dissipative Lindlad terms

$$\begin{aligned}
\hat{H}_{\mathrm{QSI}} &= J_{\perp}\sum_{i,j}(\hat{\sigma}_x^{(i)}\hat{\sigma}_x^{(j)} + \hat{\sigma}_y^{(i)}\hat{\sigma}_y^{(j)}) + \Lambda_{AF}\sum_{\boxtimes}\sum_{\langle i,j\rangle\in\boxtimes}\hat{\sigma}_z^{(i)}\hat{\sigma}_z^{(j)}, && (2.49)\\
\dot{\hat{\rho}}_s &= -\frac{i}{\hbar}[\hat{H}_{\mathrm{ice}}, \hat{\rho}_s] + \mathcal{L}_s[\hat{\rho}_s] + \mathcal{L}_A^{\mathrm{eff}}[\hat{\rho}_s] + \mathcal{L}_\kappa^{\mathrm{eff}}[\hat{\rho}_s] + \mathcal{L}_e[\hat{\rho}_s], && (2.50)\\
\mathcal{L}_\kappa^{\mathrm{eff}}[\hat{\rho}_s] &= \sum_{i,j}\frac{\tilde{\gamma}_\kappa}{2}(2\hat{\sigma}_-^{(i)}\hat{\rho}_s\hat{\sigma}_+^{(j)} - \hat{\sigma}_{gs}^{(i)}\hat{\sigma}_{sg}^{(j)}\hat{\rho}_s - \hat{\rho}\hat{\sigma}_{gs}^{(i)}\hat{\sigma}_{sg}^{(j)}), && (2.51)\\
\mathcal{L}_e[\hat{\rho}_s] &= \sum_{i}\frac{\tilde{\gamma}_e}{2}(2\hat{\sigma}_-^{(i)}\hat{\rho}_s\hat{\sigma}_+^{(i)} - \hat{\sigma}_{gg}^{(i)}\hat{\rho}_s - \hat{\rho}_s\hat{\sigma}_{gg}^{(j)}), && (2.52)
\end{aligned}$$

with effective dissipative rates $\tilde{\gamma}_\kappa = \frac{\Omega_p^2 g_c^2}{\Delta_e^2\Delta_c^2}\kappa, \tilde{\gamma}_e = \frac{\Omega_p^2}{2\Delta_e^2}\Gamma_e$ and the infinite-range XX term $J_\perp = \frac{\Omega_p^2}{\Delta_e^2}\frac{g_c^2}{\Delta_c}$.

2.5.3 Experimental parameters

In order to see the feasibility of this experiment, we would qualitatively like to have $\frac{J_{\mathrm{ring}}}{\Gamma_{\mathrm{total}}} > 10$, where

$$\begin{aligned}
J_{\mathrm{ring}} &\simeq 16\Omega_x\left(\frac{\Omega_p\delta}{\Omega\Delta_e}\right)^4\left(\frac{g_c}{\Delta_c}\right)^2\left(\frac{g_c}{\Delta_v}\right)^2 && (2.53)\\
\Gamma_{\mathrm{total}} &= \tilde{\gamma}_A + \tilde{\gamma}_s + \tilde{\gamma}_\kappa + \tilde{\gamma}_e. && (2.54)
\end{aligned}$$

For the adiabatic elimination approximation, Dr. Dong have numerically compared the dynamics of the 4-body ring-exchange interaction (Eq. 2.34) within the gauge-invariant sector with the full model in Eq. 2.49 for the minimal quantum spin ice arrangements that give rise to a single 4-body plaquette ($N = 12$ system atoms and $N = 4$ reservoir atoms). With $g_c/\Delta_c \simeq g_c/\Delta_v \simeq \Omega/\delta \simeq \Omega_p/\Delta_e \simeq 0.1$, Dr. Dong has found that there is less than 1% deviation from the effective Hamiltonian over time scales $T \sim \frac{5}{J_{\mathrm{ring}}}$. Roughly speaking, for direct $|nP_{3/2}\rangle$ Rydberg excitation with our high-power 317 nm laser fields (Chapter 4), I can maximally estimate $\Omega_x \sim 2\pi \times 10$ MHz due to the low diffraction efficiencies of the superpixel method, compared to the grating-based projections. The resulting ring-

Parameter	Formula	Result	Comments
Δ_v	N/A	-800 MHz	$\lvert 60P_{1/2}, 60P_{1/2}\rangle$ with interatomic distance 3μm
δ	N/A	300 MHz	N/A
Ω	3 mW over $\pi \times 1\mu\text{m}^2$	$\simeq 10$ MHz	Approximation: $\Omega \ll \lvert\delta + \Delta_v\rvert$
J_{iA}	$\frac{1}{4}\left(\frac{\Omega^2}{\delta} - \frac{\Omega^2}{\delta+\Delta_v}\right)$	$\simeq 0.3$ MHz	System-reservoir coupling
Ω_x	N/A	$\simeq 6$ MHz	Approximation: $\Omega_x \gg J_{iA}$
Λ_{AF}	$\frac{J_{iA}^2}{\Omega_x}$	$\simeq 15$ kHz	Approximation: $\Omega_x \gg J_{iA}$
Λ_{direct}	$\simeq \frac{1}{4}\left(\frac{\Omega}{\delta}\right)^4 \frac{\Delta_v}{\delta}$	$\simeq 12.5$ Hz	Direct interactions between system atoms.
g_{eff}	$\simeq \frac{\Omega_p g_c}{\Delta_e}$	$\simeq 150$ kHz	Effective cavity coupling rate.
$J_\perp$	$\simeq \frac{g_{\text{eff}}}{\Delta_c}$	$\simeq 1.5$ kHz	XX spin-exchange coupling.
J_{ring}	$\simeq \frac{J_\perp^2}{\Lambda_{AF}}$	$\simeq 150$ Hz	4-body ring-exchange coupling rate.
γ	$\simeq \frac{J_\perp^2}{\Lambda_{AF}}$	$\simeq 150$ Hz	4-body ring-exchange coupling rate.
$\tilde{\gamma}_s$	$\simeq \left(\frac{\Omega}{\delta}\right)^2 \Gamma_r$	$\simeq 1$Hz	Effective dissipative rate by $\lvert r\rangle$ ($\Gamma_r \simeq 1$kHz)
$\tilde{\gamma}_e$	$\simeq \frac{1}{2}\left(\frac{\Omega_p}{\Delta_e}\right)^2 \Gamma_e$	$\simeq 3$Hz	Effective dissipative rate by $\lvert e\rangle$ ($\Gamma_e \simeq 30$MHz)
$\tilde{\gamma}_\kappa$	$\simeq \left(\frac{\Omega_p g_c}{\Delta_e \Delta_c}\right)^2 \kappa$	$\simeq 1$Hz	Effective cavity induced spin decay ($\kappa \simeq 10$kHz)
$\tilde{\gamma}_A$	$\simeq \left(\frac{J_{iA}}{\Omega_x}\right)^2 \Gamma_r$	$\simeq 2.5$Hz	Effective decay by reservoir atom ($\Gamma_r \simeq 1$kHz)

Table 2.4: Experimental parameters for realizing quantum spin ice models.

exchange coupling rate is then $J_{\text{ring}} \sim 16$ kHz. On the other hand, I estimate the total decay rate $\Gamma_{\text{total}} \simeq 10$ Hz in our system. More conservatively, if we assumes 30% sum-frequency and second-harmonic-generation, I expect the coherence-to-dissipation ratio $\frac{J_{\text{ring}}}{\Gamma_{\text{total}}} \simeq 15$. In Table 2.4, I provide the laboratory parameters for our platform to realize a quantum spin ice model.

Chapter 3

UHV chamber system

In our experiment, we require a complex cluster ultra-high-vacuum (UHV) chamber system to meet two competing requirements. On the one hand, we require large background Cs vapor density and thereby an UHV environment with $P \simeq 10^{-9}$ Torr limited by background Cs atoms. This Cs-rich vacuum environment provides a means to create high-density Doppler-limited cold atomic gases in a standard magneto-optical trap (MOT). On the other hand, the lifetime of the atomic gas would be significantly limited by the surrounding room-temperature atoms. We thereby also require an XHV (extreme-ultra-high-vacuum) environment with $P \ll 10^{-10}$ Torr, in order to trap and further cool Cs atoms to its quantum-degeneracy and eventually to perform serious quantum optics experiment for elongated durations.

Our solution to this problem is to divide the UHV chamber systems into two subsystems, and to establish extreme pressure difference via a conductance-limited differential pumping tube. The differential pumping tube is designed to achieve the target pressure differential in the molecular flow limit, and also to allow the continuous transport of cold atoms. The basic experimental sequence is to collect and laser-cool a large number $N \simeq 10^{10} \sim 10^{11}$ of Cs atoms in the background-limited "Source" chamber ($P \simeq 10^{-10}$ Torr), and then optically transport a large fraction of these atoms continuously through a "pushing" field $\Omega_p(\vec{r})$ to create a cold atom fountain in the "Science" chamber for further cooling and deterministic transport operations to our science cavity platform with high-density $\rho \simeq 10^{15} \sim 10^{16}/\text{cm}^3$ at extreme X-ray limited pressures $P \simeq 10^{-13}$ Torr (Chapter 6). To the best of my knowledge in the literature, this is the lowest operating vacuum pressure for any ultracold atoms/ions experiment by a factor of 10, and is on par with cutting-edge surface physics and particle accelerator experiments (the Intersecting Storage Ring in CERN), reaching close to the pressure of interstellar void.

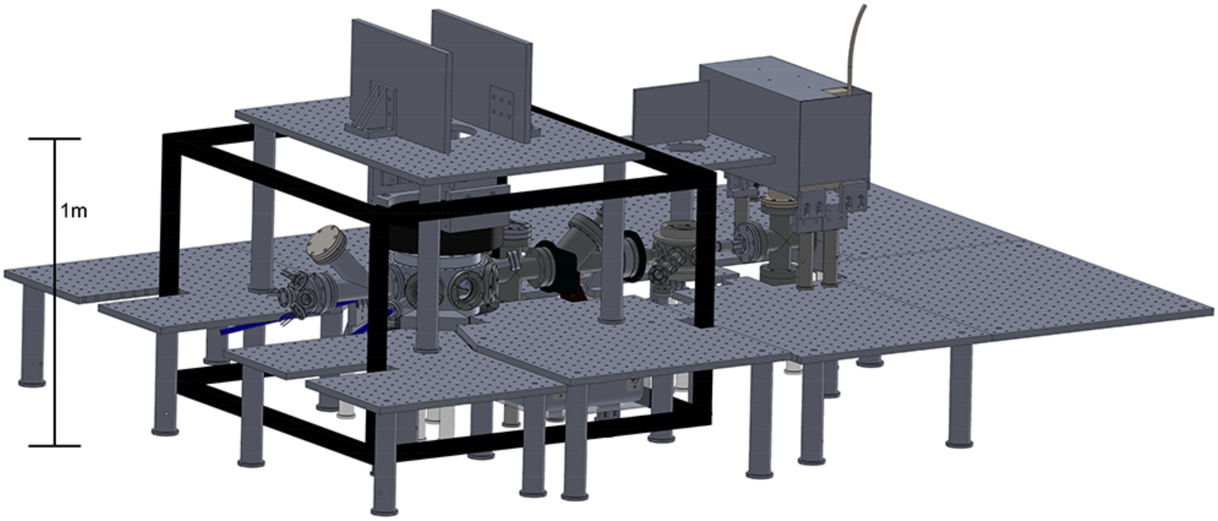

Figure 3.1: **3D CAD rendering of the UHV-XHV system.** The detailed descriptions of the sub-systems are provided in the main text.

In designing such a complex chamber, we need detailed considerations of the surface quality and material properties, vacuum passivation techniques, as well as new methods to reduce the outgassing and permeations of atmospheric noble gases to reach the XHV level pressure. I have devised a few novel techniques to achieve these extreme levels of pressure with chemical activation and surface polishing at the molecular level, as well as with "rainbow" anti-reflection coatings on the quartz viewports.With these technical advances, I was able to install a relatively complex experimental station (Chapter 6) into the main Science chamber. In collaboration with VMT, I have developed a relatively reliable recipe of controlled thick oxide layer growth on the interior of the UHV chamber as passivation layer. In collaboration with Gamma Vacuum, I have utilized a specialized XHV ion-pump, which can read out XHV-level pressures with reduced X-ray limit of the cathode wire.

Before I jump into further description of our chamber, I will first describe some cautionary design "rules" when composing a UHV chamber from scratch.

3.1 Vacuum chamber design rules

3.1.1 Vacuum-compatible materials

Components that are assembled to the chamber setup should be vacuum-compatible. In case that you also have mechanical and optical structures going inside of chamber, so do each part and as well as the adhesives shall be well-prepared for UHV environment. At pressure levels 10^{-13} Torr, we are sensitive to a monolayer of atoms coating the walls of the chamber (monolayer time in our system is approximately 1 year and mean-free path $\lambda \simeq 8 \times 10^6$ km), so that we must reduce the overall surface area by creating extremely smooth surfaces or by modifying its chemical properties so that the binding energy is less than the room-temperature thermal energy to release atoms from the chamber walls. Other important parameters of these low-outgassing materials include whether the parts are affine to abrasive chemical and electromechanical cleaning (hopefully with little chemical hazards), as well as whether the parts could be baked at a high-temperature only limited by the Con-Flat (CF) joints. Furthermore, we also need to consider the electromagnetic properties of the materials, as a small amount of ferromagnetism and static bound charges can significantly affect the ground state Zeeman and the excited Rydberg coherences. Generally, we can categorize the vacuum materials to annealed metals, ceramics, glass dielectric, and ultra-low-outgassing polymers.

Fully annealed metals

Due to its high machinability and durability, metals are generally the preferred choice of materials for vacuum applications. Moreover, metals can be vacuum-melt at high-temperature $T \simeq 3500°C$ to completely degas the atmospheric gases in the reforming process.

Austenitic stainless steels (SS) contain a high level of chromium so that at atmospheric pressure it naturally forms a dense Chromium Oxide Cr_2O layer. In fact, this thin dielectric layer is the main reason why SS does not corrode in contact with water. It is important to know that, even with vacuum melting ($T \simeq 3500°C$) and vacuum firing ($T \simeq 950°C$), the background pressure is insufficient to avoid H_2 gases that get trapped into the bulk of most metal [a]. The outgassing from the SS walls of the chamber is generally what limits

---

[a] As a cautionary note, when performing vacuum firing, it is important to notify the vendor of the annealing schedule used in our group to prevent accidental depletion of Nickel atoms. This depletion is reported to reduce the tensile strengths of SS chambers, possibly causing permanent damages to the knife edges of the CF flanges, in addition to creating weak magnetization.

the pressure of a UHV system to $\sim 10^{-10}$ Torr level. The standard method is to perform a UHV baking at $T > 350°C$, so that H_2 atoms can migrate towards the surface, which in turn would be depleted through the UHV turbo pump system. In addition to performing a UHV baking at elevated temperature $T \simeq 400°C$ with a home-made vacuum oven, we have developed a method to controllably enrich the $\mathrm{Cr_2O}$ layer on the interiors of SS304 and SS316LN through vacuum passivation in collaboration with VMT corp in South Korea. I describe this procedure in Section 3.2.3. We utilize SS304 for UHV components in large distance from the atomic cloud, as it is known to have stress-induced magnetization effect. For the Science and Source chambers, we strictly confine the materials to SS 316L(N), with (N) indicated for vacuum-remelting procedure for desorbing N_2 gases. For vacuum-welded SS parts (e.g., Tungsten Inert Gas welding), we ensure that the piece undergoes an electropolishing procedure to avoid virtual leaks and remove oxide layers.

Aluminum alloy is another great vacuum material, although most Al alloys are incompatible with the stringent outgassing requirements of our experiments. I confine our considerations only to Al 6061-T4 and Al6061-T6 (Mg and Si enriched), both of which are popular materials you could find in stock in most machine shops. The critical challenge with machined Al 6061 is the surface finish. Unlike SS, the oxidization of Al in room temperature is quite aggressive, and the surface Aluminum Oxide layers are usually porous, creating virtual leaks and increasing the overall surface area by a few orders of magnitudes. We prevent this from occurring by performing a new electropolishing recipe which we optimize for Al 6061 (Section 3.2.2). This recipe removes both the porous oxide structure and recreates an optically smooth surface valley (reducing the effective surface area). In addition to SS and Al alloys, we also use Ti 6AL4V alloy for the blade electrodes

Material	Outgassing rate (Torr-L$/s/cm^2$)	Notes
Al 6061-T4	1×10^{-14} [117]	24-hr UHV-bake @ $200°C$.
Al 6061-T6	2.8×10^{-10} [118]	10-hr UHV-bake @ $200°C$ & nitric dip
OFHC	4×10^{-11} [119]	nitric-sulfuric dip.
SS 304	1×10^{-9} [120]	commercial finish (Varian).
SS 304	4×10^{-12} [120]	20-hr UHV-bake @ $500°C$.
SS 304	2.5×10^{-10} [119]	electropolishing.
SS 304	2×10^{-14} [121]	Air-baked @ $400°C$
SS 316L	1.6×10^{-14} [121]	Air-baked @ $400°C$
Ti 6AL4V	1.8×10^{-9} [122]	N/A
Mg alloy	3×10^{-9} [122]	4-hr vacuum fire @ $800°C$

Table 3.1: Outgassing rates of fully annealed metals.

and the V-grooves of the Science cavity platform. Titanium has similar characteristics to Al 6061-T4, except that the oxide layer is generally much thinner $3-5$ nm and non-porous. In addition, Ti atoms can act as a sublimation vacuum pumping mechanism to absorb surrounding non-Noble gases! Lastly, we use Oxygen-Free-High-Conductivity (OFHC) copper for the CF gaskets for the sealants between the SS304 and SS316L UHV components. We also use OFHC as radiation shields to damp out the blackbody radiation shifts in our ULE reference cavity design (Chapter 4). Gildcop, a trademark for OFHC mixed with Alumina particles, and Copper-Beryllium alloy are both good vacuum materials with excellent tensile strengths, and are now used for the host materials of UHV chambers. The cost for these chambers were prohibitively expensive for us to implement.

UHV ceramics & polymers

Though ceramics and glass are not as easy to machine as metals, but it is still beneficial for uses in thermal and electrical insulations. We use macor, a machinable glass-ceramic by Corning, for electric breaks and ceramic components in the UHV chamber (particularly, macor 9658). Care must be made upon CNC machining to avoid brittling by stress reliefs on the macor piece. Zircon porcelain and Pyroceram 9696 are both similar to Macor. We also use fully vitrified Aluminum Oxide Al_2O_3 (known as Alumina) for the interface between Kimball Physics groove-grabber and the Science cavity platform, because of its strength and low CTE. Alumina is stable at temperatures up to $1,900°C$[b] and has very high dielectric breakdown voltage, making them suitable for the insulation stack of our high-voltage feedthroughs that drive the single-crystal shear-mode piezoelectric transducers (PZT). It is widely known that most piezoelectric ceramics are UHV compatible, but care must be given to the metallization procedures of the electrodes[c], as some PZT vendors typically use epoxy for stack PZT. We use the PZTs from APC international Inc. In addition, one must choose PZT materials with high Curie temperature T_c to avoid depolarizing the PZT ceramic upon high-temperature bake-out. Finally, when combining two different ceramic materials, it is critical to closely match the CTE between the components. In this way, we could ensure that the ceramic piece would not break down when the UHV system is under high bake-out temperature.

In terms of elastomers and polymers, we frequently use Teflon (PTFE) as the insulation layer of UHV magnet wires. Kapton tape consists of multlayer PTFE films attached by UHV adhesives. We also use PEEK for low-temperature insulation layer, as it has lower

---

[b] http://accuratus.com/alumox.html.

[c] Silver-frit-firing is a fine way to create the electrodes on PZT ceramics in terms of the UHV compatibility.

outgassing rate than PTFE and better formability. For vibration isolation platforms, we use Viton and Kalrez. For polymer, quantizing the rate of gas desorption is quite tricky, as the polymer material is quite porous and gas can penetrate through (permeability). As a rule of thumb, we never use polymer for situations where there is a large pressure differential. This would usually limit the application to high-vacuum regime $P \sim 10^{-6}$ Torr. For lubricants, we use UHV-compatible electroplated silver, MoS_2, and PVD-grown WS_2. A standard way to quantify the outgassing rate is the total mass loss (TML) and the collective volatile condensable material (CVCM), which you look up from NASA Outgassing Database[d].

Material	Outgassing (Torr-L/s/cm^2)	Temperature (^oC)	Young's Modulus
Macor	$\sim 1 \times 10^{-12}$	@ $800°C$	66.9 GPa
Alumina	1×10^{-14} [122]	@ $1,650°C$	300 GPa
PTFE	1×10^{-8} [122]	$204°C$	575 MPa
Viton E60C	6×10^{-10} [122]	$225°C$	N/A
Kapton	1×10^{-11} [122]	$400°C$	4.0 GPa
Kalrez	1×10^{-10} [122]	$200°C$	N/A

Table 3.2: Outgassing rates of fully annealed metals.

When we assemble the UHV components, the sealants and adhesives should be vacuum-compatible as well. The vacuum properties of most UHV adhesives are like black magic. In choosing the UHV epoxies, we need to choose epoxies with the lowest TML to avoid coating our high-finesse mirrors. In addition, we must ensure that the cure condition is as high as possible and that the glass temperature T_g is sufficiently high to ensure that the parts do not move during the bake-out. One anecdotal story is that a Vacseal, the usual suspect for those trying to find a UHV sealant, can actually evaporate and coat your UHV chamber, even though the outgassing rate (in terms of gas release) is actually very low. The epoxy should be close in its CTE with the host material, to avoid cracks during bake-out and stress-induced birefringence. Given the significant development cost of our system ($\sim \$1M$ for the Science cavity platform), it was critical that we understand the vacuum behaviors of the UHV epoxies.

Permeability of glasses

An important difference of UHV chambers used in AMO experiments and and in surface science is the presence of wide-viewing angle UHV glass viewports. In the limiting case

---

[d] https://outgassing.nasa.gov/help/og_help.html

of introducing Hydrogen diffusion oxide layer on SS chamber walls, the next limiting case would be the diffusion of light atoms through the amorphous network structure of the glass. These structures are relatively large and provide an effective channel for Helium to diffuse through the viewport. Much of the research on He permeability of different glasses has been carried out in the 60s and 70s [123, 124]. In Ref. [123], the author does an extensive survey to determine the glass permeability constant K (unit: cc/s/area (cm^2)/thickness (mm)/Hg pressure difference (cm)). Not all glasses are created equal, and modifier molecules doped to the SiO_2 glass material can fill these holes, resulting into very low permeation rates. Unfortunately, most dopants to glass materials are optically active, and thereby have a very strong solarization effect (the optical loss is dramatically increased, when exposed to light with wavelength below 300 nm). Since we must use near 300 nm high-power laser, we were restricted to fused silica and quartz materials viewports. However, if we were able to use other glass materials, we would have looked into aluminosilicate glass, a composite of Sapphire and silica, where it is predicted to have 5-order of magnitudes smaller K [124]. In order to prevent the permeation of Helium atoms, we instead grow thick films of atomically dense anti-reflection coatings. As we will see in the next section, these Anti-reflection (AR) coatings also play the roles of He diffusion layer.

3.1.2 Vacuum conductance

Before we move forward with the design, it is instructive to consider the two regimes of aerodynamic flows relevant for vacuum physics. The first is the viscous (continuous) flow regime in the low pressure spectrum. Here, the motion of gas particle is very much similar to what we experience at atmospheric pressure. As shown in Fig. 3.2, in this regime, the gas flows through the aperture due to the frequent intermolecular collisions that guide the flow. This occurs when the mean free path l_0 of the gas molecules is significantly shorter than the aperture size

$$l_0 = \frac{k_B T}{\sqrt{2}\pi p d_m^2}, \tag{3.1}$$

where T is the temperature (in K), p is the pressure (Pa), d_m is the molecular diameter (m), and m is the mass of the molecule.

As the system is being pumped down to high-vacuum (HV) and to ultra-high-vacuum (UHV), the mean free path l eventually becomes larger than the aperture size. This is the other regime of molecular flow limit. In this regime, if a system is connected to a pump through a small tube, the molecules would have a small line of sight (solid angle) to reach the target position, and it would take multiple reflections from the walls of the chamber until the molecule could reach the vacuum pump. Hence, the pumping speed of the gas at a particular location in the UHV chamber is also a function of the overall geometry to the vacuum pump system. That is, even with a UHV pump with infinite pumping speed, the effective pumping at the outgassing source within the chamber may be limited significantly by the "conductance" C of the system (unit of L/s)

$$
\begin{aligned}
C_{\mathrm{tube}} &= 12.4\ [\mathrm{L/s}] \times \frac{L}{D^3}, && (3.2)\\
C_{\mathrm{elbow}} &= 12.4\ [\mathrm{L/s}] \times \frac{L_{\mathrm{eff}}}{D^3}, && (3.3)\\
C_{\mathrm{aperture}} &= 11.8\pi\ [\mathrm{L/s}] \times \left(\frac{D}{2}\right)^2, && (3.4)
\end{aligned}
$$

where L is the length (cm) of the tube, D is the diameter (cm) and $L_{\mathrm{eff}} = \frac{1.33\times L}{D} \times \frac{\theta}{180}$ is the effective length (cm) of the elbow (enlarged by the θ-bend). The coefficients that relate the geometry to the conductance is given by finite-element analysis for different gas species. In the molecular flow regime, the conductance C can also be utilized to isolate the pressure differentials between two UHV chamber by designing a conductance-limited

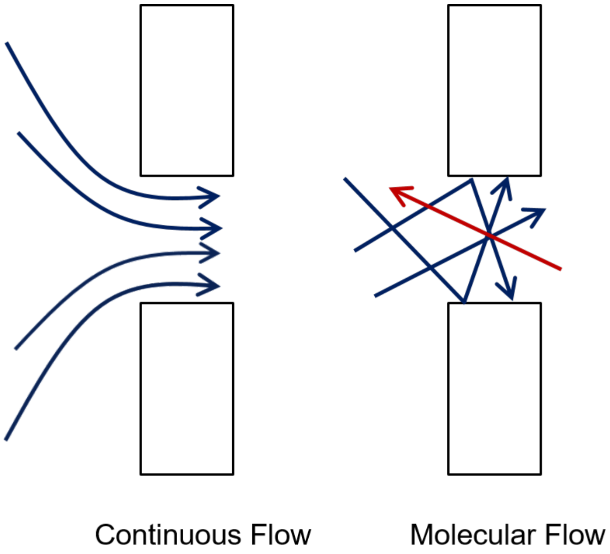

Figure 3.2: **Vacuum flow regimes.** *Left* Continuous flow. This happens in low vacuum which is also called viscous flow. *Right* Molecular flow. Gas molecules flow is suppressed by collision with the wall. Transition between two flow regimes happens around 1Pa.

UHV tube or aperture.

At an UHV pressure of 10^{-10} Torr, mean free path $l > 1$ km so that the overall system is safely in the molecular flow regime. In order to estimate the final background pressure with our design, we can readily use the concept of vacuum conductance to understand the effective pumping speed at the location, where outgassing is expected to occur. As conductance is a measure of flow, C follows the same rule as the capacitor rule, when the vacuum components are connected in series or parallel. With these toolboxes, it is possible to compute the overall conductance from the center of the UHV chamber to the UHV pump. For instance, if you find that the total conductance is only 10 L/s, you would need to choose a vacuum pump at least 10 L/s. On the other hand, installing a 100 L/s ion pump would not improve your base pressure significantly, as the pumping speed would still be conductance-limited to 10 L/s. Indeed, a large part of the UHV design effort is dedicated to optimizing the overall C to the vacuum pump, while limiting the conductance between parts with large pressure gradients. As we will see in the next section, it is important to remember that, at the XHV level, almost everything would be outgassing, including the pumps themselves. For instance, it was important for our experiment to make sure that the ion and the NEG pumps were directed away from the Science cavity platform. For the ion pump, the local plasma sputters Titanium to the walls of the ion pump that acts as a distributed sublimation pump for active gas loads, and these Ti atoms may migrate over to the Science chamber. For the NEG, there is a large degree of active gas loads during activation process, which may increase the outgassing rates on the surfaces of the mirrors. The conductance of these UHV pumps were thereby limited to the Science chamber to avoid a direct line of sight.

In a similar fashion, upon installing mechanical components within the UHV chamber, it is important to ensure that the mating of the parts has sufficient conductance for the gases to conduct away. That is, it is crucial to use vented and slotted UHV screws, and to mark venting traces on surfaces for gas removal. These sources of outgassing with significantly limited conductances (e.g., trapped air in a screw hole) are known as virtual leaks, and are one of the common mistakes in designing UHV chambers. The simple rule of thumb is to create through holes on every mating surface and create slotted lines on the screw marks.

3.1.3 Vacuum pumps

Once the UHV chamber has been designed with optimal conductance, it is now the time to choose the right UHV pump with the right pumping speed L/s. For most pumps, the

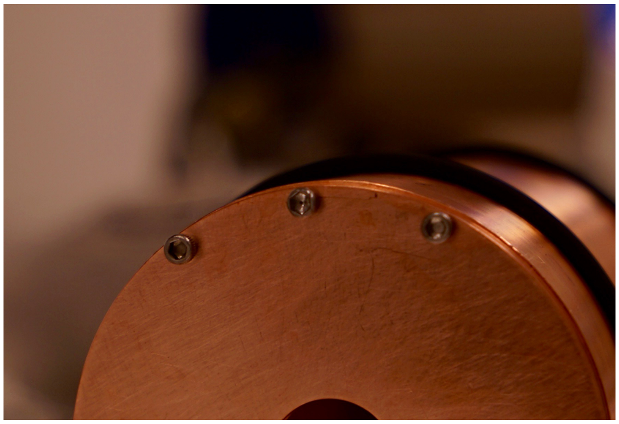

Figure 3.3: **Venting holes on the OFHC radiation shields.** A venting hole is machined through the center of the SS screw to remove virtual leaks.

pumping speed is actually a function of the type of gas, but generally the pumping speed is quoted for N_2 gas. The dominant gas loads for SS UHV chambers are H_2 molecules and He atoms, yet the pumping speeds for most pumps are very inefficient in extracting out these gas loads (and noble gas). Hence, the main challenge for XHV is to first reduce the outgassing rates for these gas loads and then to find pumping mechanisms that are effective for small atoms and noble gases. In terms of the pumping sequence, we can separate the vacuum pumps largely into two categories - extraction pumps and storage pumps. We begin with extraction pumps (scroll pump → turbo-molecular pump) to bring down the base pressure close to UHV for the storage pumps to operate. After a few baking cycles, we transition over to the storage pumps (ion pump, Ti-sublimation pump, non-evaporative-getter pump, and cryopump) and isolate the UHV system from the environment with a all-metal-gate-valve. In the following, I will describe the rationales behind our specific choices of the pumps.

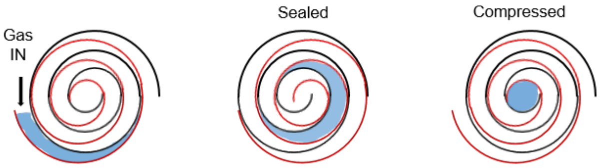

Figure 3.4: **Working principle of scroll pump.** Two Teflon scrolls enables gases to enter and be compressed. This compressed gases will be ejected with high speed. The black scroll is fixated, while the red orbits around eccentrically for gas compression.

Extraction pumps

Scroll pump In our pumping cycle, we begin a 5-minute pump down of the Agilent TwisTorr 304 FS turbo-molecular pump chamber with the IDP-3 scroll pump to the base pressure 5×10^{-2} Torr. The choice of the backing pump was made for scroll pump, because other atmospherical mechanical pumps were either not dry[e] or had the possibility of catastrophic failure (diaphragm pump[f]). Indeed, when the turbo system is turned on, we will require steady and reliable backing over many months to complete the baking and cleaning cycles. The working principle of scroll pump relies on the compression of trapped air molecules (with a scroll compressor). At the outlet of scroll pump, there are two archimedean sprials. One is fixed structure and the other is orbiting eccentrically in order to trap and compress trapped gas. As shown in Fig. 3.4, compressed gases is pushed out of scroll pump.

Turbomolecular pump After pressure reaches below 10^{-2} Torr, the next step is to turn on TwisTorr 304 FS turbopump with 6-in CF flange. Like the scroll pump, turbomolecular pump makes use of compression to establish the flow of gas in the desirable direction. The turbo fans consist of stationary and rotating blades. The injected gas is accelerated through the supersonic rotating blades to the backing scroll pump. To avoid the heating of the fans and inadverted oxidization, the turbo fan speed is controlled by a microcontroller that continuously monitors the torque of the fans and the local pressure of the turbo chamber with the Piranni gauge. After 30 minutes, our turbo system reaches a pumping speed of 300L/S (N_2 gas) and we have frequently observed the base pressure of 10^{-9} Torr of our main chambers through the inverted magnetron-Piranni gauge. The other technical detail is that our turbo pump has magnetically levitated ball bearings, so that it is compatible with moderate bake-out process to dry out water or small spills of acetones and IPA.

Storage pumps

Ion pump From around 10^{-6} Torr, we could start the ion pump. Instead of extracting the gas to the atmosphere, the ion pump operates by creating gas plasma with high voltage

---

[e] Some manufacturers may advertise that their mechanical pump is oil-free or oil-less. But even a rotary-vane pump should ideally not have oil in the pumping section because of the cold trap. In reality for UHV systems, this is inadequate as the oil can still migrate through the cold trap and coat a few monolayers on the UHV chamber walls. Some oil-less pumps are indeed oil-free, but these pumps may actually be water-soluble based fluids, which are still undesirable.

[f] Diaphragm failure involves the fracture of the diaphragm and sudden loss of vacuum.

$3 \sim 7$ kV through a cathode-anode assembly. The strong bar magnet (~ 0.1 T) on the exterior of the ion pump localizes the plasma that eventually reacts with the Titanium/-Tantalum cathode, producing metal alloys that sputters onto the wall of the ion pump chamber. Because of this sputtering process, it is possible to inadvertedly coat the anode pin with metal, thereby giving a ghost current (limited our base-pressure reading). For this reason, we usually blurp with a high voltage 10 kV repeatedly to discharge the anode pin at 10^{-6} Torr. Because the Ti sputtering rate is proportional to the pressure, we limit ourselves from continuous operation until the base pressure reaches 10^{-6} Torr. In this way, we are able to increase the lifetime of the pump and also reduce the Ti contamination in the main chamber.

In fact, for the Science chamber, the concerns with Ti contamination were serious because of our science cavity mirrors. In addition to limiting the conductance[g], we use a special diode-based XHV ion pump 45S-DIX-2V-SC-110-N (50% of Titanium and 50% of Tantalum cathode) from Gamma Vacuum with an SEM shielding that further blocks the emission path of the sputtered diode materials. With this configuration, pumping speed for N_2 gas is lower than other configurations (e.g., Starcell designs used in our Source chamber) but the chemistry of the cathode allows for noble gas pumping. We install μ-metal containers around our ion pumps to reduce the stray magnetic fields that would generally affect the internal Zeeman sublevels of our Cs atoms. Building upon Gamma Vacuum's expertise through Jefferson Laboratory, we have modified this particular batch of ion pump for an extremely thin Ti ground collector (30μm diameter) to reduce the X-ray limit[h]. With this change, we were able to monitor the vacuum pressure down to 10^{-13} Torr, better than all commercially available UHV gauges. In addition to the XHV reading of the local pressure within the ion pump chamber, we installed a nude ion gauge (X-ray limit $\sim 10^{-11}$ Torr). Because of the availability of low-outgassing XHV reading on our ion pump, we only used the ion gauges during the bake-out and the initial pumping cycles $10^{-7} \sim 10^{-11}$ Torr, as we found them to be outgassing when turned on (possibly due to internal sputter actions on the ion gauge's macor ceramic breaks).

---

[g] Simply avoiding a direct line of sight turned out to be more than effective, as sputtered Ti alloys have very large stiction coefficients with the SS walls. Unlike the conductance rules described above, which applies to non-interacting gases, Ti atoms could only reflect from the surface if it has already been enriched with many Ti monolayers.

[h] X-ray limit is the fundamental limit of cathode ion gauges, where small but non-negligible X-ray photons in the blackbody spectrum at room temperature cause photoionization on the ground collector that generates stray current fluctuation, thereby limiting our capability to read the background pressure. Since the X-ray limit is a function of the effective cross-section of the collector wire, a thin collector wire allows the reading at the XHV level pressure.

NEG pump In order to further improve the base pressure of the Science chamber, we utilized two kinds of non-evaporative-getter (NEG) pumps from Gamma Vacuum (N100) and SAES group (D100). The purpose of this passive pump was to improve the pumping speeds of H_2 gas (the dominant gas load in a UHV environment, except for He). Unlike other gettering pumps (e.g., Ti sublimation pump), the NEG pump, in principle, only emits the desorbed gases and do not rely on the evaporation of highly active metals. This has a particular advantage for the Science chamber, as the NEG pump would not only pump H_2 gas but also pump out any Ti atom that tries to reach the Science chamber. NEG pumps are made of sintered metal alloys (ZrVFe in this case) to increase the surface area, in which gas molecules are bombarded and absorbed deep into the alloy materials. The NEG pump is activated by desorbing the saturated NEG alloys at an elevated temperature ($\sim 500°C$) with an UHV oven, while being backed by the turbo pumping station. Our recipe for the activation is closely related with our baking cycle, and we will describe our protocol in the next chapter.

For next generation of UHV chambers, we have investigated the possibility of coating the inner surface of chambers with TiZrV material through our home-made DC-magnetron sputter. TiZrV is a new NEG material with very low activation temperature $200 \sim 300^o C$, and is currently being used in the CERN interstorage rings. The benefit of this method is that the NEG coating could be readily activated from the high-temperature bake, while providing a penetration barrier for H_2 gases within the SS chamber.

3.1.4 Atomic source

Instead of using Cs getter oven sources (SAES), we decided to use Cs ampoules (traced with 99.99% from Sigma Aldrich) for our atomic source. The rationale was that Cs getters use reagent materials to inhibit the oxidation rate in atmosphere, and these contaminants may limit the background (non-Cs) pressure in the Source chamber. In addition, a typical Cs getter would only contain a few mg of ^{133}Cs atoms, thereby limiting its lifetime to only a few years. Given the effort and resources put into this project, we decided for a longer term solution by using a Cs ampoule. Unlike Rb counterparts, the partial vapor pressure at room temperature is sufficient to fill the source chamber. In fact, as shown in Fig. 3.5, we control conductance with the aperture size with an all-metal angled gate-valve. We chose not to put a glass viewport, because the glass-to-metal transition[i] is known to be reactive with Cs atoms. Because Cs itself is an evaporative gettering material, when the

---

[i] Usually glass frits are fused to Kovar sleaves to avoid CTE mismatch.

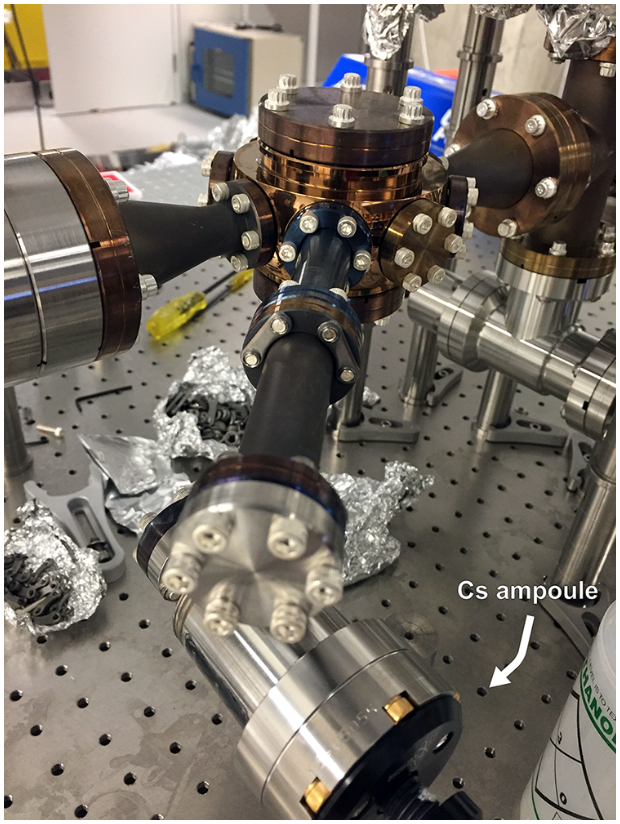

Figure 3.5: **Conductance control of Cs ampoule with all-metal gate-valves.** The flow of Cs atoms in the ampoule (Sigma Aldrich, 99.99% trace) is controlled by the opening of the UHV gate valve. The UHV gate valve assembly is attached to the Source chamber.

Cs source is isolated, the local pressure near the ampoule could be maintained at $\sim 10^{-7}$ Torr in the molecular flow regime.

In order to load the Cs atoms from the ampoule ($1g$) into the UHV chamber, I have constructed the gate-valve assembly in a N_2-filled dry glovebox in UQML by pumping out O_2 and water vapors to < 1 Torr. I was able to transfer approximately > 300 mg of Cs atoms to the source chamber. Because of the explosive reaction of Cs with atmospheric moisture, extreme care was taken to avoid chemical hazards by the exposure of the glovebox with Cs. The remaining Cs atoms were transferred to a portable vacuum box for chemical disposal. We store the unopened Cs ampoules and getter sources in a high-vacuum storage chamber to avoid oxidization.

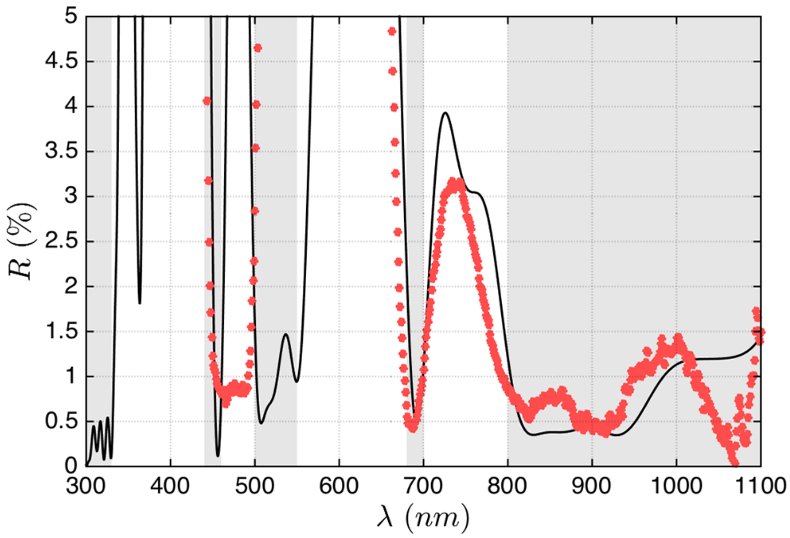

Figure 3.6: **Rainbow AR coating.** The black solid line depicts the theoretical reflectivity of our Rainbow anti-reflection coatings applied on the MPF UHV viewports based on the transfer matrix formalism. The red dots are the result of the spectrophotometric measurements (450 nm to 1200 nm) performed. The gray areas depict the functionals that compose the objective function for numerical optimization.

3.1.5 Differential pumping tube

We use a differential pumping tube to isolate the Science and Source chambers. The aperture and length of the tube are optimized both from the simulation of atomic trajectories in Chapter 5 (transfer efficiency), constrained by the conductance ratio $\frac{C_{\text{source}}}{C_{\text{science}}} < \frac{1}{200}$. This conductance ratio was determined by the expected equilibrium pressure of $\simeq 10^{-10}$ Torr in the Source chamber. The differential pumping section was formed by a SS316L microtube (Swagelok, diameter 1/8 inch, length 2 inch), and was TIG welded onto a double-sided blank CF flange. In order to reduce the possibility of forming a virtual leak, Sainath Motlakunta and Prof. Choi electropolished the part in a sulfuric-phosphorous acid recipe with $V = 13$ V. The tube was aligned at the normal of the CF flange with angular uncertainty of 0.3° on a lathe. Because the differential pumping tube connects two heavy UHV chambers, it is important to install a 1.33-in bellow as a pressure relief. We have had some bad experiences with improper pressure reliefs, which caused vacuum leaks during or after the high-temperature bake (possible due to the thermal expansion of the entire chamber).

3.1.6 UHV viewports

Although diffusion bonding methods in viewports are popular due to their strengths and high-temperature compatibilities, I have decided to go with a vacuum-brazing method developed by MPF products. Vacuum brazing works by adding a (somewhat magnetic) filler element (usually, lead alloy) to the glass-to-metal transition sleeves. The sleeve is subsequently fusion bonded to the SS316L CF flange. Because the glass-to-metal bonding is achieved with minimal heat ($300°C$ at most) to melt the filler, we do not expect significant wavefront distortion $\sim \lambda/10$ from the brazing process itself[j]. Because of the low glass temperature of the filler, this process inhibits the high-temperature bakes to $\sim 200°C$. Because we are limited to this temperature range anyway (e.g., Science cavity), I decided to install the UHV viewports after the high-temperature pre-baking cycles.

In order to reduce the scatter losses and to avoid local heating from high-power dipole trap beams, we have requested MPF to use Corning HPFS (DUV synthetic silica) glass for the viewport materials. The viewports on our Science chamber used a very unique anti-reflection (AR) coating stack technique developed within UQML for thin-film deposition, which we nickname the “Rainbow” AR coating. The name says it all. In qualitative terms, our Rainbow viewports are basically macroscopic interference filtersIt achieves remarkly low loss and scatter across a wide target wavelength region with a macroscopic coating thickness (nearly $100\mu m$)! In fact, our Rainbow viewports are basically macroscopic interference filters. Prof. Choi adopted numerical techniques developed for narrow-band multi-cavity filter designs to create a complex coating stack. This design optimizes the transmission coefficients for bilayer fused silica (SiO_2) - Scandium Oxide (Sc_2O_3) films on a fused silica substrate for the following wavelength ranges: $300 - 330$ nm (for direct Rydberg $|nP_j\rangle$ excitation lasers, 455 nm for direct $|7P_j\rangle$ imaging lasers, $500 - 550$ nm for $|6P_{3/2}\rangle \leftrightarrow |nS_j\rangle, |nP_j\rangle$ second-stage lasers, 685 nm for blue-detuned magic wavelength lasers, 852 nm or $|6S_{1/2}\rangle \leftrightarrow |6P_{3/2}\rangle$ first-stage lasers, 892 nm for $|6S_{1/2}\rangle \leftrightarrow |6P_{1/2}\rangle$ lasers, 935 nm for red-detuned magic wavelength lasers, and $1000 - 1100$ nm for low-noise far-off-resonant trapping (FORT) beams. I will revisit the coating techniques and the transfer matrix formalism in Chapter 6. We use a planetary reactive-ion RF-magnetron sputter optimized for large surfaces, with the availability of their sputter guns for Sc_2O_3 film deposition. The RF magnetron sputter techniques can grow atomically dense thin films with no porosity, and the thick films of Sc_2O_3 can act as He diffusion barrier. Because the reactive-ion RF-magnetron sputtering procedure involves high-momentum atomic deposition, there is one drawback in terms of the clear aperture attainable in such systems. The metal flanges

---

[j] The surface flatness will be distorted due to the mechanical stress after vacuum brazing. In the future, we may consider performing magnetic fluid polishing after the brazing.

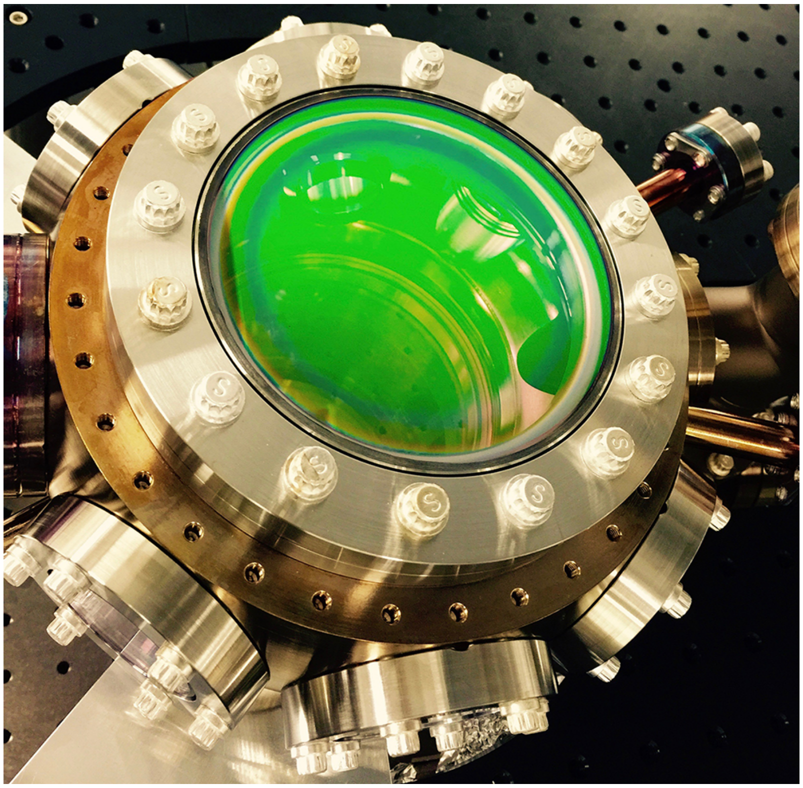

Figure 3.7: **Rainbow AR coating on 6-in UHV viewport.** The color gradient visible near the glass-to-metal sealing shows the shadowing effect due to the nearly collimated sputtered atomic beams.

also create local field lines that distort the pathways for the atomic trajectories. Hence, for our recessed UHV viewport used for the quantum-gas microscopy, MPF applied the BAAR coating between $500-1000$ nm ($R<1\%$) through a low-temperature ion-assistant deposition (IAD) process. To avoid the shadowing effect, MPF sent the vacuum-brazed glass-sleeve parts to their coating supplier, before performing the fusion bonding to the recessed tube of the CF flange.

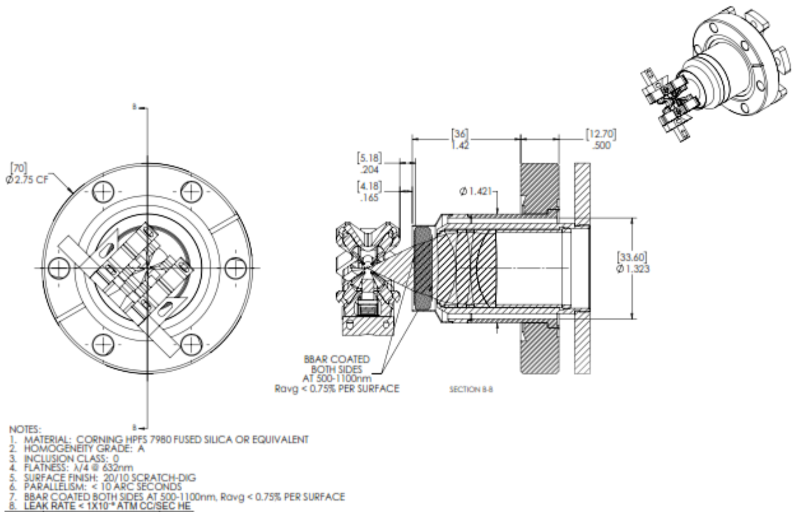

Figure 3.8: **2D layout of recessed viewport.** As our quantum gas microscope (QGM) has numerical aperture of 0.45, it should be located near optical cavity. Therefore recessed viewport is used and QGM is inserted. The sequence of optics represents our QGM object.

3.2 UHV baking procedures and preparation

3.2.1 UHV cleaning procedure

After the parts are machined[k], oil-residues must be removed with detergents (dish washer) with the UQML "dirty" sonicator for 30 minutes. After this, we ultrasonic the parts with reagent-grade (99%) or recycled spectroscopic grade alcohols (acetone) for 15 minutes[l]. Once the oil-residues are removed, we perform ultrasonication with industrial detergents with deionized water at an elevated temperature, depending on the component materials. For instance, for stainless steel parts, we use the recipe from Kimball Physics, where we repeatedly ultrasonic with 5% Micro99 for 60 minutes at $T = 50°\text{C}$ until all the organic and oil-marks are removed from the surface. When using the industrial detergents, extra care must be taken for Aluminum and their alloys (Al 6061 series), because some detergents have base pH that rapidly form porous oxide layers. I had good experience with Alconox (15 min ultrasonic at $T = 60°\text{C}$). For OFHC copper, I use a special formula, Citranox,

---

[k] It is highly desirable to request the machine shop to use water-soluble coolants.

[l] Please follow the UQML SOP, which describes the necessity of the portable carbon-filtered fume hood for ventilation.

which descales and etches away the oxygen-rich Cu surface. Cu, Al, and Ti pieces are all stored either in the oxygen-free glovebox or in the vacuum storage area to prevent the natural oxidization. For Al and some SS pieces, Sainath Motlakunta and Prof. Choi perform the electropolishing procedure, outlined in the next section. Only then, the UHV cleaning procedure could begin!

After the early stage of cleaning, the vacuum components are cleaned with UQML's "clean" ultrasonic cleaner (Read the SOP) under a local cleanroom environment[m]. Because we were aiming for XHV chamber assembly, it was necessary to maintain the laboratory's air quality on par with the QNC's nanofab. Because of the size of the UHV chambers upon assembly, it was deemed impossible to clean and assemble the vacuum components elsewhere and transport into the laboratory (some parts were sensitive to oxygen). We first install the portable chemical fume hood and check the lifetime of active carbon filters. It is critical to clean the surrounding of the benchtops and wrap with UHV aluminum foils on the surfaces nearby (with the shiny surface pointing upwards to avoid dust accumulation). The day before the actual UHV cleaning, we turn on all the Ultra Low Penetration Air (ULPA)/ High Efficiency Particulate Air (HEPA) filters that locally create class-10 cleanrooms under the optical tables. Over 24 hours, we find that the overall laboratory space can be maintained at a class-1000 cleanroom environment. We wear cleanroom clothes with hair mesh and face masks near the entrance of the laboratory, as well as lint-free class 10 latex gloves to prevent any introduction of organic. Lint-free kimwipes are used for the cloths, and ULPA-filtered 99.999%-purity N_2 cleanroom airguns are used throughout for immediately drying out the parts after immersion into spectroscopic grade (99.9%) alcohols in class-1000, so that the dried vacuum parts could be quickly transported within UHV Al foils to the safer class-10 spaces within the laboratories.

Procedures for stainless steel, aluminum (alloy), and titanium (alloy)

1. Rinse the parts with spec. grade methanol and prepare them on top of the UHV Al foil.
2. Perform ultrasonic cleaning with spec. grade methanol for 15 minutes without heating. Please remember to double check if the portable fume hood is on with maximal extraction speed.
3. Quickly rinse with spec. grade isopropanol (IPA) to remove salt residues that outgas at XHV environment.

---

[m] This is located next to the distilled water pipeline and drain.

4. Use Kimwipes with IPA for the inner side of the vacuum components, and clean the knife edges carefully with Thorlabs lens paper with teflon tip tweezer with 1 minute.
5. Perform ultrasonic cleaning with spec. grade IPA for 15 minutes without heating.
6. Use cleanroom N_2-gun to blow away residual IPA and place the cleaned components under the ULPA filter.
7. Once the parts are completely dried, cover them fully with UHV Al foil for storage. Be cautious not to touch the knife edge.
8. Store them in the class-10 area.

After the air baking, the parts should be cleaned with the same procedure as above, but by replacing the methanol with acetone. This allows the solvents to preserve the delicate Chromium Oxide barrier formed in the airbaking process.

Procedures for UHV viewports

Once all the metal components are ready to be assembled, we can now clean the delicate UHV viewports underneath of laminar flow. The key concern with the viewports is to avoid thermal shock when the parts are exposed to alcohols, as they tend to evaporatively cool the viewport. Large thermal shocks can cause damages to the glass-to-metal sealing. We do not use the ultrasonic agitation, as trapped air bubbles may damage the AR coatings. The work space of the ULPA laminar flow workstation is covered with the UHV Al foils.

1. Blow with compressed N_2 gas for dust removal and rinse with spec. grade methanol before placing the viewport to the laminar flow workstation. Please remember to double check if the portable fume hood is on with maximal extraction speed.
2. Rinse wit IPA and dry under the laminar flow workstation.
3. Soeak lens paper with IPA and swipe gently across the viewport window.
4. Store them in the class-10 area.

Procedures for screws and tools

To clean vacuum screws and tools that we use for assembly, we recycle the acetone and IPA wastes produced from cleaning the vacuum components above, and clean the parts with the ultrasonic agitation. Store them in the class-10 area.

3.2.2 Surface treatment

As I discussed in section 3.1.1, the outgassing rate is proportional to the effective surface area. Microstructures created during the CNC mills generally give an effective area several orders of magnitude larger than the surface area for an atomically smooth surface. Hence, one of the greatest challenges in vacuum technologies is to find methods to get smooth surfaces on the interior of the stainless steel UHV chamber. We begin this process during the manufacturing by requesting a mirror finish and electropolishing on the interior of the SS316L Science and Source chambers (Nor-Cal, Kimball Physics, and VMT corp.). Unfortunately, because of the complexity of the process and abundance of alloying atoms (notably Si), electropolishing is not commercially available for most Al 6000 alloys. Hence, we developed our own recipe here.

Likewise, all custom metal parts that go into the Science chamber are CNC machined and polished down at least to a mirror finish (surface roughness < 50 nm) from the machine shops[n]. After the mechanical components are cleaned through the preliminary stages[o], Sainath Motlakunta and Prof. Choi developed our own electropolishing (EP) recipes for stainless steel and AA 6061 T6 alloys to further reduce the surface roughness and to recreate non-porous oxide barriers[p]. EP removes metal debris from a workpiece by passing an electric current, while the workpiece is submerged in an electrolyte (usually acid baths). In an opposite fashion to electroplating, the workpiece is eroded to release metal ions to the surrounding solution. Because the rough "bumps" have larger surface area exposed to the solution, these are smoothen by the larger etching rate, to eventually create a smooth surface. Particularly, our EP recipe for AA 6061 T6 alloys was quite challenging because of the lack of literature, and due to the challenges of alloying Si atoms in the AA 6061 T6. When the usual EP procedures for SS parts are applied to AA 6061 T6, we observed significant amount of Si atoms deposited on the surface of the piece, leaving the object covered with semiconductor thin films and making it impossible to act as proper Faraday shields with high electric conductivity. On the other hand, pure aluminum and other AA alloy variants were either not compatible with the XHV environment and with the high-temperature bake-out necessary for driving out the H_2 atoms out of the bulk. All work was strictly performed in the IQC chemistry laboratory with proper ventilation in the acid fume hood.

---

[n] We have worked with a specific recipe for manufacturing vacuum parts with Mindrum precision, RJB, Seaborne, and the Science machine shops. So they now understand the particular procedures and restrictions on their coolants.

[o] See the first two paragraphs of Section 3.2.1.

[p] Please note that we put kapton tape on the knife edges to protect from the abrasive EP process.

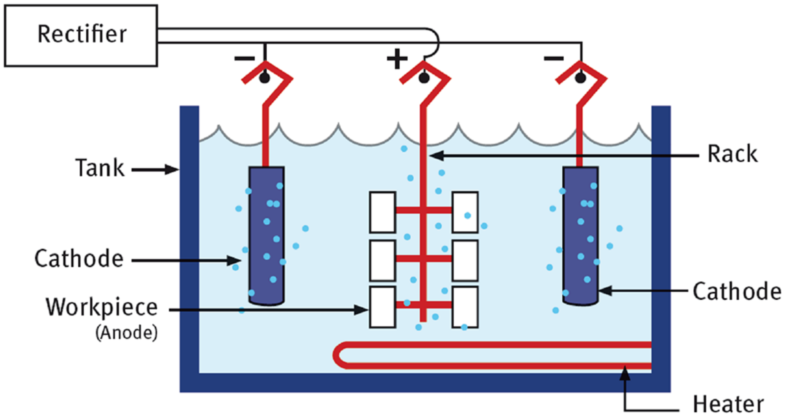

Figure 3.9: **Electropolishing procedure.** The workpiece is connected to the anodic terminal, and the separate cathode electrode is lowered into the electrolyte solution. The electric circuit, formed by the anode-cathode terminals, creates electropolishing to release metal ions, forming H_2 vapors.

EP procedures for SS parts

- Descaling and picking –
  - (a) Removal of any alkaline film created by detergents with sulfuric acid dip for 1 minute.
  - (b) Rinse with deionized water.
- Electropolish –
  - (a) The workpiece is connected to the positive terminal of a switching power supply, and act as the anode of the EP solution.
  - (b) The workpiece is submerged to the electrolyte solution, consisting of 1:1 ratio of 90% sulfuric acid and 50% phosphoric acid, at temperature $T = 60°C$, and left for 30 seconds for descaling.
  - (c) Magnetic bar stirring action removes any H_2 bubble formed on the surface of the SS piece.
  - (d) A separate copper cathode is lowered into the beaker and is connected to the negative terminal of the power supply, forming an electric circuit through the anode.

    (e) Current density is varied between $3A/dm^2 - 20A/dm^2$ for 5 minutes.

  ** After the electropolishing, the electrolyte solution transferred to the chemical waste, and the beaker is diluted by deionized water and caustic soda for neutralization.

- Post-treatment (removal of heavy atoms on the surface) –
  - (a) 60% Nitric acid dip for 30 seconds.
  - (b) 20% Nitric acid dip for 10 seconds.
  - (c) Rinse with deionized water.
  - (d) Rinse with spec. grade acetone.

EP procedures for AA 6061-T6 parts

- Descaling and picking –
  - (a) Ultrasonication with 3% Alconox detergents at $T = 60°C$ for 10 minutes.
  - (b) Rinse with deionized water.
  - (c) Immerse the workpiece into acid cleaner solution (70 mL phosphoric acid, 20 g chromic acid, 3 L deionized water) for 5 minutes.
  - (d) Because the continuous exposure to air creates an oxide layer, the AA workpiece is submerged in a cold 70% nitric acid until proceeding to the EP step[q].
- Electropolish –
  - (a) The workpiece is connected to the positive terminal of a switching power supply, and act as the anode of the EP solution.
  - (b) The workpiece is submerged to the electrolyte solution, consisting of equal weight 15% phosphoric acid, 70% sulfuric acid, 1% nitric acid, and 14% deionized water at temperature $T = 80°C$, and left for 30 seconds for descaling.
  - (c) Magnetic bar stirring action removes any H_2 bubble formed on the surface of the SS piece.

---

[q] The EP step should happen within 1 minute to avoid surface corrosion.

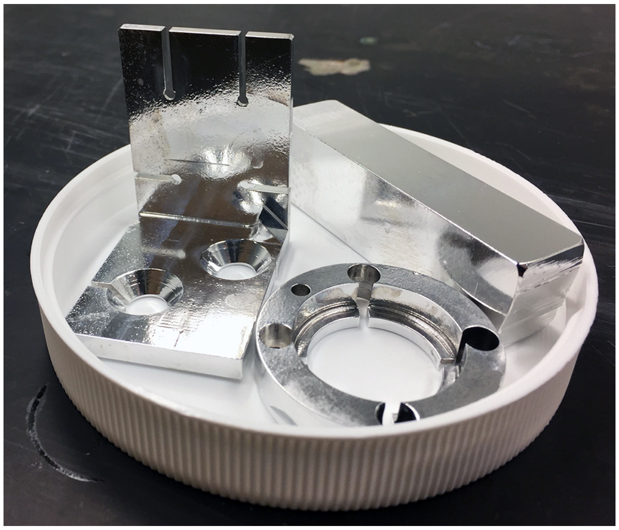

Figure 3.10: **Example of EP finishing on Al 6061-T6.** The shiny surface on AA 6061-T6 reflects the absence of porous microstructures after the EP process. The macroscopic dents are caused by the presence of H_2 bubbles in the initial recipe without magnetic stirring action.

(d) A separate stainless steel cathode is lowered into the beaker and is connected to the negative terminal of the power supply, forming an electric circuit through the anode.

(e) Current density is varied between $10A/dm^2 - 15A/dm^2$ for 2 minutes.

** After the electropolishing, the electrolyte solution transferred to the chemical waste, and the beaker is diluted by deionized water and caustic soda for neutralization.

- Post-treatment (removal of Si atoms on the surface) –
  (a) 60% Nitric acid dip for 3 minutes.
  (b) Rinse with deionized water.
  (c) Rinse with spec. grade acetone and IPA.
  (d) Immediately store into the vacuum container to prevent further oxidization.

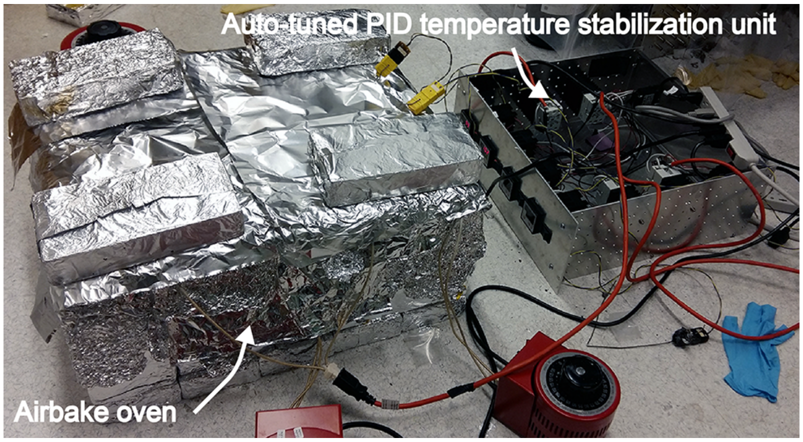

Figure 3.11: **Home-made air bake oven.** The oven is made of low-outgassing firebricks and Omega heat tapes. The temperature of the even is stabilized by auto-tunable PID circuits that regulates the solid-state relays by monitoring the thermocoupler sensors.

3.2.3 Air baking and vacuum passivation

Before the workpiece goes through the passivation process to recreate thick and dense oxide diffusion barriers, we ensure that all SS316LN pieces are vacuum fired at 950°C. This drives away most of the bulk H_2 atoms. Vacuum firing other SS pieces without N_2 enrichment is reported to have Ni depletion from the alloy, thereby significantly reducing the tensile strength and non-magnetic properties.

SS 304 and SS316L(N) contain 16 $\sim$ 26% of Chromium (e.g., SS 18-8 has about 18% of Cr atoms in number density). For most UHV workpieces, we perform a high-temperature air bake at 400°C. The O_2 gas in atmosphere can then react with the SS surface to create dense Chromium Oxide layers. I began by constructing a home-built oven that could enclose large UHV chambers in a cleanroom environment[r]. The oven was made with low-outgassing firebricks as thermal insulation. Using high-temperature heat tapes (Omega engineering), I initially degassed the firebricks and the heat tapes at 400°C for 10 hours, and wrapped the bricks with several layers of UHV Al foils. The heat tapes turned from the original gold hue to a pure white color, exposing the fiberglass insulation layer.

The oven is constructed with the UHV Al foil covered firebricks, and many layers of UHV Al foils to seal the gaps between the bricks (Fig. 3.11). With this crude oven, we were able to raise the temperature to above 400°C. The UHV workpieces are covered with

---

[r] See the cleaning section.

3-layer UHV Al foils, but extra care should be taken to avoid the foil touching sensitive parts (e.g. knife edges), as the Al foil softens at high temperature and may bond to a clean and smooth metal surface[s]. The K-series thermocoupler is taped with a Kapton tape on the outer layer. After wrapping around the work pieces with the degassed heat tapes, we insulate these pieces with addition 5-layer UHV Al foil[t].

With the K-thermocoupler, Dr. Liu used HTS/Amptek AT-BBA220-SSR PID control modules and JDA-33400-060 SSRs to create a servo loop to lock the temperature between $25 - 450°C$ with stability of 100 mK. We use this controller also to perform the UHV pre-baking at $350°C$ and UHV baking at $200°C$ (with the viewports and internal components installed). With this controller, we can maintain our baking schedules over a few weeks. Our air-baking schedule is as follows:

1. Ramp up with speed $60°C$ per hour to $400°C$.
2. Maintain the temperature at $400°C$ for 3 hours.
3. Ramp up with speed $60°C$ per hour to room-temperature.

An example of an air-baked UHV workpiece is shown in Fig. 3.12. If the steps are carefully followed, you will find a reflective metal surface with orange or brown hues depending on the Cr_2O_3 thickness.

For the second-generation science chamber, I shared our atmospheric passivation process to VMT to apply a modified vacuum passivation process. Since VMT manufactures our XHV Science chamber, the rationale was that, if they could learn the tricks of vacuum passivation, we would be able to avoid the air-baking process that elevated the entire laboratory temperature by a few $°C$, which inhibited us from working with our laser systems at the same time. Fig. 3.13 shows the fabrication procedure of XHV vacuum chamber to meet our certification standard. For the vacuum passivation, the chamber is placed inside of a larger vacuum furnace pumped with turbo and cryopumps at $P = 10^{-8}$ Torr. The Science chamber was enclosed with black CF flanges, and one of the flanges was replaced with a metal feedthrough to flow pure oxygen at a controlled rate. The interior of the Science chamber was stabilized at $P = 10^{-4}$ Torr with an O_2 gas pneumatic controller. Our Science chamber was vacuum-passivated at 450^oC for 24 hrs to form the oxide layers only on the interior surface.

---

[s] We have found that oven cleaning acids for kitchen applications are effective at dissolving Al foils.

[t] The Al foils are made intentionally with a large amount of air gaps, so that the trapped air can act as insulation layers.

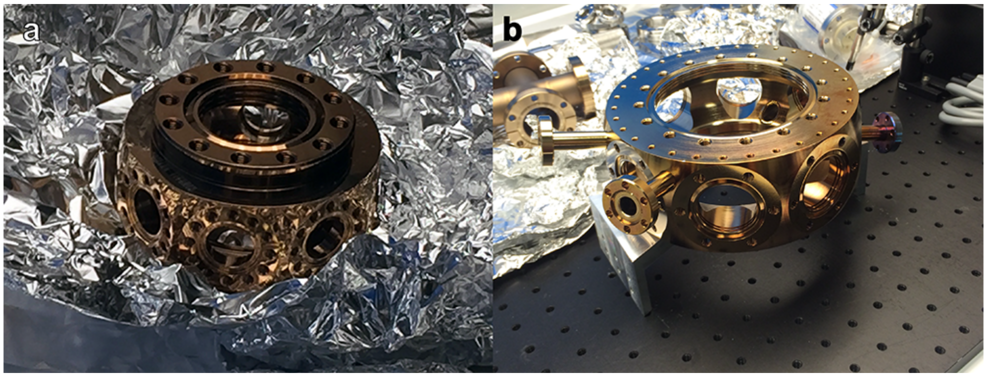

Figure 3.12: **Chromium oxide layer on SS316LN Source and Science chamber.** The brown hue on the SS316LN chamber was formed without affecting the surface roughness.

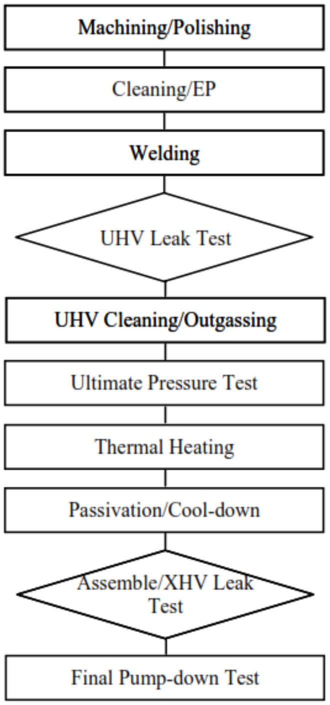

Figure 3.13: **Fabrication sequence of XHV chamber.** The diagram demonstrates the machining and surface treatment steps of XHV chamber.

3.2.4 UHV pre-baking & final UHV baking

The work function for releasing water molecules grows inversely with the number of monolayers, and it takes a large amount of thermal energy well beyond its boiling temperature to degas the last few molecular layers, with the "magic" temperature around $T_m = 180{-}190°C$ for stainless steel surface. Hence, after all the UHV components are vacuum-passivated and UHV cleaned again, we have applied a pre-baking step at $T_b = 350°C$ well above T_m. We assembled the UHV chamber with the ion pump assemblies and the getter pump on our non-magnetic SS316LN optical table, with the UHV viewports replaced with SS304 blank CF flanges. We removed the ion pumps magnetic assemblies, as the Curie temperature was lower than T_b. We wrapped the entire chamber with a few layers of UHV Al foils for distributing the heat uniformity[u], and installed degassed Omega heat tapes and K-type thermocoupler sensors for the PID controllers. We then covered the chamber with 3 additional layers of UHV Al foils to insulate the optical table from excess heat[v], as shown

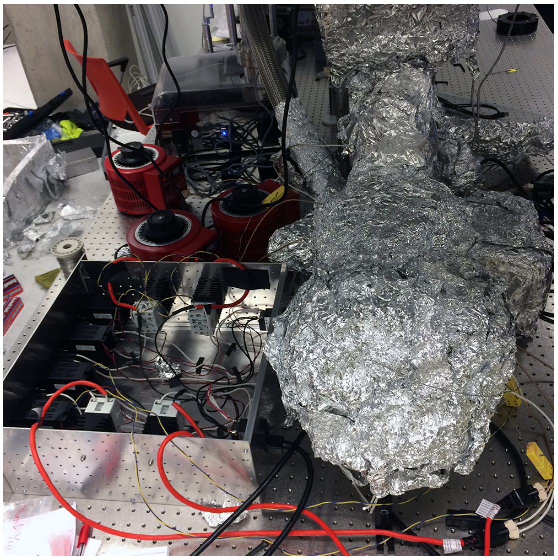

Figure 3.14: **Photo of UHV-XHV system under prebake condition at $T = 350°C$.** The UHV chamber is covered in UHV Al foils and Omega heater tape. Viewports are replaced with CF blanks.

---

[u] Any "cold" spot left on the UHV chamber would be a condensing region for the water molecules to accumulate, instead of being pumped out to the atmosphere through the turbo pump.

[v] The damping constant is reduced by a factor of two for Newport non-magnetic optical tables at $T > 80°C$.

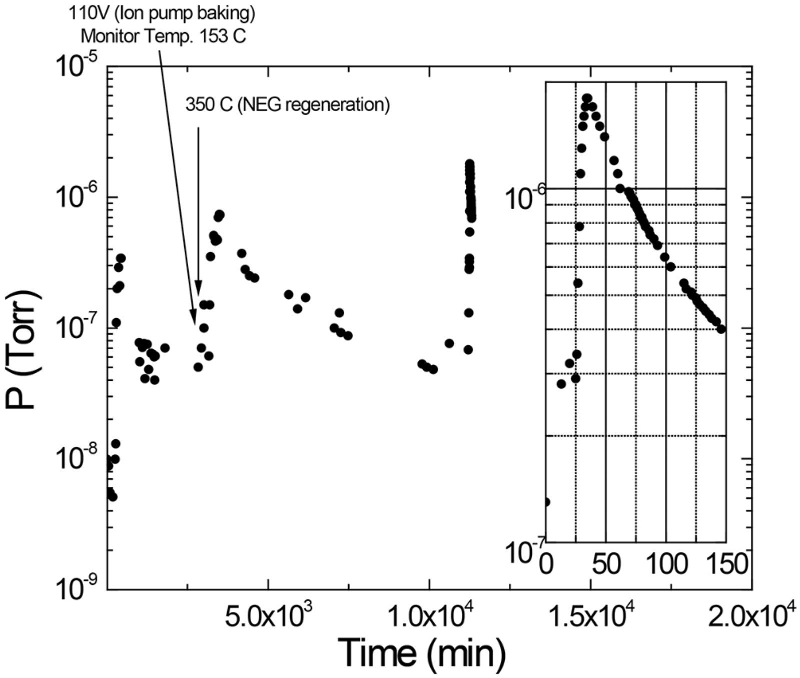

Figure 3.15: **Prebaking schedule.** We illustrate the chamber pressure as a function of time.

in Fig. 3.14.

After the system reaches 10^{-9} Torr with the turbo pumping station at room temperature, we elevate the temperature at the rate of $20°C$/hour until we reach the target temperature. We have installed extra thermocoupler sensors throughout the chamber to ensure uniformity, and installed shim heat tapes on cold spots with external Variacs. Fig. 3.15 shows our pre-baking cycle with the pressure over a week, as monitored by an integrated Piranni-inverted magnetron sensor. At $T \simeq 300°C$, we activate our NEG pump by running current of $4.5A$ until the base pressure reaches $P < 10^{-7}$ Torr[w]. This pre-activation process removes any water molecules from the surface of NEG[x], which may condense onto the chamber walls. The subsequent high-temperature bake will then drive away the water molecules from the entire chamber. Once the target temperature is reached, we wait until the system is pumped down to $\sim 10^{-8}$ Torr level for several days. At the end of the baking cycle, we perform a reconditioning cycle by retraining the NEG pump. The inset

---

[w] We ramp up the current over 5 hours to avoid overshooting the equilibrium pressure above 10^{-6} Torr.

[x] The effective surface area of the NEG pump is much larger than the entire chamber

of Fig. 3.15 shows our final regeneration procedure to sublime any H_2 molecule from the NEG bulk. We then lower the temperature of the UHV chamber to room temperature with ramp-down speed $20°C$/hour. Our experience is that for every $80°C$, the ultimate pressure is reduced by 1 decade. For $\sim 10^{-8}$ Torr at $350°C$, we thereby expect the ultimate pressure $P_u \simeq 10^{-12}$ Torr at room temperature[y]. As our ion and NEG pumps are not as conductance limited as the turbo system by a factor of 20, we would then expect another reduction in the pressure decade, resulting into $P_u < 10^{-13}$ Torr. Our reading of the pressure (via Gamma Vacuum ion pump) was limited by the X-ray limit of 1×10^{-13} Torr.

After confirming the conservative value of the ultimate pressure 1×10^{-13} Torr, we then installed the UHV viewports and other assemblies to the main chambers in late 2016. We follow through the same procedure as with the pre-bake schedule, but with reduced ramp speed $10°C$/hour and target temperature $T = 185°C$ to marginally hit the magic temperature. After 2 weeks of the final UHV baking and subsequent ramp-down, we were able to measure XHV-level pressure 1×10^{-13} Torr in the Science chamber and 3×10^{-11} Torr in the Source chamber (with the Cs ampoule isolated). When we open the Cs gate-valve, the Cs-limited pressure in the Source chamber was raised to $P \simeq 6 \times 10^{-10}$ Torr, and we were able to readily form cold atoms in a magneto-optical trap (MOT) with radiation-pressure limited number density $\sim 10^{10}$ atoms/cm^3 at $\sim 100\mu$K. Remarkably, the Science chamber pressure remained the same at 1×10^{-13} Torr with a theoretical collision-limited trap lifetime of 4 hours (two orders of magnitudes larger lifetime than any other neutral atom experiment)!

3.3 Electromagnets

The design of external electromagnetic field control requires special mounts and mechanical parts nearby (or on) the chambers, and these thermoelectrical considerations may affect the geometry of the UHV chambers. Often times, having a better electromagnet coil holder in AMO physics means that you can apply a larger bias field to modify the atomic collisional cross-sections at ultracold temperature and stay at a particular detuning with respect to a molecular Feshbach resonance. In fact, it is a widely known anecdote that one of the advantages that Debbie Jin had over everyone in the field in 2000 was the magnetic field stability of her Feshbach coil in her pioneering work on Fermi quantum-degenerate gases.

---

[y] This pressure would of course never be met only with the turbo pumps, as they have finite compression ratios.

This seemingly "boring" problem turns its head on to an important technical mastery for doing AMO experiments.

Our electromagnet in the Science chamber plays two roles – Magneto-optical trap (MOT) and control over the ratio σ_i/σ_e of inelastic to elastic collision rates for coherent Feshbach molecules Cs_2. Magneto-optical trap (MOT) requires a field-gradient $\frac{dB_z}{dz} \sim 10$ G/cm at the center of chamber for sufficiently large capture velocity v_c for room-temperature background Cs atoms. In addition, we need to consider the linearity of $\frac{dB_z}{dz}$ over a few cm to increase the capture volume of the atoms. For Cesium, it is also known that, at ultracold temperatures $< 1\mu K$ and high-densities, inelastic cold collision dominates over elastic s-wave scattering used for evaporative cooling. Feshbach resonance can be utilized to control the s-wave scattering rate for run-away evaporation of Cs atoms in an optical dipole trap down to its quantum-degeneracy [125], requiring us to stabilize the magnetic field at ~ 20.8 G with long-term stability of 1 mG. In addition, we would like to have field gradients ~ 50 G/cm to support the ultracold atoms against the gravitational potential when loading into dipole traps.

Fig. 3.16 illustrates an anti-Helmholtz configuration that allows a linear field gradient at the center of the two coils over 5 cm. In addition, it is crucial to have as little winding as possible to reduce the inductance and back-EMF upon switching large currents. Improper consideration of the magnetic field switching times (induced by fluctuating Eddy currents) will negatively affect our capabilities for efficient polarization-gradient cooling and the atomic Zeeman coherences. On the other hand, larger currents would may result with a resistive heating that mechanically drift the center position of the magnetic trap. In terms of material properties, we require the holders to be non-magnetic (to reduce stray field hysteresis), electrically insulating, and thermally highly conductive.

3.3.1 Science MOT coil geometry

To build a fast MOT coil controller with power MOSFET current switching capabilities (sub-100μs), I have limited the current to $I = 10$ A with a target field gradient $\frac{dB_z}{dz} \sim 10$ G/cm. To determine the coil geometry constrained by the UHV chamber, I simulated the magnetic field in the cylindrical coordinates (ρ, z) as follows [126]

$$\begin{aligned} B_z &= \frac{\mu_0 I}{2\pi}\frac{1}{\sqrt{(R+\rho)^2+(z-D)^2}}\left[K(k^2)+\frac{R^2-\rho^2-(z-D)^2}{(R-\rho)^2+(z-D)^2}E(k^2)\right] && (3.5) \\ B_\rho &= \frac{\mu_0 I}{2\pi}\frac{1}{\rho}\frac{z-D}{\sqrt{(R+\rho)^2+(z-D)^2}}\left[-K(k^2)+\frac{R^2+\rho^2+(z-D)^2}{(R-\rho)^2+(z-D)^2}E(k^2)\right], && (3.6) \end{aligned}$$

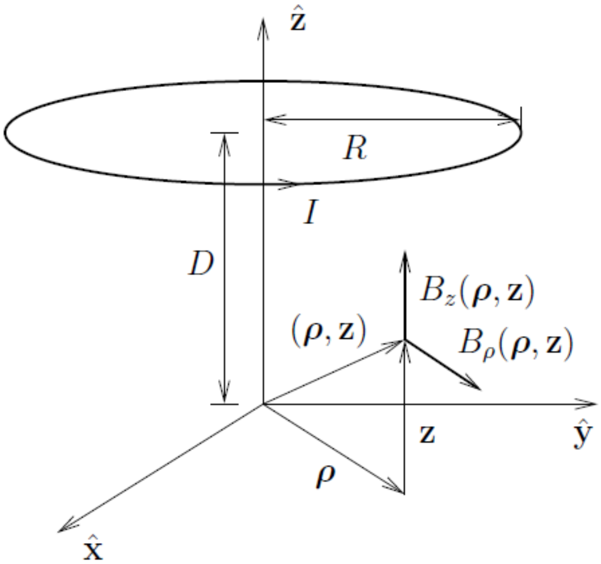

Figure 3.16: **Coil configuration in the cylindrical coordinate (ρ, z).** The current I flows counter-clockwise through the coil of radius R. For an ideal anti-Helmholtz, the current direction in the other coil at $Z = -D$ flows clockwise and the half-distance between the coils is $D = R/2$.

where $k^2 = \frac{4R\rho}{(R+\rho)^2+(z-D)^2}$ and $K(k^2)$ and $E(k^2)$ are the complete elliptic integrals for the first and second kinds. The field lines were simulated by taking into account the wire thicknesses of various cross-section geometries (square, rectangular and round magnet wires). Fig.3.18 shows our result of the magnetic field for our electromagnet coils by optimizing over the parameters $n_1, n_2, n_3, \delta x, \delta y$ for a rectangular magnet wire. I have constrained the design variations so that the optical view of the experimental platforms is not hindered by the coil holders. I obtain a B-field gradient of 10 G/cm for the parameters of Table 3.3.

Because I plan to use these coils also for inducing the Feshbach resonance at currents $> 50A$ (See the Helmholtz configuration in Fig. 3.18), we need to consider an efficient method

n_1	n_2	n_3	δx	δy	d_0	R_0
1	11	10	3 mm	2 mm	2.7 inch	2.4 inch

Table 3.3: Optimized MOT coil parameters for Science chamber for $I_p = 10$ A and target axial gradient 10 G/cm.

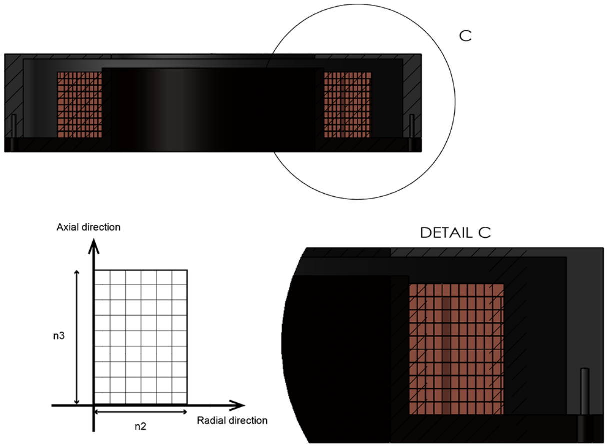

Figure 3.17: **Science MOT coil holder.** The structural parameters n_1, n_2, n_3 are numerically optimized in Fig. 3.18 when n_1, n_2, n_3 are the winding number given in the figure. The coil holder is made of Delrin-Acetal with the possibility of full potting for water cooling.

to dissipate a large amount of resistive heat generated by the ohmic loss $r(A)$, which is a function of the wire's cross-section $A = \delta x \delta y$. I have concluded to optimize the geometry for a rectangular magnet coil with polyamide-insulation coating with critical temperature $400°C$. Design of coil holder is shown in Fig. 3.17. The coil holder and the cover are made of Delrin-Acetal, a ceramic composite with thermal conductivity ($\sim$ 0.4 W/m·K) and temperature rating ($\sim 180°C$). In addition, with a complete dielectric construction, this construction would avoid any Eddy current around the coil holder altogether. We have also considered Polyetherimide (PEI) Ultem as the material of choice for the coil holders. Ultem has a higher tensile strength than Delrin-Acetal with similar thermoelectric properties. More recently, my colleague, Youn Seok Lee found a very promising thermoceramic, known as Corian, with an order of magnitude larger thermal conductivity and tensile strength.

3.3.2 Heat transfer

We considered the heat transfer for the thermal energy generated by the ohmic loss. Our magnet wire (oxygen-free copper for higher electrical conductivity) has a total resistance of $\sim 0.09\Omega$. The change in resistance would be around $3m\Omega$ with the thermal coefficient of resistivity of copper α of $\approx 4 \times 10^{-3}\ \Omega/C^{\circ}$ from the relation,

$$\frac{\Delta R}{R} = \alpha \Delta T \tag{3.7}$$

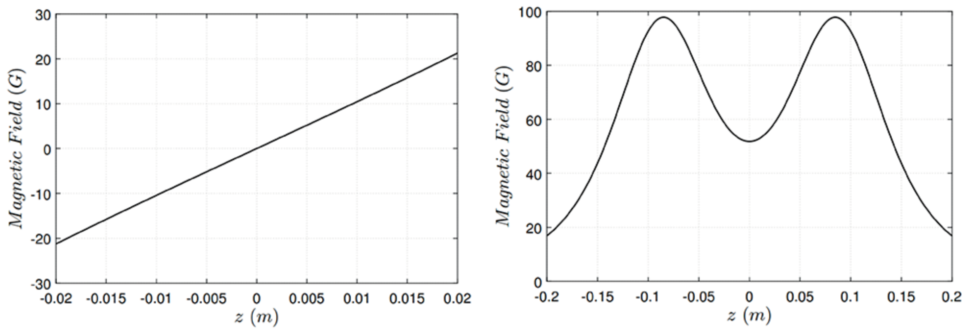

(a) Magnetic Field along axial direction
Anti-Helmholtz Configuration

(b) Magnetic Field along axial direction
Helmholtz Configuration

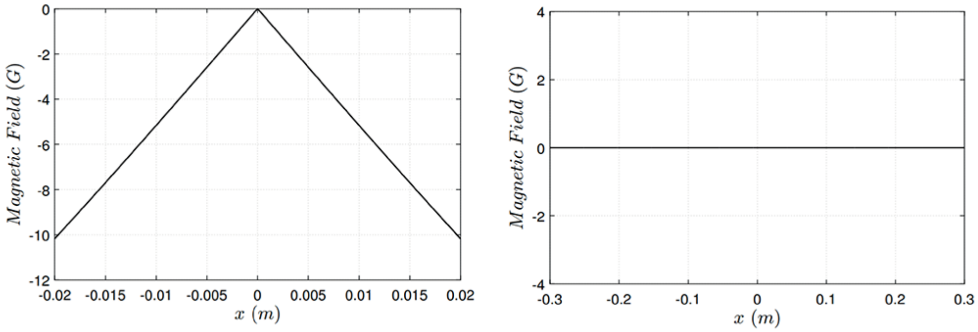

(c) Magnetic Field along radial direction
Anti-Helmholtz Configuration

(d) Magnetic Field along radial direction
Helmholtz Configuration

Figure 3.18: **Axial and radial magnetic fields for optimized geometry.** We simulate the magnetic field profiles along the axial and radial directions for both Helmholtz and Anti-Helmholtz configurations. For the former, we are interested in inducing a large bias field for accessing magnetic Feshbach resonances of Cs. For the later, we would like an axial field gradient 10 G/cm and radial gradient 5 G/cm to obtain a wide capture range for the Science MOT.

where ΔT is temperature change in K. By comparison, our feedback circuit measures the current by measuring the voltage drop across an ultrastable sense resistor R_s with temperature coefficient of $\alpha = 20$ ppm/C° (Chapter 4). Hence, the ohmic heat, by way of its impact on α of the Cu wires, can cause a long-term drift over the steady-state values of the current.

To faciliate the heat transfer, we decided to pot the empty space of Fig. 3.17 with thermal epoxy. As the thermal conductivity of a typical thermal epoxy is ~ 40 times larger than air (Table 3.4), we expect an improvement in the heat transfer relative to free-space

Material	Air	Water	Epoxy 128	Solder	Copper
α [W/m $\cdot$ K] Air	0.1	0.6	4	36	385

Table 3.4: Comparison of thermal conductivities α.

convection cooling. Generally, a good thermal conductivity of an adhesive usually originates from the metallic filler particles in the epoxy (e.g., silver epoxy). In addition, for current fast switching on the inductive load of the magnet coils, we require high dielectric strength to avoid breakdown voltages. Among the electrically insulating thermal epoxies, I identified a ceramic potting compound (Contronics Epoxy 128) with the relevant specification in Table 3.5. Epoxy 128 has a maximum operating temperature up to $260°C$ with a viscosity similar to ketchup, allowing us to fill the holder with the thermal epoxy after coil winding.

3.3.3 Coil winding procedures

It is also critical to increase the surface area that connects the layers of the rectangular magnet wires. This allows efficient heat transfer from the interior of the coil to the outer thermal potting. With the increased surface area of the potting material, the heat is dissipated through natural convection. One practical challenge is to “transfer” the spools from the original coil holder to our Delrin holder with the Cu surfaces mating to the inner Cu layer. Indeed, rectangular Copper wires generally tend to twist around its axis if the spool is taken out without a guide that straightens out the wire. From the beginning, it was obvious that we had to construct some sort of a machine to wind the coils. Fig. 3.19 shows our manual coil winding machine, which mimics some of the functionalities of winding machines for electromagnets in hydroelectric waterfall generators. As Youn seok and I wind each layer, we constantly apply 5-min epoxies on on the outer layer to avoid air bubbles in the epoxy that become local heating sites. While we have not performed this idea, Markus Greiner group has applied a mixture of glass nanospheres and high-temperature pots between the “bare” OFHC magnet wire layers to improve the heat transfer (glass has a thermal conductivity 1W/m·K). The absence of polyamide protection layer means that the Copper provides larger thermal contact between the layers with the

Material	Max. temperature [F]	Viscosity (cps)
Epoxy 128	500 (260 C)	86,000

Table 3.5: Properties of epoxy 128

glass beads forming an electrically insulation spacer. This may be an interesting idea to revisit in the future for high-field experiments.

3.4 XHV-UHV chamber system

Fig. 3.20 shows the top and side CAD views of our custom XHV-UHV cluster system (See Fig. 3.1 for the tilted 3D view to gauge the overall design). The source chamber is pumped by Agilent starcell ion pump (45 L/s for N_2). Cesium ampoule is installed within an all-metal-gate valve under a tee, which makes up 2 of the 6 laser beams for the source MOT. The background Cs pressure is controlled both by the temperature of the ampoule and by the conductance of the gate valve. The differential pumping tube is installed on the conical reducer (which was later replaced to a 1.33-in bellow for stress relief between the

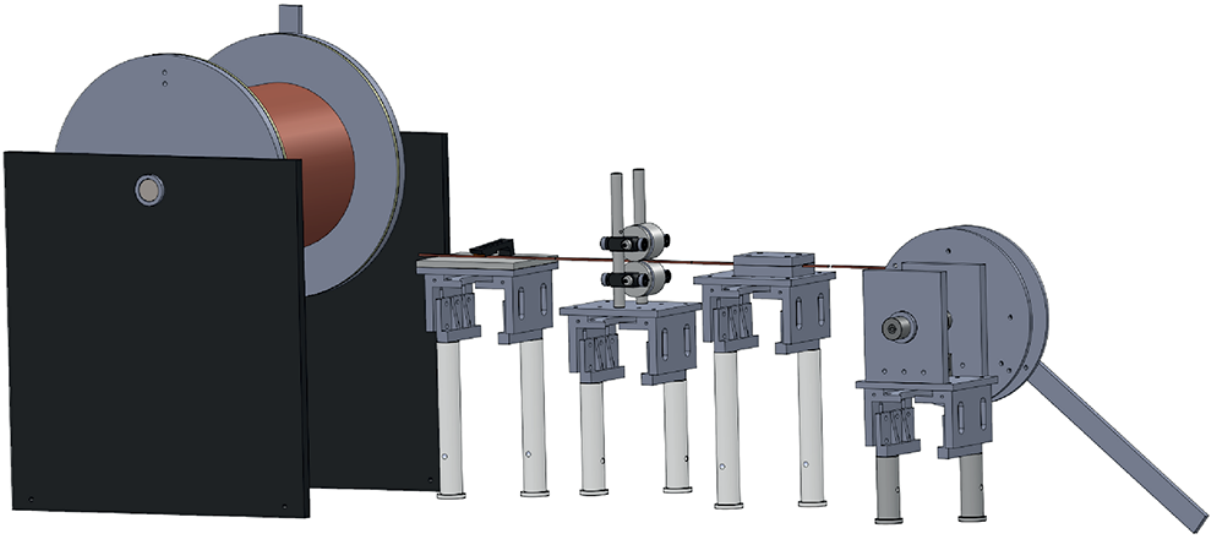

Figure 3.19: **Manual coil winding machine.** Our coil winding machine consists for 3 parts. The spool holder secures the heavy magnet wires (~ 30 kg), and the rotation is controlled by two small handles, which provide a backing force against the winding direction of the MOT coil holder. The Teflon block and silicone rubber clamp provide a breaking force to stop the winding action, if needed. The Delrin roller gives the tension for the magnet wire that is guided through the Aluminum wire guide block. The wire guide pushes against the rectangular wire with a gentle pressure, and it protected by multiple layers of Kapton tapes to protect the magnet wire from scratches.

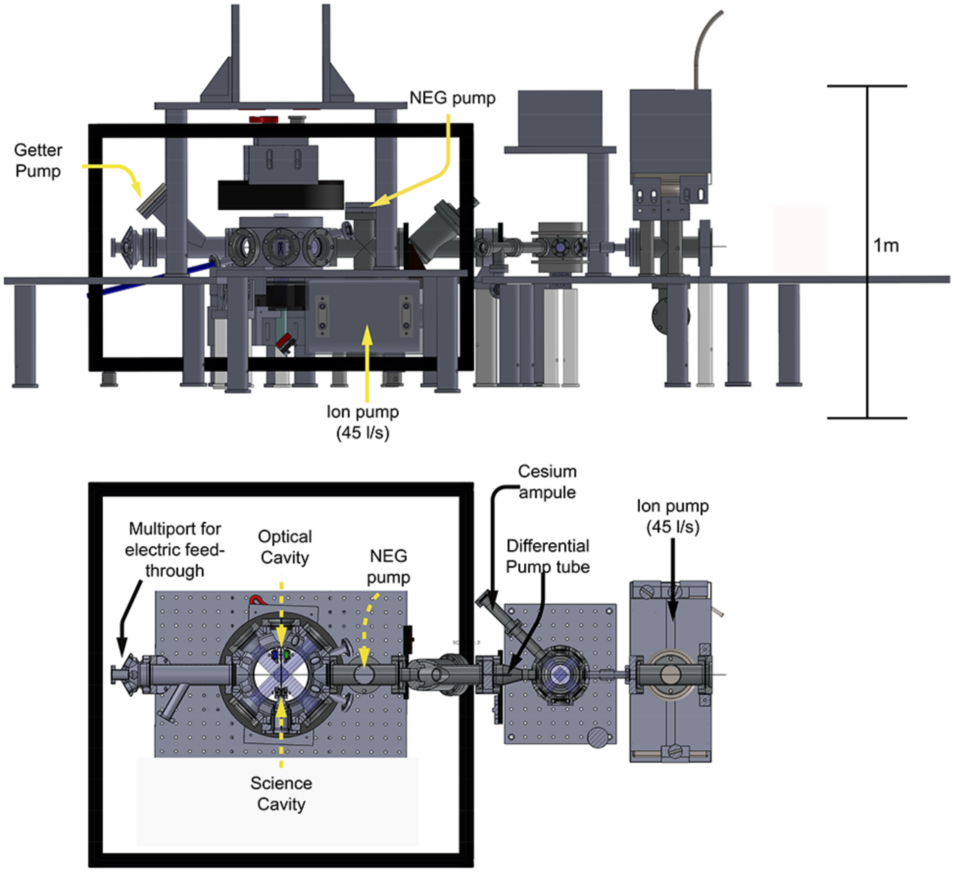

Figure 3.20: **Top and side CAD rendering of the UHV-XHV cluster system.** The top and side views of the UHV-XHV clustered system are displayed. The Source chamber is pumped by Agilent Starcell ion pump, and temperature-controlled Cs ampoule is connected with conductance-tunable valve. Magneto-optical trap (MOT) traps and cools Cs atoms to density $\sim 10^{10}/\mathrm{cm}^3$, before a pushing beam transports cold atoms through radiation pressure and dipole guiding. The geometry of the differential pumping tube is numerically optimized with the quantum trajectory simulation (Chapter 5). The Science chamber is pumped both by a modified Gamma Vacuum XHV pump, SAES non-evaporative-getter (NEG) and home-built TZV getter pumps. The cold atom fountain from the Source chamber is trapped at the center of the Science chamber by a secondary MOT. Electrically tunable lens moves the focus of a dipole trap to either the Science cavity platform or the "Rydberg-dot" cavity QED platform for further experimentation.

two chambers). The position, aperture size, and length of the differential pumping tube was optimized by the numerical simulation of the trajectories. Additionally, we installed an in-line all-metal gate valve to isolate the Science and Source chambers for vacuum diagnosis. The Science chamber is pumped by a modified Gamma Vacuum ion pump, together with SAES NEG pump. The main chamber has an angled tee that connects to a multiport feedthrough for controlling the blade electrodes and the PZTs for the many-body cavity QED and Rydberg quantum dot platforms (See Chapter 6), as well as to a home-made TZV getter pump to reach XHV level.

As a high-level description of the laser pulses and experimental sequences (further discussed in Chapter 4), we begin the experimental cycle by collecting cold Cs atoms in the Source chamber with a 6-beam magneto-optical trap (MOT) from the background to the Doppler-temperature $T_D \simeq 150\mu$K and MOT density $n \simeq 10^{10}$ atoms/cm^3 in the multiple scattering regime. We call this MOT, the Source MOT. The pushing beam exerts a dissipative radiation-pressure force on the cold atoms that create an atomic beam. As the atoms escape the Source MOT subsequently polarizes the atoms to the hyperfine $F = 3$ dark state through hyperfine optical pumping in the absence of repumping beams, which is then guided through a conservative optical potential created by the pushing laser itself. The geometry of Gaussian beam propagation of the pushing field as well as the laser parameters (detuning and strength) are determined with a quantum Monte-Carlo simulation of the open-system atomic trajectories in Chapter 5. This procedure allows us to have a continuous flux of a collimated transversely cold atomic fountain, which can be conveniently trapped in the XHV Science chamber for further manipulation.

In the Science chamber, the atomic beams are reconfined and laser-cooled in a secondary MOT (called the Science MOT). The trapped atoms are cooled through the standard sub-Doppler polarization-gradient (PG) cooling mechanism, and then spin-polarized to $F = 4$ state at $T \sim 30\mu$K. As the PG cooling takes place, an optical dipole trap (called the transport trap) is adiabatically switched on to localize the atoms to a movable optical trap with electrically-tunable liquid crystal lens. Depending on the type of experiment in Chapter 6, we move the focus of the transport trap either to the many-body cavity QED or the Rydberg quantum-dot platforms. The heating due to the recoil photons and parametric motional excitation is compensated by a tetrahedral MOT (called the t-MOT) that recools the atoms, followed by a sub-Doppler cooling with grey molasses to $T \sim 3\mu$K. The crossed FORT beams form an image plane for quantum-gas microscopy (QGM) and create a few 2D pancakes containing ultracold atoms, which we select the single plane through a microwave knife-edge evaporation. Ultracold atoms within this single layer can be cooled through a combination of degenerate Raman sideband cooling and run-away evaporation in an optical potential to reach Bose-Einstein condensate (BEC) phase. Holographic image projection through the QGM assembly creates an arbitrary potential landscape on the image plane at the magic wavelength condition for the experiment under consideration (e.g., quantum square lattice as in Chapter 2). Non-degenerate Raman sideband cooling will be employed for achieving the motional ground states along all three directions. Once all of these steps are achieved, only then the experiment could be carried out. For the actual experiment, we will require a dozen of additional ultrastable lasers spanning from 300 nm to 1100 nm (See Chapter 2 as an example and Chapter 4 for our laser systems).

In the following subsections, I provide the descriptions of the Source and Science chamber designs that achieve the objectives and optical access requirements stated above.

3.4.1 Source chamber

For the Source chamber, we have six trapping (red-detuned to the $|F=4\rangle \rightarrow |F'=5\rangle$ transition) and repumping ($|F=3\rangle \rightarrow |F'=4\rangle$) beams at 852 nm for the Source MOT, two probe beams ($|F=4\rangle \rightarrow |F'=5\rangle$ imaging excitation and $|F=4\rangle \rightarrow |F'=4\rangle$ pumping beams), and one pushing beam (blue-detuned to the $|F=4\rangle \rightarrow |F'=5\rangle$ transition). I used a spherical octagon chamber[z] with six 1.33-in CF and two 2.75-in CF UV viewports. For the pushing beam, I installed a 2.75-in CF viewports. All UHV viewports were custom-made from MPF products with BAAR ranges $600-1000$ nm (IAD coating).

For the Source MOT, I 3D-printed a coil holder out of a high-temperature resin from a Formlabs UV stereolithography system. This system produced 3D printed coil holders with smooth surfaces for heat dissipation and transfer. Because we only require 7 A to generate 10 G/cm, I used a circular AWG 14 magnet wire (winding number $(n_1, n_2) = (10, 6)$) for constructing the anti-Helmholtz coils. The MOT coil holder was directly secured onto the 2.75-in UHV viewports. Since we do need magnetic field control in the source chamber, we did not install external shim coils for field compensation. However, we have made a custom μ-metal shield enclosure (3-layer of Co-NETIC AA perfection annealed sheet from Magnetic Shield Corp.) for our Agilent ion pump (Engineering drawing can be found in the UQML cloudstation database).

As discussed in Section 3.1.4, we can control the background Cs pressure through the control of the conductance, due to the gettering characteristics of Cs atoms. For an equilibrium pressure of $P_{Cs} = 3 \times 10^{-8}$ Torr in the ampoule region at room temperature, we require a differential conductance of ≈ 100 in order to bring down the pressure in the

---

[z] We made two kinds of UHV Source chambers. The first was the stock Kimball Physics MCF275-SphOct-C2A8, and the second one was custom made from IVT Korea with identical dimensions.

Source chamber in the 10^{-10}-Torr range. In our chamber, I found that the pumping speed (N_2) of Agilent ion pump is limited to $C_{\text{ion}} = 8$ L/s at the center of the Source chamber. A fully opened 1.33-inch gate valve would have a full conductance of $C_{\text{amp}} = 4.7$ L/s, resulting into an estimated pressure of $P_{\text{source}} = (C_{\text{amp}}/C_{\text{ion}})P_{Cs} \simeq 1 \times 10^{-8}$ Torr. On the other hand, if we throttle the aperture of the gate-valve to be only 20% opened, we can dramatically reduce $C_{\text{amp}} = 0.05$ L/s, so that the Source chamber pressure will be 1×10^{-10} Torr. I have found experimentally that our method can consistently maintain the Source chamber pressure at the 1×10^{-10} Torr level, simply from conductance control.

3.4.2 Science chamber

Optical requirements

As illustrated in Fig. 3.21, at the center of the Science chamber, we illuminate collimated atomic beam with six Science MOT trapping (red-detuned to the $|F = 4\rangle \rightarrow |F' = 5\rangle$ transition) and repumping ($|F = 3\rangle \rightarrow |F' = 4\rangle$) beams for laser cooling and trapping, as well as two probe beams ($|F = 4\rangle \rightarrow |F' = 5\rangle$ imaging excitation and $|F = 4\rangle \rightarrow |F' = 4\rangle$ pumping beams) at 852 nm for running the daily diagnosis of the atomic density and temperature. These atoms are further cooled down by a built-in polarization-gradient cooling mechanism, following the termination of the local magnetic field. In order to compensate for the eddy currents around the Science chamber, Dr. Liu used an algorithm developed in Refs. [127, 128] with a home-built power MOSFET compensation circuitry (Engineering drawing can be found in the UQML cloudstation database) for field control beyond the damping constant $\tau = L/R$ given by an inductive load L. An 854 nm Optotune laser for the deterministic atom transport within the Science chamber (Chapter 5). These are largely low to medium power (< 500 mW) lasers with relatively low power density.

Near the location of the cavity platforms, however, we use high-power FORT beams (10W at 1071 nm), which are focused down to $\sim 100\mu$m, in addition to several medium powered Science lasers between 685 nm to 935 nm (Chapter 4). For the main experiment, we also use $\sim$ 1W sub-Hz 507-nm second-step excitation lasers and 3W 319-nm direct P-excitation UV lasers. Since I was concerned about the damage threshold and stray reflections for safety hazards, we were constrained to DUV fused silica viewports. The RF-magnetron sputter coatings resulted in very low scatter loss and porosity that addressed both the UHV concerns of atmospheric He diffusion as well as the optical concerns. In particular, when using UV lasers on optical viewports over prolonged periods, there are concerns for solarization effect, where the oxygen in the metal oxide layers of the AR coating can effectively be photodissociated below of bandgap frequency. Since Sc_2O_3 has a

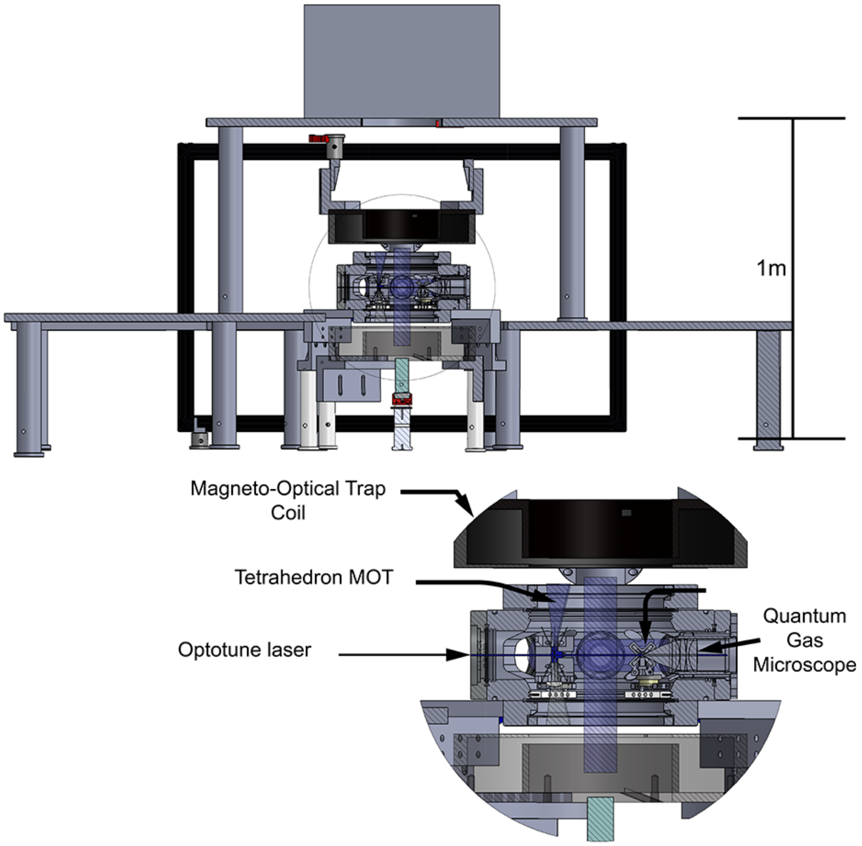

Figure 3.21: **Front CAD rendering of the UHV-XHV cluster system.** The front view of the UHV-XHV clustered system is displayed. After the secondary MOT traps and subsequently cools the Cs atoms in the Science chamber to sub-Doppler temperature $\sim 30\mu$K, an electrically tunable liquid crystal lens moves the focus of a dipole trap beam at $\lambda = 854$ nm to deterministically transport ultracold atoms to either the Science cavity platform or the Rydberg-dot cavity QED platform. Tetrahedral MOT beams recool the atoms for the parametric and recoil heatings during the conservative transport processes, followed by a grey molasses for sub-Doppler cooling to a few μK. Depending on the type of experiment, the atoms are further cooled in a FORT with non-degenerate sideband cooling to the 3D motional ground states or with dipole-based evaporative cooling runaway sequence for reaching the quantum degeneracy of superfluidity.

bandgap below 300 nm, we do not anticipate such long-term oxygen depletion on our AR

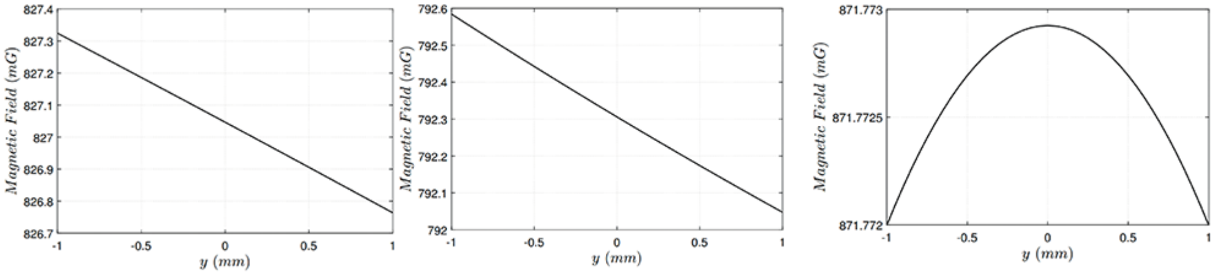

(a) Magnetic field Bx

(a) Magnetic field By

(a) Magnetic field Bz

Figure 3.22: **Bias field along the Science cavity axis.** For a 1-G magnetic field generated by a shim coil at the center of the Science chamber, we numerically simulate the local vector components of the magnetic field at the Science cavity.

coating (Section 3.1.6).

As further discussed in Chapter 6, all the materials for the Science cavity platforms were carefully examined by their optical properties when exposed to UV light under vacuum. Besides the concerns of their oxide dielectric layers, both Aluminum and Titanium are generally good conductive materials in UHV, but we do expect some photoelectrons generated by our 300 nm light for the Ti blade electrodes. These photoelectrons are by themselves not of concern, but they may be trapped on the surface oxides. We have considered the possibility of DC sputtering gold on the Ti electrodes, but we dropped this idea, due to the low adhesivity to Ti, where gold may sublime and redeposit to our pristine Science cavity mirrors during the bake out. Instead, I discuss a possible method of removal through a novel in-situ plasma cleaning procedure (See the next subsections). The single-crystal Sapphire holder is also a very good optical material with large bandgap suitable down to the X-ray frequencies, as they are common X-ray UHV viewports. However, we were not able to identify if our mirrors would survive the prolonged exposure to UV light. For IBS mirrors (SiO_2/Ta_2O_5 bilayers) commonly used in cavity QED and optical clock experiments, there is a known oxygen depletion effect for the Tantalum that reduces the optical finesse for UV mirrors. Fortunately, our metal oxide (not disclosed for proprietority) has a larger bandgap than that of Tantalum Oxide, but it remains to be seen in terms of its long-term impact. Utmost care is thereby taken during alignment stages not to scatter UV light onto the mirrors (again, considering the $1M development cost just for these mirrors!)

Bias coils

As shown in Figs. 3.20-3.21, we installed three pairs of bias coils centered around the Science chamber. We require 1% field homogeneity over $\delta x = 1$ cm both at the center of the chamber and at the cavity (approx. 3.5 cm). For a given coil dimension L, since the field homogeneity scales fractionally with $(\delta x/L)^2$, we made the square bias and shim coils of $L \simeq 1m$-scale length dimensions. The coil holders are made from non-magnetic 80-20 struts (Al6061-T6) with dimensions in Table 3.6. The numerically simulated magnetic field at the center of the Science cavity is shown in Fig. 3.22, where we assume a local field 1 G at the center of the Science chamber. We are not sensitive to the x-direction, as the atoms are localized by a cross-dipole trap to a 2D quantum gas, with atomic wavefunction localized to a few 10 nm. However, in the x- and z-directions, the atomic sites are localized within the field of view ($\sim 100\mu$m) of our quantum gas microscope system. The local magnetic field can be measured from an off-resonant stimulated Raman process with Hz level. If I assume a characteristic 2D atom cloud size of $A_c \sim (30\mu\text{m})^2$, we find that the field homogeneity is less than $\Delta B = 10\mu$G and Zeeman coherence time of $\tau \sim 1/(g_F \Delta B) = 300$ ms (without NMR-style dynamical decoupling), in addition to the precession timescales out of Zeeman clock states $|F, m_F = 0\rangle$.

We used a prototype satellite flux-gate magnetic field sensor (kindly donated from Sensorpia) for space navigation with μG sensitivity to record the stray magnetic field fluctuation. For direct measurements, we can perform co-propagating Raman spectroscopy on the trapped atoms that drives transform-limited two-photon resonant transitions between the Zeeman sublevels with one-photon detuning 10 GHz (Chapter 4). With ultra-narrow-line two-photon transition spectroscopy, I can identify the vectorial components of the local Zeeman fields with sub-Hz linewidth [129]. I refer to Appendix A of John Stockton's thesis for the practices of magnetic field nulling and the sources of magnetic field noise [130]. In addition, Prof. Choi designed the lasershelves with the particular attention to EMI shielding with Alucobond composite panels and full Aluminum construction which shield high-frequency >MHz magnetic fields generated by the electronics above the laser

Coil axis	Length	Height	Turns
X-axis	70 cm	45 cm	70
Y-axis	70 cm	45 cm	70
Z-axis	70 cm	70 cm	42

Table 3.6: Dimensions of the bias coil holder. The winding number was determined to provide ~ 1 G bias for 1 A.

shelves by 80 dB.

Cavity built-in RF plasma cleaning

The optical power densities for some of our Science lasers are sufficiently large to worry about laser-induced ionization and solarization effects (particularly for the 300-nm lasers) for the glasses that face the vacuum side of the chamber. These bound electrons will stay forever with no pathway for neutralization in an UHV environment, and may give rise to electric field inhomogeneity. These static stray fields, in addition to the time-dependent fields from the PZTs, are largely compensated by Ti blade electrodes (Chapter 6). However, it is known that thin oxide layers on Titanium may also be a source for bound photoelectrons that cannot simply conduct away to the ground. Furthermore, when a single Cs atom is deposited onto a glass dielectric, the modified workfunction of the adatom generates a sufficient large amount of artificial electric dipole moment that can be detected by BEC Bloch oscillation for the quantum reflection [131]. Surely, removing these local field homogeneities down to the single adatom level would be required in the long term.

I have developed a RF plasma cleaning method to etch away the oxide layers and to remove the Cs adatoms on the mirror surface. I only discuss the high-level description of our method. We use the Ti blade electrodes as the anode-cathode assembly in a RF sputter system, where we can localize the Argon plasma with our external anti-Helmholtz coils. As discussed in Chapter 6, we can arbitrarily control the full vectorial components of the local electric field pattern at the center of the cavity upto the second order $\vec{r}^2$, and it is possible for us to engineer the spatial gradients of the RF plasma with differential plasma etching rates between our Science cavity mirrors and the Titanium electrodes. The removal of metal oxides obviously requires much more ion momentum than the removal of bound Alkaline atom from the dielectric. We plan to use the auto-tuned matching circuit for our home-made RF/DC-magnetron sputter system to impedance match to the Ti blade electrodes. The gas feedthrough lines on the Science chamber in Fig. 3.20 are connect to a precision mass-flow-controller (MFC) through a differential leak valve, and the Science chamber system would backed by a turbo station to maintain $P \simeq 10^{-6}$ Torr to reduce the etching rates.

TZV NEG coating

Because of the home-built sputter system, we could do some crazy things incompatible with production system in a shared facility (like the RAC2 deposition systems). Using alloyed target is usually forbidden in production sputter sputter systems, as the sputtering process contaminates the main chamber. Sainath Motlakunta obtained a sputter target 1:1:1 TiZrV (TZV) alloy [132] bonded onto Cu backing plate (Matsurf Technologies), which mounts to our hybrid RF/DC AJA sputter guns. For the next UHV systems in UQML, I am considering to sputter coat the interior of the UHV chamber with TZV NEG materials. I refer to the thesis of Barcellini [133] and references therein for details of this coating recipe. I expect that these TZV NEG coatings would have large pumping speeds for H_2 atoms, low activation temperature ($190°C$), and strong passivation pumping layer to virtually limits the gas diffusion from the SS bulk.

Estimation and measurement of the ultimate pressure

In our Science chamber, we have one XHV Gamma Vacuum ion pump, and two NEG pumps. The combined conductance-limited pumping speed is $P \simeq 60$ L/s with an adjusted pumping speed (for H_2 and He atoms) $P_{\text{eff}} \simeq 6$ L/s. Using the outgassing rates for the materials in Table 3.1-3.2 and the estimated surface area from SolidWorks, we obtain the outgassing rate $Q_o = 2 \times 10^{-12}$ Torr·L/s and the viewport He permability rate $Q_{\text{He}} = 4 \times 10^{-15}$ Torr·L/s [134]. The resulting ultimate pressure is $P_u = (Q_o + Q_{\text{He}})/P_{\text{eff}} \simeq 3 \times 10^{-13}$ Torr, in line with our measured result 1×10^{-13} Torr.

Fig. 3.23 shows the final assembled UHV chamber that reached the target XHV pressure in 2016, after 6 months following the extensive procedures of UHV cleaning and passivation, pre-baking, activations, and baking cycles. Fig. 3.24 shows the second generation setup with a largely similar specification as the original system, and will be used for Rydberg atom experiments beyond the scope of this thesis. For the second generation system, we use the frit-fused UHV all-glass Science chamber, developed by Prof. Choi during his PhD at Caltech. Much of the laser systems in Chapter 4 will be shared with this new system in the future, but I will focus my work mainly on the first generation chamber.

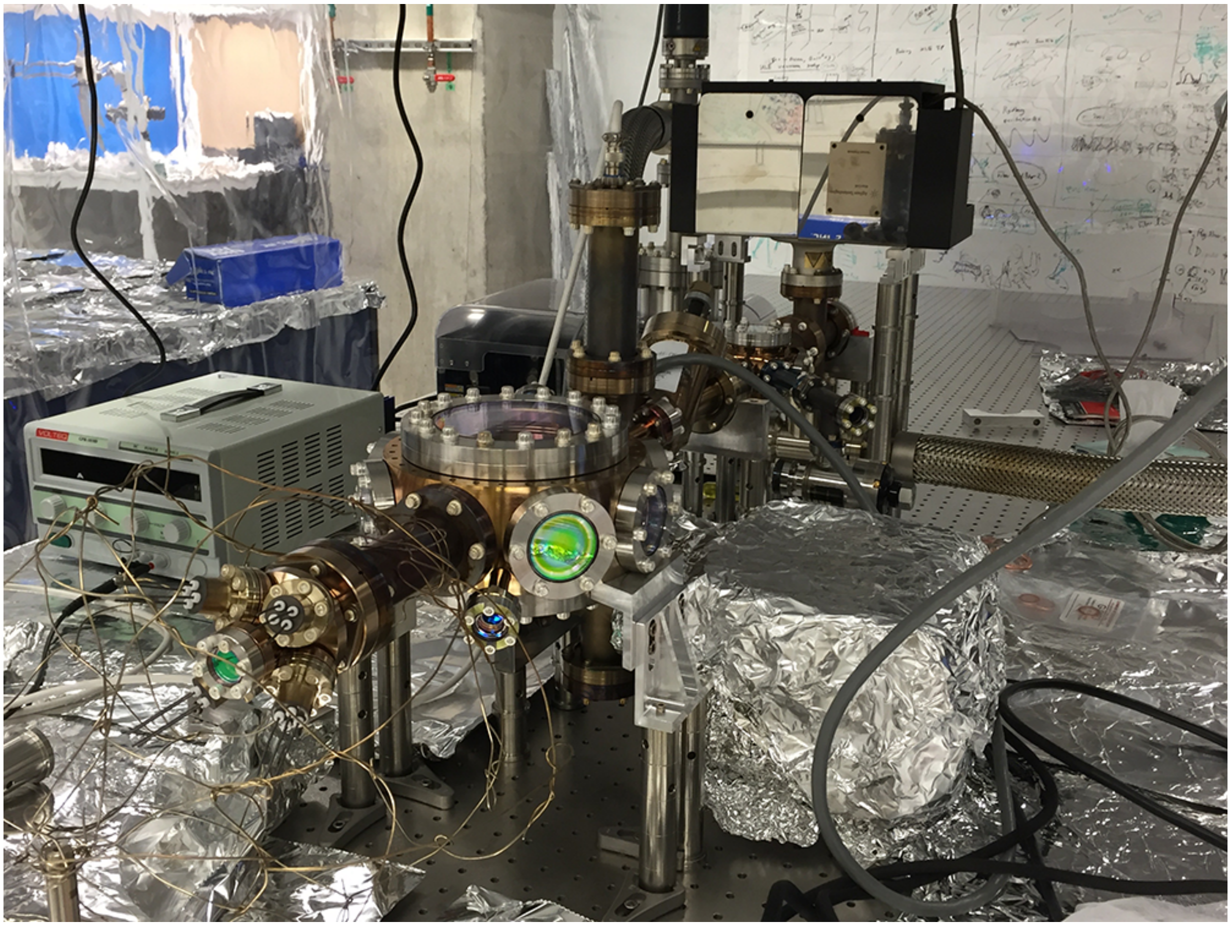

Figure 3.23: **Photo of the UHV-XHV chamber system in May 2016.** The first-generation chamber consists of non-magnetic SS components with vacuum passivation techniques detailed in the main text. We apply a Rainbow AR coating of UV-grade UHV viewports.

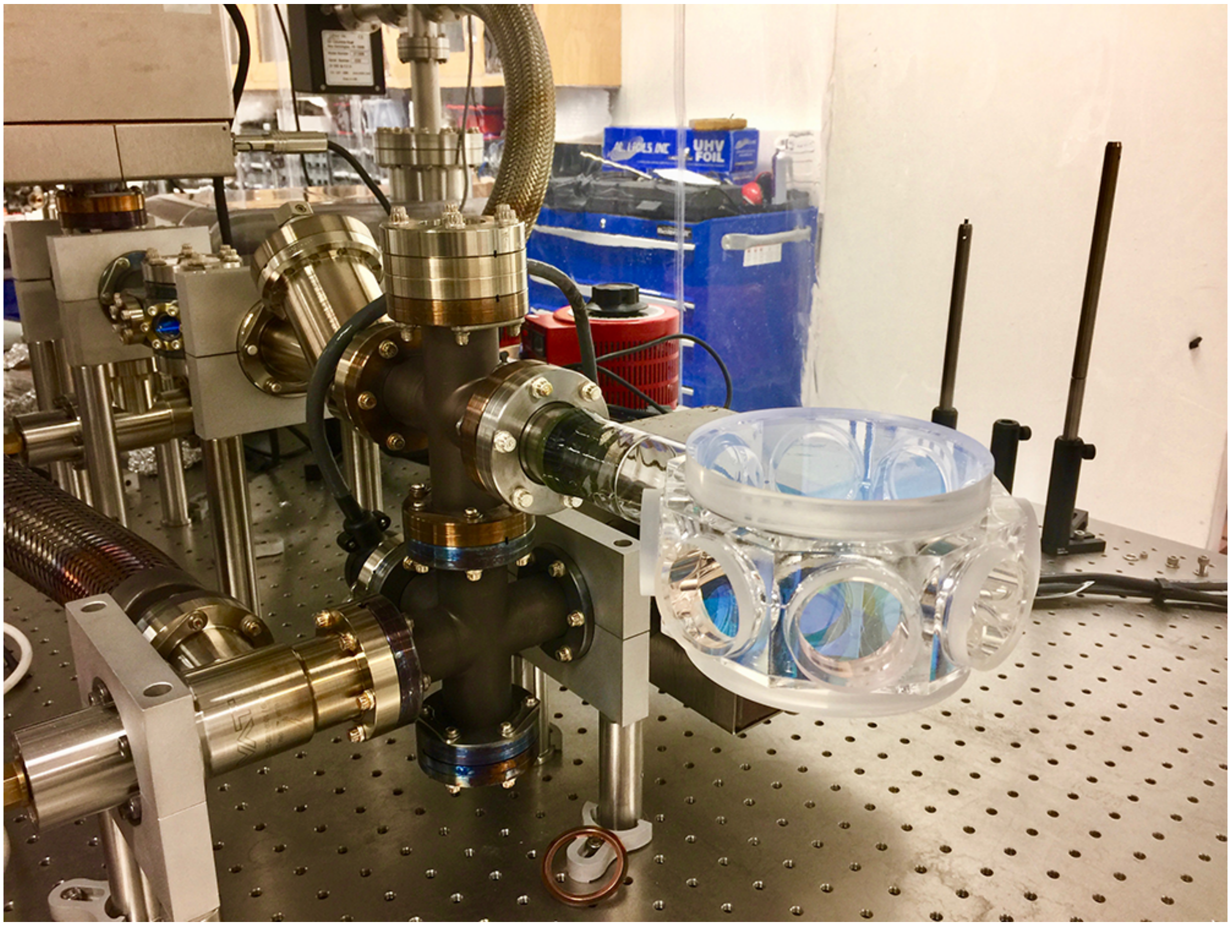

Figure 3.24: **Photo of the second generation UHV-XHV chamber system in November 2017.** The second-generation chamber uses an all-glass quartz UHV cell as the Science chamber. All glass cell has a wider viewing angle and optical access, as well as lower Eddy current current Zeeman inhomogeneous broadening.

Chapter 4

Laser and optical systems

In this chapter, I discuss a laser infrastructure, which consists of 1 Ti:S laser system, 20 phase-locked external cavity diode lasers (ECDL), 2 CW fiber lasers, and 3 stages of nonlinear wavelength conversions, with the most systems being home-made. Apart from the lasers responsible for cooling and trapping, because of the difference in energy scales, we developed highly specialized lasers that attempt to bridge the fields of optical cavity QED and Rydberg atoms. High-finesse low-loss optical cavities developed for cavity QED and optical clocks usually operate in the near-infra-red (NIR) regime, because of the reduced scatter $\propto 1/\lambda^4$ and absorption losses. On the other hand, Rydberg states usually require short-wavelength laser fields. In our laboratory, we currently have the capability to perform a direct Rydberg-$|nP_J\rangle$ excitation with a high-power laser at 319 nm (e.g., to create local spin ice rules (Chapter 2) or to perform a mesoscopic Rydberg quantum gate [135]) and to drive two-photon excitations to Rydberg $|nS_{1/2}\rangle, |nD_J\rangle$ states (507 nm frequency-doubled system), where we use the spectroscopic notation $|nL_J\rangle$ where n is the principal quantum number, L is the orbital angular momentum and J is the electron's total angular momentum. Because the transition matrix element is highly suppressed for Rydberg states, these high-power laser systems also need to be low-noise and narrow-linewidth (< 1 kHz). In addition, we would like to maintain the phase-stability of laser fields that are 100 THz apart over the dissipative lifetimes of the cavity polaritons ($\delta\tau \sim 100$ kHz in the photon regime, ~ 1 kHz/10 Hz in the Rydberg/ground-state atom regime). For instance, the cavity laser (852 nm) that probes the trapped atoms through the cavity should have a specific phase-amplitude relationship with respect to a high-power coupling field Ω_c (507 nm) that dresses the cavity polaritons with Rydberg states. Absent the access to optical frequency combs, my solution is to deploy a high-finesse optical reference cavity as a short-term clock over the relevant timescales $\delta\tau$, and to make use of transfer cavities and optical phase-lock loops to transfer the optical coherences across the spectrum. In the short term future, I plan to deploy a portable Iodine optical molecular clock at 507 nm as our absolute frequency standard, where it is routine to achieve Alan variances $\sim 10^{-14}$.

These challenges and others have driven us to develop our own home-built systems, from passive mechanical design, active optoelectronic components (resonant electro-optic modulator (EOM), low-noise avalanche photodiode (APD) and photodetectors) to the laser control electronics (high-bandwidth Proportional, Integral, Derivative (PID) circuitries with auto-relock capabilities, computer-controlled digital phase-locked loop for phase-amplitude control of over dozens of lasers down to 0.1 Hz level), and to high-finesse optical cavities. While many of these systems interface with dedicated laboratory control systems and softwares, I will not discuss the work on the Field-Programmable gate array (FPGA) control systems responsible for the real-time control of the phase-amplitudes of our laser systems and for image processing techniques out of proprietority.

4.1 Scientific objective

Before I delve onto the specific technical projects, let me take a brief moment to describe how our thought process evolved with the goal of measuring a gapless photon in a quantum spin ice system. In the beginning, there were a lot of confusion in the laboratory as to the technical requirement of the laser systems. While we do not directly involve the kinetics of the atoms, the interaction energies and the linear-like dispersion of the artificial photon extends close to $J_{\text{ring}} \sim 10$ kHz, and our temperature requirement is still quite stringent. In addition, since the dynamical spin structural factor is measured by mapping the emergent photons into real cavity photons, the laser pump fields that stimulate this process would need to be narrow linewidth. Furthermore, because the U(1) spin liquids are gapless, it may require us to build quantum systems that are sufficiently large enough to display a macroscopic phase in a low entropy lattice. Indeed, a single site missing would cause the breaking of the spin ice symmetry, thereby requiring lower noise lasers for the optical traps and sideband cooling.

In this regards, my work with Dr. Chang Liu on the design and fabrication of laser systems was quite related from the beginning to the atom assembly and quantum-gas imaging projects that have been led by Dr. Mahmood Sabooni and Youn Seok Lee in our group. There, they have been working on new methods with holographic superpixel algorithm and GPU accelerated algorithms to create real-time rearrangeable 2D optical potentials and feedback through a quantum-gas microscope. Yet, it was also a challenge

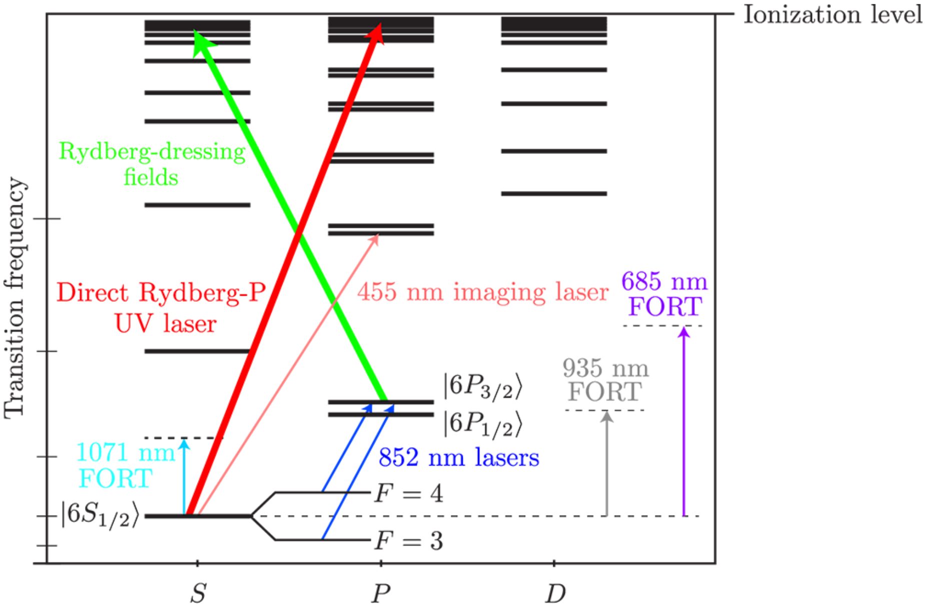

Figure 4.1: **Laser systems for the main experiment.** Details are given in the main text.

to select wavelengths for these traps, as our experiment is inherently an optically driven-dissipative one. At the magic wavelengths of D_2-line of Cs at 687 nm and 935 nm, not only could we avoid line broadening effect that dilutes the cavity coupling rate g_0, but also prevent trap fluctuations as the atoms are radiatively cooled (e.g., optical molasses or polarization-gradient cooling). While the linewidth of the laser for most cooling processes (except for non-degenerate Raman sideband cooling) is hardly a variable that would matter, the choice of the wavelength for the far-off-resonant trap (FORT) is more complex for our experiment, because photon scattering is a necessary ingredient of our experiment. Hence, Prof. Choi, Dr. Liu and I have made an extensive survey in the beginning of the laboratory to conclude with a set of wavelengths by considering not only noise-induced parametric and recoil heating effects, and optical power, but also considering the hybrid nature of our experiment, where the atoms are intrinsically coupled to the cavity fields. I will return to this issue in Chapter 6 again, as the choice of our intracavity and DMD FORT beams is related to the cavity design.

4.1.1 Reference clocks

In our laboratory, we have three main reference clocks – One in the microwave domain, and the other two in the optical domain. First, all of the RF and microwave pulses are phase-reference respect to a Rb microwave master clock. For the microwave, we have a secondary 10 GHz clock with precision dual dielectric resonating oscillator (phase lock to the main master clock).For the RF domain, we take the frequency summed outputs of the Rb clock with a phase-lock loop voltage controlled oscillator (PLL VCO). Most of these outputs are controlled through an FPGA laboratory system, and some are directly generated from digital direct synthesizer (DDS) arrays with the input oscillator locked to the 10 GHz clock. In the optical domain, we use a home-built cay-eye interference-filter (IF) feedback laser (called the IF laser 1) and stabilize to a 100 kHz reference cavity, which is then subsequently referenced to the $|F = 4\rangle \to |F = 5'\rangle$ cycling transition of Cs in a modulation-transfer spectroscopy setup. This clock is used for the phase stabilization of all the external cavity diode lasers (ECDL) for D_2-line laser cooling and trapping, but not for the much more sensitive main experimental beams.

The main clock that drives the main experiment, described in Fig. 4.1, is currently a triple-coated ATF-6010-4 ultra-low-expansion (ULE) cavity (called ULE cavity) with finesse $F \simeq 100$k at $\simeq 1071$ nm, $\simeq 400$k at 1015 nm, $\simeq 100$k at 935 nm, housed in a UHV chamber system. IF lasers stabilized to this ULE cavity are the "optical" clocks that transfer the phase coherence to other lasers in the same wavelength range (called IF-λ laser). Due to the ULE aging effect, this serves as the short-term optical clock that references its optical coherence to the other science lasers operating in 852 nm with a secondary tunable ULE cavity (called the ULE transfer cavity) with Finesse $F \simeq 100$k at 935 nm and $F \simeq 300$k at 852 nm. We have some short-term future plans to deploy a room-temperature Iodine molecular optical clock near the ionization threshold at 507 nm, where there are ultranarrow lines that could be probed to achieve optical $Q \simeq 10^{14}$ [136]. This would provide an absolute frequency standard, easing the hassles of realigning the PLL lock frequency of the master laser. Several other thermally-compensated optical cavities are used throughout the laboratory for stabilization of FORT lasers and ASE filtering. The design of this cavity, originally based on J. Barry's thesis, will be discussed later [137].

4.1.2 Experimental sequence

As shown in Fig. 4.3, we begin our experiment by collecting $\simeq 10^{10}$ cold Cs atoms in our source chamber with a magneto-optical trap (MOT) for 3 s in the multiple scattering regime at the Doppler temperature $\sim 150\mu$K. The MOT trapping beams ($P = 20$ mW, detuned by

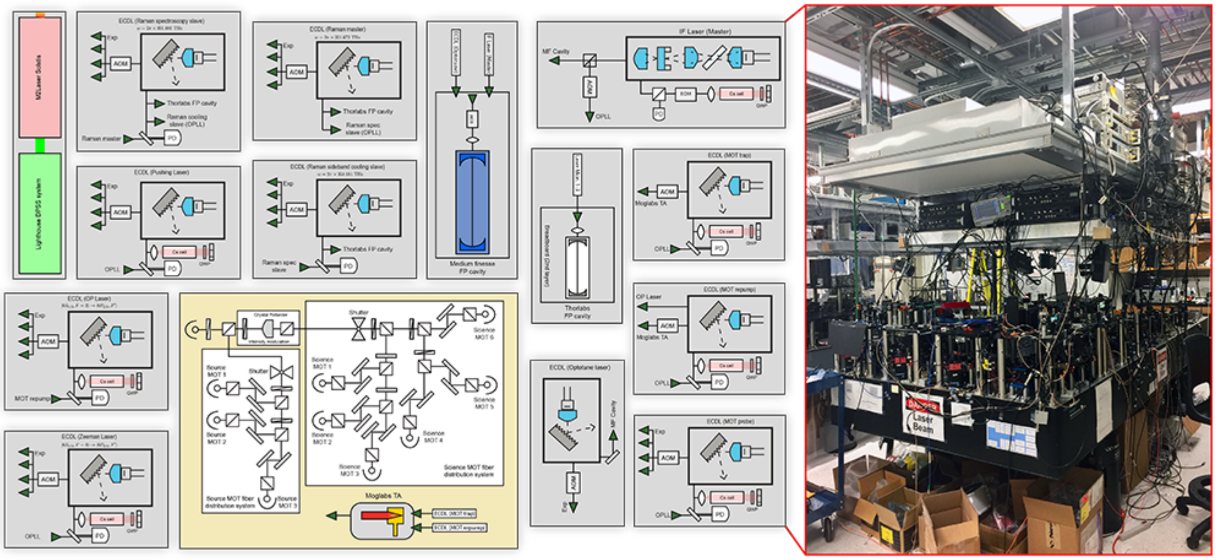

Figure 4.2: **Laser systems for cooling and trapping**. We illustrate our home-built laser systems currently installed on optical table A. IF master laser acts as the reference clock laser for all other lasers on table A through optical phase-lock loops and frequency-phase detectors with arbitrary offset frequencies upto ± 600 MHz. Lasers on this table are used for: Source/Science MOTs, tetrahedral molasses (MOPA pumped by a trapping laser near $|F = 4\rangle \rightarrow |F = 5'\rangle$ transition and a repumping laser near $|F = 3\rangle \rightarrow |F = 4'\rangle$ transition), probing and imaging laser ($|F = 4\rangle \rightarrow |F = 5'\rangle$ transition), pushing beam (1 GHz red detuned from $|F = 4\rangle \rightarrow |F = 5'\rangle$ transition), two hyperfine pumping lasers ($|F = 4\rangle \rightarrow |F = 3'\rangle$ and $|F = 3\rangle \rightarrow |F = 4'\rangle$ transitions, respectively), clock-state pumping (π-polarized $|F = 4\rangle \rightarrow |F = 4'\rangle$), degenerate Raman sideband cooling (10 GHz detuned from $|6P_{3/2}\rangle$ transition), non-degenerate Raman pairs (50 GHz $|6P_{3/2}\rangle$ transition, and phase-locked each other), and transport laser (854 nm).

Δ_t from $|6S_{1/2}, F = 4\rangle \leftrightarrow |6P_{3/2}, F = 5\rangle$ cycling transition) were derived from a Moglabs Tapered Amplifier, which is seeded by a trapping ECDL. The repumper (detuned by Δ_r from $|6S_{1/2}, F = 3\rangle \leftrightarrow |6P_{3/2}, F = 4\rangle$) is injected into the same fiber distribution network. The intensities and frequencies of these laser and all subsequent laser systems discussed are all computer-controlled with our FPGA laboratory control systems that interface with the OPLL feedback loops and the AOMs over a wide range (covering 30 dB dynamic range for intensity, and 600 MHz for the phase-frequency lock of the lasers). The output of the TA is terminated at the beginning of the experimental cycle by a home-made shutter [138].

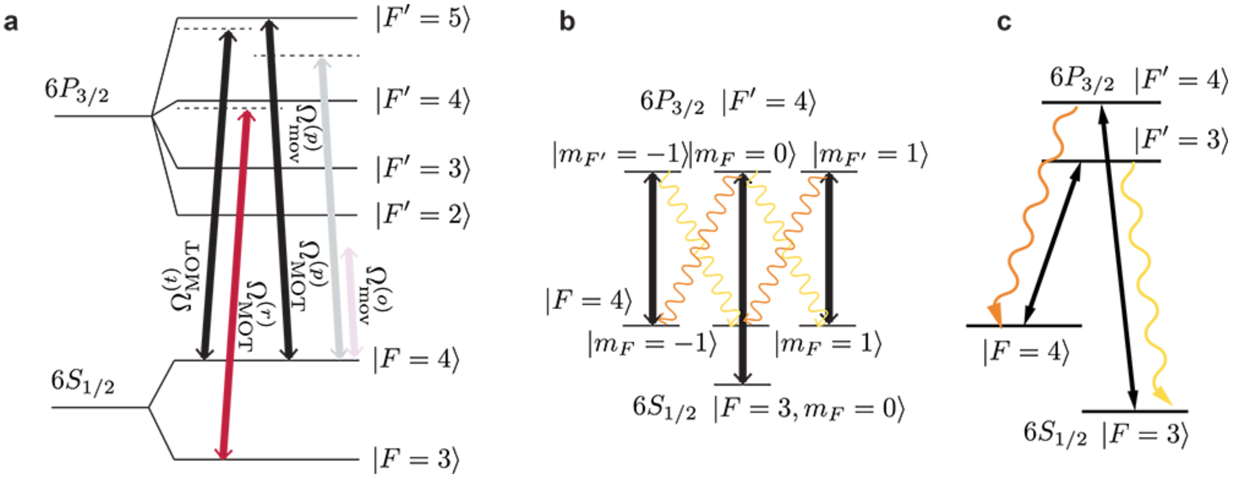

Figure 4.3: **Laser cooling and trapping beams.** **a**. Level diagram for the cooling and atom transport lasers. The MOT lasers consist of the trapping $\Omega^{(t)}_{\mathrm{MOT}}$ and repumper beams $\Omega^{(r)}_{\mathrm{MOT}}$. The laser $\Omega^{(p)}_{\mathrm{mov}}$ ($\Omega^{(o)}_{\mathrm{mov}}$) is used for the atom transfer from the Source MOT (the center of the Science chamber) to the Science MOT (to the center of the experimental platform in the Science chamber). **b**. Zeeman pumping to the clock state $|F=4, m_F=0\rangle$. **c**. Optical pumping between the hyperfine levels of $6S_{1/2}$.

As further discussed in Chapter 5, a pushing laser $\Omega^{(p)}_{mov}$ with red detuning is turned on through the MOT loading process to form a continuous flux of cold atoms. The combined force of radiation pressure from MOT beams and the pushing laser accelerates the Cs atoms with initial velocities 7 m/s. Upon ejection from the MOT region, the atoms only see the pushing laser and is subsequently optically pumped to $F=3$ state. Because of the larger detuning $\simeq 9$ GHz, the moving atoms experience largely a conservative potential of the pushing beam. By designing the appropriate geometry in Chapter 5, the atomic flux is collimated and pass through the differential pumping tube.

In the Science chamber, the atomic beams are captured and laser-cooled in a secondary 6-beam MOT (called the Science MOT) in the multiple scattering regime with trapping beam ($P = 30$ mW, detuned by Δ_t from $|6S_{1/2}, F=4\rangle \leftrightarrow |6P_{3/2}, F=5\rangle$ cycling transition) and a repumper ($P = 3$ mW at $|6S_{1/2}, F=3\rangle \leftrightarrow |6P_{3/2}, F=4\rangle$ transition). The trapped atoms are first compressed in a compressed MOT by increasing the magnetic field gradient to $30G/cm$ and reducing the repumper intensity to densities $n \sim 10^{12}/cm^3$, and it is subsequently cooled through the standard sub-Doppler polarization-gradient (PG) cooling mechanism, where I achieved $\sim 30\mu$K. The intensity control is performed by a magneto-optical filter, allowing for smooth power control from a current loop generated by the FPGA

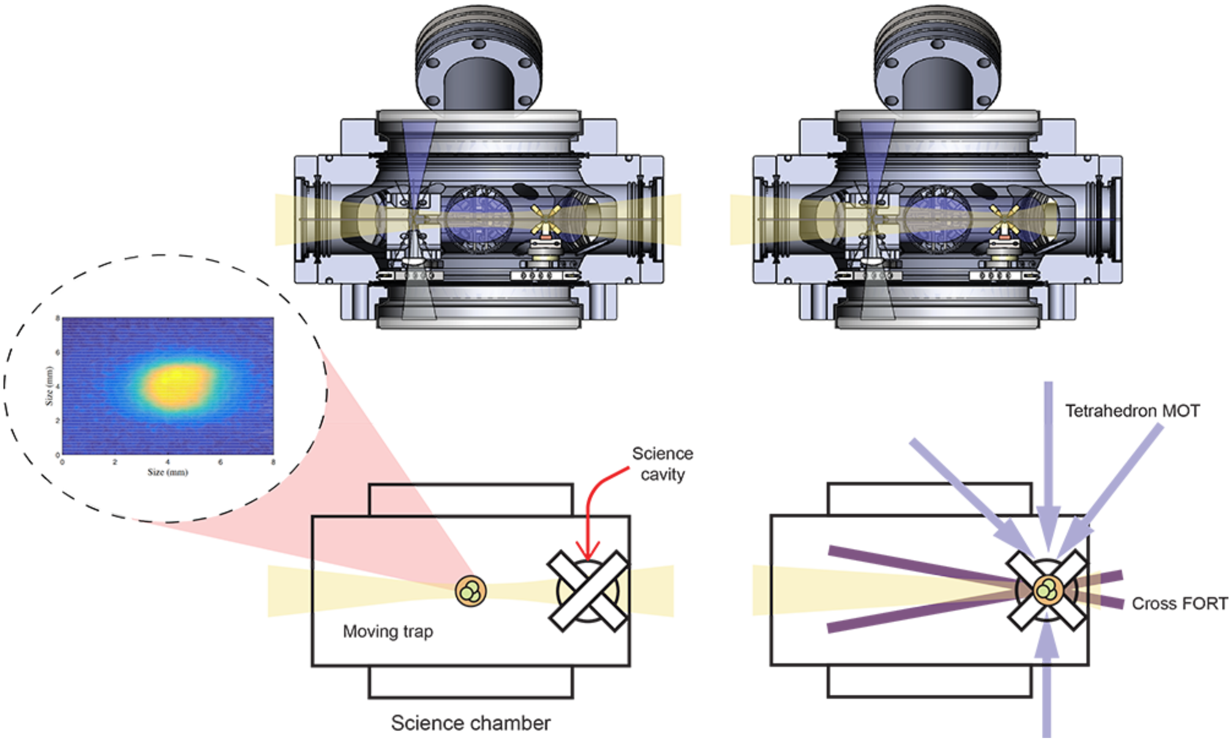

Figure 4.4: **Transport dipole trap with electrically tunable lens.** Moving optical trap is deployed to determinstically transport the Cs atoms from the center of the Science chamber to the cavity platforms. With an electrically tunable lens, the focal point of the optical trap can be dynamically tuned over ≥ 10 cm. From our estimation, the primary source of heating with the recoil scattering. The transproted atoms are then re-cooled down to $1\mu K$ from the grey molasses at the cavity center and further cooled in a crossed FORT through sideband cooling techniques.

control system. In terms of atom-transport, I have only proceeded up to this step, but have completed all the remaining laser systems to move cold atoms to the main experimental station.

At the end of the PG cooling step, I plan to adiabatically turn on the optical dipole trap (854 nm ECDL with resonant portion of ASE filtered by a 100-kHz thermally-compensated filter cavity with $F \simeq 6$k). With the electrically tunable Optotune lens, I will move the focus of the conservative trap to the either experimental stations. The heating due to the recoil scattering and parametric motional excitation is compensated by a tetrahedral

MOT (called the t-MOT) with same level configuration as Fig. 4.3 that recools the atoms within the station and prepares the atoms to $F = 4$ state. In addition, because of the geometry of the transport trap beam, the atoms will be elongated transverse to the cavity axis. According to our quantum-trajectory simulations, recooling atoms to the Doppler temperature would restore the cloud size $\sim (100\mu m) \times (20\mu m)^2$ (Chapter 5) [a].

The tetrahedral beams are then switched from the red-MOT to the grey molasses configuration [139]. Because of the wide tunability with our OPLL, the change of the roles between the trapping and repumping lasers are smoothly possible within the same optical setup in 10 ms. Unlike conventional polarization-gradient cooling mechanism in a MOT, in grey molasses, the cooling laser is surprisingly blue-detuned,δ, between $J \to J = J$ or $J-1$ where one or more internal ground state manifold is in dark state. Atoms accumulates in dark states where atomic potential is not changing along propagation direction. With the motional coupling with bright state, at $\delta = \Delta\omega_p$ where $\Delta\omega_p$ is a potential difference between the dark state and nearby bright state, atoms are optically pumped to bright state and is decayed back to dark state with a low momenta of a few $\hbar k$. Through this dark state cooling mechanism, it is possible to realize higher number density of atom from low photon scattering rate and suppressed interaction between atoms such as photon re-absorption and short ranage resonant dipole-dipole interaction. For instance, in Ref. [140], the authors have achieved $T \simeq 1\mu$K only with a grey molasses.

We use a crossed dipole trap to form an image plane for the quantum-gas microscope (QGM) with the 2D pancake aligned at the focus of the objective. Because of the small angle 20° between the two beams, the position of the pancakes are largely insensitive and it is possible to select a single lattice plane through microwave knife-edge techniques. For the dipole trap, we have split a small portion $\sim$ 300 mW from the 10 W NKT Photonics fiber laser system at 1071 nm used for synthesizing the 309-nm UV beam (more on this point in the next section). We will then perform a non-degenerate sideband cooling with Raman pairs detuned by 50 GHz from the $|6S_{1/2}\rangle \leftrightarrow |6P_{3/2}\rangle$ transition. At this point, it is possible for us to implement a runaway evaporation near Feshbach resonance at 20.8 G that controls the ratio of elastic-to-inelastic collision rates of Cs. A runaway evaporation enables a fast and efficient form of atom cooling without a severe decrease in the elastic collision rates. Different from typical evaporative cooling which reduces the optical trapping potential, external magnetic field gradient tilts and levitate the optical trap in order to cool and gather cold atoms. The merit of runaway evaporation is that trap frequency is not significantly affected by the reduced trap potential and it results in the same or larger elastic collisional

---

[a] As the main experimental platforms are displaced from the center of the Science chamber by only 3.5 cm, we have decided with this transport method (due to the absence of optical access from the other side, it was impossible for us to consider an optical conveyor belt).

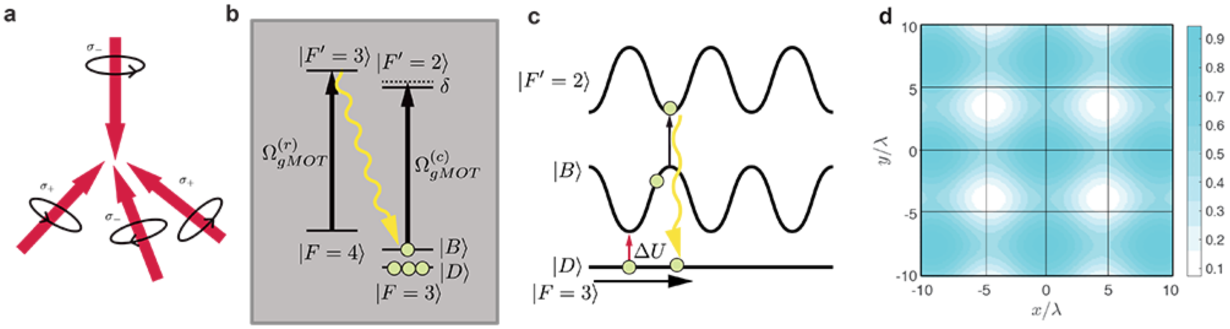

Figure 4.5: **Sub-Doppler mechanism of grey molasses in a tetrahedral MOT. a**. Four-beam configuration of grey molasses. It is called a tetrahedron molasses when all lasers have same angle. From theoretical calculation, it has been shown that cooling performance is insensitive to angle between lasers except for a certain critical angle. **b**. Laser diagram of grey molasses. A repump laser $\Omega^{(r)}_{\mathrm{gMOT}}$ prepares the atoms to $|F=3\rangle$. A blue-detuned cooling laser $\Omega^{(c)}_{\mathrm{gMOT}}$ drives the transition $|F=3\rangle \rightarrow |F'=2\rangle$. The two lowest Zeeman levels of the ground state are nearly in the dark state $|D\rangle$ and atoms accumulates in $|D\rangle$ with low momentum $\simeq \hbar k$ after a few cooling cycles. In a grey molasses, these dark states can be effectively turned bright, so that the atoms continue to experience efficient cooling. **c**. A polarization gradient (PG) cooling with nearly dark states. When the detuning δ of $\Omega^{(c)}_{\mathrm{gMOT}}$ matches with optical potential difference ΔU between the bright $|B\rangle$ and dark $|D\rangle$ states, the trapped atoms are optically pumped to the bright state $|B\rangle$ and PG cooling continues to occur. At last, atoms are collapsed to $|D\rangle$ and the number density of atom N is enhanced compared to the standard bright (red-detuned) molasses. **d**. Analytic calculation displaying the polarization-gradients caused by the four-beam configuration for our specific geometry.

rate, thereby shortening the cooling time. For Cs, in Ref. [125], the number density of atom after a runaway evaporation can be nearly $n \simeq 1.5 \times 10^{13}$ cm^{-3} within 5 s of entire cooling time by linearly increasing the magnetic field. During the process, the absolute value of the magnetic field is kept at 20.8 G where three body collision rate is suppressed to 1/40 Hz without affecting the trap confinement. Our electromagnet and controller supports such adiabatic processes at the center of the Science cavity. Examining few-body physics in a coupled atom-field system as in cavity QED system may be of interest in the future. As further discussed in Chapter 6, Dr. Sabooni will use superpixel algorithm to holographically project the potential landscape through the QGM, thereby pinning down the atoms on the lattice plane of the crossed dipole trap. For the Rydberg dot experiment,

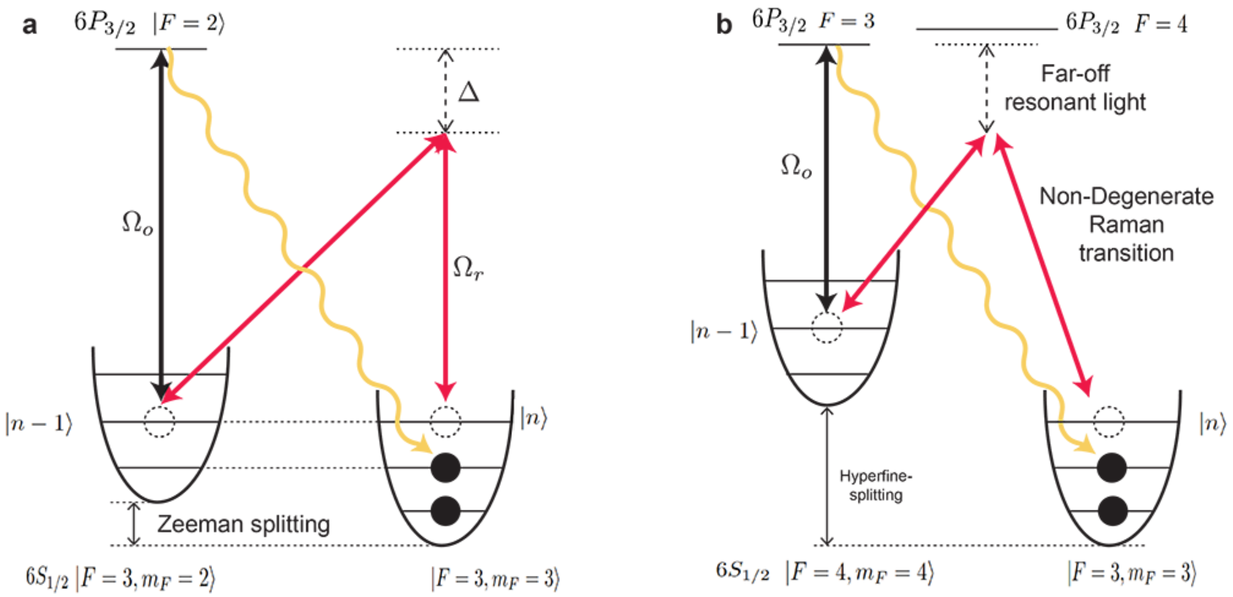

Figure 4.6: **Laser diagram of Raman sideband cooling.** **a**. Degenerate Raman sideband cooling. Two Zeeman sublevels of $|F=3\rangle$ state have degenerate motional states with an external B field. A single laser Ω_r drives a degenerate Raman coupling between $|3,3,n\rangle \leftrightarrow |3,2,n-1\rangle$. The laser Ω_p (resonant with $6S_{1/2}|F=3, m_F=2\rangle \leftrightarrow |F'=2\rangle$) optically pumps the atoms to the dark state $|3,3,n=0\rangle$. **b**. Non-degenerate Raman sideband cooling. Far-detuned Raman fields Ω_r drive $|F=3, m_F=3\rangle \leftrightarrow |F=4, m_F=4\rangle$ transition with two phase-coherent fields. Ω_o drives atoms to the $|F=3, m_F=3\rangle$ state, where the trap lifetime is significantly longer than $F=4$ [141].

we will trap the atoms using the intracavity field at the red magic wavelength 935 nm, as it is not necessary for us to confine the atoms in a 2D plane.

4.1.3 Science lasers

Once the atoms are pinned down on the 2D DMD lattice potential, we can perform a wide range of experiments. An important theme of my thesis is to go after the quantum spin liquid phase of the quantum spin ice models. So what follows here are the descriptions (and names) of the laser systems for this experiment in mind. As our infrastructure is pretty much a “machine”, we could readily devise the experimental parameters (e.g., laser frequencies) over a wide range and dynamically switch the roles of some lasers without

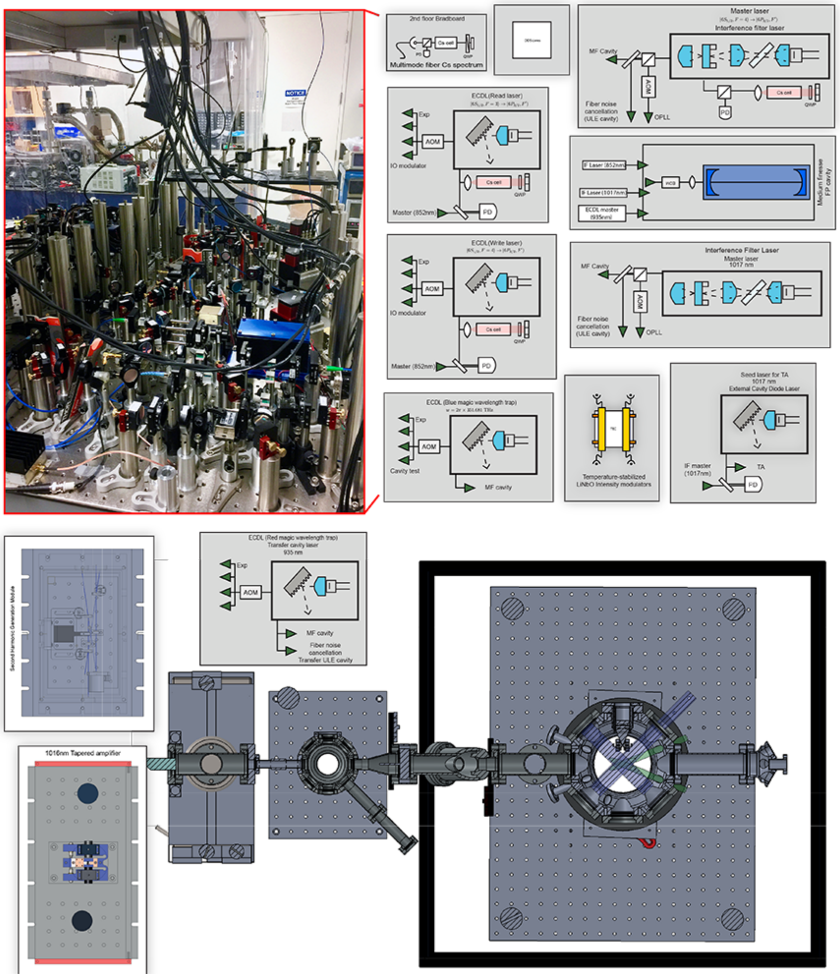

Figure 4.7: **Science lasers.** We illustrate our home-built laser system on optical table B. Unlike table A, where a single IF-master laser is used for the reference clock, the ULE cavity and the ULE transfer cavity are used to realize the phase coherence across the broad spectrum of $\simeq 240THz$ on table B. IF-935 master laser is locked to ULE and the ULE transfer cavity in tandem and transfers the optical phase coherence from IF-1017 master to IF-852 master laser. With the OPLL and frequency-doubling module, the static phase relationship is imposed between the green laser (508 nm) and cavity field (852 nm), enabling two-photon Rydberg transition.

much physical modifications.

Lasers for Cavity QED and low-energy states of Cs atoms

As shown in Fig. 4.1, Cs atoms are localized in the Science cavity by a combination of a 300 mW crossed dipole trap and a DMD potential (Chapter 6). The crossed dipole trap originates from a low-noise NKT Photonics Y10-NWR master oscillator (Yb-doped CW fiber laser, 100-kHz PZT bandwidth, tunability: 10 nm) at 1071 nm, which saturates a 10W Keopsys fiber amplifier (CYFA-PB-BW1-PM-40) [b]. The FORT laser illuminating the DMD can be either 935 nm red-detuned laser, or 687-nm blue-detuned laser with an inverted mask on the Fourier plane of the DMD. Both of these wavelengths are the magic wavelengths for Cs D_2 transitions, where we expect residual shift less than 1 kHz (differential shift between the hyperfine clock states is minimal well below 1 Hz in both cases). Because of the photoionization effects of Rydberg atoms, we will likely utilize the 687-nm blue-detuned laser, where the ground-state atoms are localized in the dark (intensity minima of the DMD potential). We also have the option to trap atoms using the intracavity field, as our Science cavity is also coated for 687 nm and 935 nm with an optical finesse $F \simeq 5\text{k}$. The advantage of this approach is that the intracavity field fluctuation is suppressed by the response function of the optical cavity, exhibiting remarkably low intensity noise and cavity-enhanced trap depths.

It is instructive to note that the optical dipole potentials of Rydberg states are almost always repulsive, because of the unavailability of higher optical states. Yet, it is surprisingly possible to capture the Cs Rydberg atoms at 687 nm. Rydberg atoms have large orbital radius, and cannot be well described by a point dipole. The breakdown of the dipole approximation implies that the Rydberg levels are perturbed not only by the dipole potential from the ground states but also by the ponderomotive potential of the scattering modes of free-electrons, dressed by the optical fields. By combining these two perturbation effects, we can actually optically trap Rydberg states at 687 nm [142]! Further reduction of the loss rate can then be achieved with time-periodic intensity modulation of the optical trap at frequencies well beyond the trap frequency $w_t \simeq 50$ kHz.

As briefly mentioned in section 4.1.1, our master IF-852 laser is used as a reference laser for the read ($|F=3\rangle \rightarrow |F=4\rangle$ transition) and write lasers ($|F=4\rangle \rightarrow |F=4\rangle$ transition). These ECDLs are eventually phase-locked to the main master IF-852 with relative linewidth below 0.1 Hz (not accounting for the Doppler shifts) with computer-controllable OPLL with the phase parked at a 100mrad precision. The read laser is used as the coupling field Ω_c in the quantum spin ice model (Chapter 2), while the write laser is used for the probing field that converts dynamical spin correlators into correlated stream of

---

[b] The overall system has a linewidth 1 kHz and residual intensity noise $\sim$ 40 dB with our intensity stabilization circuit.

cavity photons. For both lasers, we use EOspace 20 Gbs LN high-ER intensity modulators. We also have a 455-nm imaging laser, which we use for exciting atoms to $|7P_{3/2}\rangle$. We plan to use this system for future experiments requiring high-resolution microscopy (most likely experiments that only involve ground-state Cs atoms). The Science cavity is stabilized to a 935-nm slave laser, which is phase-locked to the master IF-935.

Rydberg lasers

A high-power 319-nm UV laser. For the spin ice experiment, we require a high-power direct Rydberg P excitation to Ising-gauge the spin system with $\Lambda \gg g$ where Λ is the Ising energy and g is the atom-cavity coupling rate. Because of the difficulty of dealing with high-power UV laser and the challenge of UV diode laser systems, we use commercial telecommunication fiber laser systems as the master lasers. The basic idea is to combnie two high-power telecommunication fiber lasers at 1071 nm and 1573 nm in a sum-frequency generation (SuFG) process, followed by a cavity-enhanced second-harmonic generation (SHG). We use the same 10-W 1071-nm laser system (NKT Photonics Y10-NWR master oscillator, 10W Keopsys fiber amplifier), and split a portion to be stabilized to our main master cavity ($F = 100$k) with a sub-Hz linewidth. For the 1573-nm laser, we use the NKT E15NWR CW Erbium fiber master oscillator (Yb-doped CW fiber laser, 100-kHz PZT bandwidth, tunability: 10 nm), which seeds a 10-W Er fiber amplifier (Keopsys CEFA-C-PB-HP-PM-40) optimized for narrow-linewidth CW lasers. For the sum frequency generation, we use a MgO:PPLN crystal waveguide from Covesion (MSFG647-0.5-20 with PV20 oven), optimized for high-power operation with reduced photorefractive damages (with MgO doping) with a theoretical output power 3 W for our seed powers. The resulting SuFG provides a single-frequency output at 638 nm, whose output is split for frequency stabilization to a medium Finesse cavity with the feedback returning to the 1573-nm laser. Finally, the SHG system uses a Castech BBO nonlinear crystal in an external power-build-up cavity to frequency double to 319 nm. We present the result for a similarly configured system in the later section.

A high-power 508-nm green laser. In order to access dress cavity photons with high-lying Rydberg S-states, we may also use a two-photon transition from $6S_{1/2} \rightarrow 6P_{3/2}$ at 852 nm (cavity photon) and $6P_{3/2} \rightarrow nS_{1/2}$ at 508 nm, which we colloquially call the green laser. Importantly, because cavity polaritons are coherent superposition states of the atomic spins and cavity photons, we require phase coherence between the cavity field and the green laser. As discussed in section 4.1.1, this is achieved by a transfer cavity that brings the optical coherence of an ultranarrow 1015-nm laser to 852-nm range. In order to realize an ultrastable and highly intense field at 508 nm, we constructed an ECDL (Eagleyard, EYP-RWE-1060-10020-0750-SOT01-0000[c]) at 1017 nm phase locked to the IF-1017 master laser. While the diode gain is maximized at 1030nm, the gain-bandwidth spans down to 980nm due to the AR coating, thereby allowing for a highly tunable laser. We have observed a mode-hop-free tuning range ~ 5 GHz and maximal tuning range over 50 nm. The output of this laser is then amplified by our in-house cavity-enhanced MOPA (M2K/DILAS, TA-1010-2000-CM) to ~ 1 W to produce a high-power narrow-linewidth frequency-doubled light at 508 nm.

4.2 High-performance external cavity diode laser systems

In this section, I describe several types of external cavity diode laser (ECDL) systems that I have developed as part of the MSc thesis. In our laboratory, we extensive use Littrow-based grating feedback lasers for common AMO applications throughout the laboratory. For the most stringent applications with the narrowest linewidth and widest tunability, we use the cat-eye configured interference-filter (IF) feedback laser [143, 144]. The main reason for this development, well ... besides the great fun, was that it was simply impossible to find commercial alternatives that could match the performance levels required for our experiment.

ECDL is a reasonable starting point to realize sub-Hz stable laser. For most home-built systems, the main limitation in terms of the instantaneous stability is the amatuer control electronics. But long-term drift depends primarily on the optomechanical stability to maintain the optical feedback to the gain medium. A single-mode (single transverse mode) laser diode (LD) consists of a ridge waveguide of a semiconductor gain medium of length L. Upon injection of carrier electrons, excitations in the diode bandgap convert the energy into spontaneously emitted photons under population inversion. Usually, in a Fabry-Perot (FP) cavity diode laser, one end of the waveguide is coated with high-reflectivity r_1, while the other end is simply terminated to air, forming a laser cavity with the Fresnel reflection r_2. On the other hand, in a gain chip (AR-coated diode), $r_2 \simeq 0$ with the application of AR coating or with Brewster exits. We can calculate the round trip gain G_{RT} by

$$\sqrt{G_{RT}} = r_1 r_2 \exp{(g - \alpha_i)} L e^{-j\frac{2\pi n_{\text{eff}}}{\lambda}2L}, \tag{4.1}$$

---

[c] Richardson holographic grating, 33025FL01-239H / 12.5x12.5x6 1500G 600nm Holo Grating, aluminum coated.

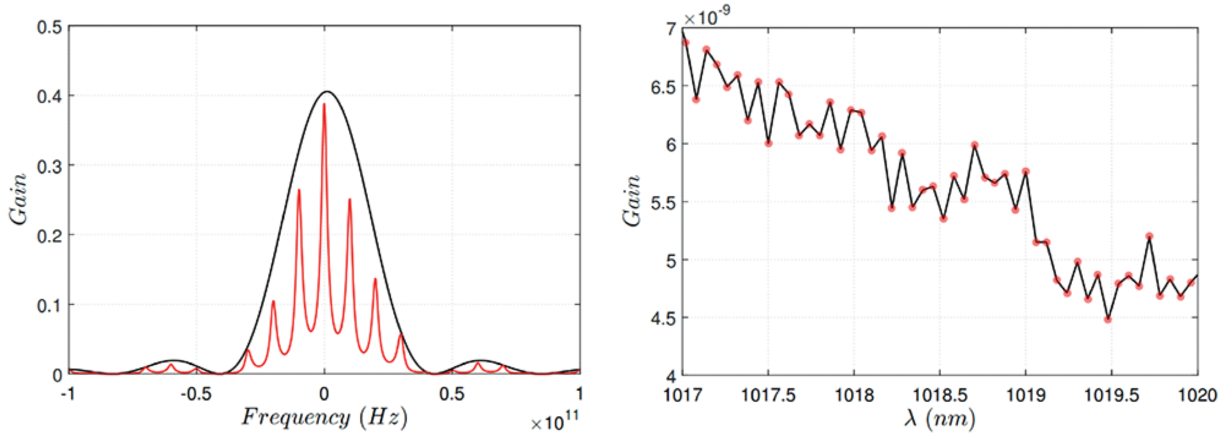

Figure 4.8: **Gain spectrum of a semiconductor diode laser. a,** Effective gain profile for a grating-feedback laser with the grating function (black solid line) and the internal mode (red solid line). **b,** ASE measurement of an FP cavity 1017 nm LD. We measured the internal FSR of laser diode ~ 0.1 nm.

where g is the gain of the diode medium, α_i are the internal losses (e.g., reabsorption), and n_{eff} is the effective index of the semiconductor waveguide. Namely, I find that the threshold condition $G_{RT} = 1$ is given by $g_t = \alpha_i + \alpha_m$, with the scattering loss $\alpha_m \propto 1/L$ of the laser mirror (e.g., imperfect polishing). For an industry standard internal mode of $750\mu m$ long gain medium, there is a free-spectral-range (FSR) of ~ 0.5 nm, and the gain function g is intrinsically sinusoidal (unless AR coating is applied).

The output lasing mode of an ECDL is selected by a competition between the periodic internal gain and the frequency-selective (e.g., grating or interference-filter) functions of the external cavity. Obviously, the best scenario occurs when the internal gain and grating agree to each other, as I calculate in Fig. 4.8. In all other cases, the output mode may not be stable and develop mode-hopping behaviors between the internal cavity modes. From Eq. 4.1, I can derive the celebrated Shawlow-Townes equation $\Delta\nu_{laser} = \frac{4\pi\hbar\Delta\nu_o^2}{P_{out}} \propto \frac{(\alpha_i+\alpha_m)\alpha_m}{P_{out}}$, which relates the output laser linewidth to the length of the laser resonator.

4.2.1 Littrow-based grating ECDL

Due to its simplicity and high-output power, I have designed a Littrow-configured ECDL instead of the Littman-Metcalf designs. In a Littrow cavity, the first-order diffraction of the holographic grating is fed back to the gain medium to select the primary wavelength.

Now, the longitudinal mode is determined by the competition between modes of the laser gain medium, the grating function and now the external cavity formed by grating's surface and the reflective surface of LD. Since a bare semiconductor laser diode typically has a bandgap gain medium over ~ 10 nm, it is possible to tune the output frequency over similar ranges by tilting the grating with the Bragg condition $\sin(\theta_{\text{out}}) + \sin(\theta_{\text{in}}) = m \times \lambda/d$. The internal and external modes' FSR should not be an integer multiple. Otherwise, you would experience a bistable output of the longitudinal modes of the cavity.

As shown in Fig. 4.10, we can categorize the stability criteria into 5 classes by the amount of optical feedback [145, 146]. In region I, the amount of feedback is just too low that it cannot exert a phase shift on the intracavity field of the gain medium. On the other hand, in region V with the largest amount of optical feedback, the output laser is stable with respect to the cavity length. However, with infinitesimal reflection from other surfaces, the output may experience severe oscillation of the external cavity modes, requiring AR coating. I would like to note that this feedback regime is also extremely difficult to achieve, because it requires that we couple nearly $\sim 10\&$ of the output power back into the gain medium, which has a slit width $\sim 1\mu m$. For the utmost stability, we try to stay in the feedback regime III. As the feedback threshold is lowered for longer cavity length, the diode laser will preferentially follow the external mode of the cavity, instead of its own internal mode. For typical diffraction efficiencies 10-20%, it is possible to maintain the ECDL in this regime with large output powers.

In stability III, the output mode of the laser is selected over a mode-hop-tuning-range (MHTR), limited by the differential response of the grating function and the external

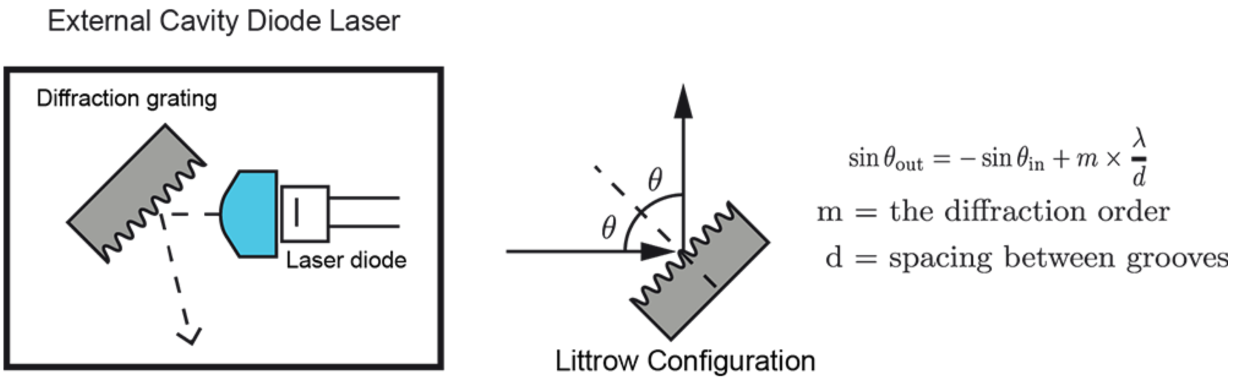

Figure 4.9: **Working principles of Littrow external cavity diode laser (ECDL).** The first-order of diffracted light is fedback the active ridge waveguide, whereas the undiffracted beam reflects off the grating to form the laser output.

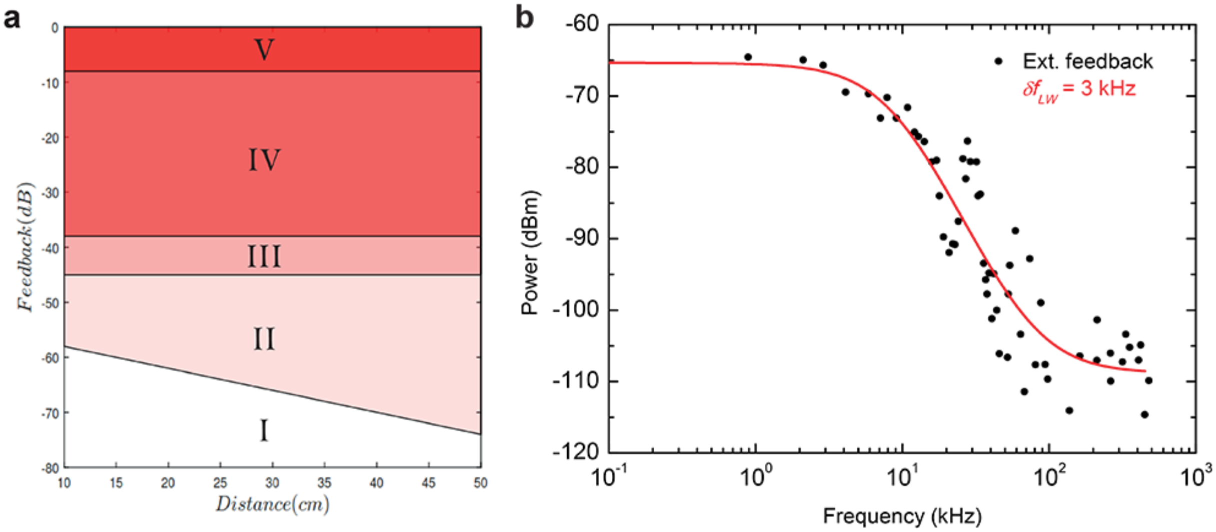

Figure 4.10: **Stability diagram of various feedback regimes and reduced linewidth with external feedback. a,** The stability regimes are classified into I-V classes by the amount of the optical feedback as a function of cavity distance. **b,** Beat note spectroscopy between two identical ECDL systems. We demonstrate a passive linewidth of 3 kHz between two independent ECDLs.

cavity modes, as the PZT tunes the grating mount. Ideally, we would like to match the differential changes of the external cavity modes ν_{ext} and the grating mode ν_g. By placing the virtual pivot point (See Fig. 4.11a) on the line of sight to the laser reflection facet at the Litrrow angle, we can match the variation $\delta\nu_{\text{ext}} = \delta\nu_g$, so that the external mode can sit close to the top of the grating function as the mount is rotated. By adding another piezo stack at the pivot point, you can translate the grating position to tune the cavity length without affecting the grating angle. Likewise, the grating could be rotating without changing the cavity length to the first order.

In order to enhance the mechanical stability of the laser resonator, I designed the grating enclosure to be monolithic, so that the grating and the laser diodes are fixed on the stainless steel (SS)18-8 component. As shown in Fig. 4.11b, we mount a diffraction grating onto to a proprietary mount that sits on the monolithic enclosure (borrowed from a similar design by Jun Ye's group) with precision springs (similar to a mirror mount). Using a precision spring-based mount has one advantage compared to passively stable flexure mounts: By reducing the mechanical load on the piezoelectric tube (PZT), we can readily achieve high PZT bandwidth. The shape of the mount and the enclosure has been

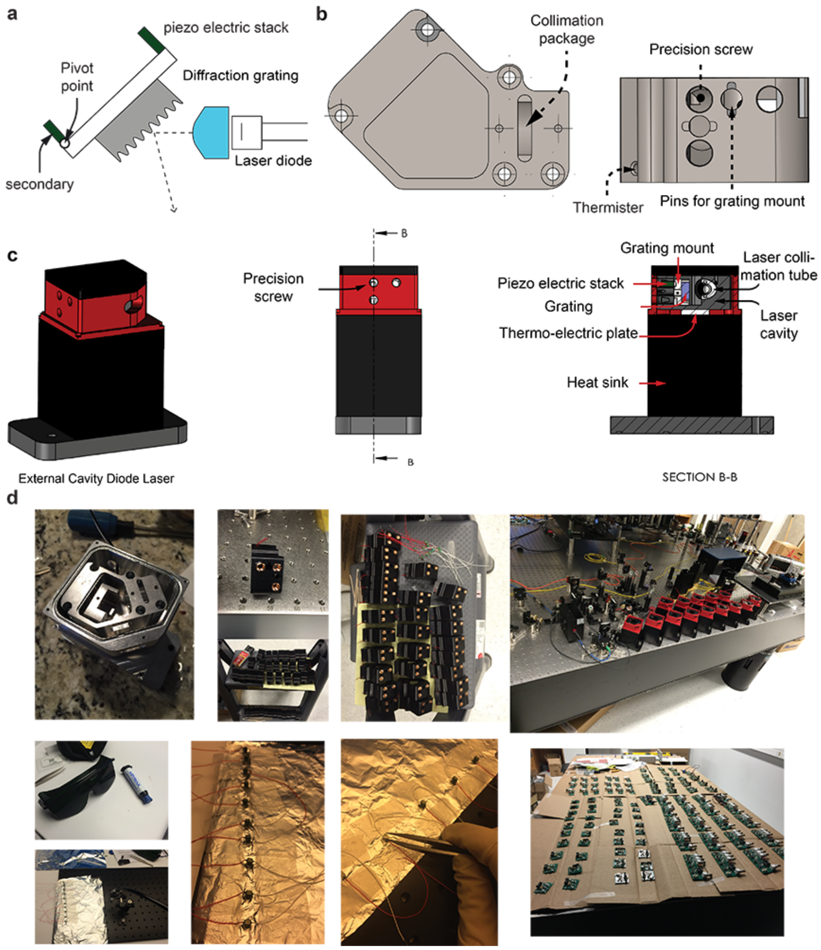

Figure 4.11: **Littrow external cavity diode laser.** **a,** Location of the pivotal point of the grating mount for enhanced MHFT range. **b,** Monolithic grating cavity design. The geometry of the grating enclosure is based on the designs from Jun Ye's group at JILA. The structural stability was optimized on COMSOL by varying the parameters of the structure. **c,** CAD design of Littrow ECDL. In section view B-B, I have shown that elements enabling temperature control and precise tunability on the incident angle of grating. A stack piezo is inserted in a deep hole at the back side of grating mount. Thermistor is located near to laser diode and glued inside of the external cavity with thermally conductive epoxy. Thermoelectric cooler plate (TEC) is sandwiched between the external cavity and the bottom heat sink. **d,** External cavity diode laser mass production! One more typical day with Chang and me in 2016.

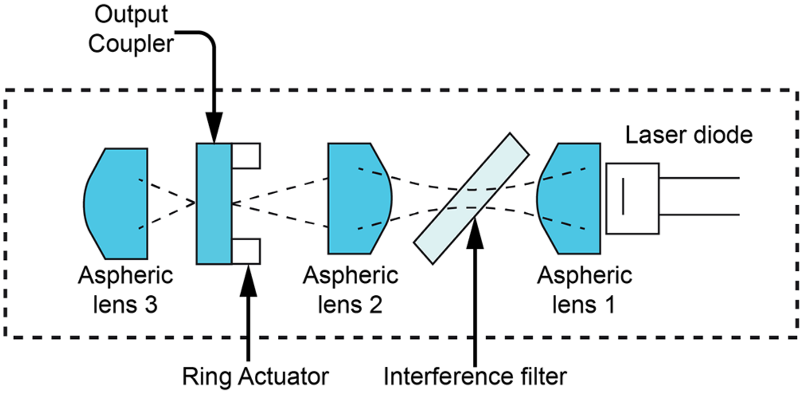

Figure 4.12: **Schematic of cat-eye geometry.** The first aspheric lens collimates laser diode's output. Cat-eye configuration is formed by the second aspheric lens and the output coupler. Independent of the displacements of the components, a ray backtracking from the output coupler would couple back to the ridge waveguide. For optimal feedback, the output coupler is glued at the effective focal point of the lens. With the ring PZT actuator, we can tune the laser over 1.5 GHz and the last aspheric lens recollimates the output.

numerically simulated and tested for its structural stability on COMSOL software.

Fig. 4.11c is a CAD rending of our Littrow ECDL. The monolithic laser cavity is hermetically sealed with Viton dampers and custom AR coated windows (Foctek). Underneath the cavity is a TEC plate mounted on an Aluminum heatsink block, which stabilizes the laser diode temperature within $\sim 100\mu$K resolution with a thermistor sensor. The AR coated window prevents air fluctuation from causing undersirable instability and humidty. For laser diodes requiring a large degree of electric cooling, we have the option of fill the cavity chamber with a N_2 gas. With these laser systems (See Fig. 4.11d for a small subset of lasers being built), we routinely achieve mode-hop-free-tuning ranges of 4 GHz and laser linewidth 1 MHz over 10 s integration time ($\sim$ 300 kHz for 100μs integration time with the instantaneous linewidth similar to those from Toptica).

4.2.2 Cat-eyed interference filter laser

Our interference filter (IF) lasers have typical cavity lengths $L_c = 7.5$ cm[d] and a free-running linewidth ~ 100 kHz over integration time 10s [e]. Long-time integrated linewidth

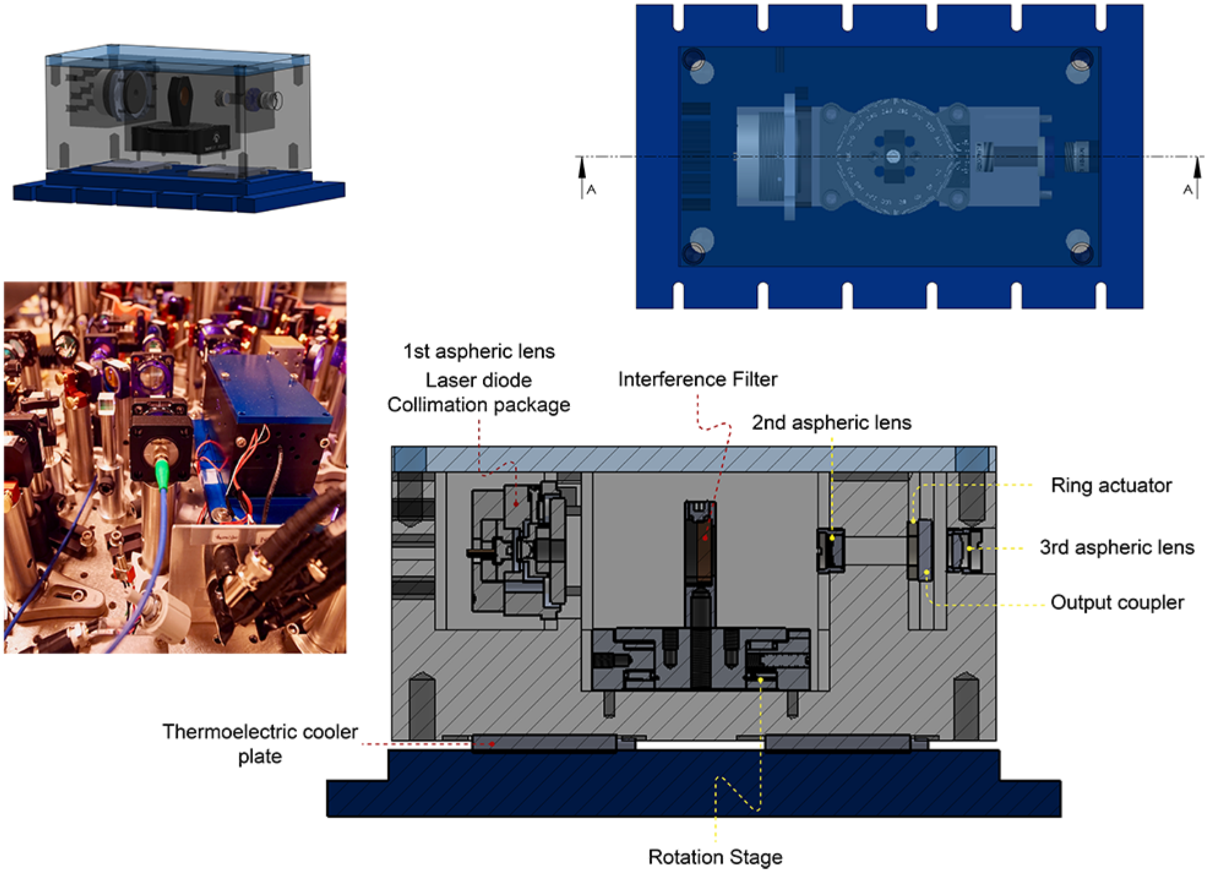

Figure 4.13: **Rendering of Interference filter laser**. The cat-eye configured interference filter laser is illustrated. The first aspheric lens collimates the laser output. Extended cavity is formed by the transmissive interference filter (0.3 nm) and output coupler (20−30% reflectivity). The second aspheric lens is used to form a cat-eye configuration for passive stability.

---

[d] The free spectrum range (FSR) of the cavity is $\simeq 1.5$ GHz.

[e] Our instantaneous linewidth is much smaller than the long-time integrated linewidth, as limited by the Shallow-Townes limit.

is a good measure to quantify the mechanical stability of the laser over relatively long-term drift (apart from the thermal drift). That is, our laser drifts less than 100 kHz over a 10s period, with the instantaneous linewidth being much smaller. In fact, on a typical day, when we drop a screwdriver onto the optical table, we typically do not see any visible change on the real-time scopes displaying our Cs Lamb dips, as if it is a still picture! Furthermore, without any active intervention, when the laser beam is blocked in a typical feedback (letting the system to freely drift), we do not see any measurable difference in the error signal when the beam is unblocked. The working principle of this passive stability is the the confocal geometry, which has a number of benefits for its mechanical stability in a Fabry-Perot cavity. As discussed in Ref. [144], the differential optical path round-tripping the laser resonator is canceled up to the first-order of ray tracing (with thin lenses). As shown in Fig. 4.12, the external cavity is formed by a rear facet of LD and the output coupler.

Narrow-linewidth interference filter (linewidth $\sim$ 0.1 nm and transmission efficiency $\sim$ 95%) is inserted in the collimated region of the cat-eye cavity to select the desired longitudinal modes ($\sim$ 0.3 nm). To maintain the narrow linewidth and high transmission, Prof. Choi worked out a single-cavity design with our partner, which is basically a dielectric microcavity with Bragg bandgaps. The tuning range of our lasers is routinely over the entire gain spectrum (100 nm for our 1015-nm gain chip). A cat-eye reflector maximizes the mechanical stability of the optical feedback and lowers the susceptibility to optical misalignment of the cavity.

In our laboratory, the cat-eye IF lasers are mainly used as the master lasers. Other grating-based ECDLs can then be readily phase-locked to these master lasers with sub-Hz relatively linewidth at arbitrary phase-frequency relationship with our dedicated controller. By pre-stabilizing these cat-eye IF laser to a medium-Finesse cavity $F \simeq 5\text{k}$, I routinely achieve sub 100 Hz linewidth. One design flaw is that the laser collimation package PAL-9B contains a short focal length $f = 2.7$ mm that exaggerates the beam astigmatism[f]. For the next-generation design, it would be good to increase the focal length of the first aspheric lens.

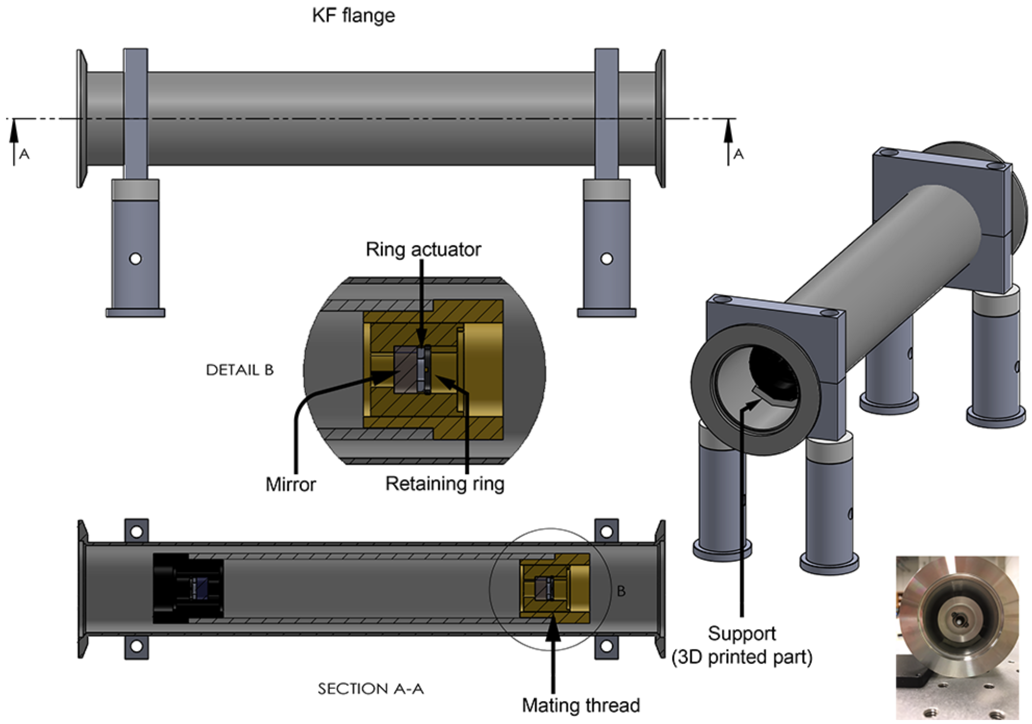

Figure 4.14: **3D rendering of thermally-compensated Fabry-perot cavity.** Composite materials, consisting of Brass, quartz, Aluminum and piezoelectric ceramic are used to compensate the overall CTE at 300 K.

4.3 Optical Fabry-Perot cavities

4.3.1 Thermally-compensated FP cavity

In our lab, we use an affordable home-built medium-finesse ($F < 10,000$) Fabry-Perot cavity designed by Dr. Liu for two purposes. First, we use these cavities to prestabilize a fluctuating laser to achieve a relatively good linewidth $\sim$ kHz and comparable to the linewidth of our ultra-high-finesse reference cavities. This stabilized laser can then used to probe the high-finesse cavity with sufficient transmitted power for the active feedback loops to recover enough P-gain to drive the loop above unity. Second, we also use these cavities for frequency and intensity filters. Since the bandwidth of the cavity is $\sim$ 100 kHz, it is suitable for filtering small signals such as the resonance fluorescence of the trapped atoms

---

[f] Typical single TE-mode ridge waveguides has astigmatism on the order $3 - 10\mu$m.

from the scattered light of the dipole beams. We can also use the cavity as an integrator to filter out the high-freuqency intensity noise, relevant for achieving low-noise optical traps. Since we use RF reactive magnetron-sputtered optical mirrors, our cavity may find good use for cases where low loss is necessary[g], but with an economy compared to IBS mirrors.

The long-term drift of a FP cavity is caused by thermal expansion of the metal spacer. I discuss the construction of high-finesse cavities out of Corning ultra-low-expansion (ULE) gasses with zero CTE[h] in the next section. Here, I focus on an economic solution developed by John Barry's thesis in Yale [137], which uses composite materials holding each mirror so that the global CTE is cancelled. With some modifications, Dr. Liu and I have realized an optical cavity that could tune the zero-crossing temperature near room-temperature without accurate knowledge of the alloying materials, while maintaining the confocal geometry.

If we only consider the effective CTE associated with the length of the cavity, we find that $\alpha_{\text{eff}} = \frac{\sum_{i=1,2,\ldots} \alpha_i L_i}{\sum_{i=1,2,\ldots} L_i} \propto \mathrm{C1} + (\alpha_1 - \alpha_2) \times \mathrm{C2}$ where $\alpha_{1,2}$ are CTE of each endcap materials. The tunability of α_{eff} heavily depends on the CTE mismatch $\Delta\alpha = \alpha_1 - \alpha_2$, and we can use this to our benefit to turn the effective CTE to be functions of L_1, L_2. For this, we use Brass and Aluminum endcaps with a 15% CTE mismatch. Unlike the original design in Ref. [137], both endcaps are movable in our system with precision-mated threads. As shown by Fig. 4.14, ring PZT ceramics are inserted between the mirrors and endcaps[i]. We use a HV chamber to shield the external environmental noise and thermally stabilize the chamber at room-temperature. ECDLs are locked through a standard Pound-Drever-Hall (PDH) method with a home-made EOM with optimized resonant frequency to achieve the widest capture range and steepest error signal. With a clock-referenced direct digital synthesizer (DDS), I was able to routinely achieve the absolute laser linewidth below 100 Hz for most of our lasers.

4.3.2 High-finesse ULE FP cavity

Apart from our commercial Ultra-low expansion (ULE) cavity from Stable Laser System (SLS) which acts as the master clock, I have designed and implemented high-finesse tunable cavities with notched ULE geometry for improved mechanical stability. As the STS ULE

---

[g] The scatter-absorption loss is less than 100 ppm for our magnetron-sputtered mirrors.

[h] Other promising candidates are Zerodur and CeramZ, all of which has zero-crossing temperature near 20°.

[i] Materials, including the quartz spacer, PZT, and mirror themselves are included in the CTE analysis, in addition to the endcaps.

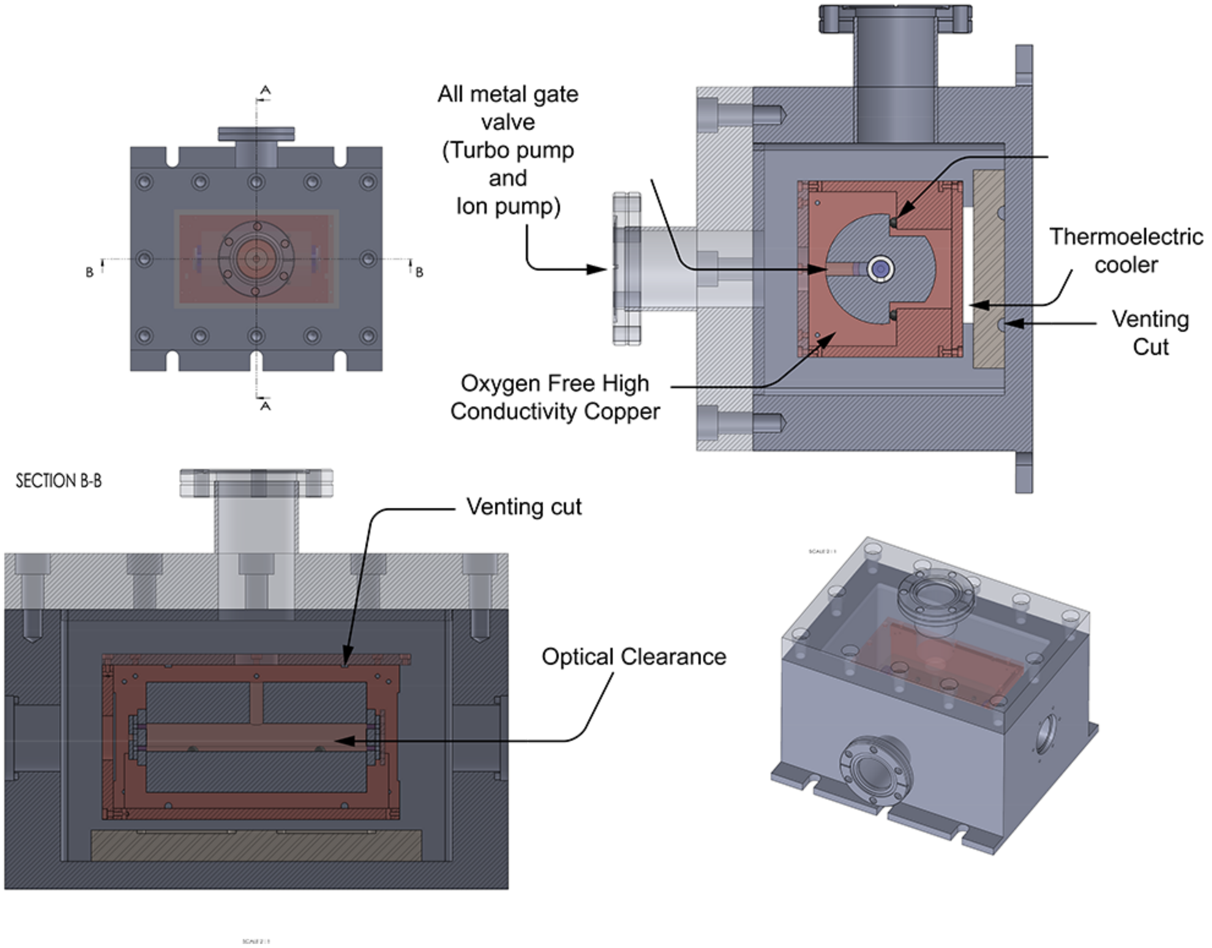

Figure 4.15: **UHV chamber for the notched ULE transfer cavity.** Notched style ULE cavity is placed in a custom UHV chamber with Viton spheres located at the Airy points for vibration-isolation. The UHV chamber is pumped by a 2 L/s ion pump.

cavity was centered around 1016 nm, we required a separate transfer cavity with the coating curve optimized at 850 nm and 935 nm. As a transfer cavity, we required PZT ceramics (usually with large CTE) to tune the cavity length but yet would like to cancel the added CTE effectively.

In terms of mechanical construction, as shown in Fig. 4.15, our notched shape ULE spacer (ULE Corning 7972) is used for cancellation of acoustic vibration and sits on a 3-stage vibration damper with Viton spheres at the Airy points to maximally damp out the mechanical excitations of our UHV chamber. The Airy points are numerically optimized with a FEM simulation to avoid the bent by gravity. The vacuum-compatible TEC and thermistor are integrated in the UHV chamber for temperature stabilization at the zero-crossing temperature. Venting holes and optical clearance are identical to the ATF reference cavity. The 2 L/s ion pump is positioned out of the line of sight. There are reported evidence that Ti sputtering and plasma generated in ion pumps can negatively affect the Ta_2O_5/SiO_2 bilayer mirrors. While the entire cavity assembly is installed on the optical table, we use a commercial minus-K vibration platform to achieve vibration block $\leq 0.5Hz$ through a negative-stiffness mechanism.

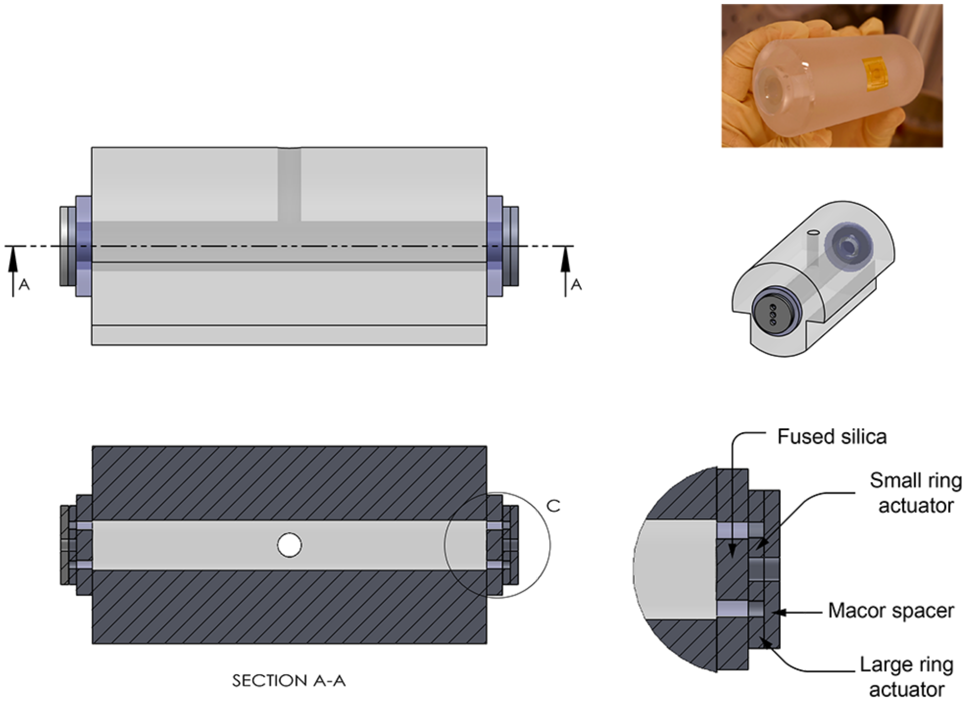

Figure 4.16: **Rendering of notched shape ULE spacer**. We illustrate the notched ULE cavity. Bilayer piezoelectric transducers are used with a fused silica mirror to compensate its CTE expansion.

Fig. 4.16 demonstrates detail of notched ULE cavity assembly. We machined a ULE glass as the spacer with surface flatness less than 3 arc minutes and surface roughness below 0.5 $\AA$. The surface flatness and roughness are crucial to optically contact the mirrors on the spacer and form a monolithic cavity. I have designed and used a special mechanical rig to maintain parallelism of the two glass surfaces by measuring the Newtonian rings

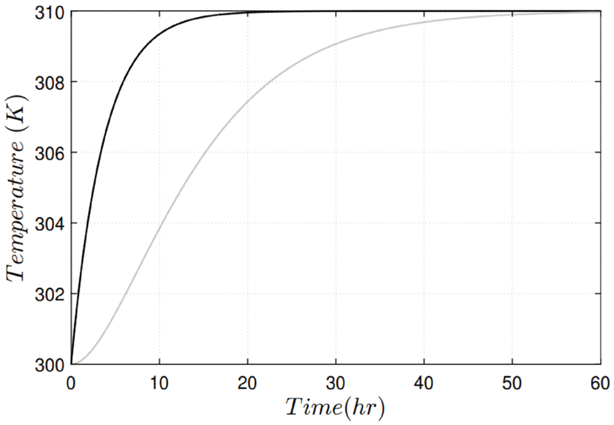

Figure 4.17: **Temperature stabilization with two layers of radiation shield.** Grey solid line depicts the temperature change of the ULE spacer for a quench $10°C$ on the exterior of the first Copper layer. Black solid line shows the temperature change of the outmost layer of the Copper shield, when the laboratory temperature is suddenly quenched.

formed during the optical bonding. For the low-loss mirrors, REO inc. has provided us concave ion beam sputtering (IBS) mirrors with a target absorption-scatter loss < 2 ppm, and optical Finesse $F \simeq 1.1 \times 10^7$ (6×10^4) at 852 nm (935 nm). The edges of the mirrors were masked during IBS coating and left as the bare superpolished surfaces for the optical bonding. There is a pair of ring actuators at each end of the ULE spacer - NAC2125 and NAC2122 from Noliac Piezo, compensating for their CTEs. We use fused silica adaptor to hold the PZTs together to compensate for the CTE of the mirror substrates themselves. From machining tolerances, I do not expect a full cancellation of the thermal expansion, but this is largely fine as it is a tunable cavity design.

Since our ULE cavity is "levitated" by thermally insulating vibration isolation polymers in a UHV environment, the only method of heat transfer to the cavity is by blackbody radiation. Suppose that there an inner layer P_2 and outer layer P_1 at thermal equilibrium state. A sudden temperature change on P_1 from T_i to T_f radiates the heat and surface of P_2 layer will absorb the heat by a rate

$$\frac{dQ}{dt} = \frac{\sigma(T_f^4 - T_2^4)}{1/A_1(1/\epsilon_1 - 1) + 1/A_2 1/\epsilon_2}, \tag{4.2}$$

where σ is a Stefan-Boltzmann constant, $A_1(A_2)$ is surface area of $P_1(P_2)$, and ϵ is the material-dependent emissivity of the surface. Accordingly, we can compute the temperature change on the inner layer as

$$\frac{dT_2}{dt} = \frac{\sigma(T_f^4 - T_2^4)}{C_2 m_2 1/A_1(1/\epsilon_1 - 1) + 1/A_2 1/\epsilon_2} = \beta_{1,2}(T_f^4 - T_2^4). \tag{4.3}$$

With two layers of copper shields and Viton O-rings, I simulated the temperature fluctuation on spacer. In simulation, I considered sudden temperature change from 300 K to 310 K on environment. As shown in Fig. 4.17, for a sudden temperature quench 10 K on the surface of the UHV chamber, it takes 50 hours for the most outer layer equilibrate, significantly damping out the original step-like thermal excitation. As we stabilize the temperature with TEC on the surface of the UHV chamber, we expect to cancel such a long-term temperature change on the surface of the chamber. In our design, the metal surfaces in the vacuum chamber are contacted through Viton O-rings, and heat may conduct through these small elastomers. However, for the Viton O-ring, it would still take more than 200 hours to respond fully under the same quench. Hence, I installed the OFHC Copper radiation shields. With the heat shields, I hope to reduce the thermal variation on the ULE spacer with homogeneous temperature distribution.

4.4 Efficient SHG module

In this section, I briefly discuss the design principles behind the cavity-enhanced SHG modules for frequency-doubling a stabilized 1017nm external cavity diode laser for Rydberg excitation $6P_{3/2} \rightarrow nS_{1/2}$ at ~ 508 nm. Based on the optimized Boyd-Kleinman factor for Gaussian beam, I found a set of optimal parameters for coupling the fundamental to the nonlinear LBO crystal with a single-pass efficiency $\eta_{SHG} = 4.9 \times 10^{-5}/W$ limited by the walk-off angle at the critical phase matching condition. External enhancement bow-tie (ring) cavity is used to build up intracavity field for efficient SHG conversion up to 80% for input power 1 W.

4.4.1 Theory for single-pass SHG conversion

I would like to refer to the Refs. [147, 148, 149, 150] for the basic theory for SHG. In summary, if we consider the dynamics of the induced electric dipole moments in a nonlinear optical crystal [151], a new field emerges from the polarization $\vec{\mathcal{P}}$ of the underlying medium, in which we consider the expansion $\vec{\mathcal{P}} = \epsilon_0 \chi^{(1)} \cdot \vec{E} + \epsilon_0 \chi^{(2)} : \vec{E}\vec{E} + \mathcal{O}(|\vec{E}|^3)$, with the electric susceptibility tensor $\chi^{(k)}$ of rank $k+1$. To the second order, we consider ($\chi^{(2)}$:

$\vec{E}\vec{E})_i = \chi^{(2)}_{ijk}\vec{E}_j\vec{E}_k$ with birefrintent crystals of uniaxial symmetry. For a plane-wave, the emitted field out of the crystal corresponds to the classic sinc function for superradiance in extended sample regime with intensity $I \sim |\frac{\sin \Delta k L/2}{\Delta k L/2}|$ with $\Delta k = 2k_{\mathrm{F}} - k_{\mathrm{SHG}}$. In order to increase the coherence length for the effective SHG interaction, one needs to achieve a phase-matching where the phase velocities of the fundamental and the harmonic are matched $n(2w_{\mathrm{F}}) = n(w_{\mathrm{SHG}})$ for cooperative emission in the forward direction.

In a bulk uniaxial birefringent nonlinear crystal, there are two ways that the phase matching condition could be achieved.

4.4.2 Critical phase matching

In critical phase matching (CPM), the angle θ with respect to the c-axis is tailored to tune the indices $n_o(\theta, w)$, $n_e(\theta, w)$ of the ordinary and extraordinary beams. For a positive uniaxial crystal as LBO (LiB_3O_5, $n_o(\theta, w) > n_e(\theta, w)$), with a proper choice, both fields are phase matched with $n_o(\theta, 2w_{\mathrm{F}}) = n_e(\theta, w_{\mathrm{F}})$, as designated Type I (labelled commonly as (e,e,0)). Type II phase matching is also available for LBO crystals with (e,o,e) or (e,o,o), which are amenable for the case of Sum Frequency Generation. This may be of more relevance to the work on direct Rydberg P excitation, which requires frequency-mixing for the 317 nm laser. One disadvantage is the presence of walk-off angle between the fundamental and harmonic beams, which reduces the cooperative effect for long crystals. Furthermore, the walk-off can cause astimagtism for the SHG field, thereby requiring compensation optics at the output. We will investigate below the feasibility for CPM for LBO crystal in an enhancement cavity.

4.4.3 Non-critical phase matching

In non-critical phase matching (NCPM), one relies on the thermal tunability of the birefringence with $\theta = 90°$ to achieve phase matching at an elevated or cooled temperature. NCPM can be conveniently achieved for wavelengths around 1100 nm and 1500 nm. While NCPM permits maximum conversion efficiency in a single pass with no walk-off angle, thermal stability is an issue, especially if the intracavity field is extremely powerful leading to thermal lensing effect. In particular, for doubling 1016 nm, we would need to heat the crystal above 100 °C.

4.4.4 Quasi phase matching

It is possible to prescribe distributed Bragg structures in nonlinear crystal by way of periodic poling for dispersion engineering with a method known as quasi-phase matching (QPM). With conductive masks, permanent change in the refractive index can be made by localized electric fields. There are several advantages of QPM, ranging from higher nonlinear coefficients d_{eff}, non-critical phase matching close to room temperature, and tunability to wavelengths not accessible by conventional CPM. Furthermore, because the process is lithographic, it is possible to build waveguide structures to enhance the interaction region beyond of what is possible in free-space (as we will discuss below). Realistic QPM materials, however, do not permit high power operation and have lower optical damage loss compared to pure bulk crystals. We will explore MgO dopped C PPLN waveguides from HCPhotonics, Covesion, and Commax as possible routes (MgO dopping allows higher damage threshold, and may allow close to unity single-pass conversion efficiency for a few 100mW). For these crystals, I am expecting cavity-enhanced conversion efficiency upto 95 % in chip-scale PPLN, and 30 % for single-pass conversion in a ridge-waveguide PPLN. We use QPM for the commercial MgO:PPLN waveguide for the UV light.

Conversion efficiency

In the case of a Gaussian field, the single-pass conversion efficiency [152, 153] is given by

$$\eta_{\text{SHG}} \simeq \frac{P_{\text{SHG}}}{P_{\text{F}}^2} = \frac{2w^2 d_{\text{eff}}^2 L k}{\pi \epsilon_0 c^3 n_{\text{F}}^3} e^{-\alpha L} h(B, \xi), \tag{4.4}$$

where $w = 2\pi c/\lambda_0$ is the angular frequency of the fundamental, d_{eff} is the effective nonlinear coefficient, L is the crystal length, and $k = 2\pi n_{\text{F}}/\lambda_{\text{F}}$ is the fundamental wave-vector. $\alpha = \alpha_{\text{F}} + \alpha_{\text{SHG}}/2$ accounts for the absorption of the fundamental α_{F} and harmonic α_{SHG}. The Boyd-Kleinman parameter $h(B, \xi)$ [153] accounts for the Guoy phases of the wavefront for Gaussian beams (via the focusing parameter $\xi = L/2z_R$ with Rayleigh distance $z_R = \pi w_{\text{F}}^2/\lambda_{\text{F}}$), walk-off angle ρ (via $B = \rho\sqrt{\pi L n_{\text{F}}/2\lambda_{\text{F}}}$) and the intensity variation across the crystal in a manner similar to the original sinc function for plane waves [154, 150]. I can calculate the Boyd-Kleinman factor with the numerical integration [153]

$$h(\sigma, B, a, \xi, f) = \frac{1}{2\xi} \int \int_{-f}^{\xi - f} d\tau d\tau' \frac{\exp(-a(\tau + \tau' + 2f) - i\sigma(\tau - \tau') - \beta^2(\tau - \tau')^2)}{(1 + i\tau)(1 + i\tau')}, \tag{4.5}$$

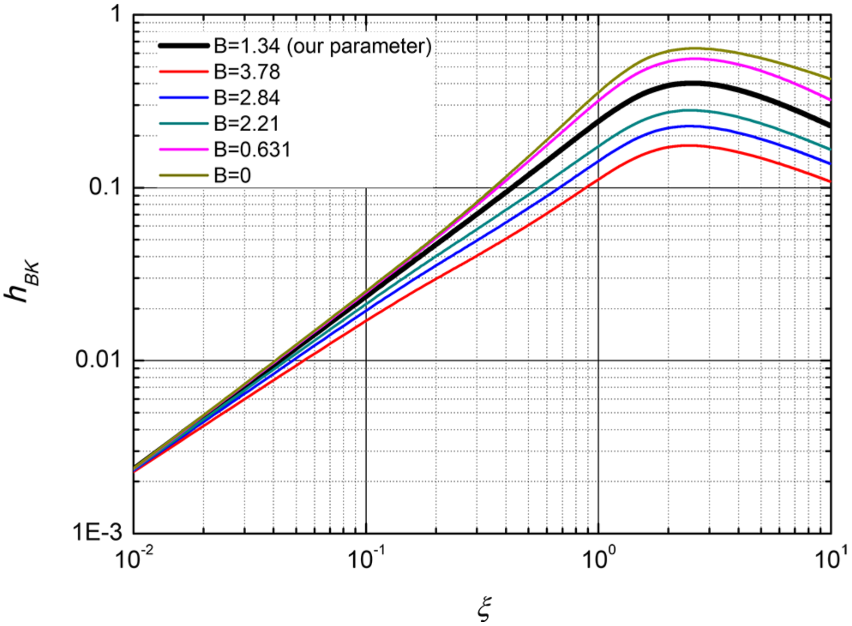

Figure 4.18: Boyd-Kleinmann factor $h(B,\xi)$ as a function of focusing parameter ξ for different walk-off parameter B.

where $\sigma = \Delta k z_R$ is the phase mismatch parameter, $\beta = B\sqrt{2/\xi}$ is the double refraction, $a = \alpha z_R$, and $f = f_c/z_R$ is the focal length.

One interesting manifestation of the Boyd-Kleinman theory is that optimal conversion occurs not exactly at the phase matching $\sigma = 0$. I have plotted the various Boyd-Kleinman factors for different walk-off angle in Fig. 4.18. As I discuss below, our experimental parameter with type I CPM for LBO corresponds to a walk-off parameter $B = 1.34$, which thereby gives single-pass conversion efficiency of $\eta_{\text{SHG}} = 5.94 \times 10^{-5} W^{-1}$ for beam-waist $w_0 = 31\mu$m and crystal length $L = 10$ mm. You can find the MATLAB codes in the UQML folder.

4.4.5 Numerical computation of single-pass conversion efficiency

Here, I provide the numerical result of the Boyd-Kleinmann factor $h(B,\xi)$ for our geometry. I have chosen LBO as the target crystal because of the high damage threshold. Although the effective nonlinearity is not as high as other materials (KTP, BBO), the possibility to build large intracavity power P_c provides a motivation to use LBO for high-power application as ours. Because NCPM requires temperature > $100°C$, we will use CPM for 1015 nm → 507 nm in type I configuration.

I have used a useful software package, SNLO v2, which contains all the crystal parameters for all sort of nonlinear crystals to obtain the correct cut angles (θ, ϕ) to achieve CPM. The relevant parameters are the crystal axes $(\theta, \phi) = (90°, 14.2°)$, (phase-matched) refractive indices $n = 1.606$, group indices $n_g(w_{\mathrm{F}}) = 1.626, n_g(w_{\mathrm{SHG}}) = 1.643$, effective nonlinearity $d_{\text{eff}} = 0.827$ pm/V, the loss parameters $\alpha_{\mathrm{F}} = 3.5 \times 10^{-2}$/m, $\alpha_{\mathrm{SHG}} = 3.3 \times 10^{-1}$/m, and the walk-off angle $\rho = 8.5$ mrad (Please refer to SHG CPM.txt file in the UQML folder for more data). For Gaussian beam-waist of $w_0 = 31\mu$m and crystal length $L = 10$ mm, we obtain a single-pass efficiency of $\eta_{\mathrm{SHG}} = 5.94 \times 10^{-5} W^{-1}$, which is about a factor of 3 smaller than the maximum efficiency if $B = 0$ (e.g., via QPM process). In order to reduce the damage threshold of the coatings and the reflectance from the crystal, we may choose a brewster-cut LBO crystal.

4.4.6 Bow-tie ring resonator

Due to the low single-pass conversion efficiency, I need to build an enhancement cavity around the crystal. I will describe the bow-tie resonator in Fig. 4.19 to achieve the required beam-waist $w_0 = 31\mu$m, and the choice of the mirror coatings for optimal impedance matching. An alternative method would be to put a reflective coating on one side of the crystal and put a curved mirror on the other, forming a FP cavity. The main disadvantage of this approach is that it forms a standing wave pattern, which in turn may cause damage to the crystal due to the large thermal gradient and poor M2 quality for the output SHG beam.

Bow-tie resonator can be easily modeled by ABCD matrices, so I will not provide description below, except to mention that we could compensate for the astigmatism caused by brewster-cut LBO crystals with choosing the angle of incidence θ_i to the curved mirrors via the relationship $R_c \tan\theta_i \sin\theta_i = L(n^2 - 1)/n^3$ [155]. For $R_c = 50$ mm mirrors, astigmatism is corrected for $\theta = 15.7°$ for a brewster-cut LBO. For optimal impedance matching in the presence of losses, let us consider the ratio of the reflected power P_r to the incident fundamental P_{F}

$$\frac{P_r}{P_{\mathrm{F}}} = \frac{(\sqrt{r_1} - \sqrt{r_m})^2}{(1 - \sqrt{r_1 r_m})^2}, \tag{4.6}$$

where r_1 is the reflectivity of the input coupler M1, and r_m is the cavity reflectance parameter $r_m = T t_{\mathrm{SHG}} r_2$. Here, T is the single-pass transmission coefficient (e.g., optical loss by the crystal), $t_{\mathrm{SHG}} = 1 - \eta_{\mathrm{SHG}} P_c$ is the transmission of the crystal, P_c is the intracavity

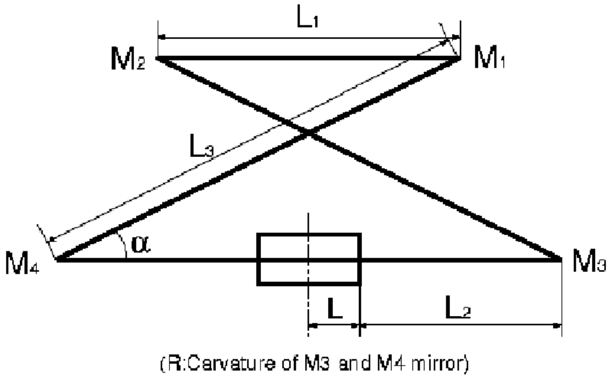

Figure 4.19: **Bow-tie ring cavity.** M_{1-4} represents the mirrors. M_3 and M_4 are spherical mirrors. L is the length of the nonlinear crystal.

power of the fundamental, r_2 is the reflectivity of M2–M4. By choosing $r_1 = r_m$, perfect impedance matching can be achieved (i.e., perfect destructive interference between the field reflected by the first mirror and the field transmitted in a single-pass.

In order to determine the intracavity power by input-output relation, we find

$$\frac{P_c}{P_{\mathrm{F}}} = \frac{1 - r_1}{(1 - \sqrt{r_1 r_m})^2}. \tag{4.7}$$

We can thereby obtain the intracavity power for different values of r_1 and optimize the impedance matching condition for a target value of P_c. The output SHG power is then given by $P_{\mathrm{SHG}} = P_c \tanh(\eta_{\mathrm{SHG}} P_c)$, which accounts for the pump depletion effect for high SHG conversion.

Utilizing the dispersive phase shift on resonance, we will lock the cavity via Haensch-Couillaud method by monitoring the polarization rotation through M1 (input coupler) [149].

In Fig. 4.20, I provide the numerical result for the impedance matching condition for the cavity parameters with $P_{\mathrm{F}} = 1$ W, single-pass coefficient (AR coating & loss of LBO) $T = 0.999$, mirror reflectivities M2–M4 $r_2 = 0.999$, and single-pass conversion efficiency $\eta_{\mathrm{SHG}} = 5.94 \times 10^{-5} W^{-1}$. We can thereby choose the mirror reflectivity for M1 to be 99 % for optimal impedance matching, if all other mirrors can have reflectivity > 99.9 % (and the AR coating for LBO can give transmission > 99.9 %). We thereby require IBS thin film coatings on these mirrors. Figs. 4.21 provide the expected conversion efficiency upto 85 % and output SHG power as a function of the power of the fundamental beam for our cavity

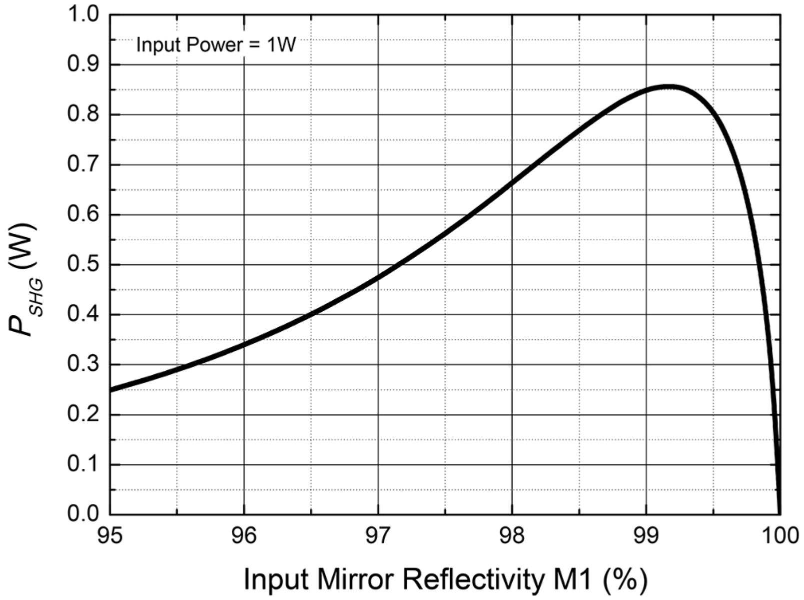

Figure 4.20: Output SHG power vs. input mirror reflectivity for the parameters: $P_{\mathrm{F}} = 1$ W, single-pass coefficient (AR coating & loss of LBO) $T = 0.999$, mirror reflectivities M2–M4 $r_2 = 0.999$, and single-pass conversion efficiency $\eta_{\mathrm{SHG}} = 5.94 \times 10^{-5} W^{-1}$. The conversion is maximized at $r_1 \simeq 99$ % with 850 mW of light at 507 nm.

geometry. Fig. 4.22 displays the mechanical construction of our SHG module design.

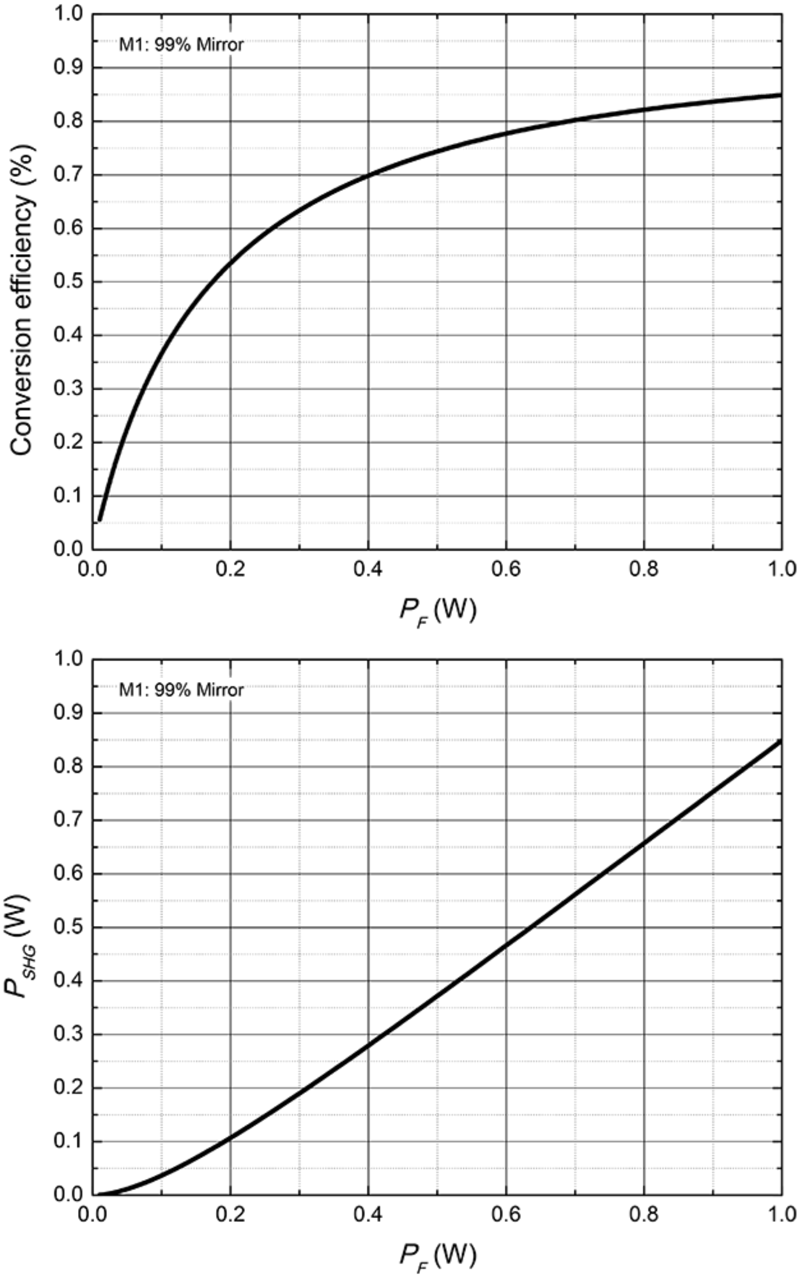

Figure 4.21: **Cavity-enhanced SHG conversion efficiency as a function of input power for our geometry.** In the simulation, we account for the pump depletion effect.

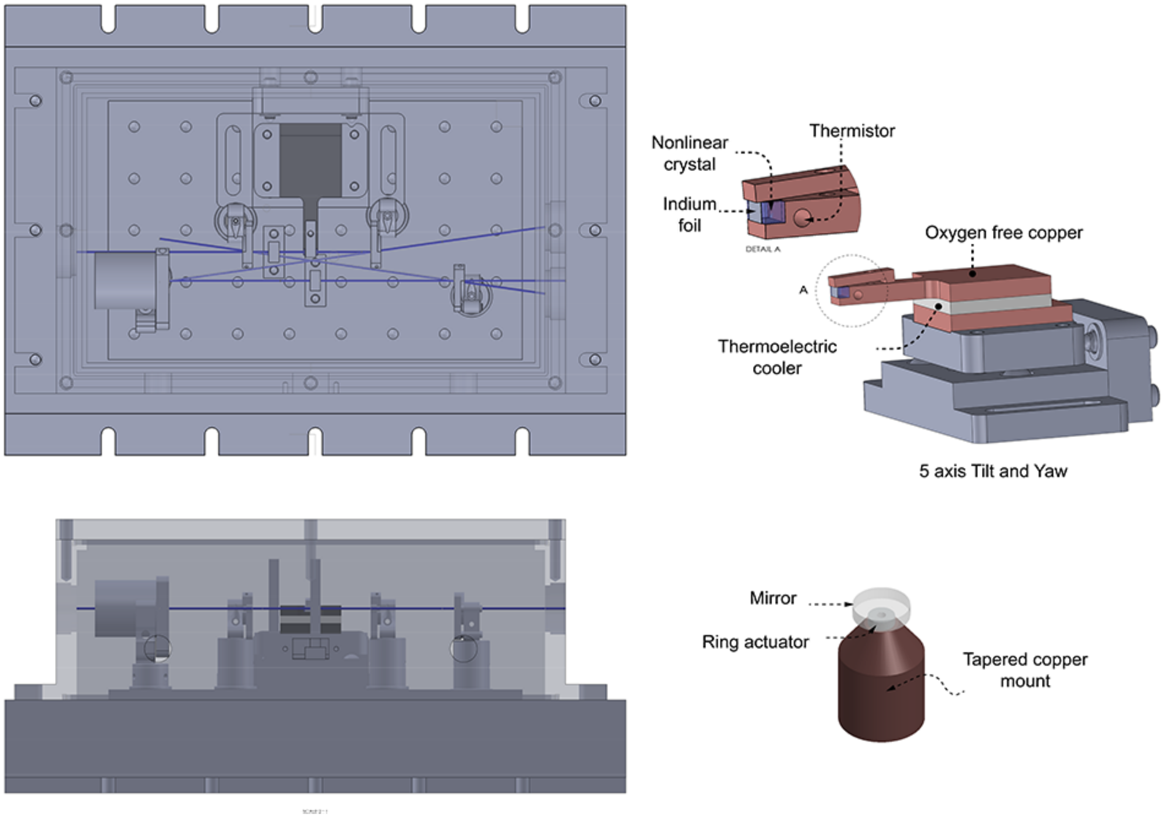

Figure 4.22: **Rendering of second harmonic generation module.** Our cavity enhanced SHG module is displayed. For mechanical stability, the mirror mounts are installed on a 2”−inch thick Al platform. The mounts are custom-designed with SS pieces. The high-speed mirror utilizes a conical copper holder that impedance-matches the PZT response to the thin mirror. OFHC copper is used for the nonlinear crystal holder, where we temperature-stabilize the copper mount with TEC. The crystal is wrapped with Indium foil to maximize the thermal contact with the copper piece.

Chapter 5

Open-system treatment of internal and external atomic DOFs

The physics of light scattering is intrinsically an "open" quantum mechanical process. For most radiative process with mean photon number $\langle n \rangle \gg 1$, a semi-classical treatment accurately describes the dressed states of the atomic internal DOFs and classical electromagnetic fields. However, for laser-cooling processes involving only a few cycles of photons (e.g., single-photon cooling [156]), there is an intrinsic form of an optomechanical coupling as the photons leaving the system exerts a fluctuating momentum transfer in the form of photon recoil. In this Chapter, I would first like to formulate a simple open system model, treating the external degrees of freedom also quantum mechanically, and then apply this method to the atom transports (reducing the motion semi-classically), the non-degenerate Raman sideband cooling, but also to the concept of single-photon cooling (involving both quantum DOFs). With this numerical package, I can optimize the experimental parameters for atom transports both for the pushing beam (from Source to Science chambers) and moving dipole traps (within the Science chamber) where the motion can be treated classically, but also readily apply to future experiments involving the quantum motion. More generally, the case of Rydberg-dressed atoms in an optical cavity is a complex spin-optomechanical system, and it would be of interest to examine the self-organization and textures of such many-body quantum systems for photons, motions, and spins.

5.1 Open system treatment

5.1.1 Quantum motion

Light scattering is an open system problem, where dissipation (spontaneous emitted photons) generates a fluctuation to the quantum motion (photon recoil) of the center of mass with $[\hat{X}_i, \hat{P}_i] = i$. In this case, we must explicitly include the external degrees of freedom (kinetic term) into the description of the Hamiltonian, and formulate a Lindblad dissipation [157]. Here, the atomic center of mass motion is a dynamical component of the system $\hat{H}_M = \sum_i \frac{\hat{\vec{P}}_i^2}{2M} + V_t(\hat{\vec{r}}_i)$, where $V_t(\hat{\vec{r}})$ is the external trapping potential.

In order to formulate the dissipator, I consider the system-reservoir interaction $\hat{H}_{SR} = \int d\vec{k} \sum_i (\kappa_k(\hat{\vec{r}}_i)\hat{\sigma}_{ge}^{(i)}\hat{a}_k^\dagger + h.c)$, where we now explicitly track the position operator $\hat{\vec{r}}_i$ into the mode function $\kappa_k(\hat{\vec{r}}_i)$. For the free-space coupling, we take the plane-wave basis $\kappa_k(\hat{\vec{r}}_i) = \kappa_k \exp(i\vec{k} \cdot \hat{\vec{r}}_i)$. The dissipative jump operator $\hat{c}_i$, derived from the quantum stochastic calculus [34], is then given by $\hat{c}_i = \hat{\sigma}_{ge}^{(i)} \exp(-i\vec{k}_0 \cdot \hat{\vec{r}}_i)$, with the dissipative atomic dynamics described by the Liouvillian superoperators $\mathcal{L}_a[\hat{\rho}] = \gamma \sum_{i,j}(2\hat{c}_i\hat{\rho}\hat{c}_j^\dagger - \hat{c}_i^\dagger\hat{c}_j\hat{\rho} - \hat{\rho}\hat{c}_i^\dagger\hat{c}_j)$. Similar argument can be made as in Section 1.2.2 for interatomic spacing $\vec{r}_{ij} > \lambda$ and neglect the correlated photon emission (accompanied by correlated mechanical excitations) with $i \neq j$

$$\mathcal{L}_a[\hat{\rho}] = \gamma \left(\sum_i 2\hat{\sigma}_{ge}^{(i)} \exp(-ik_0\hat{X}_i)\hat{\rho}\exp(ik_0\hat{X}_i)\hat{\sigma}_{eg}^{(i)} - \hat{\sigma}_{ee}^{(i)}\hat{\rho} - \hat{\rho}\hat{\sigma}_{ee}^{(i)} \right). \tag{5.1}$$

For simplicity, I have neglected the anisotropy in the dipole emission pattern in writing the above equation and suppressed to an effective one-dimensional model. This is a relevant case for trapped atoms in an optical cavity (sideband cooling), where Purcell enhancement (stimulated emission) gives rise to preferential dissipation into the cavity mode (to the laser beams). From the Lindblad term, we can see the internal degree of freedom is coupled to the external one, where damping of the internal states produces fluctuation of the external states.

For some internal Hamiltonian $\hat{H}_S$ (which may also couple the external DOFs with the spatial geometries of the laser fields), both the internal and the external wavefunctions are described by the density matrix $\hat{\rho}$, which follows the quantum master equation

$$\dot{\hat{\rho}} = i[\hat{H}, \hat{\rho}] + \sum_i \mathcal{L}_i[\hat{\rho}] + \mathcal{L}_a[\hat{\rho}], \tag{5.2}$$

where $\hat{H} = \hat{H}_S + \hat{H}_M$, and $\mathcal{L}_i$ are the dissipative superoperators for the other DOFs not directly involving motion (e.g., cavity decay).

5.1.2 Classical motion

We can return to the case of classical motion by dropping the hats from the position and momentum. In this semi-classical picture, we treat the internal DOFs quantum mechanically, while the c-number position $\vec{r}_i(t)$ and momentum $\vec{p}_i(t) = M\dot{\vec{r}}_i$ separately follow the Newtonian differential equation as point particles. However, I would still like to include the intrinsic fluctuation of the quantum jumps, as part of the classical trajectory $\vec{r}_i(t), \vec{p}_i(t)$.

The first requirement is straightforward. For a short time evolution δt (e.g., for quantum Monte-Carlo wavefunction method),

$$\begin{aligned} \vec{r}_i(t+\delta t) &= \vec{r}_i(t) + \frac{\vec{p}_i(t)}{m}\delta t \qquad (5.3) \\ \vec{p}_i(t+\delta t) &= \vec{p}_i(t) + \vec{F}_i(t)\delta t, \qquad (5.4) \end{aligned}$$

with the instantaneous conservative force $\vec{F}_i(t) = -\langle\psi(t)|\vec{\nabla}_{\vec{r}_i}\hat{H}|\psi(t)\rangle$ evaluated with the internal state $|\psi(t)\rangle$. In order to understand the effect of the jumps onto the center of mass motion $\vec{r}_i(t), \vec{p}_i(t)$, we recall $\hat{\vec{r}} = i\vec{\nabla}$ in continuous quantum mechanics. The exponential factor $\exp(\pm\frac{i}{\hbar}\vec{k}_0\cdot\hat{\vec{r}})$ in the quantum jump operator is then the raising and lowering translational operators in the momentum space $|\psi(\vec{k})\rangle$. That is, when a quantum jump occurs within the internal spin state, I can include this fluctuation to $\vec{r}_i, \vec{p}_i$ by adding a random momentum shift $\hbar\vec{k}_0$ (i.e., the photon recoil).

In what follows, I begin with the semiclassical regime by treating the motion as classical c-number, but account for the internal DOFs. I use this semiclassical approximation to compute and optimize the atom transport process. I then move onto the full formalism by putting the external DOFs on equal footing with the internal one. I can second quantize the motion around its center of mass, and simulate the motional ground-state occupation for the trapped atoms with non-degenerate Raman and cavity-enhanced sideband cooling.

5.2 A long distance atom transport with push beam technique

A push beam technique offers a simple and efficient method for atom transport over a relatively long distance. We use this method to create a continuous cold atom flux from the Source MOT to the Science MOT. The atomic beam is collimated and guided by the dipole force of the pushing beam, enabling cold atoms to pass through the small differential pumping tube (Chapter 3). Unlike traditional Zeeman slower and magnetic transport, a push beam technique requires only a single slightly diverging beam that extracts continuously cold atoms from the Source MOT to the Science MOT. By optimizing the geometry of the pushing beam, it is possible to focus the atomic beam through small slits, such as the differential pumping tube.

5.2.1 Analytical estimation of the push-beam transport efficiency

Fig. 5.1 illustrates the schematic of the pushing beam technique. In our laboratory, we follow the particular implementation of Ref. [158], instead of forming 2D MOT in the Source chamber. The atoms in the Source MOT experience the radiation pressure of the pushing laser (detuned by δ from $|F=4\rangle \to |F=5'\rangle$ with Rabi frequency Ω_p) and accelerate towards the Science chamber. As soon as the atoms escapes the repumping region of the Source MOT, they are optically pumped to the dark state $|F=3\rangle$ by the pushing field. During the transport, as the atoms are prepared in the dark state, there is minimal recoil heating with the pushing beam supporting a conservative dipole potential to confine the radial width of the atomic flux and keep them collimated over the transport distance. Dipole guiding implies that we can install differential pumping tube with a smaller conductance (and thereby better UHV environment in the Science chamber) and better transfer efficiencies, compared to other purely dissipative pushing beam methods [159, 160, 161]. The 3D MOT allows higher atomic density and cooler transversal temperature, while the small cloud size implies the slower ejection velocity and thereby relaxes the capture range v_c requirement for the Science MOT.

Unlike the original reference [158], our chamber axis is oriented perpendicular to the gravity. We thereby require a shorter transport time for the atoms to not fall below the capture position range $r_c \simeq 10$ mm (e.g., collision with the differential pumping tube) [a], preferring a larger scattering rate of the pushing laser to accelerate the atoms. On the

---

[a] The capture range is determined by the molasses volume of our MOT beams $\simeq 25$ mm with the field gradient 10 G/cm.

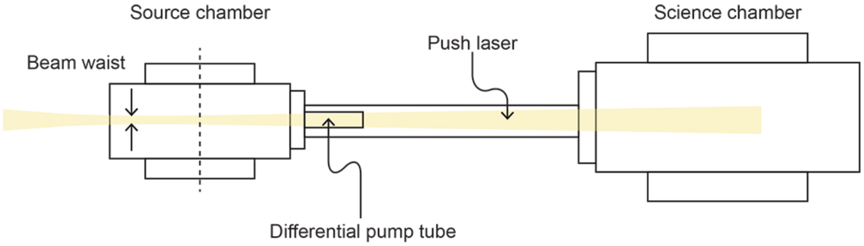

Figure 5.1: **A collimated pushing laser along chamber axis.** A push laser is collimated along the chamber axis, perpendicular to gravity. The beam waist $\simeq 200\mu m$ is located backward to the Source chamber by 23cm. Cesium atoms in the Source MOT escapes and pushed towards the Science MOT by the radiation pressure and guided by the conservative potential generated by the pushing beam.

contrary, excessive scattering rate would cause heating and delocalization in the transverse directions, thereby reducing the transfer efficiency. In addition, we require that the atoms at the final destination to be well within the capture velocity $v_c \simeq 50$ m/s of the Science MOT.

To see the detailed balances, I note that the detuning δ of the pushing laser determines the scattering rate

$$\Gamma_{sc} = \frac{\Gamma}{2}\frac{2\Omega^2}{4\delta^2 + 2\Omega^2 + \Gamma^2}, \tag{5.5}$$

where Γ and Ω are the atomic decay rate and the Rabi frequency, respectively. The diameter of the Source MOT, L_{MOT}, regulates the escape velocity with $v_{\mathrm{MOT}} = \sqrt{2\Gamma_{sc} v_{\mathrm{rec}} L_{\mathrm{MOT}}}$, where v_{rec} is the recoil velocity. With the distance between UHV chambers $L \simeq 30$ cm, I conservatively assume the pushing beam power 10 mW. Once the atoms escape the Source MOT, they rapidly get pumped to the dark state due to off-resonant Raman scattering from $|F = 4'\rangle$. Because of the finite δ, the atomic steady-state still contains a finite population in the bright state $|F = 4\rangle$.

Larger δ results in smaller scattering rate and thereby a smaller initial velocity. Because of the longer transport duration, there is a significant degree of photon recoil heating with larger kinetic energy, reducing the transfer efficiency. On the other hand, closer to resonance, the atoms are ejected with an excess initial velocity with larger kinetic energy than the capture energy of the Science MOT. The radial deviation of the atomic beam can be calculated both from the effective force of the gravity and the dipole guiding, as well as the random walk of the recoils. For the later, the RMS transverse velocity distribution of the beam is $\propto \sqrt{N_s} v_r$, where N_s is the number of scattered photons and v_r is the recoil

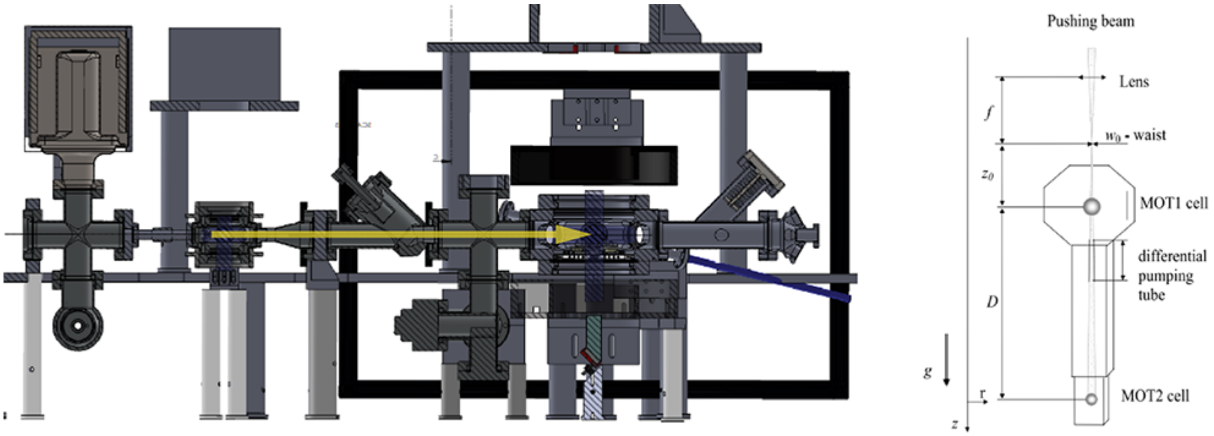

Figure 5.2: **A push-beam configuration for atom transport between two UHV chambers.** Because of the horizontal transport, for better capture efficiency, we require a larger initial velocity compared to Ref. [158].

velocity.

Fig. 5.3 shows the transport efficiency for this simple analytical pseudo model with the weighting function $\left(\frac{1}{1+x_1^{10}}\right)\left(\frac{1}{1+x_2^{10}}\right)$ (Ref. [158]), where $x_1 = \frac{v_{\text{final}}}{v_{\text{recap}}}$ and $x_2 = \frac{x_{\text{final}}}{L_{\text{MOT,science}}}$. The dotted line shows the transfer efficiency for a large Source MOT $L_{\text{MOT}} = 10$ mm. Because of the larger acceleration distance, the atoms ejected from the face of the Source MOT have larger initial velocity, which needs to be compensated by a larger detuning to limit the scattering rate Γ_{sc}. For the pushing beam near resonant $\delta \simeq 0$, the initial velocity is too large to be efficiently captured by the Science MOT, signified by the drop of transport efficiency. For a smaller cloud size $L_{\text{MOT}} \simeq 3$ mm, the initial velocity is < 20 m/s at $\delta = 10$ MHz. Accordingly, the transfer efficiency is peaked near $\delta = 0$, where a significant fraction of the steady-state population is in the dark state.

While this analytical model has good agreement with the experiment of Ref. [158], the weighting function may not be appropriate for obtaining quantitative agreement with our experiment, due to the additional requirement to support the atoms against gravity and the lack of concrete understanding of radiation pressure for a MOT operating in the regime of multiple scattering. Nonetheless, I used this analytical model to obtain some insight and the simple scaling behavior for simulating the computationally-intensive quantum trajectory.

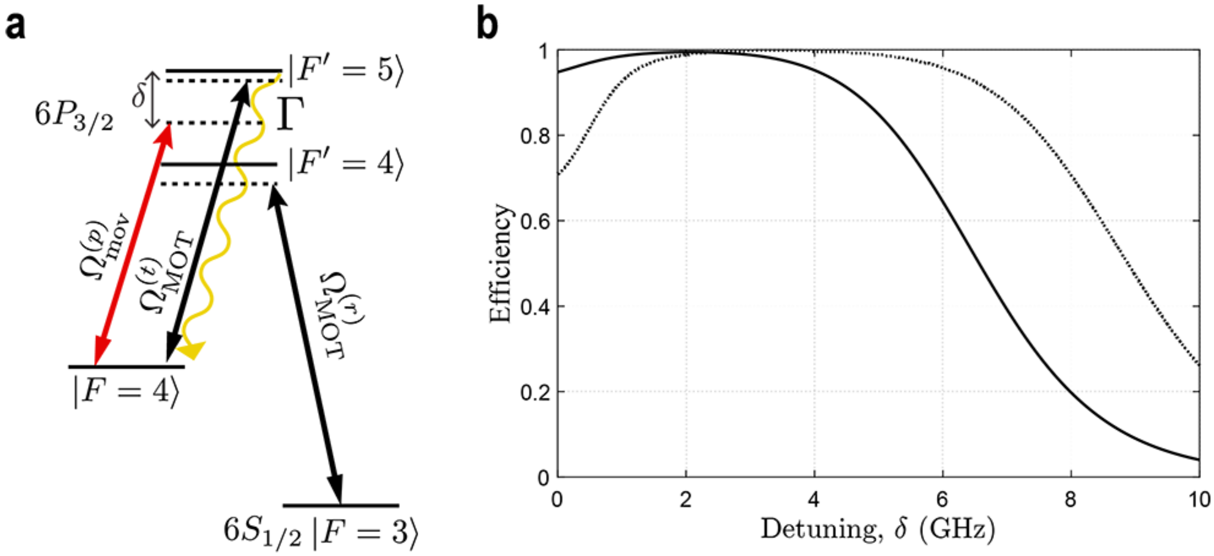

Figure 5.3: **Level diagram and transport efficiency of the pushing beam method with an analytical model. a,** Level diagram for MOT and pushing-beam atom transport. The MOT trapping laser $\Omega^{(t)}_{\rm MOT}$ drives the cycling transition ($|F = 4\rangle \leftrightarrow |F' = 5\rangle$) with detuning -10 MHz. A repumper laser $\Omega^{(r)}_{\rm MOT}$ pumps the atoms back to the trapping state $|F = 4\rangle$ for efficient cooling. A pushing laser $\Omega^{(p)}_{\rm mov}$ is at the $|F = 4\rangle \leftrightarrow |F'\rangle$ transition with detuning δ (defined with respect to the $|F = 4\rangle \leftrightarrow |F = 5'\rangle$ transition). **b,** Analytically evaluated transport efficiency as a function of the pushing laser detuning δ for the two different sizes of the Source MOTs ($L_{\rm MOT} = 3$ mm for solid line, $L_{\rm MOT} = 10$ mm for dashed line) for pushing beam laser power 10mW.

5.2.2 Quantum Monte-Carlo wavefunction method with classical motion

Here, I provide the full 3D quantum trajectories of Cs atoms, as they are transported by the pushing beam. In order to solve the master equation, I carry out the computation with the self-consistent quantum stochastic wavefunction method for the internal states, while we numerically solve for the classical Brownian trajectory of the center of mass motion $\vec{r}_i, \vec{p}_i$ (diffusion caused by recoil kicks). In the simulation, I include the full Gaussian beam geometry of the pushing beam $\Omega_p(\vec{r})$, parametrized by the beam waist $w_0 \simeq 200$ μm and its position $z_0 = -23$ cm from the center of the Source chamber. The rationale behind putting the focal point of $\Omega_p(\vec{r})$ before the Source chamber was that $\Omega_p(\vec{r})$ would be sufficiently

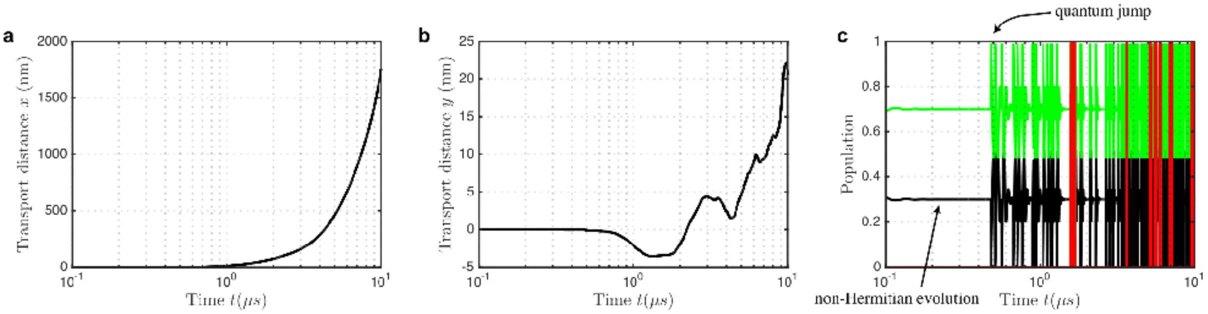

Figure 5.4: **Short-time evolution of pushing-beam atom transport in the MOT for a single trajectory. a,** As the pushing beam is oriented along $\hat{x}$-direction, the atoms are accelerated by the photon recoils with acceleration $\propto \Gamma_{sc}\vec{v}_r$. **b,** As spontaneous emission occurs, they exert random recoil kicks that diffuse the motion in the transverse directions $\hat{y}, \hat{z}$. **c,** Due to the repumping beam that restores the ground state to $|g\rangle$, the atoms experience constant scattering processes given by the quantum jumps that project the internal state. These events are uniquely associated with the sudden change in the atomic trajectory.

small to perturb the Science MOT[b]. In this way, we would be able to continuously operate the two MOTs during the loading.

We write the Hamiltonian governing this system in the rotating frame of the lasers

$$\hat{H}_p = \delta\hat{\sigma}_{ee} + \frac{\Omega_p^{(g)}(\vec{r})}{2}(\hat{\sigma}_{ge} + h.c) + \frac{\Omega_p^{(s)}(\vec{r})}{2}(\hat{\sigma}_{sp}e^{i(\delta+\Delta_{gs})t} + h.c) + \frac{\Omega_r(\vec{r})}{2}(\hat{\sigma}_{sp} + h.c) + \delta_r\hat{\sigma}_{pp}, \quad (5.6)$$

for the ground states $|g\rangle = |6S_{1/2}, F = 4\rangle, |s\rangle = |6S_{1/2}, F = 3\rangle$ and the electronically excited states $|e\rangle = |6P_{3/2}, F = 5'\rangle, |p\rangle = |6P_{3/2}, F = 3', 4'\rangle$. The Rabi frequency $\Omega_r(\vec{r})$ accounts for the spatial profile of the repumping laser in the Source MOT. We perform the finite-element analysis of the external motion $\vec{r}, \vec{p}$ under the conservative potential $U(\vec{r}) = \langle\psi(t)|\hat{H}(\vec{r})|\psi(t)\rangle \simeq \frac{|\Omega_p^{(s)}(\vec{r})|^2}{\delta+\Delta_{gs}}$, with the later relationship valid for the atoms outside the repumping region. As shown in Fig. 5.4, the quantum jumps stochastically interrupt both the classical potential $U(\vec{r})$ as well as add the recoil kicks to $\vec{r}, \vec{p}$ in random directions[c].

Fig. 5.5 shows the long-time evolution of the atomic trajectories, demonstrating that we could create a cold atom flux collimated over 30 cm with beam waist $\simeq 100\mu m$. Due to

---

[b] The saturation parameter of the pushing beam is $S \simeq 0.1$ at the Science MOT.

[c] We have three kinds of jump operators $\hat{\sigma}_{ge}$ (for the cycling transition $|g\rangle \leftrightarrow |e\rangle$), $\hat{\sigma}_{pg}$ (for the dipole allowed $|g\rangle \leftrightarrow |p\rangle$), and $\hat{\sigma}_{ps}$ (for the dipole allowed $|s\rangle \leftrightarrow |p\rangle$).

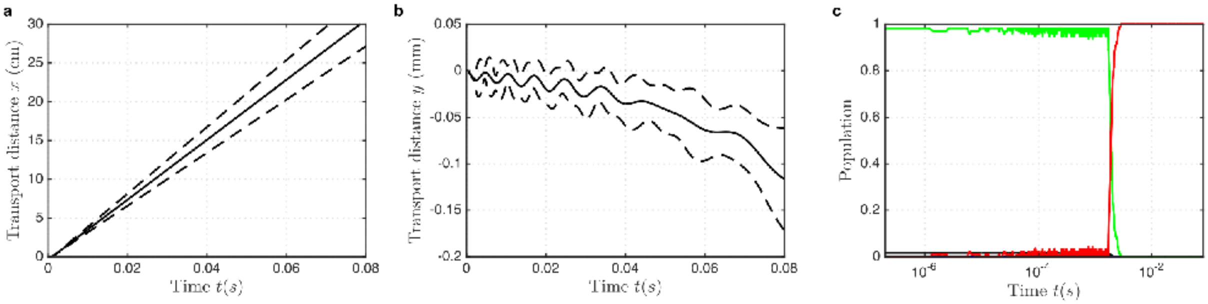

Figure 5.5: **Long-time evolution of pushing-beam atom transport. a,** Atomic trajectory along x-direction (dashed lines indicating the FWHM of the distribution function). **b,** Atomic trajectory along y-direction with gravity direction $-\hat{y}$ (dashed lines indicating the FWHM of the distribution function). In the presence of repumping mechanism, the cold atoms in the MOT are accelerated from the initial Doppler velocity distribution. As soon as the atoms leave the MOT region, they are optically pumped by an off-resonant Raman process over timescales $\tau_p \sim 1$ ms, preparing the atoms in the dark state. Being in the dark state, the atoms experience the largely conservative dipole potentials of the pushing beam with little dissipation. The average number of quantum jumps during this free-space period is < 10 recoils. **c,** The internal population during the atom transport. After 1 ms, the atoms escape the Source MOT region and are optically pumped to the dark state $|F = 3\rangle$. Atomic populations for the states $|g\rangle$, $|e\rangle$, and $|s\rangle$ are given by the green, black, and red curves.

the gravitational sag, the atomic beam is tilted downward, displaced from the center of the pushing beam axis by 100μm. This level of collimation is more than sufficient for cold atoms to pass through the differential pumping tube. With these trajectory calculations, we were able to optimize the differential conductance. The success probability for recapturing the atoms in the Science MOT is $95 \pm 10\%$, with the final atomic velocity $v_f \simeq 3$ m/s, well within the capture range of the Science MOT $v_c = 30$ m/s.

5.3 Atom transport with a moving optical dipole trap

Once the cold atoms are captured and cooled in the secondary MOT of the Science chamber, we need to transport the atoms to the target platforms. Our Science cavity platform is off-centered by $\simeq 3.5$ cm from the center of the Science chamber. I use a tunable optical dipole trap to deterministically transport the trapped atoms to the interaction region of the Science cavity platform [162]. Critically, to prevent the two-body losses, we require that the density of the atoms to be $< 10^{12}/\mathrm{cm}^3$, thereby a large trap volume. With a near-resonant dipole trap at 854 nm, we can use low-power ECDLs at ~ 50 mW at the cost of the increased recoil heating. Because of the tight axial trap frequency, it is possible to reduce the heating rate during the atom transport with faster tuning of the focal point of the dipole trap. Unlike the optical conveyor belt [163], we are not constrained by the filling factor of the lattice sites. However, any non-adiabatic correction to our trap movement translates over to the larger RMS cloud size in the axial direction, and we thereby perform additional laser cooling to reconfine the cloud size. According to my ray-trace simulation, our optical system realizes a focal length shift $\simeq 15$ cm while maintaining the beam waist. I can position the atomic cloud with RMS size $\sim 30\mu$m at the final destination, compatible with the fundamental mode of the cavity.

5.3.1 Electrically tunable lens

We use an electrically tunable Optotune lens (EL-10-30) in the optical configuration of Fig. 5.6. Current applied on the voice coil actuator presses the fluid membrane, distorting the surface of the fluid lens. The exerted pressure on the membrane linearly determines the thickness of the lens. Using the analog outputs of our laboratory control system, we plan to control the focal length of the Optotune lens. T. Esslinger's group has demonstrated that, with a similarly configured Optotune lens, it is possible to transport cold atoms over a large distance with minimal heating (maintaining the Bose-Einstein condensed phase) by using a far-off-resonant trap (FORT) with a high-power 1064 nm. While we also have the capability to use the high-power low-noise fiber lasers at 1071 nm, we were concerned with the long-term focal length shift reported in Ref. [162]. Low-power operation for our trap geometry causes significant recoil heating, but the thermal spreading in the axial direction can be overcome by recooling the atom.

With the optical configuration in Fig. 5.6, we can move the focal point of the dipole beam over 11.5 cm while maintaining the same beam wait $\sim 34\mu$m. The basic idea is to consider the composite system of the last two lenses as a thick lens. By tuning one of its focal length, we can displace both the principal plane x_p and the effective focal length f_{eff} of the thick lens, and the point spread function of the focused Gaussian beam before the Optotune lens is re-imaged over at a distance given by the magnification power of the thick lens. With the positions indicated in Fig. 5.6, the displacements of x_p, f_{eff} are canceled and give rise to a constant transverse magnification ratio over a small range of f_{eff}. This effect can be utilized to transport cold atoms over some distance $(15 - 26.5$ cm) without affecting the transverse confining optical potential (beam waist $w_0 \simeq 34\mu m$).

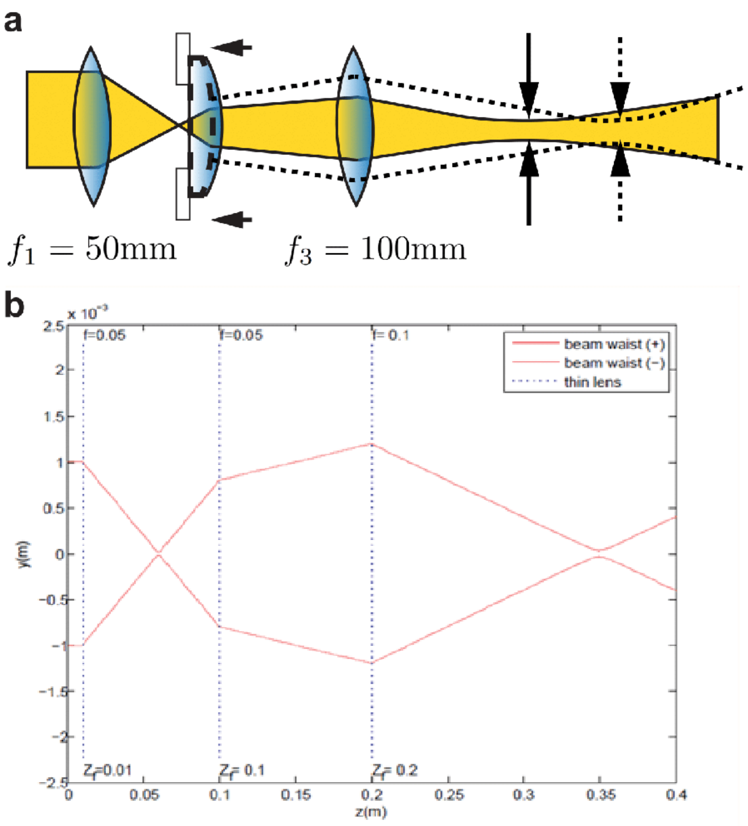

Figure 5.6: **Optical configuration for electrically tunable dipole trap.** We have three lenses in optics setup. With two lenses having $f_1 = 50$mm and $f_3 = 100$ mm focal length respectively, we achieve $\Delta f \simeq 11.5$cm while maintaining a beam waist of $34\mu m$ when electrically tunable lens f_2 is fully tuned from $50 - 120$mm.

5.3.2 Quantum Monte-Carlo wavefunction method with classical motion

The modeling of the atom transport is largely similar to previous section, except for the fact that the optical potential is now time-dependent.Because of the non-adiabatic corrections to the trap movement, I need to also model the 3D laser cooling process at the final destination for trapped atoms with a significant broadening caused by near-resonant trap. I consider a straightforward Doppler cooling with an optical molasses. While we can also engineer the sub-Doppler Sisyphus cooling by using polarization-gradient optical traps, we only confine our attention to the case of Doppler cooling for now. In the laboratory, we use the tetrahedral optical molasses geometry (Chapter 6) with red-detuning (without polarization-gradient lattice structure), which we later switch over to the blue-detuned grey molasses to add sub-Doppler cooling.

In order to include the damping force, I mimic the Zeeman sublevels of the excited ($|F = 5', m_F\rangle$) and ground state manifolds ($|F = 4, m_F\rangle$). The inclusion of the Zeeman sublevels is necessary, laser fields with polarization q in its local basis (defined by its Poynting vector) is transformed to others upon its decomposition to the rank-2 spherical tensor. For convenience, we choose the quantization axis along z, although the resulting physics should not depend on this definition. The internal states follow the basis-independent interaction Hamiltonian [93]

$$\hat{H}_{\text{int}} = \Delta \sum_q \hat{A}_q^\dagger \hat{A}_q - \frac{1}{2} \sum_q \left(\hat{A}_q \Omega_{-q}(\vec{r}) e^{i\vec{k}\cdot\vec{r}(t)} \hat{\epsilon}_q \hat{k}_{-q} + h.c. \right), \tag{5.7}$$

where $\hat{A}_q, \hat{A}_q^\dagger$ are the jump operators associated with spontaneous emission and excitation for polarization $q = \pm 1, 0$. We absorb the decomposition of the fields and the associated dipole matrix elements into the expression Ω_q for fields propagating in arbitrary directions and polarizations. We do not include the repumping process into this reduced model, as we do not include the hyperfine ground state $|F = 3, m_F\rangle$.

Fig. 5.7 shows the result of our Monte-Carlo simulation for the atom transport with electrically tunable lens. The focus of the dipole trap is assumed to be translated with velocity $v_{\text{trap}} \propto \sin(w_m t)$ with $w_m \ll w_t$, where $w_t = 50$ Hz is the axial trap frequency, in order to minimize parametric heating. In addition, we adiabatically increase the trap depth as we load the free-space atoms in 10 ms[d]. From our numerical simulation, we predict the transport efficiency of 90% over time scale 150 ms. The residual oscillation at 1 mm can be suppressed by the laser cooling in the tetrahedral molasses[e]. Fig. 5.8 displays the result of laser cooling the transported atoms in the Optotune dipole trap[f]. With this additional step, we were able to find the parameter regime that achieves localized atomic sample $20\mu m$ ($150\mu m$) along radial (axial) direction, which is sufficiently small for the subsequent grey-molasses cooling and loading into the crossed dipole trap.

---

[d] We have separately computed the loading efficiency by simulating the optical molasses in the dipole trap. We assumed the RMS gas size of 200 μm after MOT compression and polarization-gradient cooling steps, and temperature $T \sim 30\mu$K.

[e] We use the tetrahedral geometry, due to the limited optical access.

[f] Unlike the 6-beam counterpart, tetrahedral configured beams do not have a natural red-detuning polarization-gradient structure. For sub-Doppler cooling, in our experiment, we plan to utilized a dark-state cooling with blue-detuned grey molasses.

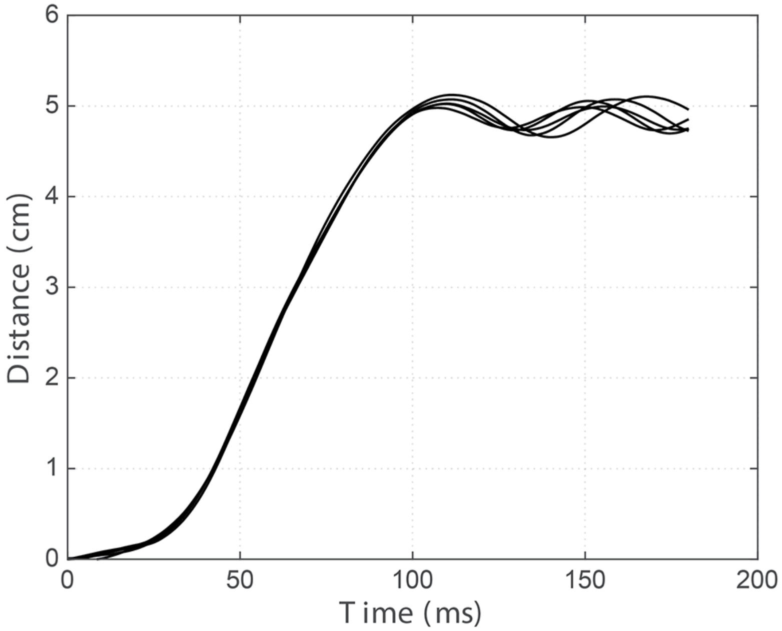

Figure 5.7: **Atom transport with a moving dipole trap.** The resulting atomic trajectories translate the cold atoms to the center of cavity in 150 ms. The residual oscillation $\Delta x \sim 1$ mm at the final destination is caused by non-adiabatic movement of the trap.

Trapping (MOT)		Optotune Laser	
Wavelength	852.3 nm	Wavelength	854.73 nm
Detuning(δ)	0.3 Γ(red)	Detuning(δ)	3×10^4 Γ(red)
Ω	$0.5 \times \sqrt{2}\ \Gamma$	Ω	$800 \times \Gamma$
Beam waist(ω_0)	9.5 mm	Beam waist(ω_0)	34 μm

Table 5.1: Parameters for electrically-tunable optical transport of cold atoms.

5.4 Non-degenerate Raman sideband cooling

In this section, I consider the external DOFs of the trapped atoms as quantum variables. Laser-cooling processes approach the recoil temperature should include the quantum fluctuations associated with the non-commutativity of the position $\hat{x}_i$ and momentum operators $\hat{p}_i$ for this DOF. Hence, we derive the open system dynamics of Raman cooling with the focus on the parameter space realizable for single atom traps in DMD optical potentials.

As shown in Fig. 4.6b, in a traditional setting, non-degenerate sideband cooling occurs

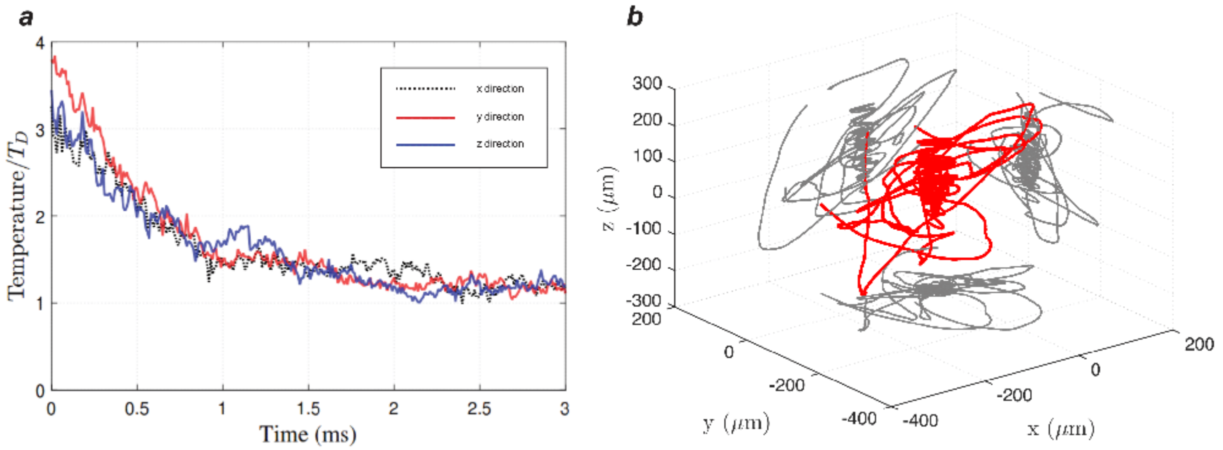

Figure 5.8: **Simulation of 3-dimensional molasses cooling. a.** Temperature of atom cloud in 3-dimension axis after molasses cooling. Within 3 ms, the atoms are cooled from $\leq$ 1mK to Doppler temperature. **b.** Loading atoms into a narrow dipole trap. Molasses cooling and additional dipole trap are used to load atoms within $20\mu m$.

by stroboscopically interleaving two Hamiltonians $\hat{H}^{(1)}, \hat{H}^{(2)}$. The system evolves with a Master equation in a coarse-grained fashion, leaving the motional ground-state $|D\rangle = |s, 0\rangle$ as the unique dark-state of the Lindblad dissipator. The resulting steady-state is thereby the pure motional ground state $|s, 0\rangle$. In the first step, $\hat{H}^{(1)}$ couples the internal spin state to the external motion with an off-resonant Raman transition $\Omega_{\text{eff}}(\hat{x}_i) = \tilde{\Omega}_{\text{eff}} e^{i\Delta k_{12}\hat{x}_i}$ with $\tilde{\Omega}_{\text{eff}} = \frac{\Omega_1\Omega_2}{\Delta_e}$, with the two-photon detuning δ nearly resonant with the trap frequency w_t of the atoms with the evolution $|s, n\rangle \rightarrow |g, n-1\rangle$. The entropy is extracted through the optical pumping process with $|g, n-1\rangle \rightarrow |s, n-1\rangle$ (in the Lamb-Dicke limit).

In the rotating frame of the laser, we can write the sideband Hamiltonian

$$\hat{H}^{(1)} = \sum_i w_t \hat{b}_i^\dagger \hat{b}_i + \tilde{\Omega}_{\text{eff}}(e^{i\Delta k_{12}\hat{x}_i} e^{i\delta t} \hat{\sigma}_{gs}^{(i)} + e^{-i\Delta k_{12}\hat{x}_i} e^{-i\delta t} \hat{\sigma}_{sg}^{(i)}), \tag{5.8}$$

and second quantize the center of mass motion at its equilibrium position with $\hat{x}_i \rightarrow x_0(\hat{b}_i + \hat{b}_i^\dagger)$, where x_0 is the zero-point motion. Here, we assume some form of an external optical trap (in our case, the DMD potential) with trap frequency w_t. We can then Taylor expand the exponentials in the powers of the Lamb-Dicke parameter $\eta_R = \Delta k x_0 \ll 1$, and make integrate out the oscillatory terms with $\delta \simeq w_t$. We thereby obtain the sideband

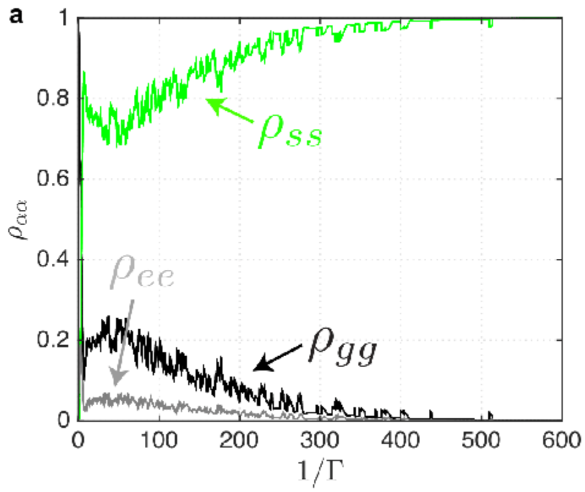

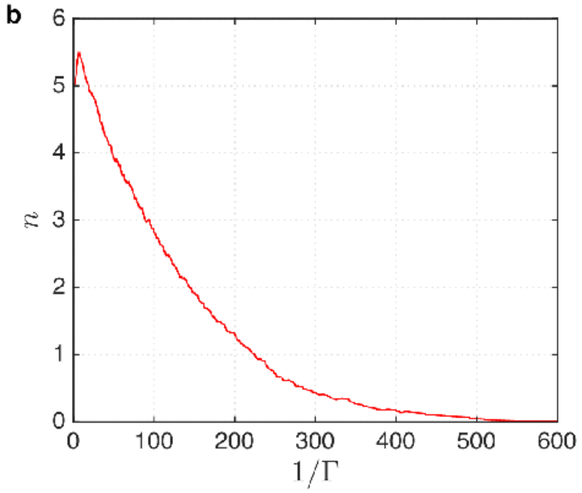

Figure 5.9: **Non-degenerate Raman sideband cooling. a,** Internal dynamics and optical pumping. **b,** Ground-state preparation with Raman sideband cooling. Optical pumping beam nearly resonant with $|g\rangle \rightarrow |e\rangle$ initializes the atomic system into $|s\rangle$. In the Lamb-Dicke regime, the radiative process suppresses Raman processes which change the phonon number. The sideband Hamiltonian couples the internal and external DOFs with $\sim \hat{\sigma}_{gs}\hat{a} + h.c.$ The only dark state in this system is given by $|s\rangle \otimes |0\rangle$.

Hamiltonian

$$\hat{H}^{(1)} \simeq \sum_i w_t \hat{b}_i^\dagger \hat{b}_i + \tilde{\Omega}_{\text{eff}} \eta_R (\hat{b}_i \hat{\sigma}_{gs}^{(i)} + \hat{b}_i^\dagger \hat{\sigma}_{sg}^{(i)}) + \delta \hat{\sigma}_{gg}^{(i)}, \tag{5.9}$$

with the local phonons $\hat{b}_i$.

The optical pumping step can be modeled with the master equation

$$\begin{aligned} \dot{\hat{\rho}} &= -i[\hat{H}^{(2)}, \hat{\rho}] + \mathcal{L}[\hat{\rho}], & (5.10) \\ \mathcal{L}[\hat{\rho}] &= \sum_i \frac{\Gamma}{2} \left(2\hat{c}_i \hat{\rho} \hat{c}_i^\dagger - \hat{\rho} \hat{c}_i^\dagger \hat{c}_i - \hat{c}_i^\dagger \hat{c}_i \hat{\rho} \right), & (5.11) \\ \hat{H}^{(2)} &= \sum_i w_t \hat{b}_i^\dagger \hat{b}_i + \Delta_p \hat{\sigma}_{ee}^{(i)} + \Omega_p (\hat{\sigma}_{ge}^{(i)} + h.c), & (5.12) \end{aligned}$$

with the quantum jump operator $\hat{c}_i^{(g)} = \hat{\sigma}_{ge}^{(i)} e^{i\eta_0(\hat{b}_i + \hat{b}_i^\dagger)}$ and $\hat{c}_i^{(s)} = \hat{\sigma}_{se}^{(i)} e^{i\eta_0(\hat{b}_i + \hat{b}_i^\dagger)}$, where $\eta_0 = kx_0 \ll 1$ is the Lamb-Dicke parameter. With $\eta_0 \ll 1$, the quantum jump projection does not alter the motional state, and Raman transitions are highly suppressed.

Fig. 5.9 demonstrates the Raman sideband cooling for the parameter achievable with the DMD potential. We use the following Cs energy levels: $|g\rangle = |6S_{1/2}, F = 4, m_F = 4\rangle$, $|s\rangle = |6S_{1/2}, F = 3, m_F = 3\rangle$, and $|e\rangle = |6S_{1/2}, F = 4'\rangle$. In addition, we assume the effective Rabi frequency for the Raman fields $\tilde{\Omega}_{\text{eff}} \simeq 10$ kHz with single-photon detuning $\Delta_e \simeq 10$ GHz, the trap frequency $w_t \simeq 100$ kHz, and optical pumping Rabi frequency $\Omega_p = 10$ MHz and detuning -30 MHz. For this parameter set, we predict motional ground state preparation with $> 90\%$.

5.5 Conclusion

Here, I have developed a flexible toolbox to study the impact of atom-field interactions to classical and quantum motion. In the semiclassical domain, I used this numerical platform to optimize the parameters for the two atom transport techniques in our laboratory. I have also examined the case of Raman sideband cooling by explicitly quantizing the motion, the relevant cooling mechanism for atoms in the DMD potentials with large trap frequencies. More generally, I can also deal with quantized electromagnetic fields of the cavity. Here, cavity relaxation acts as the entropy channel for the collective motion of the atoms. I have deliberately not included this analysis in the thesis for length concerns. Furthermore, similar to our formulation of the Dicke Hamiltonian in Chapter 1, I have derived the effective low-energy Hamiltonian for the quantum motions and spins, where we bring local Rydberg-mediated mechanical interactions into the story. I leave the detailed analysis of this exciting possibility as future work in relation to Section 1.1 with complex phase diagrams beyond of self-organization effects.

Chapter 6

Science cavity platform: Development of new generation of optical mirrors

In this chapter, I first describe our experimental platform for achieving strong collective coupling in the regime of strong Rydberg blockade, which we call the Rydberg quantum dot platform. The analogy of our platform to quantum dots refers to the case of semiconductor (bosonic) excitons, where strong exchange and Coulombic interactions between electrons and holes play the role of the blockade physics to constrain the excitation dynamics between vacuum (no electron-hole pair) and single exciton. In a similar fashion, we can create a significant energy cost for multiple Rydberg collective excitations, so that the atom-cavity dynamics governed by the cooperative coupling of a macroscopic atomic ensemble can be constrained in the lowest two atomic excitation manifolds, effectively inducing the quantum optical nonlinearity of the Jaynes-Cummings ladder (Chapter 2.3). The benefit of our collective encoding with Rydberg excitation is that the figure of merit, $C_N = \frac{4Ng_0^2}{\kappa\gamma_\perp}$, is the function of the atom number N and can be arbitrarily enhanced without the stringent requirements of diffraction effects that limit the cavity volume of macroscopic mirrors. Conservatively, we estimate an enhanced C_N that improves the state-of-the-art by a factor 10^3 [95] (Chapter 2.3).

I then discuss a new regime of many-body QED, in which cavity polaritons are dressed by Rydberg excitations and proximally interact each other to give rise to a series of emergent spaghetti physics, as discussed in Section 2.1. In the strong coupling regime with $g_0 \gg \kappa, \Gamma$, cavity photon acquires the short-ranged properties of the Rydberg atom and

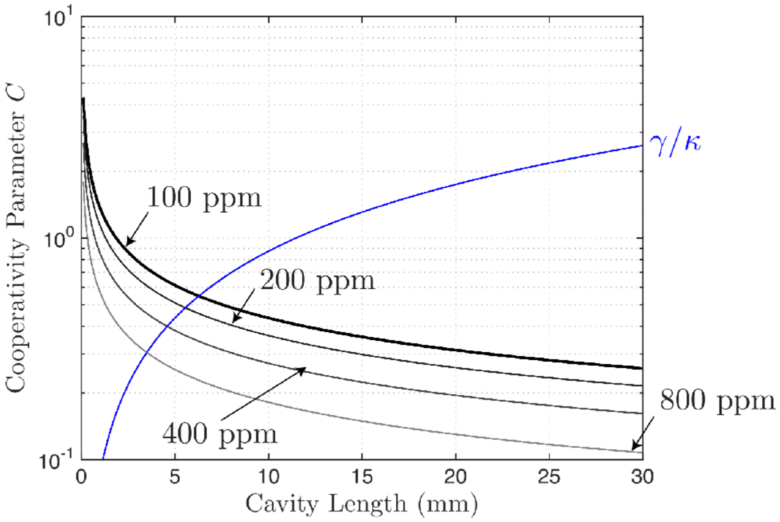

Figure 6.1: **Single-atom cooperativity for Rydberg-dot experimental platform.** We plot the cooperativity parameter C for our Layertec mirrors (radius of curvature $R_c = 20$ cm and mirror transmission $T = 400$ ppm at 852 nm) as a function of cavity length L_c for different absorption-scatter losses (100 ppm, 200 ppm, 400 ppm, and 800 ppm). The blue solid line depicts the ratio γ/κ to determine the dissipative branching ratio. At $L_c = 10$ mm, $\gamma/\kappa \simeq 1$.

the cavity polaritons begin to strongly interact each other. In the limit of Ising constraint $\Lambda \gg g$, the cavity polaritons develop complex effective Hamiltonians within each of the gauge-invariant subspaces. For instance, we can examine emergent quantum spin ice behavior, where cavity polaritons are constrained by the energy cost of gauge-boson quanta (magnetic monopole). Matter field of spin and vison excitations is coupled to an artificial gauge photon of compact QED in the Hamiltonian formulation of lattice gauge theories.

6.1 Rydberg quantum-dot platform

In the Rydberg quantum dot platform, we aim to attain cavity QED parameters with $g_0 < \gamma$ and $g \simeq \kappa$ with a large mode volume $V_c = A_{\text{eff}} L_c$. The combination of the collectively enhanced coupling $g_0 \to \sqrt{N} g_0$ and the strong Rydberg blockade recovers the strong coupling regime $\sqrt{N} g_0 \gg (\kappa, \gamma)$ of cavity QED with the Jaynes-Cummings-like quantum optical nonlinearity. In order to preserve the Rydberg physics and use larger collective encoding $\sqrt{N}$, we require the mirror spacing L_c to be relatively large. On the other hand, in order to map back to the Jaynes-Cummings model (hard-core boson limit of the collective operators), we must also ensure that the size L_a of the atomic ensemble is smaller than the Rydberg blockade radius r_c. For a high-lying Rydberg state $|100S_{1/2}\rangle$, we estimate $r_c \simeq 30\mu m$. In this section, I discuss the target cavtiy QED parameters and provide our design of the Rydbert-dot platform that allows Faraday shielding and high-resolution microscopy.

6.1.1 Cavity QED parameters

We define a set of parameters that characterize our cavity QED platform with spherical mirrors. For a dipole matrix element $\mu_{ge} \simeq 3.8 \times 10^{-29} C \cdot m$ for the transition $|g\rangle \leftrightarrow |e\rangle$ ($|g\rangle = |6S_{1/2}\rangle$ and $|e\rangle = |6P_{3/2}\rangle$), I estimate the vacuum Rabi splitting $g_0 = \sqrt{\frac{\mu_{ge}^2 w_c}{2\hbar\epsilon_0 V_m}}$ from the cavity mode volume $V_m = \pi w_0^2 L_c$, where w_0 and L_c are the waist and the length of the fundamental mode of the cavity, respectively. For spherical mirrors, we can additionally define the Rayleigh ranges of each mirror (M_1 and M_2 mirrors with ROCs R_1, R_2), $z_1 = \frac{-Lg_2(1-g_1)}{g_1(1-g_2)+g_2(1-g_1)}$ and $z_2 = \frac{Lg_1(1-g_2)}{g_1(1-g_2)+g_2(1-g_1)}$. We can then obtain the beam waist of the fundamental mode as $w_0 = \sqrt{\frac{\lambda L_c}{\pi}\sqrt[4]{\frac{g_1 g_2(1-g_1 g_2)}{(g_1+g_2-2g_1 g_2)^2}}}$ for the g-factor $g_i = 1 - L_c/R_i$ of the cavity stability diagram. I estimate the cavity decay rate κ from the cavity finesse $\mathcal{F}$ with $\kappa = \frac{\pi FSR}{\mathcal{F}}$, where $FSR = \frac{c}{2L_c}$ is the free-spectral-range of the cavity and $\mathcal{F} = \frac{2\pi}{T_1+T_2+\delta_1+\delta_2}$, where T_i and δ_i are the transmission and absorption-scatter loss of the respective mirror M_i. I can then express the cavity QED parameters (g_c, κ, γ), with the transverse decay rate $\gamma \simeq 2.6$ MHz for $|g\rangle \leftrightarrow |e\rangle$ of Cesium.

Fig. 6.1 illustrates the scaling behavior of the cooperativity factor

$$C = \frac{4g_0^2}{\gamma\kappa} \gg 1 \tag{6.1}$$

for our cavity QED parameter with our Layertec mirrors ($T = 400$ ppm at 852 nm and $R_c = 20$ cm). We aim to set for $g_0 < (\kappa, \gamma)$ with $\kappa \simeq \gamma$. We require the later requirement, as we would like to stay in the regime where both the cavity and atomic dissipation play a similar role. When $g_N = \sqrt{N} g_0 \gg (\kappa, \gamma)$, we would not be able to eliminate either of the degrees of freedoms DOFs. At $L_c = 10$ mm, I obtain the cavity QED parameters with absorption-scatter loss $\delta = 100$ ppm

$$(g_0, \kappa, \gamma) = 2\pi \times (0.57, 1.2, 2.5) \text{ MHz}, \tag{6.2}$$

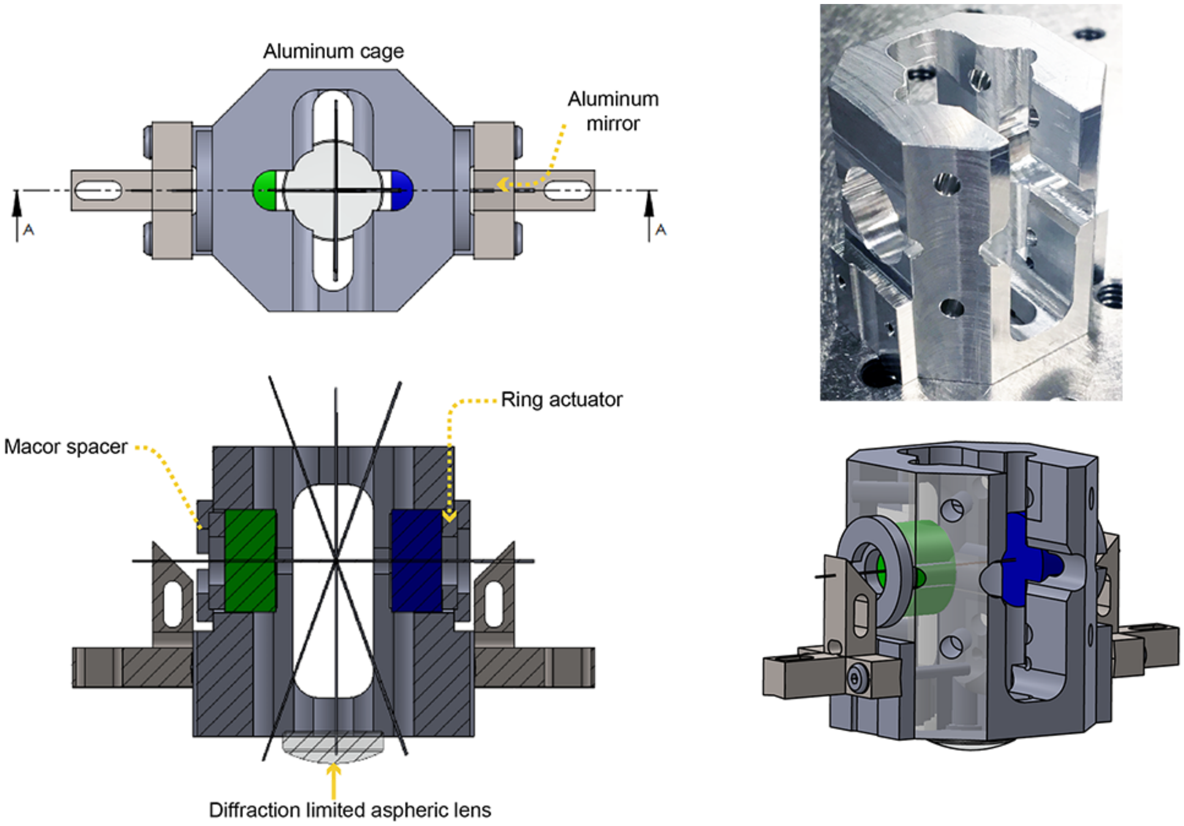

Figure 6.2: **Cavity Rydberg-dot platform.** The experimental cage is Computer-Numerical-Control (CNC) machined out of heat-treated Aluminum (Al) 6061-T6. In collaboration with our partner, we fabricate the Aluminum mirror with a single-point diamond machine with surface roughness $\sim 8\AA$. The full Aluminum construction allows for the Faraday shielding of high-voltage electrodes of the piezoelectric transducer (PZT) ceramics. Titanium wires act as impedance-matched external RF coils with Forster resonance between the Rydberg states. Medium-finesse cavity is formed by two Layertec mirrors, supported by UHV Noliac NAC2123 PZT ceramic with Teflon-coated wires. For high-resolution imaging, we use a diffraction-limited asphere with theoretical optical resolution $2\mu m$. The atoms are transported by the electrically tunable dipole trap, and sub-Doppler cooled by the tetrahedral grey molasses.

in the weak coupling regime ($C = 0.43$). With a very conservative estimate $N = 1000$ atoms within the blockade radius $\simeq 30\mu m$, I obtain the collectively-enhanced cooperativity parameter $C_N \simeq 500 \gg 1$ deep into the strong coupling regime of cavity QED.

I used the Layertec spherical mirrors with reactive RF-magnetron sputtered thin films (TiO_2 /SiO_2 bilayer stacks) on superpolished mirror substrates, instead of the more pristine IBS processes. The radius of curvature $r_c \simeq 20$ cm is measured with the Zygo interferometric surface profiler. Before the shipment, Layertec also characterized the transmission with an in-situ laser photometer during the magnetron deposition process. The absorption-scatter loss is estimated from the ring-down spectroscopy, where they measured the total loss 150 ppm. Upon arrival, I perform dark-field microscopy to examine any surface defect, followed by a ring-down measurement at the target wavelength. For mirror cleaning, we use the recipe developed in Ref. [164], as well as the optimized Argon-based plasma cleaning for organic removals (e.g., PMMA photoresist films), and proprietary organic removal polymers.

6.1.2 Experimental station

Due to the lower finesse and our confidence with the Science cavities (Section 6.2), we have approached the cavity construction with no moving part for manual alignment. We machine a single-block of Al 6061-T6 alloy to fabricate the experimental cage system at the Science machine shop. The entire structure is constructed with a length tolerance $\sim 25\mu m$ and an angular deviation 9 arc-min for the cavity axis. Without any moving part, the cavity alignment and mode matching are passively achieved. We use an UHV multi-stack ring actuator (Noliac NAC2123) with vacuum-fired silver electrodes. The Al cage acts as an effective Faraday cage for shielding the electric fields of the high-voltage electrodes. The mechanical stability is ensured with Kalrez elastometric dampers (Section 6.2), which mount to the Kimball Physics groove-grabbers. For XHV operation, we reduce the effective surface area by diamond lapping the Al6061-T6 cage and perform vacuum heat treatments.

The Layertec mirrors are attached to the Noliac PZT with Epotek 353ND, and the UHV shielded cables are wire-bonded with H60D silver compounds. We do the cable management with Macor ceramics and Ti groove-grabbers. Ultra-thin Ti wires (thickness 125μm) are bonded to the surface of the Al cage to shield high-frequency noise. At the bottom of the cage system, the lens holder is precision-cut to passively align the diffraction-limited aspherical lens to the center of the cavity mode. This simple single large asphere system can achieve diffraction-limited performance with optical resolution $2\mu m$ without spherical aberration-correction of the 6-mm UHV viewports. The numerical aperture is 0.2 with a working-distance 22.4 mm. Our OSLO ray-tracing modeling estimates a field of view $(50\mu m)^2$ with diffraction-limited modulation-transfer function (MTF) up to the cutoff spatial frequency.

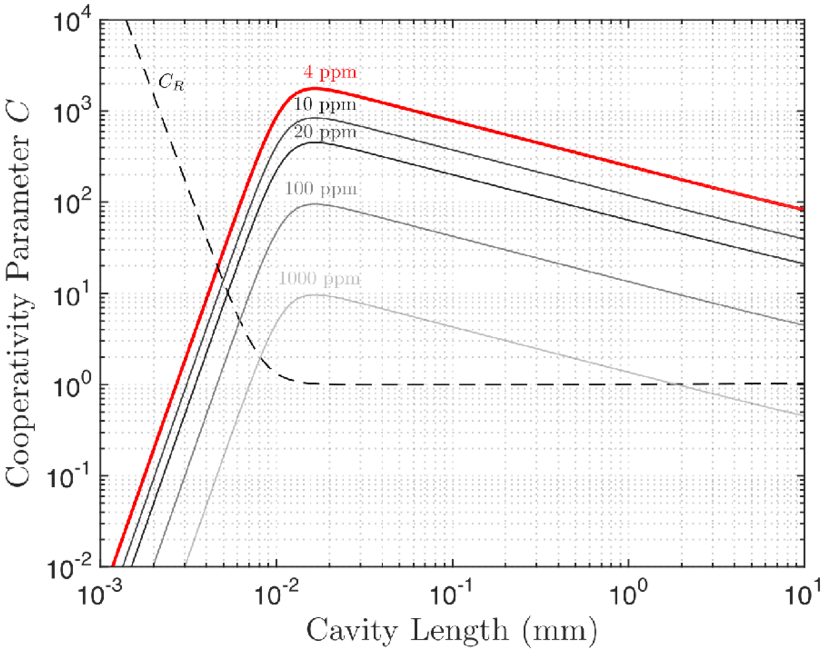

Figure 6.3: **Cavity QED parameters for many-body QED platform.** In order to include the impact of the intrinsic dephasing by the Rydberg atom-surface interaction, we modify the cooperativity parameter C with the atomic decoherence rate, given by the Casimir shift for a Rydberg atom to a metal surface. The cooperativity parameter is plotted for different levels of mirror transmission $T = 4-1000$ ppm with absorption-scatter loss 1.5 ppm. For short cavity lengths $L_c < 100\mu m$, the Rydberg levels are significantly modified by the Casimir shift of the mirrors, resulting in larger atomic decoherence rate and reduced C. We choose the cavity length $L_c \simeq 1$ mm with minimal Casimir decoherence of the Rydberg levels.

6.2 Many-body QED experimental platform

For the many-body QED experiments, we require both the strong coupling regime of cavity QED as well as the strong Rydberg blockade effect, namely

$$g_0, \Lambda \gg \kappa, \Gamma, \tag{6.3}$$

where we further demand $\Lambda \gg g_0$ for the quantum spin ice models (Chapter 2). In order to stay in this very challenging regime, we have developed several proprietary technologies, including a new thin-film coating stack that pushes the mirror losses to the new limits of ion-beam sputtered (IBS) thin films with Finesse $\mathcal{F} \simeq 5 \times 10^5$.

For the single-atom single-photon strong coupling, we are constrained by the relatively small mode-volume of the optical cavities, in which the surface forces significantly broaden and shift the narrow-line Rydberg transition. More importantly, Rydberg atoms are well-known surface force and electromagnetic field quantum sensors at frequency ranges below the microwave domain. In fact, when scaled by its physical footprints, one could argue that Rydberg states possess the largest static and dynamic electric dipole moment with the absolute electrometry sensitivity better than the X-band antennas. While this exaggerated property may be of great utility for applied research of developing atomic quantum sensors, it presents a unique challenge of integrating Rydberg atoms to small-mode volume optical cavities. The situation is somewhat different from the "modestly easier task" of coupling trapped ions to small mode-volume optical cavities [165], a major milestone of the trapped ion community. This is because, for ions, the internal states are largely decoupled from the external forces of the Coulomb interaction. For Rydberg states, the stray electric fields directly couple to the stark shift of the internal Rydberg levels, so that it affects not only the external DOFs but also causes decoherence. We have developed a set of methods to tackle this technological challenge with 8-point diamond-turned electrodes, as I describe in the following sections.

Finally, we would like to perform high-resolution quantum-gas microscopy to image single atoms, and carve optical potential landscapes with the digital mirror device. We shamelessly take advantage of the spectacular advances made by the groups of Markus Greiner and Immanuel Bloch [166, 167]. Unlike Ref. [168], we use the superpixel algorithm [169] to logically encode the phase-amplitude onto the binary digital mirror device (DMD) pattern with DLP technolgoy, and use GPU computing for the real-time rearrangement and preparation of low-entropic states of single atoms on the 2D image plane. As the later part is the work by Youn Seok Lee and Dr. Mahmood Sabooni in our group, I will only briefly describe the high-level ideas without delving into the details.

6.2.1 Cavity QED parameters: Casimir modification

To properly account for the perturbation of the Rydberg states by the proximal surface, we modify the cooperativity parameter

$$\tilde{C} = \frac{4g_0^2}{\kappa\tilde{\gamma}}, \tag{6.4}$$

where we add other sources of atomic decoherence to $\tilde{\gamma} = \gamma + \sum_i \gamma_R^{(i)}$ associated with the Rydberg atom physics. While the cooperativity parameter as the figure of merit favors smaller mode-volume and smaller L_c for traditional cavity QED, our QED platform needs to balance the two competing requirements. On the one hand, we require $g \gg (\kappa, \gamma)$, where γ is the bare decay rate of the atoms. On the other hand, we also demand that the level shift δ_R and spontaneous emission noise γ_R caused by the excited Rydberg state are negligible, compared to the cavity coupling rate g_0. As shown in Fig. 6.3, the reduced V_m enhances the vacuum Rabi splitting g_0, while the surface perturbation is manifested by the increased atomic dissipation rate $\tilde{\gamma}$, effectively diminishing $\tilde{C} \to 0$ for $L_c < 20\mu m$.

At the fundamental level, the enhanced atomic decoherence rate of the Rydberg atoms is caused by the Casimir-Polder surface potentials Δ_{CP} of a Rydberg atom interacting with the dielectric surface. Conservatively, I considered a Rydberg-atom metal surface interaction in the van der Waals regime [170]. While external charges (e.g., bound charges and adatom deposits on the mirror surfaces) can in principle be shielded by the Faraday effect, the Casimir shift of the mirror cannot be eliminated without extreme nanophotonic engineering, because Δ_{CP} has to do with the modification in the vacuum density of states $\rho(\nu)$ for an atom in proximity to the surface (i.e., it is a genuine QED effect!).

In Fig. 6.3, I calculated the cavity QED parameters with the modified cooperativity parameter for a range of mirror transmitivities T with a fixed absorption-scatter loss $\delta = 1.5$ ppm. For $\tilde{\gamma}$, we calculate the van der Waals (vdW) level shift for a single Rydberg atom in the state $|100S_{1/2}\rangle$ with a distance $L_c/2$ away from a perfectly conducting metallic planar surface [170][a]. In addition, I included the blackbody-limited decoherence rate of the Rydberg levels (Appendix A), as we use room-temperature UHV chambers. We find that, for $L_c < 20\mu m$, there is a significant reduction of the effective cooperativity parameter, due to the inhomogeneous broadening of the Rydberg-surface interaction, with the optimal $\tilde{C}$ peaked at $L_c = 20\mu m$. For a larger cavity length, there is a modest reduction of $\tilde{C}$.

As our model does not include other practical challenges of the surface forces (e.g., photoionized bound charges on dielectric surfaces and photoelectric effect on metals from the UV excitation beam, as well as surface adatom deposition [131]), we have intentionally chosen $L_c = 1$ mm and set the cavity transmission $T = 4$ ppm, with single-atom cooperativity of $\tilde{C} \simeq 300$. COMSOL simulation shows that the surface patch charges at this cavity length do not cause significant the decoherence to our Rydberg atoms, and that the stray field from the PZTs is the primary source of dephasing mechanism. The cavity QED

---

[a] The assumption of metal surface is conservative, because the surface force of the dielectric is reduced by the finite Fresnel reflectivity and the reduced image dipole.

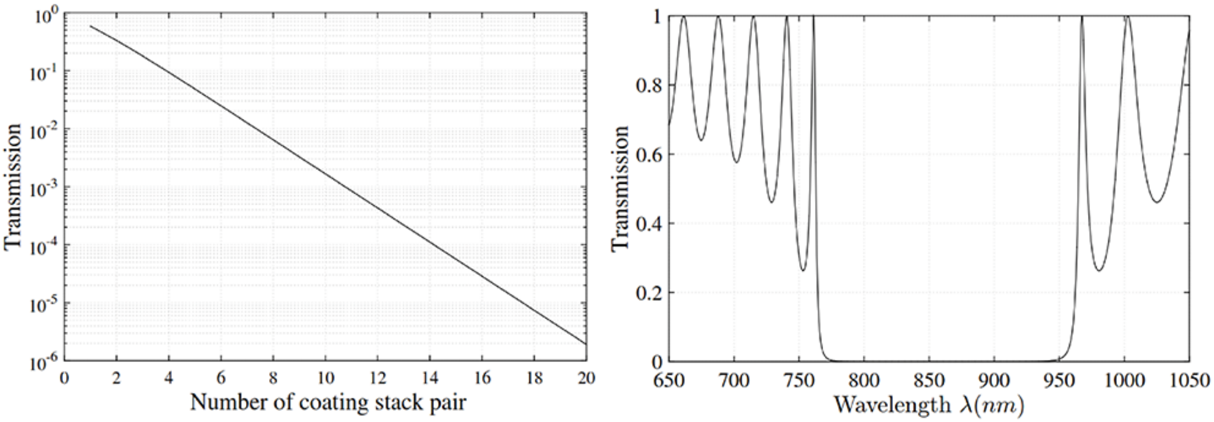

Figure 6.4: **Transmission of a quarter-wave stack Bragg mirror. a,** Resonant transmission with the number N of layers for a bilayer structure at the design wavelength $\lambda_d = 852$ nm. We assume the bilayer coating materials SiO_2 and Ta_2O_5. **b,** Transmission curve as a function of probe wavelength λ at coating stack $N = 18$.

parameters are given by

$$(g_0, \kappa, \tilde{\gamma}) = 2\pi \times (4, 0.1, 2.5) \text{ MHz}. \tag{6.5}$$

The longer L_c permits the use of long-working distance high-NA microscope objectives for single-atom imaging and trapping. In our platform, we plan to shield and compensate the fields generated by the surface patch charges and the stray sources with precision-machined 8-point electrodes.

6.2.2 High-finesse optical cavity

While we cannot identify the proprietary thin-film structures of our optical cavity developed by Prof. Choi, I am allowed to describe the overriding principle for our new IBS thin-film materials and optical cavities. To this end, let me revisit the conventional supermirrors used in the cavity QED and optical clock communities around the world. State-of-the-art optical cavities consist of a quarter-wave stack on mirror substrates in the NIR range. Because of the limited technologies to make good UV mirrors, we concentrate here on the Ion-Beam-Sputtered (IBS) Ta_2O_5/SiO_2 bilayer thin films (with low bandgap near the UV range) on superpolished glass substrates with record optical finesse in the NIR range.

Superpolishing is a method for creating atomically smooth and curved optical substrates. To see the importance of the surface roughness, we note that, for sub-wavelength refractive defects, radiative loss is mainly caused by coherent Rayleigh scattering, where the scattering loss $S = (4\pi\delta_{sc}/\lambda)^2$ is a quadratic function of the surface roughness δ_{sc}. We use the superpolished fused silica substrates from REO. All of our mirror substrates are postselected through AFM measurements and surface profilers within a single superpolishing batch with the surface roughness $\delta_{sc} < 0.3\mathring{A}$ and the theoretical scatter loss $S \simeq 0.2$ ppm. With the atom-by-atom IBS thin films, it is possible to create ultra-low-scatter optical mirror with the same δ_{sc} as the host substrate.

The second challenge to low-loss mirror is to reduce the absorption coefficient A of the IBS thin films (metal oxides). Amorphous films are required to reduce spontaneous Raman scattering of the intracavity field into the thin-film's lattice vibrations (as found in semiconductor micro-cavities). In a reactive ion-beam sputtering, high-energy ions hit a metal target to create a nearly collimated high-momentum Tantalum atomic beam, accelerated towards the substrate. At the location of the substrate, a secondary ion beam is assisted to stimulate the chemical reaction with O_2 atoms near the substrate and deposit highly dense non-porous high-index Ta_2O_5 thin films with excellent stoichiometry. After the IBS coating, it is a standard procedure to anneal the reflective coatings in oxygen-dense environment at $\sim 400°C$ to improve the oxygen homogeneity, to reduce the scattering loss, and to improve the stoichiemetry. Imperfect oxygen surface chemistry causes the absorption losses with state-of-the-art IBS process from REO and ATF, pushing the absorption loss to $A \simeq 1.5 - 10$ ppm [171, 164]. We thereby partition the loss of an optical mirror $\mathcal{L}_{\text{tot}} = T + A + S$ with $\mathcal{L}_{\text{tot}} + R = 1$, where $T(R)$ is the mirror transmittivity (reflectivity).

Our general strategy is to improve the absorption loss A by optimizing the IBS process for a higher index metal oxide film to replace the absorptive Ta_2O_5 layers. To see this, let me introduce the transfer matrix formalism of light propagation with the notations in Ref. [164]. We consider a simple bilayer alternating quarter-wave stack structure with the layer thickness $h_i = \lambda_d/4$ for the refractive index $n_i \in \{n_L, n_H\}$, where n_L (n_H) is the refractive index for the low-index SiO_2 (high-index Ta_2O_5) at the design wavelength λ_d. Each coating layer i is represented by a transfer matrix

$$M_i = \begin{bmatrix} \cos(kh_i) & \frac{i\sin(kh_i)}{Y_i} \\ iY_i \sin(kh_i) & \cos(kh_i) \end{bmatrix}, \tag{6.6}$$

where $Y_i = \sqrt{\frac{\epsilon_0}{\mu_0}} n_i$ and $k = 2\pi/\lambda$. We can also model the absorption-scatter loss $\delta \in \{A, S\}$ with the transfer matrix

$$M_{\text{loss}} = \begin{bmatrix} 1 & \frac{\delta}{4} \\ \frac{\delta}{4} & 1 \end{bmatrix}. \tag{6.7}$$

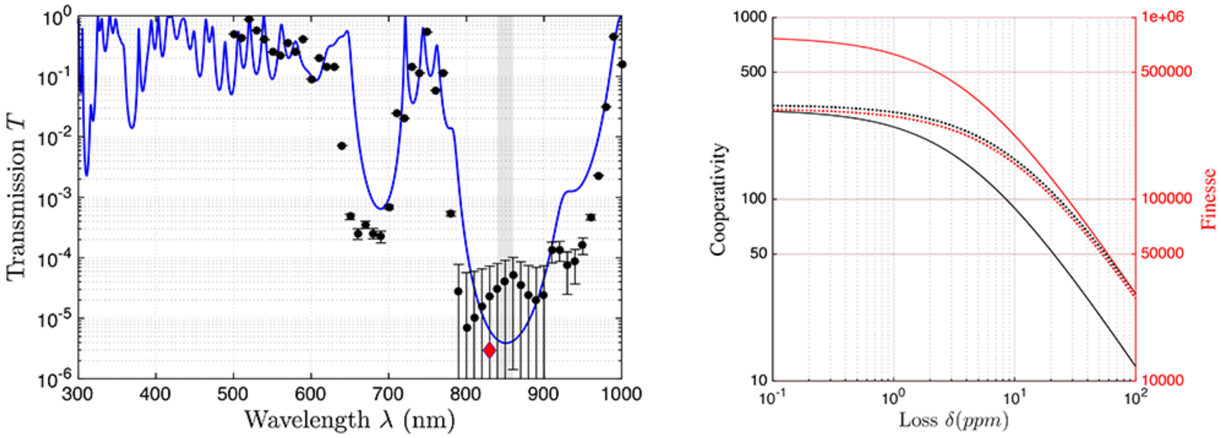

Figure 6.5: **Cavity QED parameters. a,** Cavity mirror transmission is simulated with the transfer matrices. The data points are the result of the spectrophotometry transmission measurement with significant errors at the 10 ppm level. $T = 3$ ppm is determined at 830 nm by laser-based photometric measurements. **b,** Comparison of cavity QED parameters (Cooperativity and Finesse) with the state of art. Our result is shown as the solid line, whereas the parameter of Hood *et al.* [164] is shown as dashed line.

Generally, the absorption loss A is distributed across the metal oxide layers, but we attribute the coating absorption loss with a single transfer matrix M_{loss} on the surface layer.

The overall N-layered structure of the IBS mirror can then be represented by $M_{1,2} = (M_{\text{Ta}_2\text{O}_5} \times M_{\text{SiO}_2})^N M_{\text{Ta}_2\text{O}_5} M_{\text{loss}}$. At the design wavelength λ_d, we find that the transmission of the mirror $T = \frac{1}{n_H}\left(\frac{n_L}{n_H}\right)^{2N}$ is exponentially suppressed by the number of layers N, with the exponent being the refractive index contrast $\frac{n_L}{n_H} \simeq \frac{1}{1.55}$ (for $\text{SiO}_2/\text{Ta}_2\text{O}_5$), as shown in Fig. 6.4a. Our result is numerically consistent with the ATF optical cavities of Refs. [164, 172]. The immediate benefit of using higher-index IBS thin films is that it exponentially suppresses the absorption loss $A \simeq A_0 \exp(-L_m/L_0)$ with the distributed thickness L_m of the metal oxides.

In our laboratory, we use a high-index metal oxide with ~ 30 % larger index contrast than the traditional $\text{Ta}_2\text{O}_5/\text{SiO}_2$ mirrors, with excellent thin-film stoichiometry in a reactive sputtering. Combining our numerical recipe to complex chirped stacks (See the Rainbow UHV viewport in Chapter 3), we have designed and fabricated the cavity mirrors with our partners shown in Fig. 6.5a. Precise laser-based spectrophotometer confirmed the mirror transmission $T = 3.5$ ppm at 830 nm with loss $\delta \sim 1$ ppm. A careful cavity-ring down spectroscopy was performed by our partners at 830 nm with the loss partition method in Ref. [164], and measured the total cavity loss ~ 1.5 ppm. With the chirped design, our coating stack also supports other wavelengths as well. Prof. Choi designed the mirror coating to be compatible with the red-detuned (blue-detuned) magic wavelength condition of Cesium at $\lambda_r(\lambda_b) = 935(687)$ nm for precision-spectroscopy. In addition, our cavity also supports the direct Rydberg-P excitation at 319 nm, although it remains to be seen whether the metal oxides would experience oxygen depletion effects and solarizations [173]. With $L_c = 1$ mm, we achieve the cavity QED parameters of Eq. 6.5 with optical Finesse $\mathcal{F} \simeq 500,000$!

The process tree of the fabrication is as follows:

1. REO fabricates the 7.75-mm diameter superpolished fused silica substrates with surface roughness $\delta_{sc} < 0.3\mathring{A}$ (AFM measurements) for $R_c = 5, 10$ cm (surface profiled). Microscope image is taken and sent to our partner for IBS coating. The entrance surface is tilted by 3° to avoid cavity back-reflection.
2. IBS coating (Partner A)
    (a) Upon the receipt of the substrates, perform dark-field microscopy and confirm the cleaniness of the mirror substrates.
    (b) Apply PMMA photoresist masks on the entrance surface
    (c) Perform the IBS deposition with optimized process over 20 hours (after 10 hours of UHV baking), followed by thermal annealing
    (d) Apply PMMA photoresist masks on the reflective surfaces, and perform the AR coating on the entrance surface
    (e) A small subset (one pair of mirrors in each coating run) undergoes quality check with ring-down and laser-based photometric spectroscopy
3. Glass machining (Partner B)
    (a) Upon the receipt of the mirrors, confirm the conditions of the PMMA masks.
    (b) Diamond CNC machining to cone down the original REO mirror substrates down to the Caltech 1 mm-by-3 mm chamferred design
4. UQML/IQC
    (a) Upon the receipt of the mirrors, perform PMMA removal in spectroscopic grade acetone, followed by spin-coating cleaning and polymer-based liftoff

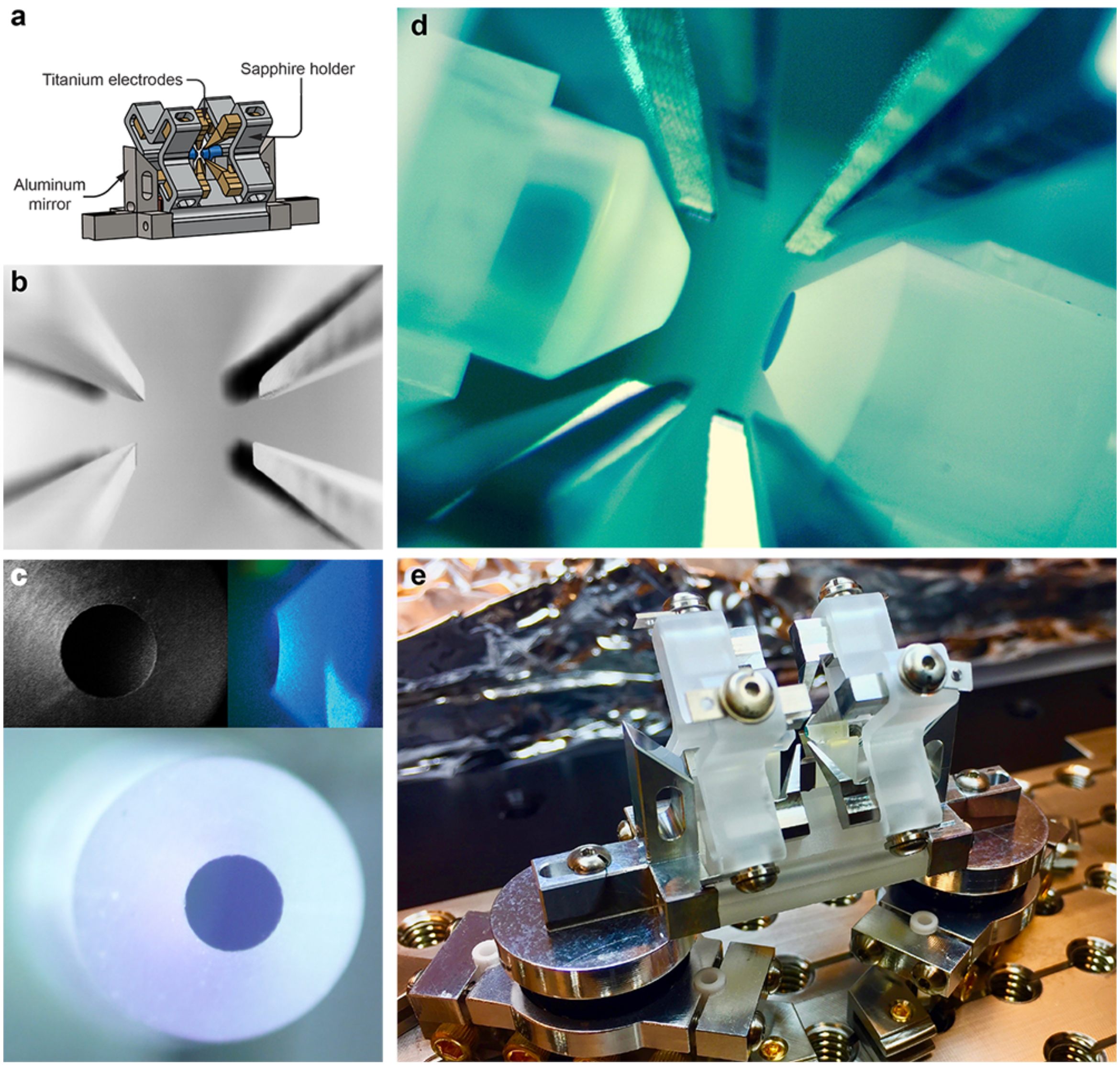

Figure 6.6: **Many-body QED platform.** **a,** CAD rendering of the experimental platform. **b,** High-resolution microscopy of 8-point electrodes. **c,** Dark-field microscopy for characterization and mirror cleaning. **d,** Top-view microscope image illustrating the high-finesse cavity with coned geometry and the diamond-machined Titanium electrodes. **e,** Photo of the many-body QED platform integrated to the superpolished Al mirrors, and single-crystal Sapphire electrode holder.

(b) High-resolution dark and bright-field microscopy for surface inspection (Fig. 6.6c)

(c) Cavity assembly for ring-down spectroscopy at various wavelengths in the UHV chambers and final assembly for many-body QED station

6.2.3 Single-crystal Al_2O_3 platform and piezoelectric motion control

In order to optimally couple external laser fields to the science cavity and to mode-match the cavity quantum fields to the detection system, we need an extreme form of passive and active mechanical engineering. As shown in Fig. 6.6a, our experimental station consists of the Sapphire cage, Science cavity, and the 8-point field-compensation systems.

There were a few design considerations that went into the choice of material for the cage system, besides the UHV/XHV requirements. First, we need a strong dielectric with a large enough band gap for the experimental platform to prevent charge buildup from high-power lasers. Second, we require extremely mechanical rigidity and tensile strength. Third, the CTE of the material shall match the expansion rate of Titanium 8-point electodes. The only UHV/XHV dielectric material, which satisifed all these conditions, was a single-crystal Sapphire Al_2O_3. Al_2O_3 has band gap at $\sim$ 250 nm, and our high-power 319-nm laser beam cannot create patch charges. Sapphire is also one of the strongest materials (second to diamond!), and very good thermal conductivity comparable to that of most metals. In addition, the CTE matches that of Ti within 20% so that the cage system can be integrated and mated with Ti components, with the length tolerances maintained throughout the UHV baking cycles. As shown in Fig. 6.6e, with partner B, we machine the entire experimental platform out of a nearly defect-free single piece of single-crystal Sapphire, a highly non-trivial and costly fabrication procedure given its complex 3D structure. As a vibration isolation stage, we use passive dampers with a custom-molded Kalrez elastomers similar in shape to the NewDamp elastometric isolator, where the shape function was optimized by COMSOL structural mechanics module. All initial design and idea were given by Prof. Choi, and Dr. Liu performed the CAD drawing and implemented the field compensation simulation.

As shown in Fig. 6.7, our Science cavity is mounted on fused silica V-groove blocks (with Epotek 353ND) to relieve the stress-induced birefringence on the IBS thin films. The V-groove were machined with $20\mu m$ tolerances to ensure that the mirror axis is aligned with respect to each other. A single-crystal shear-mode PZT ceramic (custom-ordered from APC International without any electrode) is mounted on top of a $100\mu m$ thick macor piece

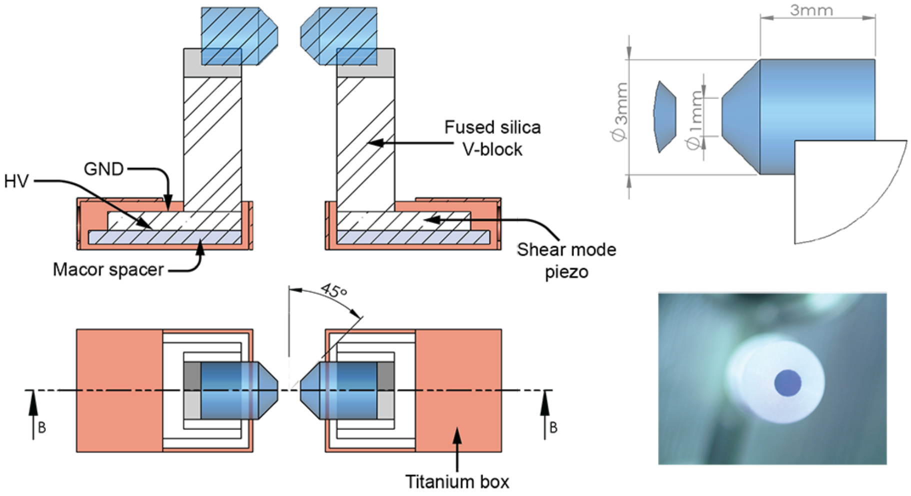

Figure 6.7: **Detailed view of the Science cavity construction and Faraday shielding of high-voltage PZT electrodes.** Cavity mirrors are glued on fused silica v-block by UHV comaptible glue. Shear mode piezo is implied for fine tuning of cavity length and high voltage side is insulated by macor spacer below. Titanium box is to shield electric field from high voltage around 400V on shear mode piezo.

with Epotek H21D silver compounds. We use a single-crystal PZT, instead of the multilayer stack, as we need to stabilize the mirrors position uncertainty $\delta x \simeq \frac{1}{1000} \times \frac{\lambda}{4\mathcal{F}} \simeq \frac{1}{1000} \times 25$ fm ($\sim 1/40$ of the charge radius of a single proton[b]). The ground-plane is aligned towards the Science cavity, as the ground-plane acts as a distributed Faraday shield.

Because the single-crystal shear-mode PZT requires a 400 V for $0.5\mu m$ displacement, our numerical simulation suggests that it is critical to further shield the stray fields generated from the PZTs by at least 60 dB (with Rydberg Stark shift 3 kHz for 400 V). As shown in Fig. 6.7, $50\mu m$-thick Titanium plates surround the shear-mode PZTs as an effective faraday cage to attenuate the electric field generated by the high-voltage electrodes. We will describe the efficacies of our Faraday shields and external field control systems in the next section, as supported by analytic and computational multiphysics models. Aluminum mirrors (Al 6061-T6) are installed at the rear-ends of the cavity mirrors. In this way, we can couple external fields to the fundamental cavity mode through the vertical UHV viewport (Fig. 6.8). The Aluminum mirrors were single-point diamond turned to

---

[b] We developed a proprietary high-voltage amplifier with reduced noise to meet this stringent requirement of S/N ratio of 70 dB. Indeed, our home-made high-voltage source has a RMS noise level of $100\mu V$ over $1kV$ at $1-10Hz$ with a SNR $\simeq 70dB$

yield surface roughness $8\mathring{A}$.

The optical cavity was aligned using a stabilized He:Ne laser at 633 nm with 1 MHz linewidth. The Science cavity has a moderate finesse $\mathcal{F} \sim \mathcal{O}(10^3)$ at this wavelength, and we use this laser beam to align the respective mirrors for mode matching. 5-axis translational tilt-roll stages are used together with a PZT actuator for precision alignments. Table 6.1 includes the material properties of all the components used in the cavity assembly.

6.2.4 Faraday shielding and external field control with 8-point electrodes

Highly-excited Rydberg states are extremely sensitive to stray electric fields. They cause inhomogeneous Stark-shift broadening of the Rydberg levels for small fields. For large fields, the static electric field can ionize the Rydberg atoms with the ponderomotive force. However, for cavity QED, we require single-crystal shear-mode PZTs with voltages ~ 400 V. Indeed, our COMSOL simulation shows that the charges generated by the high-voltage electrodes of the PZT stacks give rise an electric field $E \simeq 5$ kV/m at the center of the cavity. On the other hand, we demand that the stray fields have electric field strengths $\ll 0.05V/m$, so that the Stark shift is on the order of the natural linewidth of the Rydberg state $|100S_{1/2}\rangle$ from our quantum-defect theory calculation. Hence, we require a minimum Faraday shielding factor of 50 dB.

Dr. Liu employed two countermeasures for stray field compensation. First, she has surrounded the high-voltage PZT electrodes with a single layer of Titanium plates. From her COMSOL simulation, this cage itself can alone attenuate the PZT fields by 45 dB.

Material	CTE($10^{-6}m/(mK)$)	Temp. rating(^oC)	Outgassing rate
Titanium (pure)	$8.5-9$	600	1.8×10^{-9}
Sapphire	5.3	2030	NA
Fused silica	0.55	200	NA
Aluminum (AL6061 T6)	23.6	160	2.8×10^{-10}
Piezoceramic 850	NA	360	NA
Kalrez(Dupont)	NA	300	$1\times10^{-10}-6\times10^{-10}$
Alumina(Al_2O_3)	8.1		$1\times10^{-9}-1\times10^{-8}$
Epotek 353ND	54	NA	1.8×10^{-9}
Epotek H21D	42	NA	1×10^{-9}

Table 6.1: Table of component properties

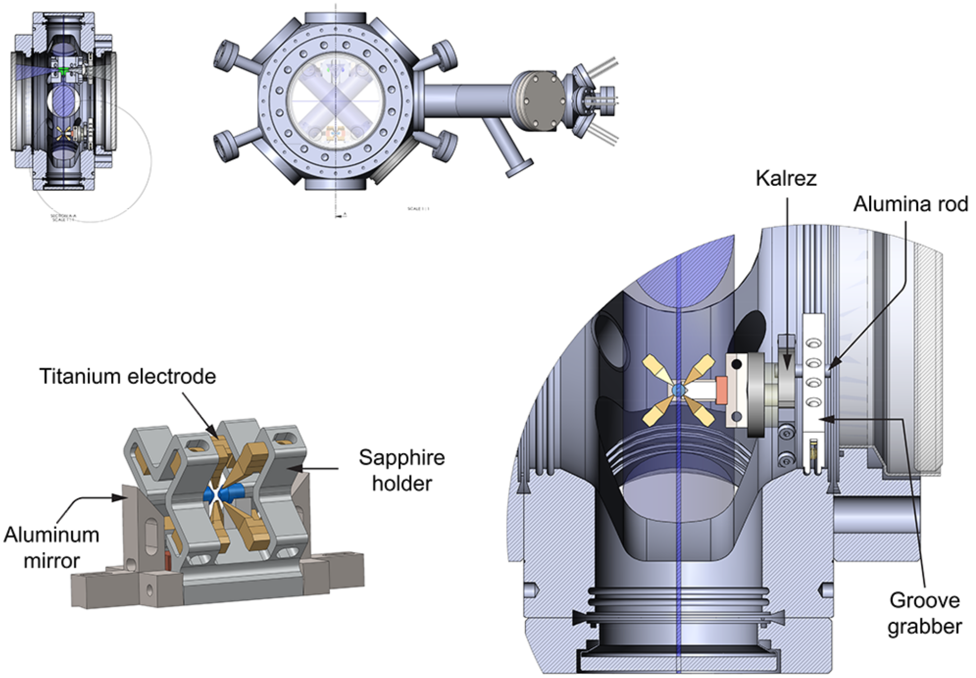

Figure 6.8: **Rendering of the many-body QED platform installed in the Science chamber.** The many-body QED platform consists of Sapphire cage, Science cavity, and 8-point field-compensation systems. Precision-polished Aluminum mirrors are integrated to the platform to provide optical access to the cavity fundamental mode, and the entire mechanical platform is vibration-isolated by passive Kalrez dampers, custom-molded into a numerically optimized geometry.

Second, we have fabricated an 8-point electrode system, made of single-point diamond-turned Titanium blades with surface roughness $\sim 10\AA$. These electrodes not only shield the stray fields from the PZTs but also from the unavoidable patch charges on the mirror surfaces. Fig. 6.9 illustrates the finite-element method (FEM) electromagnetic simulation of our many-body QED platform. Prof. Choi has measured the absolute positions of the fabricated electrodes with imaging uncertainty $\simeq 10\mu m$, where $d = 2\sqrt{2}mm$ and $s_{1,2,3,4} = 750/719/725/712\mu m$. Dr. Liu found that we could reduce the Stark shift of the high-lying Rydberg state $|100S_{1/2}\rangle$ state by less than 1 kHz, even when the PZT electrode is charged to 1 kV! The unbalanced compensated field lines in Fig. 6.9d are due to the spatial misalignments of the Ti electrodes.

Mechanically, smooth and well-defined geometries of these electrodes were necessary,

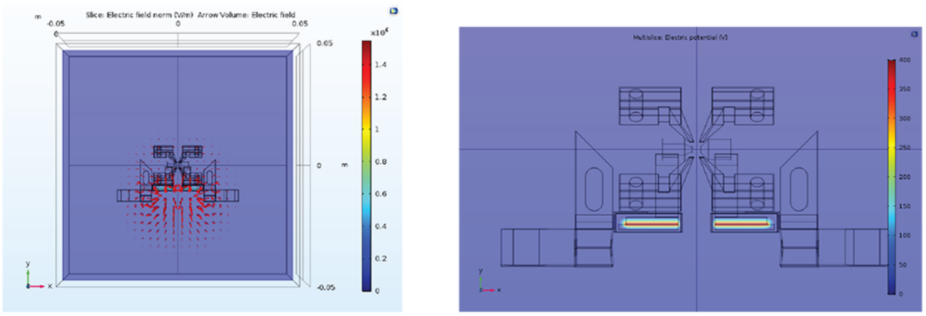

(a) vector components of electric field (b) magnitude of electric field

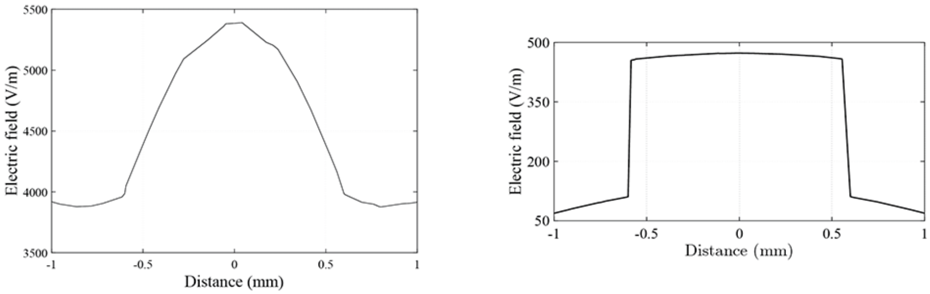

(c) Electric field along cavity axis without shielding effect (d) Electric field along cavity axis including shielding effect

Figure 6.9: **FEM simulation of stray-field compensation with Faraday enclosure and 8-point electrode systems. a,** Vector components of the electric field generated by the PZT actuators. **b,** Magnitude of the electric field with the Titanium Faraday shield enclosure. **c,** The electric field magnitude along the cavity axis without any passive shielding. **d,** Demonstration of a shielding factor 60 dB with the combination of Titanium Faraday shields and external 8-point electrodes. The asymmetry in the field lines is caused by the misalignment of the Ti electrodes.

as any sharp edge can seed electric charges as point sources, where fluctuating charges be pinned down by the local potentials of the surface defects. In fact, we have engineered the tip of the electrodes to be nearly atomically smooth in a sphere of 100μm diameter, which was achieved through laser ablation technique, where the surface tension of laser ablated Ti collapses into smooth spheres. These points can then act as external charging tips as effective Faraday shielding (when the electrodes are grounded), but also as external field control system for polarizing and preparing the dipole orientations of anisotropic Rydberg states (e.g., higher angular momentum states).

Prof. Choi and Dr. Liu have designed the electrode blades based on an analytical

8-point charge model [174]. Namely, we assume that the electric field can be computed by the charges at the locations of the 8 tips, as supported by the expensive COMSOL FEM simulation. As shown in Fig. 6.10, by tuning the relative geometries of the electrodes, we have optimized the 8-point model to create any static electric field $\vec{E}(\vec{r})$ up to the quadratic form by individually charging the electrodes. With the 8-point electrodes, we can thereby cancel out inhomogeneous field broadening within the Science cavity up to the first order. In addition, as shown in Fig. 6.10c, we can create sharp zero fields for single-site Rydberg addressing, as well as ion-trap style electrodynamical trapping of Rydberg states (Fig. 6.10d). For $|100S_{1/2}\rangle$ state, the resolution of the single-site addressability with field control is given by $\sim$ 100 nm with residual Stark shift of 2 kHz, well below the optical resolution of our quantum-gas microscope as well as the characteristic lattice constants $a_0 \simeq 400$ nm. In Fig. 6.11, we have investigated the field fluctuation caused by the mechanical tolerances of the 8-point electrodes.

6.2.5 Real-time manipulation with holographic projection of optical potential landscapes

While I was not directly involved in much of this work, I have helped designed the many-body QED platform to be compatible with the Special Optics high-NA microscope objective. Early work was carried out by Prof. Choi and Dr. Liu, followed by Dr. Sabooni's work on the superpixel and Hungarian algorithms. For these reasons, I only provide minimal materials for the description.

For the quantum spin ice experiment, a single missing atom can completely break the ice rule. A single defect can, thereby, collapse the quantum spin liquid in the ground-state manifold. On the other hand, the loading efficiencies in microscopic optical traps are limited by the collisional blockade mechanism. Namely, photo-assisted two-body collision rates can dominate over all other rates, opening up a channel to photo-associate Cs_2 molecules with 50% probability. While this effect can be used as an efficient way for parity measurements, it presents a challenge to prepare a many-body system into its low-entropic Mott insulating state with success probability $P \sim \left(\frac{1}{2}\right)^N \to 0$ for N atoms.

One powerful method has been the utilization of the superfluid-to-Mott insulator transition in the Bose-Hubbard model, where it is possible to create a microscopic atom array with almost no defect [166]. Another method is to modify the Lenner-Johns potentials of the molecular transitions by dressing the Cs atoms with a weak blue-detuned field during loading. This causes a light shift to the excited molecular transition, thereby shielding the Cs atoms from colliding each other. However, both of these methods are not applicable

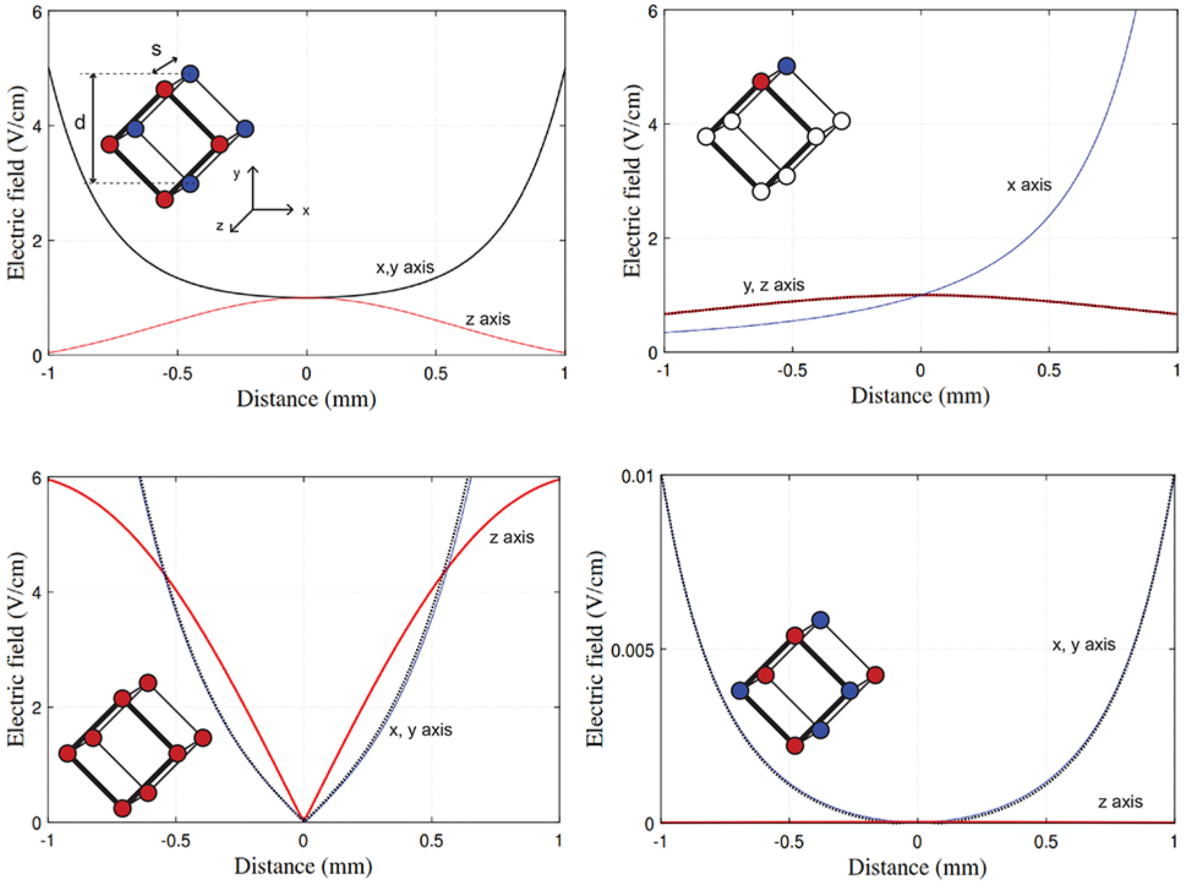

Figure 6.10: **Electric field configurations with the 8-point charge model.** Each circles represent the positions of electrode tips in a 8-point charge model. Red (blue) color represents the positive (negative) charge, while white color is the electric ground.

for $N \simeq 100$ atomic systems, where we require very large N to observe the illusive gapless excitations of artificial photons!

Here, Dr. Sabooni used a Ti DLP3000 digital mirror device (DMD) to form a dynamical optical trap that is holographically projected onto the image plane. Unlike other existing methods [168] with quantum-gas microscopy, we use the superpixel algorithm in Ref. [169] in order to logically map the phase-amplitudes onto the physically binary sub-pixels of MEMS mirror arrays on the DMD device. In addition, we use GPU-accelerated CUDA framework to compute the holographic images and parallelize the lookup tables to create

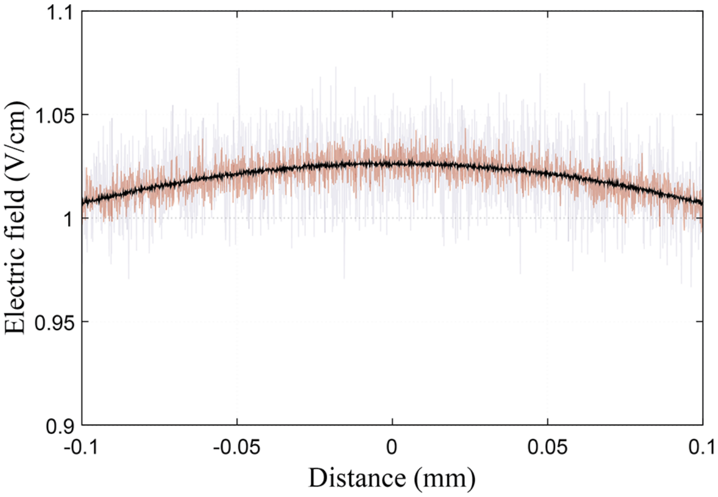

Figure 6.11: **Uncertainty analysis of the electrode positions with the 8-point charge model.** Each curve shows the electric field offset caused by the position uncertainty of the electrodes. Black solid line is electric field along cavity axis with position uncertainty of $1\mu m$ with 3% DC offset. Grey line is the result for position uncertainty $25\mu m$ with 8% of DC offset.

a real-time streaming to reconfigure the trapped atoms. In this way, it is possible for us to rearrange a macroscopic atom array. Currently, he can compute the optimal reconfiguration for 100 atoms within 100 ms.

Our quantum-gas microscope is based on a custom objective from Special Optics. It is a custom-built microscope objective based on our UHV viewport information (namely, with glass thickness compensation). The numerical aperture of the objective is 0.5 over $700 - 1000$ nm, with a working distance 23.4 mm. With the OSLO simulation, we have confirmed that it is possible to operate this objective for sub-wavelength imagine with $|6S_{1/2}\rangle \rightarrow |7P_{3/2}\rangle$ transition at 455 nm, albeit with a focal length shift $-100\mu m$, which can be compensated with finite-correction at the input pupils. The peak-to-valley wavefront error is set less than $1/10\lambda$ at $850 - 940nm$, and the field of view is $150\mu m$.

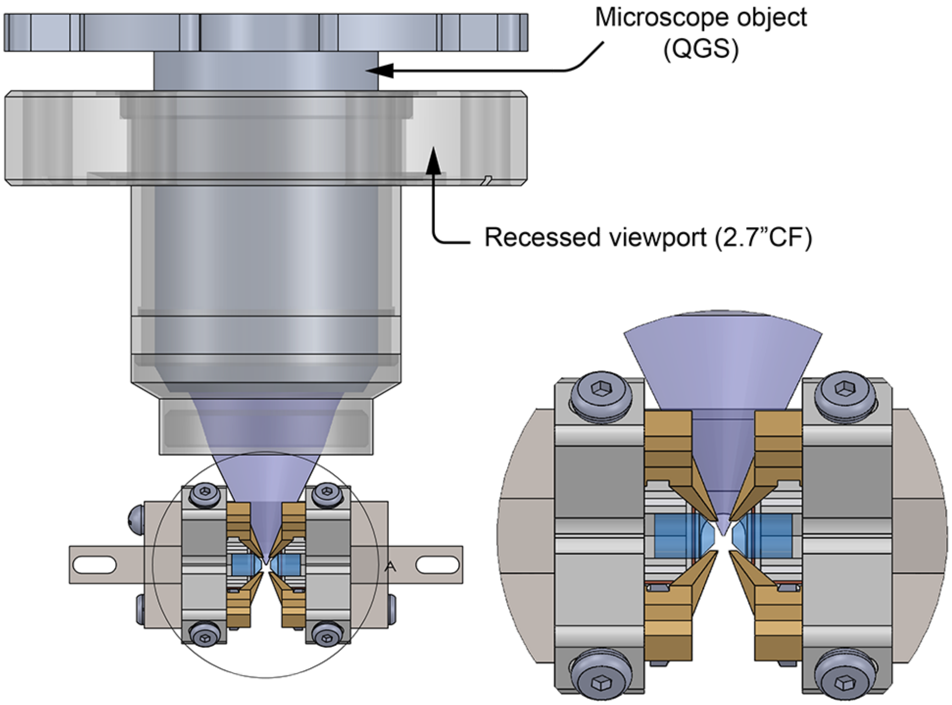

Figure 6.12: **Many-body QED platform integrated with a quantum-gas microscope.** High-resolution custom microscope objective is used with viewport aberration correction with NA= 0.45. Optical potential landscape is projected to the quantum gas, creating arbitrary 2D atomic arrays.

Chapter 7

Conclusion

In my MSc thesis, I have mainly discussed a set of technological advances that addressed major challenges in three distinct research areas – Quantum gas (Chapter 3 and Chapter 5), optical clock (Chapter 4), and cavity QED (Chapter 6).

Our effort towards many-body QED began with the development of extreme-high-vacuum (XHV) chamber system, tailored for state-of-art AMO experiments (Chapter 3). I have explored and developed new vacuum passivation techniques, as well as Rainbow anti-reflection (AR) coating methods to address the unique challenges of utilizing UV-wavelength high-power laser fields and electrically sensitive Rydberg states, and of requiring the ultra-low base pressure for achieving long-lived atomic quantum matter. The result of our effort is the lowest operating base pressure of $P \simeq 10^{-13}$ Torr for an AMO experiment.

In Chapter 4, I discussed our laser infrastructure with wavelength ranges spanning over an octave, from 317 nm to 1571 nm, and our method of phase-synchronizing these laser fields. I also discussed our work on efficiently frequency-converting high-power ultra-narrow-band optical fields for high-lying Rydberg excitations, and Science cavity stabilization. In Chapter 5, I provided the driven-dissipative framework of self-consistently treating both the internal and external states of neutral atoms. Using quantum Monte-Carlo wave-function method, I have optimized the cold atom transport processes, both between the Source and Science chambers, and within the Science chamber. I discussed the case of fully quantizing the external motion and applied the formalism for non-degenerate Raman sideband cooling for atoms in a high-finesse cavity. Finally, I provided potential pathways to utilize the nonlinear phonon spectrum as quantum spin system, and speculated as future work on how such phonon-phonon interactions may be utilized for simulating self-organized many-body models, such as Lieb-Liniger model and 1D Tonks-Girardeau Bose gas.

In Chapter 6, I have discussed the critical challenges of combining strongly coupled cavity QED system with Rydberg states, and how we mitigate the extraordinary surface potentials and charging effects with Faraday shielding system. I described our Science cavity, which required the development of new thin-film IBS coating stack for record-level optical finesse $\mathcal{F} \sim 5 \times 10^5$. At the moment, we currently possess the laboratory capabilities to perform proof-of-concept experiments that demonstrate essential features of many-body QED. In this chapter, I describe the present experiments (Rydberg quantum-dot and quantum spin ice) that we are working on, and provide a short-term vision of potential experiments for the next 3–4 years. The experimental platform that I have helped to develop is, in some sense, a laboratory platform that could be applied to a wide variety of research areas with minor modifications, from quantum communication and computation, to quantum sensing and simulation.

7.1 Rydberg quantum-dot

7.1.1 Present work

We are trying to perform the first experimental demonstration of the Rydberg quantum-dot and to observe collectively-enhanced cooperativity factor $C_N \sim 10^3$ in the regime of full Rydberg blockade. Within the low-energy sector of each of the excitation subspace, the optical nonlinearity in our system is identical to that of the Jaynes-Cummings (JC) model (Chapter 2). The structural nonlinearity of the effective JC spectrum can be inferred from the measured autocorrelation function $g^{(2)}(\tau) \ll 1$, as the two-photon suppression is caused by the phenomena of photon blockade. By modifying the dressing strength of the Rydberg states, we can continuously map the crossover from the Tavis-Cummings (TC) model with non-interacting atoms to the effective JC model, caused by the Rydberg blockade, as shown in Fig. 2.7.

From the viewpoint of many-body physics, both the TC and JC models are interesting spin-boson Hamiltonians with close relationship with the Kondo problem. The autocorrelation function for photons measured through the optical cavity can be understood as a string order $g^{(2)} \propto \frac{1}{N^2} \sum_{ijkl} \langle \hat{\sigma}_+^{(i)} \hat{\sigma}_+^{(j)} \hat{\sigma}_-^{(k)} \hat{\sigma}_-^{(l)} \rangle$ with the input-output formalism. The resulting $g^{(2)}$ can utilized as an order-parameter for examining whether this transition is simply a cross-over or a quantum phase transition. We are currently capable of transporting ultracold atoms to the interaction region with little recoil heating, and have recently installed the new quantum-dot platform into the UHV chamber. We expect to complete this experiment in the next few months, where we hope to observe unprecedented vacuum

Rabi splitting $g_0 \sim 1$ GHz with the cavity QED parameters $(\sqrt{N}g_0, \kappa, \gamma) = (10^3, 0.5, 2.5)$ MHz.

7.1.2 Future direction

Cavity-based quantum network and computation

The enhanced single-quanta-level optical nonlinearity can be utilized for demonstrating the early proposals for quantum networks and quantum computing with conventional cavity QED setups [175, 16, 176, 177, 14]. Many of these proposals have been translated over to circuit QED experiments, and have been understood by the AMO community too far ahead of its time with the parameter space that typical neutral and ionic atoms can occupy. With neutral atoms, since we can easily manipulate 10^6 atoms with inherent indistinguishability, there is a room for optical cavity QED to contribute and compete with superconducting counterparts.

In our experiment, we can take advantage of the collectively enhanced cooperativity factor $C_N \sim 10^3$ in the effective JC model. Our quantum-dot platform further allows single-site addressability with optical resolution $\sim 2\mu$m. We can easily envision to couple our real-time rearrangement capabilities to shelve atoms spatially to the anti-node of the cavity to protect these storage atoms from the cavity-mediated quantum gates. By virtue of single-site addressing and collective enhancement, we have the capability to perform arbitrary ultrafast two-qubit gates [176, 177] through cavity-mediated interactions with gate rates $J_{ij} \simeq N g_{\text{eff}}^2/\Delta \sim 10$ MHz between the long-lived hyperfine clock states of any two Cs atoms with second-long coherence times. In the short term, the total number of atoms with single-site addressability would likely be limited to $N \sim 100$ atoms, due to the technical limitation of our DMD device. We believe that it is possible for us to make rudimentary progress in this direction, without significantly developing new laser addressing technologies, for $N \sim 30 - 40$ atoms with fully programmable connectivity J_{ij}. It remains to be seen if we could take advantage of the theoretical scaling of the entanglement fidelity $F \sim 1 - 1/C_N$ with respect to the cooperativity $C_N \sim 10^3$.

Superradiant laser and optical-to-microwave converter

In a typical laser, the characteristic bandwidth of the gain medium is many order of magnitude wider than that of the cavity mode. Hence, the laser output is narrowed by the effective optical feedback of the cavity modes. In our experiment, we can access the so-called superradiant laser regime [178, 179], where the laser operates in the bad cavity limit.

Here, the gain medium is ultra-narrow-band compared to the transmission bandwidth of the cavity, and the laser stability is decoupled from the mechanical vibrations of the cavities. Such a laser can be utilized for optical clock applications by putting an ensemble of atomic species (e.g., Yb atoms) typically used for optical lattice clocks. In this sense, the superradiant laser is an active optical clock, where the lasing feedback occurs on a clock transition of the trapped atoms.

Rydberg states are long-lived and require narrow-linewidth laser to access high-lying Rydberg states. In the limit of strong Rydberg blockade, the doubly excitations are highly suppressed in the ultracold atomic sample, thereby realizing an effective spin$-1/2$ system that is coupled to the resonator mode. Cavity QED in such a regime can be considered as a "single-atom" laser operating with threshold intracavity photon number $n_0 = \frac{\gamma_\perp^2}{2Ng_0^2} \simeq 10^{-8}$! Utilizing the narrow-linewidth transition with optical $Q \sim 10^{13}$, we can realize an UV superradiant laser with Allen variance $\sim 10^{15}$ for a single-atom gain $C_N \sim 10^2 - 10^3$. The main challenge with this direction is whether it is possible to achieve high-degree of electromagnetic shielding, which may cause Stark inhomogeneous broadening of the Rydberg states. We also have some ideas with the DRDC, where we plan to combine superradiant lasing with Rydberg-enhanced microwave transitions between the Rydberg's angular momentum states. In this scheme, we estimate single-photon-level conversion of microwave photons to and from optical photons in the NIR range. The primary limitation in this direction would be the background microwave photons at room temperature.

Quantum Ising annealing machines with single-site addressability

Absent any cavity-mediated spin-spin interaction, the Rydberg lattice system in our hand is a natural long-range transverse Ising model. We can utilize direct Rydberg-Rydberg interaction with single-site addressability of our high-resolution imaging system for quantum annealing application. We could program the spin-exchange coefficients by projecting arbitrary 2D potential landscapes, where the interaction coefficients J_{ij} encode the optimization problem. With Rydberg-dressing techniques, we can adiabatically turn on the $J_{ij}(t)$ by the laser power, which dresses the hyperfine qubits, to evolve the trivial ground state of ferromagnetically phased atoms into that of the target Hamiltonian. Without cavity coupling, the range of the connectivity (locality of the interaction) would likely be limited to $3 - 4$ sites for $N \sim 100$ atoms, without further improving the resolution of our DMD device. Nonetheless, this would represent a considerable advance in the field.

Multimode cavity QED with ultrastrong coupling: Transversal waveguide QED

An exciting direction with our Rydberg quantum-dot platform is to utilize the collectively-enhanced atom-cavity coupling rate $\sqrt{N}g_0 \simeq 1$ GHz for multimode cavity QED. In this domain, the non-degenerate transversal modes of the spherical cavity can all couple to the Rydberg-blockaded atomic ensemble, where the discrete modes represent the dispersion of the resonator. In the limiting case of infinite transverse modes, we can consider this as a 2D version of waveguide QED in photonic slab. Here, the 2D photonic bandgap of the photonic crystal is occupied by the non-degenerate transversal modes of an empty cavity. Similar to the conventional waveguide QED regime, we expect to observe atom-field bound states and renormalized spin-spin interactions in the bandgaps. The main question in this direction is the sphericality of the mirrors that defines the energies of the higher-order Hermite-Gauss modes of the resonator. Nonetheless, we may be able to perform proof-of-principle experiments with a few transversal modes.

Quantum chemistry: The assembly of Rydberg optical Feshbach molecules

Our experimental platform has the capability to image and manipulate individual atoms, and to excite them to high-lying Rydberg states. In fact, we believe that we are the only group capable of achieving both the single-site addressability and direct Rydberg excitation at the moment. Combining these two powerful methods enables us to do basic molecular spectroscopy of long-ranged Rydberg molecules. Previous work in this area indirectly measured the bond lengths of the Rydberg molecules, absent the spatial resolution to observe the molecules themselves. In our experiment, we can controllably place two Cs atoms in proximity $\sim 2-3\mu m$, and cause quantum-chemical reactions by exciting them to high-lying Rydberg states. The Born-Oppenheimer potential of the Rydberg molecules can further dress the ground-state potential to cause optical Feshbach resonance, allowing long-ranged ground-state Cs_2 molecules. We can further detect these molecules and simulate the reaction rates that depend on the initial spin states of the atoms at ultracold temperature. For this experiment, it would be useful to integrate an UHV-compatible multi-channel-plate (MCP) detector with unit quantum efficiency for single charge detection. In this way, we can utilize the MCP signal to discriminate the Rydberg ions from the Rydberg molecules.

7.2 Many-body QED

7.2.1 Present work

Currently, we have assembled the many-body QED platform with the high-finesse optical cavity and 8-point electrodes. We are currently in the stage of integrating this platform into the XHV Science chamber, along with the Rydberg quantum-dot platform. Since we share the UHV chamber for both platforms, we can readily also start the many-body QED experiment, upon completing the Rydberg quantum-dot experiment. In fact, this is the present goal.

Here, we are trying to utilize single-atom-level strong coupling $g_0 > \kappa, \gamma_\perp$ for injecting quantum fluctuation into the spin ice background. In the first experiment, we are first planning to detect the emergent spinon (magnetic monopoles) in the thermal spin ice model by arranging atoms into the checkerboard pattern, as described in Chapter 2. These magnetic monopoles can be optically imaged through a high-resolution quantum-gas microscope, and we may observe the dipolar interaction between these fractionalized gauge charges. The extensive ground-state degeneracy can be detected by reconstructing the 2D band structure with optical Bragg spectroscopy with ultracold atoms.

In the second experiment, we plan to utilize the cavity vacuum to introduce the quantum fluctuation to melt the extensively degenerate ice configuration states [180]. Certainly, the most exciting would be the discovery of a quantum spin liquid phase through the measurement of dynamical spin structural factor $\mathcal{S}(\vec{k}, w)$. $\mathcal{S}(\vec{k}, w)$ measures the dispersion of the quantum liquid by creating a gapless artificial photon, and we hope to observe the linear cone-like dispersion of these topological excitations. Absent achieving this paramount goal, we believe that it is certainly possible to detect the emergent electric charge (vison excitation), as these are gapped topological defects of the order J_{ring}. We may observe Abelian braiding statistics by implementing string operation on the empty plaquettes with controlled ring-exchange interactions. We hope to begin these experiments next year.

7.2.2 Future direction

Kitaev honeycomb and 2D Levin-Wen string-net models

Recently, Dr. Dong and Prof. Choi have developed an analog method to synthesize the Kitaev honeycomb model with Rydberg atoms with our many-body QED platform [181]. Similar to the localized Rydberg-mediated spin-spin interaction (Section 2.5.1), we can create the anisotropic coupling that depends on the bond direction of the honeycomb model. In this setting, we can also apply the topological braiding operation by encoding the string operations with the cavity photons [101], where homodyne detection of the cavity-relaxed field can be utilized to measure the braiding matrices of the non-Abelian anyonic vortices. The main challenge with this direction is the cavity photon lifetime $1/\kappa$, which may be too short for the reasonably long string operator to the complete its evolution.

Dr. Dong and Prof. Choi have developed a method to create an effective 3-body interaction by using a generalized Rydberg Forster resonance. These interactions can be utilized to create 3-body Ising terms in a honeycomb lattice, known as the Levin-Wen string-net model. It remains to be seen whether the reduced 3-body interaction coefficient is sufficiently large, compared to the realistic decoherence rate, caused by photoionization of the strong Rydberg excitation fields. Beyond the standard quantum defect theories, we would need to estimate the impact of the ponderomotive force on the Rydberg electron in the background of a strong laser field.

Many-body QED: Spaghetti regime

We currently have the capability to move $\Lambda \ll g_0$ to and from $\Lambda \gg g_0$, and explore the entire parameter space of Fig. 1.5. When we set the detunings Δ_a, Δ_p of the cavity and laser fields near resonance of the transition frequency, it is no longer possible to adiabatically eliminate the atomic and photonic degrees of freedom. We have called this domain, "Spaghetti regime," because we currently lack the theoretical capability to clearly understand the essential physics. The good news is that we certainly have the laboratory capability to access the physics of this regime. One unknown is the mirror degradation upon exposure to ultracold atoms. Our backup plan is to use the RF plasma cleaning through the 8-point electrodes. Hopefully, this method would allow us to reduce the absorption losses caused by the metallic monolayer of Cs atoms deposited onto the super mirrors.

Bibliography

[1] Nielsen, M. A. & Chuang, I. L. *Quantum Computation and Quantum Information* (Cambridge University Press, Cambridge, 2000).

[2] Blatt, R. & Wineland, D. Entangled states of trapped atomic ions. *Nature* **453**, 1008 (2008).

[3] Bloch, I. Quantum coherence and entanglement with ultracold atoms in optical lattices. *Nature* **453**, 1016 (2008).

[4] Clarke, J. & Wilhelm, F. K. Superconducting quantum bits. *Nature* **453**, 1031 (2008).

[5] Hanson, R. & Awschalom, D. D. Coherent manipulation of single spins in semiconductors. *Nature* **453**, 1043–1049 (2008). URL `http://dx.doi.org/10.1038/nature07129`.

[6] Kimble, H. J. The quantum internet. *Nature* **453**, 1023–1030 (2008).

[7] Ladd, T. D. *et al.* Quantum computers. *Nature* **464**, 45 (2010).

[8] Schäfer, V. M. *et al.* Fast quantum logic gates with trapped-ion qubits. *Nature* **555**, 75 (2018).

[9] Bloch, I., Dalibard, J. & Nascimbène, S. Quantum simulations with ultracold quantum gases. *Nature Phys.* **8**, 267 (2012).

[10] Georgescu, I. M., Ashhab, S. & Nori, F. Quantum simulation. *Rev. Mod. Phys.* **86**, 153 (2014).

[11] Fowler, A. G., Mariantoni, M., Martinis, J. M. & Cleland, A. N. Surface codes: Towards practical large-scale quantum computation. *Phys. Rev. A* **86**, 032324 (2012).

[12] Lekitsch, B. *et al.* Blueprint for a microwave trapped ion quantum computer. *Science Adv.* **3**, e1601540 (2017).

[13] Copsey, D. *et al.* Toward a scalable, silicon-based quantum computing architecture. *IEEE J. Selected Topics in Quantum Electronics* **9**, 1552 (2003).

[14] Reiserer, A. & Rempe, G. Cavity-based quantum networks with single atoms and optical photons. *Rev. Mod. Phys.* **87**, 1379 (2015).

[15] Lodahl, P., Mahmoodian, S. & Stobbe, S. Interfacing single photons and single quantum dots with photonic nanostructures. *Rev. Mod. Phys.* **87**, 347 (2015).

[16] Cirac, J. I., Zoller, P., Kimble, H. J. & Mabuchi, H. Quantum state transfer and entanglement distribution among distant nodes in a quantum network. *Phys. Rev. Lett.* **78**, 3221–3224 (1997). URL `http://dx.doi.org/10.1103/PhysRevLett.78.3221`.

[17] Gottesman, D. & Chuang, I. L. Demonstrating the viability of universal quantum computation using teleportation and single-qubit operations. *Nature* **402**, 390–393 (1999).

[18] Amico, L., Fazio, R., Osterloh, A. & Vedral, V. Entanglement in many-body systems. *Rev. Mod. Phys.* **80**, 517–576 (2008). URL `http://dx.doi.org/10.1103/RevModPhys.80.517`.

[19] Briegel, H.-J., Dür, W., Cirac, J. I. & Zoller, P. Quantum repeaters: the role of imperfect local operations in quantum communication. *Phys. Rev. Lett.* **81**, 5932–5935 (1998).

[20] Briegel, H.-J., van Enk, S. J., Cirac, J. & Zoller, P. *The Physics of Quantum Information*, 192 (Springer, New York, 2000).

[21] Duan, L.-M., Lukin, M. D., Cirac, J. I. & Zoller, P. Long-distance quantum communication with atomic ensembles and linear optics. *Nature* **414**, 413–418 (2001).

[22] Rovelli, C. & Smolin, L. Spin networks and quantum gravity. *Phys.Rev. D* **52**, 5743 (1995).

[23] Saffman, M., Walker, T. G. & Mølmer, K. Quantum information with rydberg atoms. *Rev. Mod. Phys.* **82**, 2313 (2010).

[24] Gallagher, T. F. *Rydberg atoms* (Cambridge University Press, 2005).

[25] Hood, C. J., Kimble, H. J. & Ye, J. Characterization of high-finesse mirrors: Loss, phase shifts, and mode structure in an optical cavity. *Phys. Rev. A* **64**, 033804 (2001).

[26] Jaynes, E. & Cummings, F. Comparison of quantum and semiclassical radiation theories with application to the beam maser. *Proc. IEEE.* **51**, 89 (1963).

[27] Rabi, I. I. On the process of space quantization. *Phys. Rev.* **49**, 324 (1936).

[28] Dicke, R. H. Coherence in spontaneous radiation processes. *Phys. Rev.* **93**, 99–110 (1954). URL `http://link.aps.org/doi/10.1103/PhysRev.93.99`.

[29] Tavis, M. & Cummings, F. Exact solution for an n-molecule—radiation-field hamiltonian. *Phys. Rev.* **170**, 379 (1968).

[30] Sudarshan, E. C. G. Equivalence of semiclassical and quantum mechanical descriptions of statistical light beams. *Phys. Rev. Lett.* **10**, 277 (1963).

[31] Glauber, R. J. Coherent and incoherent states of the radiation field. *Phys. Rev.* **131**, 2766 (1963).

[32] Carmichael, H. J. *Statistical Methods in Quantum Optics*, vol. I (Springer, Berlin, 1999).

[33] Carmichael, H. J. *Statistical Methods in Quantum Optics*, vol. II (Springer, Berlin, 1999).

[34] Gardiner, C. & Zoller, P. *Quantum noise: a handbook of Markovian and non-Markovian quantum stochastic methods with applications to quantum optics* (Springer Science, 2004).

[35] Dalibard, J., Castin, Y. & Molmer, K. Wave-function approach to dissipative processes in quantum optics. *Phys. Rev. Lett.* **68**, 580 (1992).

[36] Kwiat, P. G. *et al.* New high-intensity source of polarization-entangled photon pairs. *Phys. Rev. Lett.* **75**, 4337 (1995).

[37] Thompson, R. J., Rempe, G. & Kimble, H. J. Observation of normal-mode splitting for an atom in an optical cavity. *Phys. Rev. Lett.* **68**, 1132 (1992).

[38] Brune, M. *et al.* Observing the progressive decoherence of the “meter” in a quantum measurement. *Phys. Rev. Lett.* **77**, 4887 (1996).

[39] Wallraff, A. *et al.* Strong coupling of a single photon to a superconducting qubit using circuit quantum electrodynamics. *Nature* **431**, 162 (2004).

[40] Yoshie, T. *et al.* Vacuum rabi splitting with a single quantum dot in a photonic crystal nanocavity. *Nature* **432**, 200 (2004).

[41] McKeever, J., Boca, A., Boozer, A. D., Buck, J. R. & Kimble, H. J. Experimental realization of a one-atom laser in the regime of strong coupling. *Nature* **425**, 268 (2003).

[42] Rempe, G., Thompson, R. J., Brecha, R. J., Lee, W. D. & Kimble, H. J. Optical bistability and photon statistics in cavity quantum electrodynamics. *Phys. Rev. Lett.* **67**, 1727 (1991).

[43] Miller, R. *et al.* Trapped atoms in cavity QED: coupling quantized light and matter. *Journal of Physics B: Atomic, Molecular and Optical Physics* **38**, S551–S565 (2005). URL http://stacks.iop.org/0953-4075/38/S551.

[44] Buhmann, S. Y. & Welsh, D.-G. Dispersion fores in marosopi quantum eletrodynamis. *arxiv quant-ph* (2007).

[45] Milonni, P. W. Why spontaneous emission? *Am. J. Phys.* **52**, 340 (1984).

[46] Lehmberg, R. H. Radiation from an n-atom system i. general formalism. *Phys. Rev. A* **2**, 883 (1970).

[47] Lehmberg, R. H. Radiation from an n-atom system ii. spontaneous emission from a pair of atoms. *Phys. Rev. A* **2**, 889 (1970).

[48] Michael P. Schneider, T. S., Stawiarski, C., Schmitteckert, P. & Busch, K. Green's function formalism for waveguide qed applications. *Phys. Rev. A* **93**, 013828 (2016).

[49] Asenjo-Garcia, A., Moreno-Cardoner, M., Albrecht, A., Kimble, H. J. & Chang, D. E. Exponential improvement in photon storage fidelities using subradiance and "selective radiance" in atomic arrays. *Phys. Rev. X* **7**, 031024 (2017).

[50] Chang, D. E., Jiang, L., Gorshkov, A. V. & Kimble, H. J. Cavity qed with atomic mirrors. *New J. Phys.* **14**, 063003 (2012).

[51] Scully, M. O. Collective Lamb shift in single photon Dicke superradiance. *Phys. Rev. Lett.* **102**, 143601 (2009). URL http://link.aps.org/doi/10.1103/PhysRevLett.102.143601.

[52] Schlosser, N., Reymond, G. & Grangier, P. Collisional blockade in microscopic optical dipole traps. *Phys. Rev. Lett.* **89**, 023005 (2002). URL http://link.aps.org/abstract/PRL/v89/e023005.

[53] Norcia, M. A., Lewis-Swan, R. J., Cline, J. R., Zhu, B. & Ana M. Rey, J. K. T. Cavity mediated collective spin exchange interactions in a strontium superradiant laser. *arXiv.* 1711.03673 (2017).

[54] Fleischhauer, M. & Lukin, M. D. Dark-state polaritons in electromagnetically induced transparency. *Phys. Rev. Lett.* **84**, 5094–5097 (2000). 10.1103/PhysRevLett.84.5094.

[55] Sørensen, A. & Mølmer, K. Entanglement and extreme spin squeezing. *Phys. Rev. Lett.* **86**, 4431–4434 (2001). URL http://dx.doi.org/10.1103/PhysRevLett.86.4819.

[56] Thompson, R. J., Turchette, Q. A., Carnal, O. & Kimble, H. J. Nonlinear spectroscopy in the strong-coupling regime of cavity qed. *Phys. Rev. A* **57**, 3084 (1998).

[57] Hammerer, K., Sørensen, A. S. & Polzik, E. S. Quantum interface between light and atomic ensembles. *Rev. Mod. Phys.* **82**, 1041–1093 (2010). URL http://dx.doi.org/10.1103/RevModPhys.82.1041.

[58] Baumann, K., Guerlin, C., Brennecke, F. & Esslinger, T. The dicke quantum phase transition with a superfluid gas in an optical cavity. *Nature* **464**, 1301 (2010).

[59] Leonard, J., Morales, A., Zupancic, P., Esslinger, T. & Donner, T. Supersolid formation in a quantum gas breaking a continuous translational symmetry. *Nature* **543**, 87 (2017).

[60] Kempe, J., Kitaev, A. & Regev, O. The complexity of the local hamiltonian problem. *SIAM J. Comput.* **35**, 1070 (2006).

[61] Zohar, E., Cirac, J. I. & Reznik, B. Quantum simulations of lattice gauge theories using ultracold atoms in optical lattices. *Rep. Prog. Phys.* **79**, 014401 (2016).

[62] Chandrasekharan, S. & Wiese, U.-J. Quantum link models: A discrete approach to gauge theories. *Nucl. Phys. B* **492**, 455 (1997).

[63] Biamonte, J. D. & Love, P. J. Realizable hamiltonians for universal adiabatic quantum computers. *Phys. Rev. A* **78**, 012352 (2008).

[64] Balents, L. Spin liquids in frustrated magnets. *Nature* **464**, 199 (2010).

[65] Ross, K., Savary, L., Gaulin, B. & Balents, L. Quantum excitations in quantum spin ice. *Phys. Rev. X* **1**, 021002 (2011).

[66] Gingras, M. J. P. & McClarty, P. A. Quantum spin ice: a search for gapless quantum spin liquids in pyrochlore magnets. *Rep. Prog. Phys.* **77**, 056501 (2014).

[67] Debnath, S. *et al.* Observation of hopping and blockade of bosons in a trapped ion spin chain. *Phys. Rev. Lett.* **120**, 073001 (2018).

[68] Fregoso, B., Sun, K., Fradkin, E. & Lev, B. L. Biaxial nematic phases in ultracold dipolar fermi gases. *New J. Phys.* **11**, 103003 (2009).

[69] N. Q. Burdick, Y. T. & Lev, B. L. A long-lived spin-orbit-coupled dipolar fermi gas. *Phys. Rev. X* **6**, 031022 (2016).

[70] Ni, K.-K. *et al.* A high phase-space-density gas of polar molecules. *Science* **322**, 231 (2008).

[71] Ni, O. S., K.-K. *et al.* Dipolar collisions of polar molecules in the quantum regime. *Nature* **464**, 1324 (2010).

[72] Micheli, A., Brennen, G. K. & Zoller, P. A toolbox for lattice-spin models with polar molecules. *Nature Phys.* **2**, 341 (2006).

[73] Henkel, N., Nath, R. & Pohl, T. Three-dimensional roton excitations and supersolid formation in rydberg-excited bose–einstein condensates. *Phys. Rev. Lett.* **104**, 195302 (2010).

[74] Pupillo, G., Micheli, A., Boninsegni, M., Lesanovsky, I. & Zoller, P. Strongly correlated gases of rydberg-dressed atoms: quantum and classical dynamics. *Phys. Rev. Lett.* **104**, 223002 (2010).

[75] Macri, T. & Pohl, T. Rydberg dressing of atoms in optical lattices. *Phys. Rev. A* **89**, 011402 (2014).

[76] Jaksch, D. *et al.* Fast quantum gates for neutral atoms. *Phys. Rev. Lett.* **85**, 2208 (2000).

[77] Lukin, M. D. *et al.* Dipole blockade and quantum information processing in mesoscopic atomic ensembles. *Phys. Rev. Lett.* **87**, 037901 (2001).

[78] Urban, E. *et al.* Observation of rydberg blockade between two atoms. *Nature Phys.* **5**, 110 (2009).

[79] Gaetan, A. *et al.* Observation of collective excitation of two individual atoms in the rydberg blockade regime. *Nature Phys.* **5**, 115 (2009).

[80] Rydberg, J. R. On the structure of the line-spectral of the chemical elements. *Phil. Mag.* **29**, 331 (1890).

[81] Connerade, J.-P. *Highly Excited Atoms* (Cambridge University Press, 1998).

[82] Mukherjee, R., Millen, J., Nath, R., Jones, M. P. A. & Pohl, T. Many-body physics with alkaline-earth rydberg lattices. *J. Phys. B* **44**, 184010 (2011).

[83] Safronova, M. S., Johnson, W. R. & Derevianko, A. Relativistic many-body calculations of energy levels, hyperfine constants, electric-dipole matrix elements, and static polarizabilities for alkali-metal atoms. *Phys. Rev. A* **60**, 4476 (1999).

[84] Safronova, M. S. & Johnson, W. R. All-order methods for relativistic atomic structure calculations. *Adv. At. Mol. Opt. Phys.* **55**.

[85] Martin, W. C. & Wiese, W. L. *Atomic spectroscopy* (AIP Press, 1996).

[86] Fano, U. & Rau, A. R. P. *Atomic Collisions and Spectra* (Academic Press, 1986).

[87] M. Marinescu, H. R. S. & Dalgarno., A. Dispersion coefficients for alkali-metal dimers. *Phys. Rev. A* **49**, 982 (1994).

[88] Corney, A. *Atomic and Laser Spectroscopy* (Oxford University Press, 1977).

[89] Li, W., Mourachko, I., Noel, M. W. & Gallagher, T. F. Millimeter-wave spectroscopy of cold rb rydberg atoms in a magneto- optical trap. *Phys. Rev. A* **67**, 052502 (2003).

[90] Tauschinsky, F. A., Newell, R. G., van Linden van den Heuvell, H. B. & Spreeuw, R. J. C. Measurement of 87rb rydberg-state hyperfine splitting in a room-temperature vapor cell. *Phys. Rev. A* **87**, 042522 (2013).

[91] Arimondo, E., Inguscio, M. & Violino, P. Experimental determinations of the hyperfine structure in the alkali atoms. *Rev. Mod. Phys.* **49**, 31 (1977).

[92] Sibalic, N., Pritchard, J. D., Adams, C. S. & Weatherill, K. J. Arc: An open-source library for calculating properties of alkali rydberg atoms. *Comp. Phys. Comm.* **220**, 319 (2017).

[93] Lacroute, C. *et al.* A state-insensitive, compensated nanofiber trap. *New J. Phys.* **14**, 023056 (2012).

[94] Guerlin, C., Brion, E., Esslinger, T. & Mølmer, K. Cavity quantum electrodynamics with a rydberg-blocked atomic ensemble. *Phys. Rev. A* **82**, 053832 (2010).

[95] Thompson, J. D. *et al.* Coupling a single trapped atom to a nanoscale optical cavity. *Nature* **340**, 1202 (2013).

[96] Tiecke, T. G. *et al.* Nanophotonic quantum phase switch with a single atom. *Nature* **508**, 241 (2014).

[97] Li, X. & Sarma, S. D. Exotic topological density waves in cold atomic rydberg-dressed fermions. *Nature Comm.* **6**, 7137 (2014).

[98] Glaetzle, A. W. *et al.* Quantum spin-ice and dimer models with rydberg atoms. *Phys. Rev. X* **4**, 041037 (2014).

[99] Choi, K. S., Goban, A., Papp, S. B., van Enk, S. J. & Kimble, H. J. Entanglement of spin waves among four quantum memories. *Nature* **468**, 412–416 (2010). URL `http://dx.doi.org/10.1038/nature09568`.

[100] Hung, C.-L., Gonzalez-Tudela, A., Cirac, J. I. & Kimble, H. J. Quantum spin dynamics with pairwise-tunable, long-range interactions. *Proc. Natl. Acad. Sci. U.S.A.* **113**, E4946 (2016).

[101] Dong, Y., Lee, Y.-S. & Choi, K. S. Waveguide qed toolboxes for synthetic quantum matter. *arXiv:1712.02020* (2017).

[102] Anderson, P. W. Ordering and antiferromagnetism in ferrites. *Phys. Rev.* **102**, 1008 (1956).

[103] Harris, M. J., Bramwell, S. T., McMorrow, D. F., Zeiske, T. & Godfrey, K. W. Geometrical frustration in the ferromagnetic pyrochlore $\mathrm{ho}_2\mathrm{ti}_2\mathrm{o}_7$. *Phys. Rev. Lett.* **79**, 2554 (1997).

[104] Harris, M. J., Bramwell, S. T., McMorrow, D. F., Zeiske, T. & Godfrey, K. W. Geometrical frustration in the ferromagnetic pyrochlore $\mathrm{ho}_2\mathrm{ti}_2O_7$. *Phys. Rev. Lett.* **79**, 2554 (1997).

[105] Bramwell, S. T. & Gingras, M. J. P. Spin ice state in frustrated magnetic pyrochlore materials. *Science* **294**, 1495 (2001).

[106] Melko, R. G., den Hertog, B. C. & Gingras, M. J. P. Long-range order at low temperatures in dipolar spin ice. *Phys. Rev. Lett.* **87**, 067203 (2001).

[107] pyrochlore oxides, M. Gardner, jason s. and gingras, michel j. p. and greedan, john e. *Rev. Mod. Phys.* **82**, 53 (2010).

[108] Fennell, T. *et al.* Magnetic coulomb phase in the spin ice $ho_2ti_2o_7$. *Science* **326**, 415 (2009).

[109] Castelnovo, C., Moessner, R. & Sondhi, S. L. Magnetic monopoles in spin ice. *Nature* **451**, 42 (2008).

[110] Henley, C. L. Power-law spin correlations in pyrochlore antiferromagnets. *Phys. Rev. B* **71**, 014424 (2005).

[111] Hermele, M., Fisher, M. P. A. & Balents, L. Pyrochlore photons: The $u(1)$ spin liquid in a $s = \frac{1}{2}$ three-dimensional frustrated magnet. *Phys. Rev. B* **69**, 064404 (2004).

[112] Henry, L.-P. & Roscilde, T. Order-by-disorder and quantum coulomb phase in quantum square ice. *Phys. Rev. Lett.* **113**, 027204 (2014).

[113] Rokhsar, D. S. & Kivelson, S. A. Superconductivity and the quantum hard-core dimer gas. *Phys. Rev. Lett.* **61**, 2376 (1988).

[114] Kogut, J. & Susskind, L. Hamiltonian formulation of wilson's lattice gauge theories. *Phys. Rev. D* **11**, 395–408 (1975). URL `https://link.aps.org/doi/10.1103/PhysRevD.11.395`.

[115] Lucile Savary, L. B. Coulombic quantum liquids in spin-1/2 pyrochlores. *Phys. Rev. Lett.* **108**, 037202 (2012).

[116] Glaetzle, A. W. *et al.* Quantum spin-ice and dimer models with rydberg atoms. *Phys. Rev. X* **4**, 041037 (2014).

[117] Halama, H. J. & Herrera, J. C. Thermal desorption of gases from aluminum alloy al6061, their rates and activation energies. *J. Vac. Sci. Tech.* **13**, 1 (1976).

[118] Yamamoto, R. M. & Harvey, J. Outgassing measurements and results used in designing the doublet iii neutral beam injection system. *Symposium on engineering problems of fusion research* (1979).

[119] Strausser, Y. Review of outgassing results. *Varian Associates* (1967).

[120] Yoshikawa, Y. Outgassing rates before, during and after bake-out for various vacuum and first wall candidate materials of a large tokamak device. *ULVAC* (2000).

[121] Park, C. D., Chung, S. M., Liu, X. & Li, Y. Reduction in hydrogen outgassing from stainless steels by a medium-temperature heat treatment. *J. Vac. Sci. Tech. A* **26**, 1166 (2008).

[122] Patrick, T. J. Space environment & vacuum properties of spacecraft materials. *Vacuum* **31**, 105 (1981).

[123] Altemose, V. O. Helium diffusion through glass. *J. App. Phys.* **32**, 1309 (1961).

[124] Shelby, J. E. & Eagan, R. J. Helium migration in sodium aluminosilicate glasses. *J. Cer. Soc.* **59**, 2916 (1976).

[125] Hung, C.-L., Zhang, X., Gemelke, N. & Chin, C. Accelerating evaporative cooling of atoms into bose-einstein condensation in optical traps. *Phys. Rev. A* **78**, 011604 (2008).

[126] Bergeman, T., Erez, G. & Metcalf, H. J. Magnetostatic trapping fields for neutral atoms. *Phys. Rev. A* **35**, 1535 (1987).

[127] Dedman, C. J., Baldwin, K. G. H. & Colla, M. Fast switching of magnetic fields in a magneto-optic trap. *Rev. Sci. Instrum.* **72**, 4055 (2001).

[128] Carlos L. Garrido Alzar, D. O. J. H. M. E. S. P., Plamen G. Petrov. Compensation of eddy-current-induced magnetic field transients in a mot. *arxiv quant-ph* (2007).

[129] Ringot, J., Szriftgiser, P. & Garreau, J. C. Subrecoil Raman spectroscopy of cold Cesium atoms. *Phys. Rev. A* **65**, 013403 (2001). 10.1103/PhysRevA.65.013403.

[130] Stockton, J. *Continuous quantum measurement of cold alkali-atom spins.* Ph.D. thesis, California Institute of Technology, Pasadena, CA (2006).

[131] Obrecht, J. M., Wild, R. J. & Cornell, E. A. Measuring electric fields from surface contaminants with neutral atoms. *Phys. Rev. A* **75**, 062903 (2007).

[132] Benvenuti, C. A novel route to extreme vacua: the non-evaporable getters thin film coatings. *Vacuum* **53**, 219 (1999).

[133] Barcellini, C. *Non-Evaporable Getter Thin Film Coatings for Vacuum Applications*. Ph.D. thesis, Politecnico di Milano, Geneva (2014).

[134] Wong, M. *Pressure Accumulation in PMT due to Helium Permeation*. Fermi National Laboratory, engineering note edn.

[135] Müller, M., Lesanovsky, I., Weimer, H., Büchler, H. P. & Zoller, P. Mesoscopic rydberg gate based on electromagnetically induced transparency. *Phys. Rev. Lett.* **102**, 170502 (2009). URL https://link.aps.org/doi/10.1103/PhysRevLett.102.170502.

[136] Ye, J., Ma, L. S. & Hall, J. L. Molecular iodine clock. *Phys. Rev. Lett.* **87**, 270801 (2001). URL https://link.aps.org/doi/10.1103/PhysRevLett.87.270801.

[137] Barry, J. *Laser cooling and slowing of a diatomic molecule*. Ph.D. thesis, Yale University (2013).

[138] Grace H. Zhanga, A. K., Boris Braverman & Vuletic, V. Note: Fast compact laser shutter using a direct current motor and three-dimensional printing. *Rev. Sci. Instrum.* **86**, 126105 (2015).

[139] Shimizu, F., Shimizu, K. & Takuma, H. Four-beam laser trap of neutral atoms. *Opt. Lett.* **16**, 339 (1991).

[140] D. Boiron, D. R. M. P. V., C. Triché & Grynberg, G. Three-dimensional cooling of cesium atoms in four-beam gray optical molasses. *Phys. Rev. A* **52**, R3425 (1995).

[141] Kaufman, A. M., Lester, B. J. & Regal, C. A. Cooling a single atom in an optical tweezer to its quantum ground state. *Phys. Rev. X* **2**, 041014 (2012). URL https://link.aps.org/doi/10.1103/PhysRevX.2.041014.

[142] Dutta, S. K., Guest, J. R., Feldbaum, D., Walz-Flannigan, A. & Raithel, G. Ponderomotive optical lattice for rydberg atoms. *Phys. Rev. Lett.* **85**, 5551–5554 (2000). URL https://link.aps.org/doi/10.1103/PhysRevLett.85.5551.

[143] Baillard, X. *et al.* Interference-filter-stabilized external-cavity diode lasers. *Opt. Comm.* **266**, 609 (2005).

[144] Gilowski, M. *et al.* Narrow bandwidth interference filter-stabilized diode laser systems for the manipulation of neutral atoms. *Opt. Comm.* **280**, 443 (2007).

[145] Tkach, R. W. & Chraplyvy, A. R. Regimes of feedback effects in 1.5-um distributed feedback laser. *IEEE J. Lightw. Technol.* **JLT-4**, 1655 (1986).

[146] Donati, S., Fellow, L. & Horng, R.-H. The diagram of feedback regimes revisited. *IEEE Journal of selected topics in quantum electronics* **19** (2013).

[147] Freegard, T. & Zimmermann, C. On the design of enhancement cavities for second harmonic generation. *Opt. Comm.* **199**, 435 (2001).

[148] Polzik, E. S. & Kimble, H. J. Frequency doubling with knbo3 in an external cavity. *Opt. Lett.* **16**, 1400 (1991).

[149] Haensch, T. & Couillaud, B. Laser frequency stabilization by polarization spectroscopy of a reflecting reference cavity. *Opt. Comm.* **35**, 441 (1980).

[150] Yamaguchi, A. *Metastable state of ultracold and quantum de- generate Ytterbium atoms: High-resolution spectroscopy and cold collisions.* Ph.D. thesis, Kyoto University (2008).

[151] Dmitriev, V. G., Gurzadyan, G. G. & Nikogosyan, D. N. *Handbook on Nonlinear optical crystals* (Springer, 1991).

[152] Eckardt, R. C., Masuda, H., Fan, Y. X. & Byer., R. L. Absolute and relative nonlinear optical coefficients of kdp, kd?p, bab2o4, liio3, mgo:linbo3, and ktp measured by phase-matched second harmonic generation. *IEEE J. Quant. Electron.* **26**, 922 (1990).

[153] Boyd, G. D. & Klienman, D. Parametric interaction of focused gaussian light beams. *J. App. Phys.* **39**, 3597 (1968).

[154] S. P. Velsko, L. D. . C. H., M. Webb. Phase-matched harmonic generation in lithium triborate (lbo). *IEEE J. Quant. Electron.* **27**, 2182 (1991).

[155] Hald, J. Second harmonic generation in an external ring cav- ity with a brewster-cut nonlinear crystal: theoretical considera- tions. *Opt. Comm.* **197**, 169 (2001).

[156] Bannerman, S. T., Price, G. N., Viering, K. & Raizen, M. G. Single-photon cooling at the limit of trap dynamics: Maxwell's demon near maximum efficiency. *New J. Phys.* **11**, 063044 (2009).

[157] Ritsch, H., Domokos, P., Brennecke, F. & Esslinger, T. Cold atoms in cavity-generated dynamical optical potentials. *Rev. Mod. Phys.* **85**, 553 (2013).

[158] Dimova, E. *et al.* Continuous transfer and laser guiding between two cold atom traps. *Eur. Phys. J. D* **42**, 299 (2007).

[159] Myatt, C. J., Newbury, N. R., Ghrist, R. W., Loutzenhiser, S. & Wieman, C. E. Multiply loaded magneto-optical trap. *Opt. Lett.* **21**, 290 (1996).

[160] Swanson, T. B., Asgeirsson, D., Behr, J. A., Gorelov, A. & Melconian, D. Efficient transfer in a double magneto-optical trap system. *J. Opt. Soc. Am. B* **15**, 2641 (1998).

[161] Wohlleben, W., Chevy, F., Madison, K. & Dalibard, J. An atom faucet. *Eur. Phys. J. D* **15**, 237 (2001).

[162] Julian Leonard, A. M. T. M. K. T. E., Moonjoo Lee & Donner, T. Optical transport and manipulation of an ultracold atomic cloud using focus-tunable lenses. *New J. Phys.* **16**, 093028 (2014).

[163] Kuhr, S. *et al.* Coherence properties and quantum state transportation in an optical conveyor belt. *Phys. Rev. Lett.* **91**, 213002 (2003). URL `https://link.aps.org/doi/10.1103/PhysRevLett.91.213002`.

[164] Hood, C. J., Kimble, H. J. & Ye, J. Characterization of high-finesse mirrors: Loss, phase shifts, and mode structure in an optical cavity. *Phys. Rev. A* **64**, 033804 (2001). URL `http://link.aps.org/abstract/PRA/v64/e033804`.

[165] Northup, T. E. & Blatt, R. Quantum information transfer using photons. *Nature Photon.* **8**, 356 (2014).

[166] Bakr, W. S. *et al.* Probing the Superfluid-to-Mott insulator transition at the Single-Atom level. *Science* **329**, 547–550 (2010). URL `http://www.sciencemag.org/cgi/content/abstract/329/5991/547`.

[167] Sherson, J. F. *et al.* Single-atom-resolved fluorescence imaging of an atomic mott insulator. *Nature* **467**, 68 (2010).

[168] Zupancic, P. *et al.* Ultra-precise holographic beam shaping for microscopic quantum control. *Opt. Express* **24**, 13881 (2016).

[169] Goorden, S. A., Bertolotti, J. & Mosk, A. P. Superpixel-based spatial amplitude and phase modulation using a digital micromirror device. *Opt. Express* **22**, 17999 (2014).

[170] Sandoghdar, V., Sukenik, C. I., Hinds, E. A. & Haroche, S. Direct measurement of the van der waals interaction between an atom and its images in a micron-sized cavity. *Phys. Rev. Lett.* **68**, 3432 (1992).

[171] Rempe, G., Thompson, R. J., Kimble, H. J. & Lalezari, R. Measurement of ultralow losses in an optical interferometer. *Opt. Lett.* **17**, 363 (1992).

[172] Northup, T. *Coherent control in cavity QED*. Ph.D. thesis, California Institute of Technology (2008).

[173] Gangloff, D. *et al.* Preventing and reversing vacuum-induced optical losses in high-finesse tantalum (v) oxide mirror coatings. *Opt. Express* **14**, 18014 (2015).

[174] Hofmann, C. S. *et al.* An experimental approach for investigating many-body phenomena in rydberg-interacting quantum systems. *Frontiers of Physics* **9**, 571 (2014).

[175] Parkins, A. S., Marte, P., Zoller, P. & Kimble, H. J. Synthesis of arbitrary quantum states via adiabatic transfer of zeeman coherence. *Phys. Rev. Lett.* **71**, 3095 (1993). URL http://link.aps.org/abstract/PRL/v71/p3095.

[176] Duan, L. M. & Kimble, H. J. Scalable photonic quantum computation through cavity-assisted interactions. *Phys. Rev. Lett.* **92**, 127902 (2004). URL http://link.aps.org/doi/10.1103/PhysRevLett.92.127902.

[177] Duan, L. M., Wang, B. & Kimble, H. J. Robust quantum gates on neutral atoms with cavity-assisted photon scattering. *Phys. Rev. A* **72**, 032333 (2005). URL http://link.aps.org/doi/10.1103/PhysRevA.72.032333.

[178] Norcia, M. A. *et al.* Frequency measurements of superradiance from the strontium clock transition. *Phys. Rev. X* **8**, 021036 (2018). URL https://link.aps.org/doi/10.1103/PhysRevX.8.021036.

[179] Bohnet, J. G. *et al.* A steady-state superradiant laser with less than one intracavity photon. *Nature* **484**, 78 (2012).

[180] Dong, Y. & Choi, K. S. Emergent photons in frustrated qed of rydberg-dressed square ice model. *Submitted to Science Adv.* (2018).

[181] Dong, Y. & Choi, K. S. Non-abelian braiding interferometry with cavity rydberg polaritons. *In preparation* (2018).

Appendix A

Atom-atom interaction coefficients and radiative characteristics of Rydberg states

In this Appendix, we present the numerical results of the quantum defect theory described in Chapter 2, for the van der Waals interaction coefficients and radiative characteristics.

n	n^*	τ (s)	τ_{bb} (s)	f (THz)	$\langle J'\|\|e\hat{r}\|\|J\rangle$	r_L (μm)	$C_6(\mathrm{GHz} \cdot \mu m^6)$
6.0000	2.3292	0.0000	-0.0000	335.1200	4.4890	0.0017	0.0000
7.0000	3.3737	0.0000	-0.0000	652.5100	0.2790	0.0037	0.0000
8.0000	4.3886	0.0000	-0.0000	770.7300	0.0810	0.0063	-0.0000
9.0000	5.3956	0.0000	-0.0000	828.5400	0.0822	0.0096	0.0000
10.0000	6.3994	0.0000	-0.0000	861.2100	-0.0541	0.0136	0.0000
11.0000	7.4017	0.0000	-0.0000	881.4900	0.0393	0.0182	0.0000
12.0000	8.4032	0.0000	-0.0000	894.9500	-0.0303	0.0235	-0.0000
13.0000	9.4043	0.0000	-0.0000	904.3400	0.0244	0.0295	0.0000
14.0000	10.4050	0.0000	-0.0000	911.1600	-0.0202	0.0361	0.0000
15.0000	11.4060	0.0000	-0.0000	916.2500	0.0172	0.0434	0.0000
16.0000	12.4060	0.0000	-0.0000	920.1700	-0.0148	0.0514	-0.0000
17.0000	13.4060	0.0000	-0.0000	923.2400	0.0130	0.0600	0.0000
18.0000	14.4070	0.0000	-0.0000	925.6900	-0.0115	0.0693	0.0000
19.0000	15.4070	0.0000	-0.0000	927.6800	0.0103	0.0793	0.0000
20.0000	16.4070	0.0000	-0.0000	929.3200	-0.0093	0.0899	0.0000
21.0000	17.4070	0.0000	-0.0000	930.6900	0.0084	0.1013	0.0000
22.0000	18.4070	0.0000	-0.0000	931.8300	-0.0077	0.1133	0.0000
23.0000	19.4070	0.0000	-0.0000	932.8100	0.0071	0.1259	0.0000
24.0000	20.4080	0.0000	-0.0000	933.6400	-0.0065	0.1392	0.0000
25.0000	21.4080	0.0000	-0.0000	934.3600	0.0061	0.1532	-0.0000
26.0000	22.4080	0.0000	-0.0000	934.9900	-0.0056	0.1679	0.0000
27.0000	23.4080	0.0001	-0.0000	935.5400	0.0053	0.1832	0.0000
28.0000	24.4080	0.0001	-0.0000	936.0200	-0.0049	0.1992	0.0007
29.0000	25.4080	0.0001	-0.0000	936.4500	0.0046	0.2159	0.0011
30.0000	26.4080	0.0001	-0.0000	936.8200	-0.0044	0.2333	0.0016

Table A.1: Van der Waals interaction coefficients $C_6(\mathrm{GHz} \cdot \mu m^6)$ and radiative characteristics of $|6S_{1/2}\rangle \rightarrow |nP_{1/2}\rangle$ for $n \in \{6 - 30\}$. (n^*) n is the (effective) principal quantum number, τ (τ_{bb}) is the (blackbody-limited) radiative lifetime (s), r_L is the LeRoy's radius, $\langle J'||e\hat{r}||J\rangle$ and f is the reduced matrix element (ea_0) and the transition frequency (Hz) for the transition $|6S_{1/2}\rangle \rightarrow |nP_{1/2}\rangle$.

n	n^*	τ (s)	τ_{bb} (s)	f (THz)	$\langle J'\vert\vert e\hat{r}\vert\vert J\rangle$	r_L (μm)	$C_6(\mathrm{GHz} \cdot \mu m^6)$
31.0000	27.4080	0.0001	-0.0000	937.1600	0.0041	0.2513	0.0024
32.0000	28.4080	0.0001	-0.0001	937.4700	-0.0039	0.2699	0.0035
33.0000	29.4080	0.0001	-0.0001	937.7400	0.0037	0.2893	0.0051
34.0000	30.4080	0.0001	-0.0001	937.9800	-0.0035	0.3093	0.0072
35.0000	31.4080	0.0001	-0.0001	938.2100	0.0033	0.3300	0.0102
36.0000	32.4080	0.0001	-0.0001	938.4100	-0.0032	0.3514	0.0142
37.0000	33.4080	0.0001	-0.0001	938.5900	0.0030	0.3734	0.0196
38.0000	34.4080	0.0002	-0.0001	938.7600	-0.0029	0.3961	0.0272
39.0000	35.4080	0.0002	-0.0001	938.9200	0.0028	0.4194	0.0369
40.0000	36.4080	0.0002	-0.0001	939.0600	-0.0027	0.4435	0.0497
41.0000	37.4080	0.0002	-0.0001	939.1900	0.0026	0.4682	0.0664
42.0000	38.4080	0.0002	-0.0001	939.3100	-0.0024	0.4936	0.0880
43.0000	39.4080	0.0002	-0.0002	939.4200	0.0024	0.5196	0.4103
44.0000	40.4080	0.0003	-0.0002	939.5300	-0.0023	0.5463	0.5392
45.0000	41.4080	0.0003	-0.0002	939.6200	0.0022	0.5737	0.7040
46.0000	42.4080	0.0003	-0.0002	939.7100	-0.0021	0.6018	0.9133
47.0000	43.4080	0.0003	-0.0002	939.8000	0.0020	0.6305	1.1778
48.0000	44.4080	0.0003	-0.0002	939.8700	-0.0020	0.6599	1.5102
49.0000	45.4080	0.0004	-0.0003	939.9500	0.0019	0.6899	1.2028
50.0000	46.4080	0.0004	-0.0003	940.0100	-0.0018	0.7207	1.4550
51.0000	47.4080	0.0004	-0.0003	940.0800	0.0018	0.7521	1.8334
52.0000	48.4080	0.0004	-0.0003	940.1400	-0.0017	0.7841	2.2990
53.0000	49.4080	0.0005	-0.0003	940.1900	0.0017	0.8169	2.8688
54.0000	50.4080	0.0005	-0.0004	940.2500	-0.0016	0.8503	3.5612
55.0000	51.4080	0.0005	-0.0004	940.3000	0.0016	0.8843	4.0590
56.0000	52.4080	0.0006	-0.0004	940.3400	-0.0015	0.9191	5.4664
57.0000	53.4080	0.0006	-0.0004	940.3900	0.0015	0.9545	6.7078
58.0000	54.4080	0.0006	-0.0005	940.4300	-0.0014	0.9906	8.2023
59.0000	55.4080	0.0007	-0.0005	940.4700	0.0014	1.0273	10.0530
60.0000	56.4080	0.0007	-0.0005	940.5100	-0.0014	1.0648	15.6090

Table A.2: Van der Waals interaction coefficients $C_6(\mathrm{GHz} \cdot \mu m^6)$ and radiative characteristics of $|6S_{1/2}\rangle \rightarrow |nP_{1/2}\rangle$ for $n \in \{31 - 60\}$. (n^*) n is the (effective) principal quantum number, τ (τ_{bb}) is the (blackbody-limited) radiative lifetime (s), r_L is the LeRoy's radius, $\langle J'||e\hat{r}||J\rangle$ and f is the reduced matrix element (ea_0) and the transition frequency (Hz) for the transition $|6S_{1/2}\rangle \rightarrow |nP_{1/2}\rangle$.

n	n^*	τ (s)	τ_{bb} (s)	f (THz)	$\langle J'\|\|e\hat{r}\|\|J\rangle$	r_L (μm)	C_6(GHz $\cdot\, \mu m^6$)
61.0000	57.4080	0.0007	-0.0006	940.5400	0.0013	1.1029	18.9030
62.0000	58.4080	0.0008	-0.0006	940.5800	-0.0013	1.1416	22.8170
63.0000	59.4080	0.0008	-0.0006	940.6100	0.0013	1.1811	25.8360
64.0000	60.4080	0.0008	-0.0007	940.6400	-0.0012	1.2212	30.9850
65.0000	61.4080	0.0009	-0.0007	940.6700	0.0012	1.2619	37.0520
66.0000	62.4080	0.0009	-0.0007	940.7000	-0.0012	1.3034	44.1770
67.0000	63.4080	0.0010	-0.0008	940.7200	0.0011	1.3455	51.5890
68.0000	64.4080	0.0010	-0.0008	940.7500	-0.0011	1.3883	61.1570
69.0000	65.4080	0.0011	-0.0008	940.7700	0.0011	1.4317	72.3810
70.0000	66.4080	0.0011	-0.0009	940.8000	-0.0011	1.4758	86.2750
71.0000	67.4080	0.0012	-0.0009	940.8200	0.0010	1.5206	101.5500
72.0000	68.4080	0.0012	-0.0010	940.8400	-0.0010	1.5661	119.9600
73.0000	69.4080	0.0013	-0.0010	940.8600	0.0010	1.6122	140.5200
74.0000	70.4080	0.0013	-0.0011	940.8800	-0.0010	1.6590	164.2300
75.0000	71.4080	0.0014	-0.0011	940.9000	0.0010	1.7064	188.7000
76.0000	72.4080	0.0014	-0.0012	940.9100	-0.0009	1.7546	219.0100
77.0000	73.4080	0.0015	-0.0012	940.9300	0.0009	1.8034	254.3100
78.0000	74.4080	0.0016	-0.0013	940.9500	-0.0009	1.8528	294.7100
79.0000	75.4080	0.0016	-0.0013	940.9600	0.0009	1.9030	342.2000
80.0000	76.4080	0.0017	-0.0014	940.9800	-0.0009	1.9538	394.9100
81.0000	77.4080	0.0018	-0.0015	940.9900	0.0008	2.0053	454.7100
82.0000	78.4080	0.0018	-0.0015	941.0100	-0.0008	2.0574	521.1700
83.0000	79.4080	0.0019	-0.0016	941.0200	0.0008	2.1102	589.6300
84.0000	80.4080	0.0020	-0.0016	941.0300	-0.0008	2.1637	695.9700
85.0000	81.4080	0.0021	-0.0017	941.0500	0.0008	2.2179	790.7300
86.0000	82.4080	0.0021	-0.0018	941.0600	-0.0008	2.2727	901.9000
87.0000	83.4080	0.0022	-0.0018	941.0700	0.0008	2.3282	1028.6000
88.0000	84.4080	0.0023	-0.0019	941.0800	-0.0007	2.3844	1171.1000
89.0000	85.4080	0.0024	-0.0020	941.0900	0.0007	2.4412	1331.4000
90.0000	86.4080	0.0025	-0.0021	941.1000	-0.0007	2.4987	1510.1000

Table A.3: Van der Waals interaction coefficients $C_6(\mathrm{GHz} \cdot \mu m^6)$ and radiative characteristics of $|6S_{1/2}\rangle \rightarrow |nP_{1/2}\rangle$ for $n \in \{61 - 90\}$. (n^*) n is the (effective) principal quantum number, τ (τ_{bb}) is the (blackbody-limited) radiative lifetime (s), r_L is the LeRoy's radius, $\langle J'||e\hat{r}||J\rangle$ and f is the reduced matrix element (ea_0) and the transition frequency (Hz) for the transition $|6S_{1/2}\rangle \rightarrow |nP_{1/2}\rangle$.

n	n^*	τ (s)	τ_{bb} (s)	f (THz)	$\langle J' \vert\vert e\hat{r} \vert\vert J \rangle$	r_L (μm)	C_6(GHz $\cdot\, \mu m^6$)
91.0000	87.4080	0.0025	-0.0021	941.1100	0.0007	2.5569	1712.1000
92.0000	88.4080	0.0026	-0.0022	941.1200	-0.0007	2.6157	1939.2000
93.0000	89.4080	0.0027	-0.0023	941.1300	0.0007	2.6752	2192.5000
94.0000	90.4080	0.0028	-0.0024	941.1400	-0.0007	2.7354	2475.5000
95.0000	91.4080	0.0029	-0.0025	941.1500	0.0007	2.7963	2790.9000
96.0000	92.4080	0.0030	-0.0026	941.1600	-0.0006	2.8578	3143.1000
97.0000	93.4080	0.0031	-0.0026	941.1700	0.0006	2.9200	3535.6000
98.0000	94.4080	0.0032	-0.0027	941.1700	-0.0006	2.9828	3971.7000
99.0000	95.4080	0.0033	-0.0028	941.1800	0.0006	3.0464	4456.1000
100.0000	96.4080	0.0034	-0.0029	941.1900	-0.0006	3.1106	4993.7000

Table A.4: Van der Waals interaction coefficients $C_6(\text{GHz} \cdot \mu m^6)$ and radiative characteristics of $|6S_{1/2}\rangle \rightarrow |nP_{1/2}\rangle$ for $n \in \{91 - 100\}$. (n^*) n is the (effective) principal quantum number, τ (τ_{bb}) is the (blackbody-limited) radiative lifetime (s), r_L is the LeRoy's radius, $\langle J' || e\hat{r} || J \rangle$ and f is the reduced matrix element (ea_0) and the transition frequency (Hz) for the transition $|6S_{1/2}\rangle \rightarrow |nP_{1/2}\rangle$.

n	n^*	τ (s)	τ_{bb} (s)	f (THz)	$\langle J'\|\|e\hat{r}\|\|J\rangle$	r_L (μm)	$C_6(\mathrm{GHz}\cdot\mu m^6)$
6.0000	2.3617	0.0000	-0.0000	351.7300	6.3238	0.0018	0.0000
7.0000	3.4039	0.0000	-0.0000	657.9400	0.5760	0.0038	0.0000
8.0000	4.4206	0.0000	-0.0000	773.2100	0.2180	0.0064	0.0000
9.0000	5.4278	0.0000	-0.0000	829.8800	0.1883	0.0097	0.0000
10.0000	6.4317	0.0000	-0.0000	862.0100	-0.1298	0.0137	0.0000
11.0000	7.4340	0.0000	-0.0000	882.0100	0.0972	0.0184	0.0000
12.0000	8.4356	0.0000	-0.0000	895.3100	-0.0767	0.0237	0.0000
13.0000	9.4367	0.0000	-0.0000	904.6000	0.0628	0.0297	0.0000
14.0000	10.4370	0.0000	-0.0000	911.3400	-0.0527	0.0363	0.0000
15.0000	11.4380	0.0000	-0.0000	916.4000	0.0451	0.0436	0.0000
16.0000	12.4390	0.0000	-0.0000	920.2800	-0.0393	0.0516	0.0000
17.0000	13.4390	0.0000	-0.0000	923.3300	0.0346	0.0603	0.0000
18.0000	14.4390	0.0000	-0.0000	925.7600	-0.0308	0.0696	0.0000
19.0000	15.4390	0.0000	-0.0000	927.7400	0.0277	0.0796	-0.0000
20.0000	16.4400	0.0000	-0.0000	929.3700	-0.0250	0.0903	-0.0000
21.0000	17.4400	0.0000	-0.0000	930.7300	0.0228	0.1016	0.0000
22.0000	18.4400	0.0000	-0.0000	931.8700	-0.0209	0.1137	0.0000
23.0000	19.4400	0.0000	-0.0000	932.8400	0.0192	0.1263	0.0000
24.0000	20.4400	0.0000	-0.0000	933.6700	-0.0178	0.1397	0.0000
25.0000	21.4400	0.0000	-0.0000	934.3900	0.0165	0.1537	0.0000
26.0000	22.4400	0.0000	-0.0000	935.0100	-0.0154	0.1684	0.0000
27.0000	23.4400	0.0000	-0.0000	935.5500	0.0144	0.1837	0.0000
28.0000	24.4400	0.0000	-0.0000	936.0300	-0.0135	0.1998	0.0000
29.0000	25.4400	0.0001	-0.0000	936.4600	0.0127	0.2165	0.0000
30.0000	26.4400	0.0001	-0.0000	936.8400	-0.0120	0.2338	0.0000

Table A.5: Van der Waals interaction coefficients $C_6(\mathrm{GHz}\cdot\mu m^6)$ and radiative characteristics of $|6S_{1/2}\rangle \rightarrow |nP_{3/2}\rangle$ for $n \in \{6-30\}$. (n^*) n is the (effective) principal quantum number, τ (τ_{bb}) is the (blackbody-limited) radiative lifetime (s), r_L is the LeRoy's radius, $\langle J'||e\hat{r}||J\rangle$ and f is the reduced matrix element (ea_0) and the transition frequency (Hz) for the transition $|6S_{1/2}\rangle \rightarrow |nP_{3/2}\rangle$.

n	n^*	τ (s)	τ_{bb} (s)	f (THz)	$\langle J' \vert\vert e\hat{r} \vert\vert J \rangle$	r_L (μm)	$C_6(\text{GHz} \cdot \mu m^6)$
31.0000	27.4410	0.0001	-0.0000	937.1700	0.0113	0.2519	0.0001
32.0000	28.4410	0.0001	-0.0000	937.4800	-0.0107	0.2706	0.0001
33.0000	29.4410	0.0001	-0.0000	937.7500	0.0101	0.2899	0.0001
34.0000	30.4410	0.0001	-0.0001	937.9900	-0.0096	0.3100	0.0001
35.0000	31.4410	0.0001	-0.0001	938.2100	0.0092	0.3307	0.0002
36.0000	32.4410	0.0001	-0.0001	938.4200	-0.0087	0.3521	0.0003
37.0000	33.4410	0.0001	-0.0001	938.6000	0.0083	0.3741	0.0004
38.0000	34.4410	0.0001	-0.0001	938.7700	-0.0080	0.3968	0.0005
39.0000	35.4410	0.0001	-0.0001	938.9200	0.0076	0.4202	0.0037
40.0000	36.4410	0.0002	-0.0001	939.0600	-0.0073	0.4443	0.0496
41.0000	37.4410	0.0002	-0.0001	939.2000	0.0070	0.4690	0.1724
42.0000	38.4410	0.0002	-0.0001	939.3200	-0.0068	0.4944	0.2303
43.0000	39.4410	0.0002	-0.0001	939.4300	0.0065	0.5205	0.3053
44.0000	40.4410	0.0002	-0.0001	939.5300	-0.0063	0.5472	0.4019
45.0000	41.4410	0.0002	-0.0002	939.6300	0.0060	0.5746	0.5256
46.0000	42.4410	0.0003	-0.0002	939.7200	-0.0058	0.6027	0.6829
47.0000	43.4410	0.0003	-0.0002	939.8000	0.0056	0.6314	0.8820
48.0000	44.4410	0.0003	-0.0002	939.8800	-0.0054	0.6608	1.1324
49.0000	45.4410	0.0003	-0.0002	939.9500	0.0052	0.6909	1.4460
50.0000	46.4410	0.0003	-0.0002	940.0200	-0.0051	0.7217	1.8365
51.0000	47.4410	0.0004	-0.0002	940.0800	0.0049	0.7531	1.5964
52.0000	48.4410	0.0004	-0.0003	940.1400	-0.0048	0.7852	1.9372
53.0000	49.4410	0.0004	-0.0003	940.2000	0.0046	0.8179	2.4236
54.0000	50.4410	0.0004	-0.0003	940.2500	-0.0045	0.8514	3.0185
55.0000	51.4410	0.0005	-0.0003	940.3000	0.0043	0.8855	3.7450
56.0000	52.4410	0.0005	-0.0003	940.3500	-0.0042	0.9202	4.6251
57.0000	53.4410	0.0005	-0.0004	940.3900	0.0041	0.9557	5.7300
58.0000	54.4410	0.0005	-0.0004	940.4300	-0.0040	0.9918	9.1623
59.0000	55.4410	0.0006	-0.0004	940.4700	0.0039	1.0286	11.1860
60.0000	56.4410	0.0006	-0.0004	940.5100	-0.0038	1.0660	13.6090

Table A.6: Van der Waals interaction coefficients $C_6(\text{GHz} \cdot \mu m^6)$ and radiative characteristics of $|6S_{1/2}\rangle \to |nP_{3/2}\rangle$ for $n \in \{31 - 60\}$. (n^*) n is the (effective) principal quantum number, τ (τ_{bb}) is the (blackbody-limited) radiative lifetime (s), r_L is the LeRoy's radius, $\langle J' || e\hat{r} || J \rangle$ and f is the reduced matrix element (ea_0) and the transition frequency (Hz) for the transition $|6S_{1/2}\rangle \to |nP_{3/2}\rangle$.

n	n^*	τ (s)	τ_{bb} (s)	f (THz)	$\langle J'\|\|e\hat{r}\|\|J\rangle$	r_L (μm)	$C_6(\text{GHz} \cdot \mu m^6)$
61.0000	57.4410	0.0006	-0.0005	940.5500	0.0037	1.1041	16.4990
62.0000	58.4410	0.0007	-0.0005	940.5800	-0.0036	1.1429	19.9370
63.0000	59.4410	0.0007	-0.0005	940.6100	0.0035	1.1824	24.0130
64.0000	60.4410	0.0007	-0.0006	940.6400	-0.0034	1.2225	28.0430
65.0000	61.4410	0.0008	-0.0006	940.6700	0.0033	1.2633	33.0320
66.0000	62.4410	0.0008	-0.0006	940.7000	-0.0032	1.3047	39.4120
67.0000	63.4410	0.0008	-0.0006	940.7200	0.0032	1.3469	46.8580
68.0000	64.4410	0.0009	-0.0007	940.7500	-0.0031	1.3897	54.6840
69.0000	65.4410	0.0009	-0.0007	940.7700	0.0030	1.4331	66.1710
70.0000	66.4410	0.0010	-0.0007	940.8000	-0.0029	1.4773	77.9960
71.0000	67.4410	0.0010	-0.0008	940.8200	0.0029	1.5221	92.1840
72.0000	68.4410	0.0011	-0.0008	940.8400	-0.0028	1.5676	109.3700
73.0000	69.4410	0.0011	-0.0009	940.8600	0.0028	1.6137	127.7400
74.0000	70.4410	0.0012	-0.0009	940.8800	-0.0027	1.6605	149.3500
75.0000	71.4410	0.0012	-0.0009	940.9000	0.0026	1.7080	174.1900
76.0000	72.4410	0.0013	-0.0010	940.9200	-0.0026	1.7562	201.0700
77.0000	73.4410	0.0013	-0.0010	940.9300	0.0025	1.8050	233.0900
78.0000	74.4410	0.0014	-0.0011	940.9500	-0.0025	1.8545	270.9000
79.0000	75.4410	0.0014	-0.0011	940.9600	0.0024	1.9046	314.1600
80.0000	76.4410	0.0015	-0.0012	940.9800	-0.0024	1.9555	362.9500
81.0000	77.4410	0.0015	-0.0012	940.9900	0.0023	2.0070	418.5400
82.0000	78.4410	0.0016	-0.0013	941.0100	-0.0023	2.0591	481.7700
83.0000	79.4410	0.0017	-0.0013	941.0200	0.0023	2.1120	552.0100
84.0000	80.4410	0.0017	-0.0014	941.0300	-0.0022	2.1655	633.1700
85.0000	81.4410	0.0018	-0.0014	941.0500	0.0022	2.2197	725.0500
86.0000	82.4410	0.0019	-0.0015	941.0600	-0.0021	2.2745	829.4300
87.0000	83.4410	0.0019	-0.0016	941.0700	0.0021	2.3300	946.7300
88.0000	84.4410	0.0020	-0.0016	941.0800	-0.0021	2.3862	1078.9000
89.0000	85.4410	0.0021	-0.0017	941.0900	0.0020	2.4431	1227.6000
90.0000	86.4410	0.0021	-0.0017	941.1000	-0.0020	2.5006	1394.7000

Table A.7: Van der Waals interaction coefficients $C_6(\text{GHz} \cdot \mu m^6)$ and radiative characteristics of $|6S_{1/2}\rangle \rightarrow |nP_{3/2}\rangle$ for $n \in \{61 - 90\}$. (n^*) n is the (effective) principal quantum number, τ (τ_{bb}) is the (blackbody-limited) radiative lifetime (s), r_L is the LeRoy's radius, $\langle J'||e\hat{r}||J\rangle$ and f is the reduced matrix element (ea_0) and the transition frequency (Hz) for the transition $|6S_{1/2}\rangle \rightarrow |nP_{3/2}\rangle$.

n	n^*	τ (s)	τ_{bb} (s)	f (THz)	$\langle J' \| e\hat{r} \| J \rangle$	r_L (μm)	$C_6(\mathrm{GHz} \cdot \mu m^6)$
91.0000	87.4410	0.0022	-0.0018	941.1100	0.0019	2.5588	1581.7000
92.0000	88.4410	0.0023	-0.0019	941.1200	-0.0019	2.6177	1791.9000
93.0000	89.4410	0.0024	-0.0020	941.1300	0.0019	2.6772	2027.1000
94.0000	90.4410	0.0024	-0.0020	941.1400	-0.0019	2.7374	2290.0000
95.0000	91.4410	0.0025	-0.0021	941.1500	0.0018	2.7983	2583.4000
96.0000	92.4410	0.0026	-0.0022	941.1600	-0.0018	2.8598	2910.7000
97.0000	93.4410	0.0027	-0.0022	941.1700	0.0018	2.9220	3275.9000
98.0000	94.4410	0.0028	-0.0023	941.1700	-0.0017	2.9849	3681.7000
99.0000	95.4410	0.0029	-0.0024	941.1800	0.0017	3.0485	4132.7000
100.0000	96.4410	0.0030	-0.0025	941.1900	-0.0017	3.1127	4633.5000

Table A.8: Van der Waals interaction coefficients $C_6(\mathrm{GHz} \cdot \mu m^6)$ and radiative characteristics of $|6S_{1/2}\rangle \rightarrow |nP_{3/2}\rangle$ for $n \in \{91 - 100\}$. (n^*) n is the (effective) principal quantum number, τ (τ_{bb}) is the (blackbody-limited) radiative lifetime (s), r_L is the LeRoy's radius, $\langle J' || e\hat{r} || J \rangle$ and f is the reduced matrix element (ea_0) and the transition frequency (Hz) for the transition $|6S_{1/2}\rangle \rightarrow |nP_{3/2}\rangle$.

n	n^*	τ (s)	τ_{bb} (s)	f (THz)	$\langle J'\vert\vert e\hat{r}\vert\vert J\rangle$	r_L (μm)	$C_6(\mathrm{GHz}\cdot\mu m^6)$
0.0000	0.0000	0.0000	0.0000	0.0000	0.0000	0.0013	0.0000
7.0000	2.9199	0.0000	-0.0000	203.9600	6.4790	0.0029	0.0000
8.0000	3.9344	0.0000	-0.0000	377.2800	-1.4915	0.0052	0.0000
9.0000	4.9405	0.0000	-0.0000	455.0400	0.7853	0.0082	0.0000
10.0000	5.9437	0.0000	-0.0000	496.6900	-0.5185	0.0119	0.0000
11.0000	6.9456	0.0000	-0.0000	521.6200	0.3804	0.0162	0.0000
12.0000	7.9468	0.0000	-0.0000	537.7200	-0.2965	0.0212	0.0000
13.0000	8.9476	0.0000	-0.0000	548.7200	0.2405	0.0268	0.0000
14.0000	9.9482	0.0000	-0.0000	556.5700	-0.2007	0.0332	0.0000
15.0000	10.9490	0.0000	-0.0000	562.3700	0.1711	0.0402	0.0000
16.0000	11.9490	0.0000	-0.0000	566.7700	-0.1483	0.0478	0.0000
17.0000	12.9490	0.0000	-0.0000	570.2000	0.1303	0.0562	0.0000
18.0000	13.9490	0.0000	-0.0000	572.9100	-0.1157	0.0652	0.0000
19.0000	14.9500	0.0000	-0.0000	575.1000	0.1036	0.0748	0.0000
20.0000	15.9500	0.0000	-0.0000	576.8800	-0.0936	0.0852	0.0000
21.0000	16.9500	0.0000	-0.0000	578.3700	0.0851	0.0962	0.0000
22.0000	17.9500	0.0000	-0.0000	579.6100	-0.0778	0.1079	0.0000
23.0000	18.9500	0.0000	-0.0000	580.6600	0.0716	0.1202	0.0000
24.0000	19.9500	0.0000	-0.0000	581.5500	-0.0661	0.1333	0.0000
25.0000	20.9500	0.0000	-0.0000	582.3200	0.0613	0.1469	0.0000
26.0000	21.9500	0.0000	-0.0000	582.9900	-0.0570	0.1613	0.0000
27.0000	22.9500	0.0000	-0.0000	583.5700	0.0533	0.1763	0.0000
28.0000	23.9500	0.0000	-0.0000	584.0800	-0.0499	0.1920	-0.0034
29.0000	24.9500	0.0000	-0.0000	584.5300	0.0469	0.2084	-0.0055
30.0000	25.9500	0.0000	-0.0000	584.9300	-0.0442	0.2254	-0.0086

Table A.9: Van der Waals interaction coefficients $C_6(\mathrm{GHz}\cdot\mu m^6)$ and radiative characteristics of $|6P_{3/2}\rangle \rightarrow |nS_{1/2}\rangle$ for $n \in \{6-30\}$. (n^*) n is the (effective) principal quantum number, τ (τ_{bb}) is the (blackbody-limited) radiative lifetime (s), r_L is the LeRoy's radius, $\langle J'||e\hat{r}||J\rangle$ and f is the reduced matrix element (ea_0) and the transition frequency (Hz) for the transition $|6P_{3/2}\rangle \rightarrow |nS_{1/2}\rangle$.

n	n^*	τ (s)	τ_{bb} (s)	f (THz)	$\langle J'\|\|e\hat{r}\|\|J\rangle$	r_L (μm)	$C_6(\mathrm{GHz} \cdot \mu m^6)$
31.0000	27.4410	0.0001	-0.0000	937.1700	0.0113	0.2519	0.0001
32.0000	28.4410	0.0001	-0.0000	937.4800	-0.0107	0.2706	0.0001
33.0000	29.4410	0.0001	-0.0000	937.7500	0.0101	0.2899	0.0001
34.0000	30.4410	0.0001	-0.0001	937.9900	-0.0096	0.3100	0.0001
35.0000	31.4410	0.0001	-0.0001	938.2100	0.0092	0.3307	0.0002
36.0000	32.4410	0.0001	-0.0001	938.4200	-0.0087	0.3521	0.0003
37.0000	33.4410	0.0001	-0.0001	938.6000	0.0083	0.3741	0.0004
38.0000	34.4410	0.0001	-0.0001	938.7700	-0.0080	0.3968	0.0005
39.0000	35.4410	0.0001	-0.0001	938.9200	0.0076	0.4202	0.0037
40.0000	36.4410	0.0002	-0.0001	939.0600	-0.0073	0.4443	0.0496
41.0000	37.4410	0.0002	-0.0001	939.2000	0.0070	0.4690	0.1724
42.0000	38.4410	0.0002	-0.0001	939.3200	-0.0068	0.4944	0.2303
43.0000	39.4410	0.0002	-0.0001	939.4300	0.0065	0.5205	0.3053
44.0000	40.4410	0.0002	-0.0001	939.5300	-0.0063	0.5472	0.4019
45.0000	41.4410	0.0002	-0.0002	939.6300	0.0060	0.5746	0.5256
46.0000	42.4410	0.0003	-0.0002	939.7200	-0.0058	0.6027	0.6829
47.0000	43.4410	0.0003	-0.0002	939.8000	0.0056	0.6314	0.8820
48.0000	44.4410	0.0003	-0.0002	939.8800	-0.0054	0.6608	1.1324
49.0000	45.4410	0.0003	-0.0002	939.9500	0.0052	0.6909	1.4460
50.0000	46.4410	0.0003	-0.0002	940.0200	-0.0051	0.7217	1.8365
51.0000	47.4410	0.0004	-0.0002	940.0800	0.0049	0.7531	1.5964
52.0000	48.4410	0.0004	-0.0003	940.1400	-0.0048	0.7852	1.9372
53.0000	49.4410	0.0004	-0.0003	940.2000	0.0046	0.8179	2.4236
54.0000	50.4410	0.0004	-0.0003	940.2500	-0.0045	0.8514	3.0185
55.0000	51.4410	0.0005	-0.0003	940.3000	0.0043	0.8855	3.7450
56.0000	52.4410	0.0005	-0.0003	940.3500	-0.0042	0.9202	4.6251
57.0000	53.4410	0.0005	-0.0004	940.3900	0.0041	0.9557	5.7300
58.0000	54.4410	0.0005	-0.0004	940.4300	-0.0040	0.9918	9.1623
59.0000	55.4410	0.0006	-0.0004	940.4700	0.0039	1.0286	11.1860
60.0000	56.4410	0.0006	-0.0004	940.5100	-0.0038	1.0660	13.6090

Table A.10: Van der Waals interaction coefficients $C_6(\mathrm{GHz} \cdot \mu m^6)$ and radiative characteristics of $|6P_{3/2}\rangle \rightarrow |nS_{1/2}\rangle$ for $n \in \{31 - 60\}$. (n^*) n is the (effective) principal quantum number, τ (τ_{bb}) is the (blackbody-limited) radiative lifetime (s), r_L is the LeRoy's radius, $\langle J'||e\hat{r}||J\rangle$ and f is the reduced matrix element (ea_0) and the transition frequency (Hz) for the transition $|6P_{3/2}\rangle \rightarrow |nS_{1/2}\rangle$.

n	n^*	τ (s)	τ_{bb} (s)	f (THz)	$\langle J'\|\|e\hat{r}\|\|J\rangle$	r_L (μm)	$C_6(\mathrm{GHz} \cdot \mu m^6)$
61.0000	57.4410	0.0006	-0.0005	940.5500	0.0037	1.1041	16.4990
62.0000	58.4410	0.0007	-0.0005	940.5800	-0.0036	1.1429	19.9370
63.0000	59.4410	0.0007	-0.0005	940.6100	0.0035	1.1824	24.0130
64.0000	60.4410	0.0007	-0.0006	940.6400	-0.0034	1.2225	28.0430
65.0000	61.4410	0.0008	-0.0006	940.6700	0.0033	1.2633	33.0320
66.0000	62.4410	0.0008	-0.0006	940.7000	-0.0032	1.3047	39.4120
67.0000	63.4410	0.0008	-0.0006	940.7200	0.0032	1.3469	46.8580
68.0000	64.4410	0.0009	-0.0007	940.7500	-0.0031	1.3897	54.6840
69.0000	65.4410	0.0009	-0.0007	940.7700	0.0030	1.4331	66.1710
70.0000	66.4410	0.0010	-0.0007	940.8000	-0.0029	1.4773	77.9960
71.0000	67.4410	0.0010	-0.0008	940.8200	0.0029	1.5221	92.1840
72.0000	68.4410	0.0011	-0.0008	940.8400	-0.0028	1.5676	109.3700
73.0000	69.4410	0.0011	-0.0009	940.8600	0.0028	1.6137	127.7400
74.0000	70.4410	0.0012	-0.0009	940.8800	-0.0027	1.6605	149.3500
75.0000	71.4410	0.0012	-0.0009	940.9000	0.0026	1.7080	174.1900
76.0000	72.4410	0.0013	-0.0010	940.9200	-0.0026	1.7562	201.0700
77.0000	73.4410	0.0013	-0.0010	940.9300	0.0025	1.8050	233.0900
78.0000	74.4410	0.0014	-0.0011	940.9500	-0.0025	1.8545	270.9000
79.0000	75.4410	0.0014	-0.0011	940.9600	0.0024	1.9046	314.1600
80.0000	76.4410	0.0015	-0.0012	940.9800	-0.0024	1.9555	362.9500
81.0000	77.4410	0.0015	-0.0012	940.9900	0.0023	2.0070	418.5400
82.0000	78.4410	0.0016	-0.0013	941.0100	-0.0023	2.0591	481.7700
83.0000	79.4410	0.0017	-0.0013	941.0200	0.0023	2.1120	552.0100
84.0000	80.4410	0.0017	-0.0014	941.0300	-0.0022	2.1655	633.1700
85.0000	81.4410	0.0018	-0.0014	941.0500	0.0022	2.2197	725.0500
86.0000	82.4410	0.0019	-0.0015	941.0600	-0.0021	2.2745	829.4300
87.0000	83.4410	0.0019	-0.0016	941.0700	0.0021	2.3300	946.7300
88.0000	84.4410	0.0020	-0.0016	941.0800	-0.0021	2.3862	1078.9000
89.0000	85.4410	0.0021	-0.0017	941.0900	0.0020	2.4431	1227.6000
90.0000	86.4410	0.0021	-0.0017	941.1000	-0.0020	2.5006	1394.7000

Table A.11: Van der Waals interaction coefficients $C_6(\mathrm{GHz} \cdot \mu m^6)$ and radiative characteristics of $|6P_{3/2}\rangle \rightarrow |nS_{1/2}\rangle$ for $n \in \{61-90\}$. (n^*) n is the (effective) principal quantum number, τ (τ_{bb}) is the (blackbody-limited) radiative lifetime (s), r_L is the LeRoy's radius, $\langle J'||e\hat{r}||J\rangle$ and f is the reduced matrix element (ea_0) and the transition frequency (Hz) for the transition $|6P_{3/2}\rangle \rightarrow |nS_{1/2}\rangle$.

n	n^*	τ (s)	τ_{bb} (s)	f (THz)	$\langle J'\|\|e\hat{r}\|\|J\rangle$	r_L (μm)	$C_6(\mathrm{GHz}\cdot\mu m^6)$
91.0000	87.4410	0.0022	-0.0018	941.1100	0.0019	2.5588	1581.7000
92.0000	88.4410	0.0023	-0.0019	941.1200	-0.0019	2.6177	1791.9000
93.0000	89.4410	0.0024	-0.0020	941.1300	0.0019	2.6772	2027.1000
94.0000	90.4410	0.0024	-0.0020	941.1400	-0.0019	2.7374	2290.0000
95.0000	91.4410	0.0025	-0.0021	941.1500	0.0018	2.7983	2583.4000
96.0000	92.4410	0.0026	-0.0022	941.1600	-0.0018	2.8598	2910.7000
97.0000	93.4410	0.0027	-0.0022	941.1700	0.0018	2.9220	3275.9000
98.0000	94.4410	0.0028	-0.0023	941.1700	-0.0017	2.9849	3681.7000
99.0000	95.4410	0.0029	-0.0024	941.1800	0.0017	3.0485	4132.7000
100.0000	96.4410	0.0030	-0.0025	941.1900	-0.0017	3.1127	4633.5000

Table A.12: Van der Waals interaction coefficients $C_6(\mathrm{GHz}\cdot\mu m^6)$ and radiative characteristics of $|6P_{3/2}\rangle \rightarrow |nS_{1/2}\rangle$ for $n \in \{91-100\}$. (n^*) n is the (effective) principal quantum number, τ (τ_{bb}) is the (blackbody-limited) radiative lifetime (s), r_L is the LeRoy's radius, $\langle J'||e\hat{r}||J\rangle$ and f is the reduced matrix element (ea_0) and the transition frequency (Hz) for the transition $|6P_{3/2}\rangle \rightarrow |nS_{1/2}\rangle$.

n	n^*	τ (s)	τ_{bb} (s)	f (THz)	$\langle J'\|\|e\hat{r}\|\|J\rangle$	r_L (μm)	$C_6(\mathrm{GHz}\cdot\mu m^6)$
0.0000	0.0000	0.0000	0.0000	325.4700	-2.1152	0.0000	0.0000
7.0000	4.5253	0.0000	-0.0000	429.1700	0.9939	0.0063	0.0000
8.0000	5.5248	0.0000	-0.0000	482.0300	-0.6186	0.0097	0.0000
9.0000	6.5246	0.0000	-0.0000	512.5400	0.4382	0.0137	0.0000
10.0000	7.5245	0.0000	-0.0000	531.7100	-0.3339	0.0184	0.0000
11.0000	8.5245	0.0000	-0.0000	544.5400	0.2666	0.0238	0.0000
12.0000	9.5245	0.0000	-0.0000	553.5500	-0.2199	0.0298	0.0000
13.0000	10.5240	0.0000	-0.0000	560.1200	0.1858	0.0365	0.0000
14.0000	11.5240	0.0000	-0.0000	565.0500	-0.1598	0.0439	0.0000
15.0000	12.5250	0.0000	-0.0000	568.8400	0.1396	0.0519	0.0000
16.0000	13.5250	0.0000	-0.0000	571.8300	-0.1233	0.0607	0.0000
17.0000	14.5250	0.0000	-0.0000	574.2200	0.1101	0.0701	-0.0000
18.0000	15.5250	0.0000	-0.0000	576.1700	-0.0991	0.0801	0.0000
19.0000	16.5250	0.0000	-0.0000	577.7700	0.0898	0.0908	-0.0000
20.0000	17.5250	0.0000	-0.0000	579.1000	-0.0819	0.1022	0.0000
21.0000	18.5250	0.0000	-0.0000	580.2300	0.0751	0.1143	0.0000
22.0000	19.5250	0.0000	-0.0000	581.1900	-0.0693	0.1270	0.0000
23.0000	20.5250	0.0000	-0.0000	582.0100	0.0641	0.1404	0.0000
24.0000	21.5250	0.0000	-0.0000	582.7200	-0.0596	0.1545	0.0000
25.0000	22.5250	0.0000	-0.0000	583.3300	0.0556	0.1693	0.0000
26.0000	23.5250	0.0000	-0.0000	583.8700	-0.0520	0.1847	0.0000
27.0000	24.5250	0.0000	-0.0000	584.3500	0.0488	0.2007	0.0000
28.0000	25.5250	0.0000	-0.0000	584.7700	-0.0459	0.2175	0.0000
29.0000	26.5250	0.0000	-0.0000	585.1400	0.0433	0.2349	0.0000
30.0000	27.5250	0.0000	-0.0000	585.4700	-0.0409	0.2530	0.0000

Table A.13: Van der Waals interaction coefficients $C_6(\mathrm{GHz}\cdot\mu m^6)$ and radiative characteristics of $|6P_{3/2}\rangle \rightarrow |nD_{3/2}\rangle$ for $n \in \{6-30\}$. (n^*) n is the (effective) principal quantum number, τ (τ_{bb}) is the (blackbody-limited) radiative lifetime (s), r_L is the LeRoy's radius, $\langle J'||e\hat{r}||J\rangle$ and f is the reduced matrix element (ea_0) and the transition frequency (Hz) for the transition $|6P_{3/2}\rangle \rightarrow |nD_{3/2}\rangle$.

n	n^*	τ (s)	τ_{bb} (s)	f (THz)	$\langle J'\|\|e\hat{r}\|\|J\rangle$	r_L (μm)	$C_6(\mathrm{GHz}\cdot\mu m^6)$
31.0000	27.4410	0.0001	-0.0000	937.1700	0.0113	0.2519	0.0001
32.0000	28.4410	0.0001	-0.0000	937.4800	-0.0107	0.2706	0.0001
33.0000	29.4410	0.0001	-0.0000	937.7500	0.0101	0.2899	0.0001
34.0000	30.4410	0.0001	-0.0001	937.9900	-0.0096	0.3100	0.0001
35.0000	31.4410	0.0001	-0.0001	938.2100	0.0092	0.3307	0.0002
36.0000	32.4410	0.0001	-0.0001	938.4200	-0.0087	0.3521	0.0003
37.0000	33.4410	0.0001	-0.0001	938.6000	0.0083	0.3741	0.0004
38.0000	34.4410	0.0001	-0.0001	938.7700	-0.0080	0.3968	0.0005
39.0000	35.4410	0.0001	-0.0001	938.9200	0.0076	0.4202	0.0037
40.0000	36.4410	0.0002	-0.0001	939.0600	-0.0073	0.4443	0.0496
41.0000	37.4410	0.0002	-0.0001	939.2000	0.0070	0.4690	0.1724
42.0000	38.4410	0.0002	-0.0001	939.3200	-0.0068	0.4944	0.2303
43.0000	39.4410	0.0002	-0.0001	939.4300	0.0065	0.5205	0.3053
44.0000	40.4410	0.0002	-0.0001	939.5300	-0.0063	0.5472	0.4019
45.0000	41.4410	0.0002	-0.0002	939.6300	0.0060	0.5746	0.5256
46.0000	42.4410	0.0003	-0.0002	939.7200	-0.0058	0.6027	0.6829
47.0000	43.4410	0.0003	-0.0002	939.8000	0.0056	0.6314	0.8820
48.0000	44.4410	0.0003	-0.0002	939.8800	-0.0054	0.6608	1.1324
49.0000	45.4410	0.0003	-0.0002	939.9500	0.0052	0.6909	1.4460
50.0000	46.4410	0.0003	-0.0002	940.0200	-0.0051	0.7217	1.8365
51.0000	47.4410	0.0004	-0.0002	940.0800	0.0049	0.7531	1.5964
52.0000	48.4410	0.0004	-0.0003	940.1400	-0.0048	0.7852	1.9372
53.0000	49.4410	0.0004	-0.0003	940.2000	0.0046	0.8179	2.4236
54.0000	50.4410	0.0004	-0.0003	940.2500	-0.0045	0.8514	3.0185
55.0000	51.4410	0.0005	-0.0003	940.3000	0.0043	0.8855	3.7450
56.0000	52.4410	0.0005	-0.0003	940.3500	-0.0042	0.9202	4.6251
57.0000	53.4410	0.0005	-0.0004	940.3900	0.0041	0.9557	5.7300
58.0000	54.4410	0.0005	-0.0004	940.4300	-0.0040	0.9918	9.1623
59.0000	55.4410	0.0006	-0.0004	940.4700	0.0039	1.0286	11.1860
60.0000	56.4410	0.0006	-0.0004	940.5100	-0.0038	1.0660	13.6090

Table A.14: Van der Waals interaction coefficients $C_6(\mathrm{GHz}\cdot\mu m^6)$ and radiative characteristics of $|6P_{3/2}\rangle \rightarrow |nD_{3/2}\rangle$ for $n \in \{31-60\}$. (n^*) n is the (effective) principal quantum number, τ (τ_{bb}) is the (blackbody-limited) radiative lifetime (s), r_L is the LeRoy's radius, $\langle J'||e\hat{r}||J\rangle$ and f is the reduced matrix element (ea_0) and the transition frequency (Hz) for the transition $|6P_{3/2}\rangle \rightarrow |nD_{3/2}\rangle$.

n	n^*	τ (s)	τ_{bb} (s)	f (THz)	$\langle J'\|\|e\hat{r}\|\|J\rangle$	r_L (μm)	$C_6(\mathrm{GHz}\cdot\mu m^6)$
61.0000	57.4410	0.0006	-0.0005	940.5500	0.0037	1.1041	16.4990
62.0000	58.4410	0.0007	-0.0005	940.5800	-0.0036	1.1429	19.9370
63.0000	59.4410	0.0007	-0.0005	940.6100	0.0035	1.1824	24.0130
64.0000	60.4410	0.0007	-0.0006	940.6400	-0.0034	1.2225	28.0430
65.0000	61.4410	0.0008	-0.0006	940.6700	0.0033	1.2633	33.0320
66.0000	62.4410	0.0008	-0.0006	940.7000	-0.0032	1.3047	39.4120
67.0000	63.4410	0.0008	-0.0006	940.7200	0.0032	1.3469	46.8580
68.0000	64.4410	0.0009	-0.0007	940.7500	-0.0031	1.3897	54.6840
69.0000	65.4410	0.0009	-0.0007	940.7700	0.0030	1.4331	66.1710
70.0000	66.4410	0.0010	-0.0007	940.8000	-0.0029	1.4773	77.9960
71.0000	67.4410	0.0010	-0.0008	940.8200	0.0029	1.5221	92.1840
72.0000	68.4410	0.0011	-0.0008	940.8400	-0.0028	1.5676	109.3700
73.0000	69.4410	0.0011	-0.0009	940.8600	0.0028	1.6137	127.7400
74.0000	70.4410	0.0012	-0.0009	940.8800	-0.0027	1.6605	149.3500
75.0000	71.4410	0.0012	-0.0009	940.9000	0.0026	1.7080	174.1900
76.0000	72.4410	0.0013	-0.0010	940.9200	-0.0026	1.7562	201.0700
77.0000	73.4410	0.0013	-0.0010	940.9300	0.0025	1.8050	233.0900
78.0000	74.4410	0.0014	-0.0011	940.9500	-0.0025	1.8545	270.9000
79.0000	75.4410	0.0014	-0.0011	940.9600	0.0024	1.9046	314.1600
80.0000	76.4410	0.0015	-0.0012	940.9800	-0.0024	1.9555	362.9500
81.0000	77.4410	0.0015	-0.0012	940.9900	0.0023	2.0070	418.5400
82.0000	78.4410	0.0016	-0.0013	941.0100	-0.0023	2.0591	481.7700
83.0000	79.4410	0.0017	-0.0013	941.0200	0.0023	2.1120	552.0100
84.0000	80.4410	0.0017	-0.0014	941.0300	-0.0022	2.1655	633.1700
85.0000	81.4410	0.0018	-0.0014	941.0500	0.0022	2.2197	725.0500
86.0000	82.4410	0.0019	-0.0015	941.0600	-0.0021	2.2745	829.4300
87.0000	83.4410	0.0019	-0.0016	941.0700	0.0021	2.3300	946.7300
88.0000	84.4410	0.0020	-0.0016	941.0800	-0.0021	2.3862	1078.9000
89.0000	85.4410	0.0021	-0.0017	941.0900	0.0020	2.4431	1227.6000
90.0000	86.4410	0.0021	-0.0017	941.1000	-0.0020	2.5006	1394.7000

Table A.15: Van der Waals interaction coefficients $C_6(\mathrm{GHz}\cdot\mu m^6)$ and radiative characteristics of $|6P_{3/2}\rangle \rightarrow |nD_{3/2}\rangle$ for $n \in \{61-90\}$. (n^*) n is the (effective) principal quantum number, τ (τ_{bb}) is the (blackbody-limited) radiative lifetime (s), r_L is the LeRoy's radius, $\langle J'||e\hat{r}||J\rangle$ and f is the reduced matrix element (ea_0) and the transition frequency (Hz) for the transition $|6P_{3/2}\rangle \rightarrow |nD_{3/2}\rangle$.

n	n^*	τ (s)	τ_{bb} (s)	f (THz)	$\langle J'\|\|e\hat{r}\|\|J\rangle$	r_L (μm)	$C_6(\text{GHz}\cdot\mu m^6)$
91.0000	87.4410	0.0022	-0.0018	941.1100	0.0019	2.5588	1581.7000
92.0000	88.4410	0.0023	-0.0019	941.1200	-0.0019	2.6177	1791.9000
93.0000	89.4410	0.0024	-0.0020	941.1300	0.0019	2.6772	2027.1000
94.0000	90.4410	0.0024	-0.0020	941.1400	-0.0019	2.7374	2290.0000
95.0000	91.4410	0.0025	-0.0021	941.1500	0.0018	2.7983	2583.4000
96.0000	92.4410	0.0026	-0.0022	941.1600	-0.0018	2.8598	2910.7000
97.0000	93.4410	0.0027	-0.0022	941.1700	0.0018	2.9220	3275.9000
98.0000	94.4410	0.0028	-0.0023	941.1700	-0.0017	2.9849	3681.7000
99.0000	95.4410	0.0029	-0.0024	941.1800	0.0017	3.0485	4132.7000
100.0000	96.4410	0.0030	-0.0025	941.1900	-0.0017	3.1127	4633.5000

Table A.16: Van der Waals interaction coefficients $C_6(\text{GHz}\cdot\mu m^6)$ and radiative characteristics of $|6P_{3/2}\rangle \rightarrow |nD_{3/2}\rangle$ for $n \in \{91-100\}$. (n^*) n is the (effective) principal quantum number, τ (τ_{bb}) is the (blackbody-limited) radiative lifetime (s), r_L is the LeRoy's radius, $\langle J'||e\hat{r}||J\rangle$ and f is the reduced matrix element (ea_0) and the transition frequency (Hz) for the transition $|6P_{3/2}\rangle \rightarrow |nD_{3/2}\rangle$.

n	n^*	τ (s)	τ_{bb} (s)	f (THz)	$\langle J'\|\|e\hat{r}\|\|J\rangle$	r_L (μm)	$C_6(\mathrm{GHz}\cdot\mu m^6)$
0.0000	0.0000	0.0000	0.0000	326.7600	-6.1860	0.0000	0.0000
7.0000	4.5342	0.0000	-0.0000	429.8000	2.9403	0.0063	0.0000
8.0000	5.5337	0.0000	-0.0000	482.3800	-1.8381	0.0097	0.0000
9.0000	6.5336	0.0000	-0.0000	512.7500	1.3050	0.0137	0.0000
10.0000	7.5336	0.0000	-0.0000	531.8500	-0.9958	0.0184	0.0000
11.0000	8.5336	0.0000	-0.0000	544.6400	0.7958	0.0238	0.0000
12.0000	9.5336	0.0000	-0.0000	553.6200	-0.6568	0.0299	0.0000
13.0000	10.5340	0.0000	-0.0000	560.1700	0.5551	0.0366	0.0000
14.0000	11.5340	0.0000	-0.0000	565.0900	-0.4778	0.0440	0.0000
15.0000	12.5340	0.0000	-0.0000	568.8700	0.4173	0.0520	0.0000
16.0000	13.5340	0.0000	-0.0000	571.8500	-0.3689	0.0607	0.0000
17.0000	14.5340	0.0000	-0.0000	574.2400	0.3293	0.0701	0.0000
18.0000	15.5340	0.0000	-0.0000	576.1800	-0.2964	0.0802	0.0000
19.0000	16.5340	0.0000	-0.0000	577.7800	0.2687	0.0909	0.0000
20.0000	17.5340	0.0000	-0.0000	579.1200	-0.2452	0.1023	0.0000
21.0000	18.5340	0.0000	-0.0000	580.2400	0.2249	0.1144	0.0000
22.0000	19.5340	0.0000	-0.0000	581.1900	-0.2073	0.1272	0.0000
23.0000	20.5340	0.0000	-0.0000	582.0100	0.1919	0.1406	0.0000
24.0000	21.5340	0.0000	-0.0000	582.7200	-0.1784	0.1546	-0.0000
25.0000	22.5340	0.0000	-0.0000	583.3400	0.1663	0.1694	0.0000
26.0000	23.5340	0.0000	-0.0000	583.8800	-0.1556	0.1848	0.0000
27.0000	24.5340	0.0000	-0.0000	584.3500	0.1460	0.2009	0.0000
28.0000	25.5340	0.0000	-0.0000	584.7700	-0.1374	0.2177	0.0000
29.0000	26.5340	0.0000	-0.0000	585.1400	0.1295	0.2351	0.0000
30.0000	27.5340	0.0000	-0.0000	585.4800	-0.1224	0.2532	0.0000

Table A.17: Van der Waals interaction coefficients $C_6(\mathrm{GHz}\cdot\mu m^6)$ and radiative characteristics of $|6P_{3/2}\rangle \rightarrow |nD_{5/2}\rangle$ for $n \in \{6-30\}$. (n^*) n is the (effective) principal quantum number, τ (τ_{bb}) is the (blackbody-limited) radiative lifetime (s), r_L is the LeRoy's radius, $\langle J'||e\hat{r}||J\rangle$ and f is the reduced matrix element (ea_0) and the transition frequency (Hz) for the transition $|6P_{3/2}\rangle \rightarrow |nD_{5/2}\rangle$.

n	n^*	τ (s)	τ_{bb} (s)	f (THz)	$\langle J'\|\|e\hat{r}\|\|J\rangle$	r_L (μm)	$C_6(\mathrm{GHz}\cdot\mu m^6)$
31.0000	28.5340	0.0000	-0.0000	585.7800	0.1160	0.2719	0.0000
32.0000	29.5340	0.0000	-0.0000	586.0400	-0.1100	0.2914	-0.0000
33.0000	30.5340	0.0000	-0.0000	586.2900	0.1046	0.3115	-0.0000
34.0000	31.5340	0.0000	-0.0000	586.5100	-0.0996	0.3322	0.0000
35.0000	32.5340	0.0000	-0.0000	586.7100	0.0950	0.3537	-0.0000
36.0000	33.5340	0.0000	-0.0000	586.8900	-0.0907	0.3758	-0.0000
37.0000	34.5340	0.0000	-0.0000	587.0600	0.0868	0.3986	-0.0227
38.0000	35.5340	0.0000	-0.0000	587.2100	-0.0831	0.4220	-0.0313
39.0000	36.5340	0.0000	-0.0000	587.3500	0.0797	0.4461	-0.0426
40.0000	37.5340	0.0000	-0.0000	587.4800	-0.0765	0.4709	-0.0577
41.0000	38.5340	0.0000	-0.0000	587.6000	0.0735	0.4964	-0.0774
42.0000	39.5340	0.0000	-0.0000	587.7100	-0.0707	0.5225	-0.1030
43.0000	40.5340	0.0000	-0.0000	587.8100	0.0681	0.5493	-0.1362
44.0000	41.5340	0.0000	-0.0000	587.9100	-0.0656	0.5768	-0.1788
45.0000	42.5340	0.0001	-0.0000	588.0000	0.0633	0.6049	-0.2332
46.0000	43.5340	0.0001	-0.0000	588.0800	-0.0611	0.6337	-0.2697
47.0000	44.5340	0.0001	-0.0000	588.1600	0.0591	0.6632	0.3381
48.0000	45.5340	0.0001	-0.0000	588.2300	-0.0571	0.6934	0.4289
49.0000	46.5340	0.0001	-0.0000	588.3000	0.0553	0.7242	0.5407
50.0000	47.5340	0.0001	-0.0000	588.3600	-0.0536	0.7556	0.6783
51.0000	48.5340	0.0001	-0.0000	588.4200	0.0519	0.7878	0.8472
52.0000	49.5340	0.0001	-0.0000	588.4800	-0.0503	0.8206	1.0534
53.0000	50.5340	0.0001	-0.0000	588.5300	0.0488	0.8541	1.3041
54.0000	51.5340	0.0001	-0.0000	588.5800	-0.0474	0.8883	1.6080
55.0000	52.5340	0.0001	-0.0000	588.6200	0.0461	0.9231	1.9748
56.0000	53.5340	0.0001	-0.0000	588.6700	-0.0448	0.9586	2.4160
57.0000	54.5340	0.0001	-0.0000	588.7100	0.0435	0.9948	2.9451
58.0000	55.5340	0.0001	-0.0000	588.7500	-0.0424	1.0316	3.5773
59.0000	56.5340	0.0001	-0.0000	588.7900	0.0412	1.0691	1.4366
60.0000	57.5340	0.0001	-0.0000	588.8200	-0.0402	1.1073	1.6034

Table A.18: Van der Waals interaction coefficients $C_6(\mathrm{GHz}\cdot\mu m^6)$ and radiative characteristics of $|6P_{3/2}\rangle \rightarrow |nD_{5/2}\rangle$ for $n \in \{31-60\}$. (n^*) n is the (effective) principal quantum number, τ (τ_{bb}) is the (blackbody-limited) radiative lifetime (s), r_L is the LeRoy's radius, $\langle J'||e\hat{r}||J\rangle$ and f is the reduced matrix element (ea_0) and the transition frequency (Hz) for the transition $|6P_{3/2}\rangle \rightarrow |nD_{5/2}\rangle$.

n	n^*	τ (s)	τ_{bb} (s)	f (THz)	$\langle J'\|\|e\hat{r}\|\|J\rangle$	r_L (μm)	$C_6(\mathrm{GHz}\cdot\mu m^6)$
61.0000	58.5340	0.0001	-0.0001	588.8600	0.0391	1.1461	1.9002
62.0000	59.5340	0.0001	-0.0001	588.8900	-0.0382	1.1856	2.2454
63.0000	60.5340	0.0001	-0.0001	588.9200	0.0372	1.2258	2.6635
64.0000	61.5340	0.0002	-0.0001	588.9500	-0.0363	1.2667	5.0719
65.0000	62.5340	0.0002	-0.0001	588.9800	0.0354	1.3082	5.9834
66.0000	63.5340	0.0002	-0.0001	589.0000	-0.0346	1.3504	7.0405
67.0000	64.5340	0.0002	-0.0001	589.0300	0.0338	1.3933	8.2636
68.0000	65.5340	0.0002	-0.0001	589.0500	-0.0330	1.4368	9.6757
69.0000	66.5340	0.0002	-0.0001	589.0700	0.0323	1.4810	11.3020
70.0000	67.5340	0.0002	-0.0001	589.1000	-0.0316	1.5259	11.5640
71.0000	68.5340	0.0002	-0.0001	589.1200	0.0309	1.5714	13.4230
72.0000	69.5340	0.0002	-0.0001	589.1400	-0.0302	1.6176	15.6860
73.0000	70.5340	0.0002	-0.0001	589.1600	0.0296	1.6645	20.8740
74.0000	71.5340	0.0002	-0.0001	589.1700	-0.0289	1.7120	24.1190
75.0000	72.5340	0.0003	-0.0001	589.1900	0.0283	1.7603	27.8130
76.0000	73.5340	0.0003	-0.0001	589.2100	-0.0278	1.8091	32.0120
77.0000	74.5340	0.0003	-0.0001	589.2200	0.0272	1.8587	36.7750
78.0000	75.5340	0.0003	-0.0001	589.2400	-0.0267	1.9089	42.1710
79.0000	76.5340	0.0003	-0.0001	589.2500	0.0262	1.9598	47.6450
80.0000	77.5340	0.0003	-0.0001	589.2700	-0.0256	2.0114	54.2940
81.0000	78.5340	0.0003	-0.0002	589.2800	0.0252	2.0636	62.1520
82.0000	79.5340	0.0003	-0.0002	589.3000	-0.0247	2.1165	70.7780
83.0000	80.5340	0.0003	-0.0002	589.3100	0.0242	2.1701	80.4730
84.0000	81.5340	0.0004	-0.0002	589.3200	-0.0238	2.2243	91.3530
85.0000	82.5340	0.0004	-0.0002	589.3300	0.0233	2.2792	103.5500
86.0000	83.5340	0.0004	-0.0002	589.3500	-0.0229	2.3348	117.1900
87.0000	84.5340	0.0004	-0.0002	589.3600	0.0225	2.3911	133.6900
88.0000	85.5340	0.0004	-0.0002	589.3700	-0.0221	2.4480	150.8900
89.0000	86.5340	0.0004	-0.0002	589.3800	0.0217	2.5056	170.0700
90.0000	87.5340	0.0004	-0.0002	589.3900	-0.0214	2.5638	191.4200

Table A.19: Van der Waals interaction coefficients $C_6(\mathrm{GHz}\cdot\mu m^6)$ and radiative characteristics of $|6P_{3/2}\rangle \rightarrow |nD_{5/2}\rangle$ for $n \in \{61-90\}$. (n^*) n is the (effective) principal quantum number, τ (τ_{bb}) is the (blackbody-limited) radiative lifetime (s), r_L is the LeRoy's radius, $\langle J'||e\hat{r}||J\rangle$ and f is the reduced matrix element (ea_0) and the transition frequency (Hz) for the transition $|6P_{5/2}\rangle \rightarrow |nD_{5/2}\rangle$.

n	n^*	τ (s)	τ_{bb} (s)	f (THz)	$\langle J' \vert\vert e\hat{r} \vert\vert J \rangle$	r_L (μm)	$C_6(\text{GHz} \cdot \mu m^6)$
91.0000	88.5340	0.0005	-0.0002	589.4000	0.0210	2.6227	215.1700
92.0000	89.5340	0.0005	-0.0002	589.4100	-0.0207	2.6823	241.5700
93.0000	90.5340	0.0005	-0.0002	589.4200	0.0203	2.7426	270.5800
94.0000	91.5340	0.0005	-0.0003	589.4200	-0.0200	2.8035	302.8100
95.0000	92.5340	0.0005	-0.0003	589.4300	0.0197	2.8651	338.6600
96.0000	93.5340	0.0005	-0.0003	589.4400	-0.0193	2.9274	377.7900
97.0000	94.5340	0.0006	-0.0003	589.4500	0.0190	2.9904	422.3900
98.0000	95.5340	0.0006	-0.0003	589.4600	-0.0187	3.0540	470.8100
99.0000	96.5340	0.0006	-0.0003	589.4600	0.0185	3.1183	524.1600
100.0000	97.5340	0.0006	-0.0003	589.4700	-0.0182	3.1832	582.9300

Table A.20: Van der Waals interaction coefficients $C_6(\text{GHz} \cdot \mu m^6)$ and radiative characteristics of $|6P_{3/2}\rangle \rightarrow |nD_{5/2}\rangle$ for $n \in \{91 - 100\}$. (n^*) n is the (effective) principal quantum number, τ (τ_{bb}) is the (blackbody-limited) radiative lifetime (s), r_L is the LeRoy's radius, $\langle J' || e\hat{r} || J \rangle$ and f is the reduced matrix element (ea_0) and the transition frequency (Hz) for the transition $|6P_{3/2}\rangle \rightarrow |nD_{5/2}\rangle$.